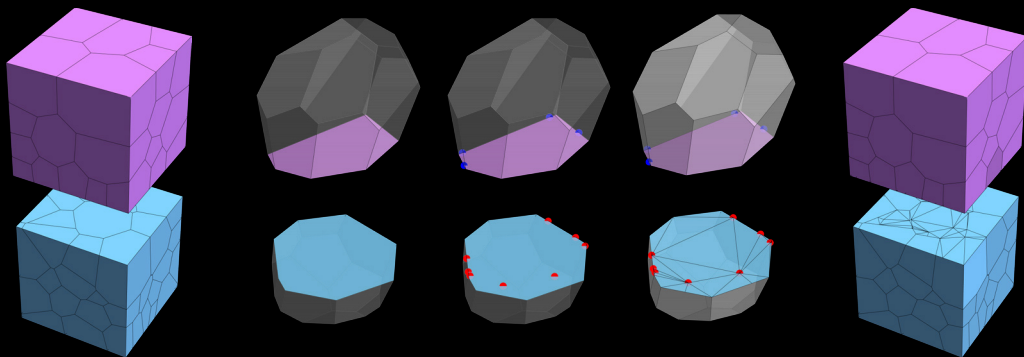
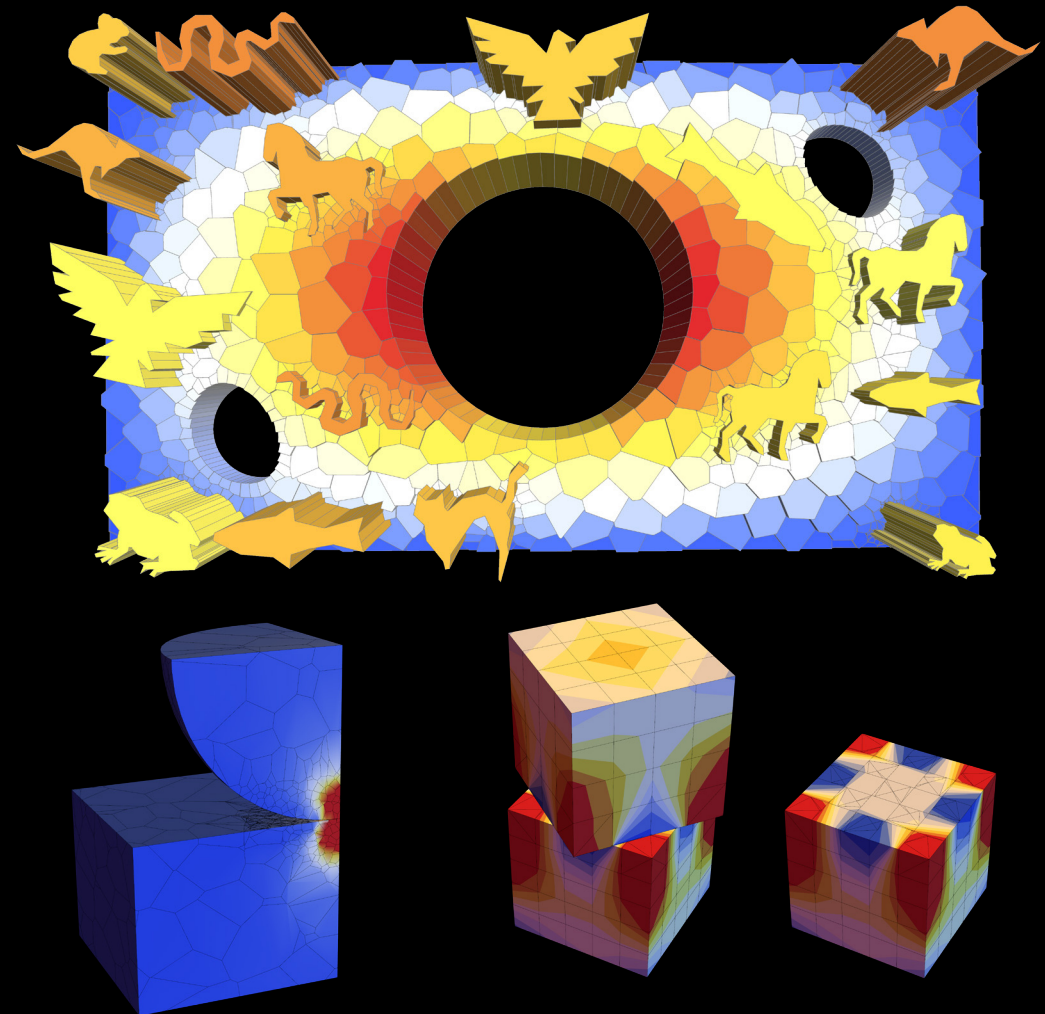


The Virtual Element Method (VEM) rises as a generalization of the popular Finite Element Method (FEM) and offers greater flexibility in dealing with complex geometries, overcoming FEM's limitations in terms of simple element topologies. This research focuses on applying VEM for modeling of three-dimensional contact and dynamic behavior. It presents a novel projection algorithm for modeling three-dimensional contact problems by modifying the contact interface mesh to obtain matching meshes at the interface and thus allow a simple node-to-node contact. Numerical examples, including benchmark problems, demonstrate the effectiveness of the developed formulations compared to classical FEM approaches. Ultimately, this book provides valuable insights into the potential of VEM for efficient and accurate numerical predictions, highlighting its applications in various fields and its ability to handle complex engineering challenges.



Mertcan Cihan | A Virtual Element Method for Contact Modeling and Dynamics



A Virtual Element Method for Contact Modeling and Dynamics

Von der Fakultät für Maschinenbau
der Gottfried Wilhelm Leibniz Universität Hannover

zur Erlangung des akademischen Grades

Doktor-Ingenieur

Dr.-Ing.

genehmigte Dissertation

von

M. Sc. Mertcan Cihan

geboren am 26.12.1992 in Bremen

2023

Herausgeber:

Prof. em. Dr.-Ing. habil. Dr. h.c. mult. Dr.-Ing. E.h. Peter Wriggers

Verwaltung:

Institut für Kontinuumsmechanik
Gottfried Wilhelm Leibniz Universität Hannover
An der Universität 1
30823 Garbsen

Tel: +49 511 762 3220

Fax: +49 511 762 5496

Web: www.ikm.uni-hannover.de

© M. Sc. Mertcan Cihan

Institut für Kontinuumsmechanik
Gottfried Wilhelm Leibniz Universität Hannover
An der Universität 1
30823 Garbsen

Alle Rechte, insbesondere das der Übersetzung in fremde Sprachen, vorbehalten. Ohne Genehmigung des Autors ist es nicht gestattet, dieses Heft ganz oder teilweise auf photomechanischem, elektronischem oder sonstigem Wege zu vervielfältigen.

ISBN 978-3-941302-51-8

1. Referent: Prof. em. Dr.-Ing. habil. Dr. h.c. mult. Dr.-Ing. E.h. Peter Wriggers

2. Referent: Prof. Dr. Eugenio Oñate

Tag der Promotion: 22.06.2023

This work is dedicated to my grandfathers, Zeki Karasu and Güler Cihan, who both passed away during the Covid pandemic.

Görüşmek üzere güzel insanlar...

Zusammenfassung

Eine Verringerung von Ressourcen und die damit einhergehende Energieknappheit führen zu einem erhöhten Bedarf an virtuellen Entwicklungsprozessen und effizienter Produktentwicklung. Dieser Trend verdeutlicht die Bedeutung der Digitalisierung und den daraus resultierenden Bedarf an effizienten und hoch genauen numerischen Vorhersagemethoden für die Produktentwicklung. Aufgrund ihrer Flexibilität und mit steigenden Rechnerkapazitäten ersetzen numerische Methoden allmählich und stetig physikalische Tests in der industriellen Produktentwicklung.

Die Finite Elemente Methode ist vielleicht die bekannteste und am weitesten verbreitete numerische Methode in Industrie und Wissenschaft. Durch die zunehmenden Rechnerkapazitäten und die Weiterentwicklung dieser Methoden in den letzten Jahren hat sich die Zahl der Anwendungsbereiche vergrößert. Numerische Methoden werden unter anderem im Bauwesen, im Automobilbau, in der Schifffahrt, in der Luft- und Raumfahrt und in der Geotechnik eingesetzt. Bei komplexen Geometrien erweist sich jedoch die räumliche Diskretisierung des Gebiets als ein sehr zeitaufwändiger Prozess. Da die klassische Finite Elemente Methode auf einfache, regelmäßig geformte Elementgeometrien beschränkt ist, würde eine allgemeinere Auswahl von Elementgeometrien mehr Flexibilität bieten. Innerhalb der netzbasierten Methoden sind polygonale Methoden eine hilfreiche Alternative und haben sich bereits in Industrie und Wissenschaft bewährt. Allerdings scheinen die meisten dieser Methoden einen höheren Rechenaufwand zu erfordern, und neben dem bereits erwähnten Vorteil der flexiblen Elementgeometrien treten auch gewisse Nachteile auf. Eine relativ neue Methode, die Virtuelle Elemente Methode, verspricht gute numerische Eigenschaften und kann als eine Verallgemeinerung der klassischen Finite Elemente Methode angesehen werden. Wie bei allen neuen Methoden müssen auch hier verschiedene Anwendungen in der Industrie und Wissenschaft untersucht werden, bevor die Methode kommerziell eingesetzt werden kann.

Diese Arbeit befasst sich mit der Anwendung der Methode der virtuellen Elemente auf dynamisches und elasto-plastisches Materialverhalten. Um elastische und plastische Inkompressibilität zu behandeln, wird auch eine gemischte virtuelle Elementformulierung vorgestellt. In einem weiteren Schritt wird die Virtuelle Elemente Methode zur Modellierung dreidimensionaler Kontaktprobleme mit verschiedenen Kontaktdiskretisierungen verwendet. Es wird ein neuer Projektionsalgorithmus vorgestellt, welcher das Netz an der Kontaktschnittstelle so manipuliert, dass eine sehr einfache und effiziente Knoten-zu-Knoten Kontaktformulierung verwendet werden kann.

Es werden verschiedene numerische Beispiele für alle oben genannten Anwendungen behandelt, darunter auch Benchmark-Probleme wie der klassische Patch-Test. Um einen geeigneten Vergleich durchzuführen, werden die entwickelten Formulierungen mit verschiedenen Finite Elemente Formulierungen verglichen. Als letztes Beispiel werden alle Modelle, einschließlich Plastizität, Dynamik und Kontakt, gekoppelt, um einen mechanischen Stoß zu modellieren.

Schlagnworte: Virtuelle Elemente Methode, Polygonale Methoden, Dynamik, Gemischte Methoden, Kontaktmechanik, Mechanischer Stoß, Stabilisierte Methoden

Abstract

Decreasing resources and limited energy results in a greater demand for virtual development processes and efficient product development. This trend points out the importance of digitalization and the subsequent need for efficient and accurate numerical prediction methods for product development. Due to their flexibility, numerical methods are gradually and steadily replacing physical tests in industrial product developments.

The finite element method is perhaps the most well-known and widely used numerical method in industry and science. Increasing computer capabilities and further developments of these methods in recent years have increased the amount of application fields, including civil, automotive, naval, space and geo-technical engineering. However, along with complex geometries the spatial discretization of the domain emerges as a very time consuming step. Due to the fact that the classical finite element method is restricted to basic regular shaped element topologies, a more general choice of element shapes would give more flexibility.

Within mesh-based methods, polygonal methods are a helpful alternative and showed great performance in engineering and science. However, most of these methods seem to need more computational effort and beside the aforementioned advantage of flexible element shapes, disadvantages appear as well. A relatively new method, the virtual element method, promises great numerical properties and can be seen as a generalization of the classical finite element method. All new methods need to be investigated for different applications in engineering and science before they can be applied commercially.

This work deals with the application of the virtual element method to dynamic and elastoplastic material behavior. To deal with elastic and plastic incompressibility, a mixed virtual element formulation is presented as well. As a further development, the virtual element method is used to model three dimensional contact with different contact discretizations. A new projection algorithm is developed to manipulate the mesh at the contact interface, such that a very simple and efficient node-to-node contact formulation can be used.

Various numerical examples for all aforementioned applications are performed, including benchmark problems such as the classical patch test. For comparison purposes, different finite element formulations are also adopted. As a final example, all models, including plasticity, dynamics and contact, are coupled to model mechanical impact.

Keywords: Virtual element method, Polygonal methods, Dynamic, Mixed methods, Contact mechanics, Impact, Stabilized methods

Acknowledgements

At the end of a long and challenging yet enjoyable road, I would like to express my heartfelt gratitude to everyone who has supported and believed in me during my journey. First and foremost, I would like to express my deepest appreciation to Prof. em. Dr.-Ing. habil. Dr. h.c. mult. Dr.-Ing. E.h. Peter Wriggers for his trust, exceptional supervision and the opportunity to work at the Institute of Continuum Mechanics while giving me the most possible freedom in doing my research.

I am immensely grateful to Prof. Dr. Eugenio Oñate for serving as my second supervisor and providing invaluable insights and comments on this work. Additionally, I extend my deepest thanks to Prof. Dr.-Ing. habil. Philipp Junker for his kindness and unwavering support throughout my academic journey.

I would also like to extend my sincere thanks to Dr. Blaž Hudobivnik, who was always available with an open door whenever I had questions or faced challenges. I am also thankful to Dr.-Ing. Alex Ricker, my former office colleague, for fostering a pleasant and supportive work environment. My heartfelt appreciation also goes to Dr.-Ing. Meisam Soleimani and Dr.-Ing. Tobias Bode for their valuable suggestions.

Furthermore, I would like to acknowledge Vera Halfar and Vanessa Wunnenberg for their constant support with bureaucratic issues, Jens Bsdok and Timo Rabing for helping me out with IT problems and Volker Meine for drawing most of the figures in this work. I am also thankful to all my current and former colleagues for all the discussions, moments of entertainment, and their emotional support.

Lastly, I would like to show my deepest gratitude to the most important persons in my life.

Hayatım boyunca beni destekleyen, haklarını asla ödeyemeyeceğim annem Menşure ve babam Ademe teşekkürlerimi sunarım.

Hannover, July 2023

Mertcan Cihan

Contents

1	Introduction	1
1.1	Motivation and state of the art	1
1.2	Structure of this work	4
2	Continuum solid mechanics	5
2.1	Kinematics and stresses	5
2.1.1	Motion and deformation gradient	5
2.1.2	Strain measures	7
2.1.3	Stress measures	7
2.2	Balance laws	8
2.2.1	Balance of mass	8
2.2.2	Balance of linear and angular momentum	8
2.2.3	Balance of energy	11
2.2.4	Entropy inequality	12
2.3	Constitutive equations	14
2.3.1	Hyperelasticity	14
2.3.2	Finite elasto-plasticity	15
2.4	Weak form of equilibrium	16
2.4.1	Principle of virtual work	16
2.4.2	Hamilton's principle of stationary action	17
2.4.3	Hu-Washizu principle	18
3	Computational contact mechanics	19
3.1	Contact kinematics	20
3.2	Treatment of contact constraints	21
3.2.1	Penalty method	21
3.2.2	Lagrange multiplier method	21
3.2.3	Augmented Lagrange method	22
3.3	Contact discretization	22
4	Virtual element method	25
4.1	The concept of discretization	25
4.2	The finite element method and the differences to the virtual element method	27
4.3	Virtual element space and projection operator	30
4.4	Construction of the virtual element	31

4.4.1	Integration over triangles	32
4.4.2	Integration over edges	34
4.5	Construction of the potential function	37
4.5.1	Time discretization	37
4.5.2	Displacement based formulation	38
4.5.3	Stabilization techniques	40
4.5.4	Mixed formulation	42
4.6	Load approximation	43
4.7	Solution scheme and linearization of static and dynamic formulation	45
4.8	Solution scheme and linearization of plasticity	47
4.9	Validation	49
4.9.1	Patch test	49
4.9.2	Projection test	50
4.9.3	Eigenvalue and tangent comparison of finite and virtual element method	51
5	Contact modeling via the virtual element method	55
5.1	Node-to-surface approach	55
5.2	Node-to-node approach	57
5.2.1	Algorithmic treatment of node-to-node contact	59
5.2.2	Algorithmic treatment of the global search for node-to-surface contact	60
5.2.3	Implementation aspects	60
5.3	Surface-to-surface approach	62
6	Numerical examples	69
6.1	Comparison of edge-integration and trig-integration	69
6.1.1	3D Cook's membrane	69
6.2	Dynamics	70
6.2.1	Eigenvalue analysis	73
6.2.2	Wave propagation in longitudinal beams	76
6.2.3	Transversal beam vibration	79
6.2.4	2D Cook's membrane problem	81
6.2.5	Wave propagation in a bar	82
6.2.6	Transversal vibration of a thick beam	83
6.2.7	Vibration of a thick plate	87
6.2.8	Summary and conclusions	87
6.3	Elasto-plasto dynamics	89
6.3.1	Necking problem	90
6.3.2	3D beam	91
6.3.3	Taylor Anvil test	93
6.3.4	Punch problem	96
6.3.5	Summary and conclusions	99
6.4	Node-to-node contact	100
6.4.1	Contact patch test	100
6.4.2	Hertzian problem	101

6.4.3	Rotating blocks	103
6.4.4	Summary and conclusion	105
6.5	Surface-to-surface contact	107
6.5.1	Contact patch test	107
6.5.2	Comparison of surface-to-surface and node-to-node contact	108
6.5.3	Summary and conclusion	109
6.6	Coupled Taylor Anvil impact	110
7	Conclusions	113
7.1	Achievements	113
7.2	Outlook	114
A		117
A.1	Divergence theorem	117
A.2	Finite element shape functions	118
A.2.1	One-Dimensional shape functions	118
A.2.2	Two-Dimensional shape functions	118
A.2.3	Three-Dimensional shape functions	118
A.3	Gauss-Integration	119
	Bibliography	120
	List of Figures	131
	List of Tables	135
	CURRICULUM VITAE	136

Chapter 1

Introduction

1.1 Motivation and state of the art

In recent years, enormous efforts have been made to achieve economic efficiency and financial cost reductions within the product development process, which depends on various factors. However, the development of commercial mechanical products requires a final approval, which has a major impact on the production costs, especially for components that involve an interaction with humans. The authors in THOMKE & FUJIMOTO (2000) showed a comprehensive study on advanced product development steps for crash tests at BMW AG in Germany. The authors concluded that a physical prototype based testing requires about 60 times higher costs, including all efforts. Beside that, the total time for the crash tests can be decreased from several months for using a physical prototype up to few days or weeks by using computational methods during the product development process, see THOMKE & FUJIMOTO (2000).

Numerical methods are already widely used for mechanical component approvals and throughout the whole product development process, onward with the concept phase and proceeding through series production and product release. Recent research activities over the past decades in combination with increasing computing performance have improved the predictive capability of numerical methods in individual disciplines to a very high level, see SABAT & KUNDU (2021). To satisfy future requirements due to more sophisticated production processes and higher demand on efficiency regarding decreasing resources, the virtual development process and numerical methods must be further improved. The typical steps within a whole numerical simulation framework are shown in Fig. 1.1. The geometry decomposition, which can be seen as a preparation for the construction of the mesh, and the mesh generation together with eventual mesh manipulations consume most of the time, see HARDWICK ET AL. (2005). The authors in HARDWICK ET AL. (2005) have shown that about half of the time spend for those preparations and mesh generation, see Fig. 1.2. Thus the meshing process can be seen as a main bottleneck of mesh based numerical methods in industrial applications. Among all mesh based numerical methods, the classical finite element method (FEM) is the most common one. It has already been demonstrated that it can be used in a variety of fields and provides appropriate results. However, mesh generation can still be a challenging task, in particularly when dealing with complex structures. The restriction to simple element topologies makes the meshing process difficult. In recent

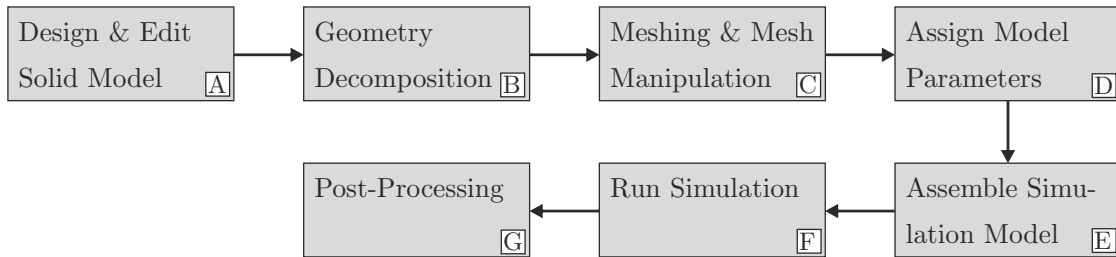


Figure 1.1 – Simulation process steps from HARDWICK ET AL. (2005).

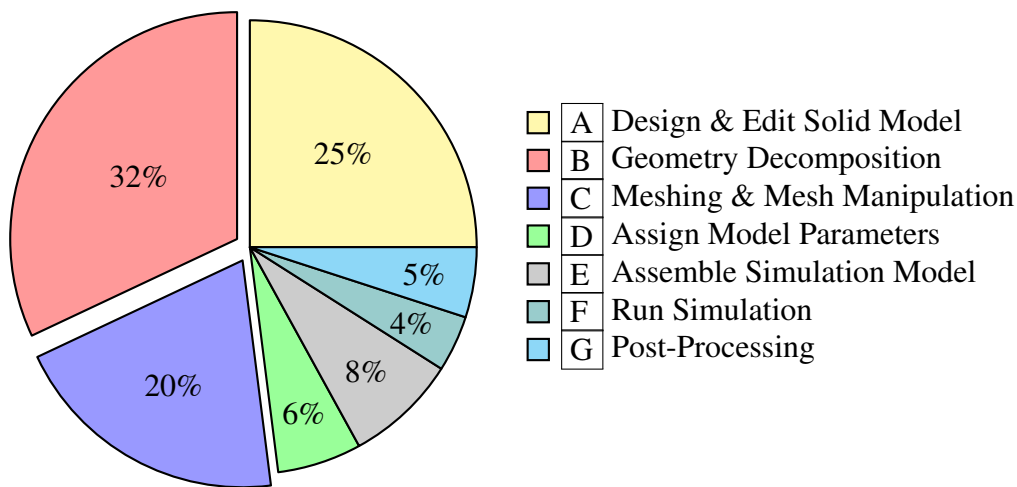


Figure 1.2 – Engineering time for commercial modeling (normalized) from HARDWICK ET AL. (2005).

years, extensions of FEM towards more generalized formulations regarding element topologies have been introduced. Being more flexible in terms of element shapes can make the meshing process easier and can reduce the time for the mesh generation. The polygonal finite element method (PFEM) in MEYER ET AL. (2002); SUKUMAR & TABARRAEI (2004), the discontinuous Galerkin finite element method (DGFEM) in WIRASAET ET AL. (2014); CANGIANI ET AL. (2014) or the mimetic finite difference method (MFD) in BEIRÃO DA VEIGA ET AL. (2009); BREZZI ET AL. (2005b,a) are just a part of a huge variety of different polygonal methods, which can be found in the literature, see PERUMAL (2018). The latter motivated the development of the virtual element method (VEM), which was first introduced around 2012 in BEIRÃO DA VEIGA ET AL. (2013a). VEM gained high interest quickly in both mathematics and engineering communities. However, like for all newly introduced methods, applications to new fields have to be investigated and verified. Further investigations need to be made to proof its stability and robustness, until VEM can be accepted for commercial applications. A major advantage of VEM lies in its general formulation and flexibility in the use of arbitrary element shapes with an arbitrary number of nodes as can be seen in Fig. 1.3. It has significant benefits in solving problems on polygonal meshes and the difficulties encountered in integrating complex functions resulting from barycentric

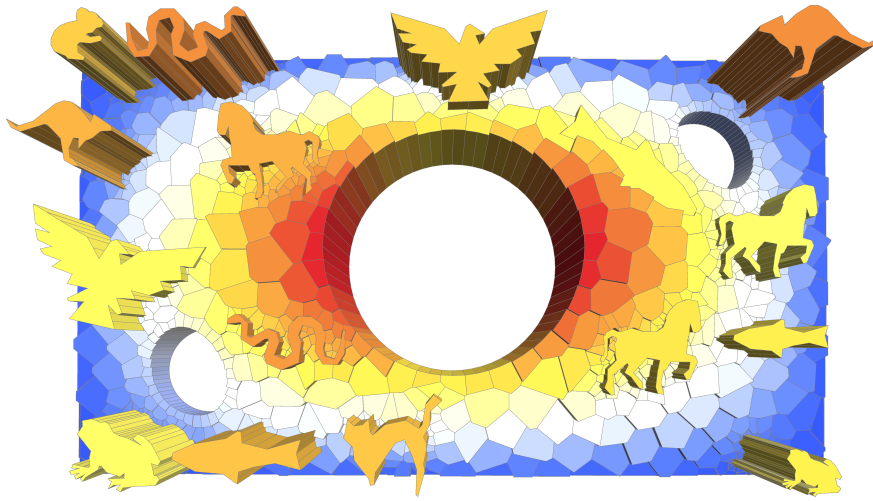


Figure 1.3 – Virtual element discretization with arbitrary shaped elements, including non-convex animal type elements.

coordinates in PFEM are completely avoided, see PERUMAL (2018).

However, the approximation of the unknowns solely with the VEM projection function leads to a rank deficient structure of the problem. For this reason, a stabilization is required and it increases the computational costs. VEM has already been applied to a variety of application fields in engineering and science as for example for solid mechanics with small and finite strain elasticity in BEIRÃO DA VEIGA ET AL. (2013b) and ARTIOLI ET AL. (2017a), GAIN ET AL. (2014), gradient elasticity in WRIGGERS & HUDOBIVNIK (2023), elastodynamics in PARK ET AL. (2019b) and PARK ET AL. (2019a), plasticity in HUDOBIVNIK ET AL. (2018), ARTIOLI ET AL. (2017b) and ALDAKHEEL ET AL. (2019), phase field fracture in ALDAKHEEL ET AL. (2018) and HUSSEIN ET AL. (2020), discrete fracture in HUSSEIN ET AL. (2019), MARFIA ET AL. (2022), CHOI ET AL. (2023) and NGUYEN-THANH ET AL. (2018), contact problems in WRIGGERS ET AL. (2016), WRIGGERS & RUST (2019), ALDAKHEEL ET AL. (2020) and SUN ET AL. (2023) and many other engineering problems. The method can be applied to any problem type that can be treated by FEM. However, because of its advantageous properties, VEM makes particular sense for very specific problems. For instance, VEM can be used for contact problems with non conforming meshes at the contact interface to introduce new nodes in to an existing mesh by projection algorithms to obtain matching meshes at the contact interface. As a consequence, a very simple node-to-node contact treatment can be realized, as have been done in WRIGGERS ET AL. (2016) and WRIGGERS & RUST (2019) for 2D problems. Furthermore, modeling of discrete fracture paths is another main field of application, where virtual elements can be split in to new elements to model discrete cracks in a very simple way, as have been done in HUSSEIN ET AL. (2019) and HUSSEIN ET AL. (2020).

The goal of this work is to apply VEM for contact modeling in 3D, similarly to the ideas introduced in WRIGGERS ET AL. (2016). Additionally dynamic and plastic material behavior will be considered in order to model mechanical impact. Different contact discretizations will be introduced. The ultimate aim of this work is to gain experience and demonstrate

potentials in the aforementioned engineering applications for future works.

As a remark, parts of this thesis have been published previously in different publications, which were written in the last three years, namely CIHAN ET AL. (2021c), CIHAN ET AL. (2021a), CIHAN ET AL. (2021b) and CIHAN ET AL. (2022).

1.2 Structure of this work

This work is divided into 7 chapters. The fundamentals of continuum solid mechanics, including kinematics, balance laws, constitutive equations and weak form of equilibrium are described in **Chapter 2**.

The theory of computational contact mechanics, along with the contact kinematics, different contact discretizations and the treatment of contact constraints in the weak form of equilibrium, is summarized in **Chapter 3**.

Chapter 4 gives a more detailed description of the VEM, starting with the discretization. The construction of the virtual element is demonstrated in an efficient manner with the help of the software tool AceGen, which results in potential formulations. Different integration schemes for the computation of the virtual parameters, which are essential for the construction of virtual elements are described in detail. The construction of tangents requires a stabilization in the framework of VEM, which will be explained additionally. The solution scheme for elastostatic, -dynamic and -plastic material behaviour are presented. Simple benchmark tests including the classical patch test are demonstrated for validation purpose.

The modeling of contact problems is described in **Chapter 5** by means of different contact discretization schemes, namely node-to-surface, surface-to-surface and node-to-node contact. The latter requires a mesh adaption during the simulation which is induced by a node insertion algorithm.

To demonstrate the performance of the introduced formulations, various numerical examples for elasto-dynamic, elasto-plasto dynamic and contact applications are shown in **Chapter 6**, including well known benchmark problems like the Cook's membrane problem and the Taylor Anvil test. As a summarizing example, a coupled simulation of an impact problem including contact, dynamic and plastic material behavior is presented in the last section.

Concluding remarks and possible future works are discussed in **Chapter 7**.

Chapter 2

Continuum solid mechanics

In the following chapter, tools for the description of deformation of solid bodies will be introduced. Here the continuum approach is applied, which describes the Body \mathcal{B} by a set of continuously distributed points $\mathcal{P} \in \mathcal{B}$, which are also called material points. For a consistent description of the deformation, kinematics and balance laws are needed, which are connected through constitutive material equations. An overview to continuum mechanics is given in WRIGGERS (2008).

2.1 Kinematics and stresses

2.1.1 Motion and deformation gradient

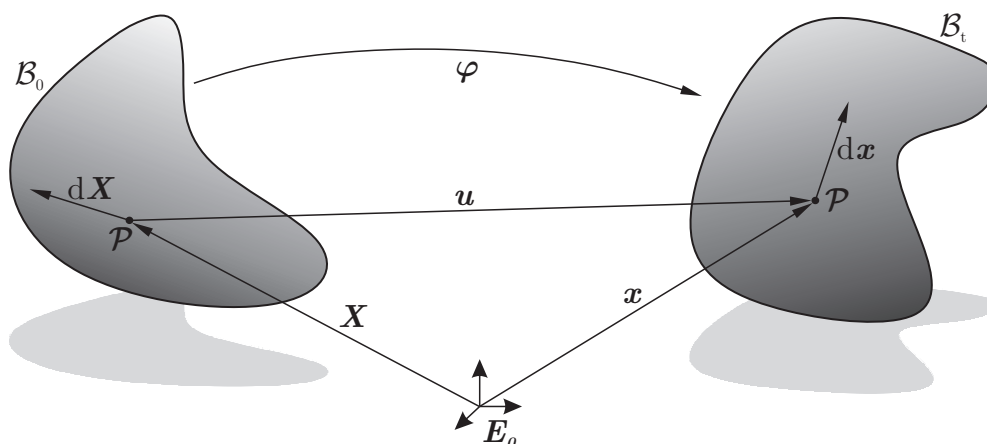


Figure 2.1 – Motion of a body from the initial configuration \mathcal{B}_0 to the current configuration \mathcal{B}_t .

Consider an elastic body \mathcal{B}_0 in its initial, undeformed, stress free configuration \mathcal{R}_0 , at time t_0 , consisting of a set of material points \mathcal{P} in the three dimensional Euclidean space \mathbb{R}^3 , as illustrated in Fig. 2.1. Due to a deformation φ , the body takes the form \mathcal{B}_t in the deformed configuration at time t . To represent a deformation state, for each material point \mathcal{P} ,

a position vector for each time t can be assigned. The material point position in the current configuration can be described by the position vector \mathbf{x} for a given configuration through the one-to-one mapping φ as:

$$\mathbf{x} = \varphi(\mathbf{X}, t) = \mathbf{X} + \mathbf{u}(\mathbf{X}, t), \quad (2.1)$$

where $\mathbf{u}(\mathbf{X}, t)$ is the displacement and \mathbf{X} represents the position of a material point in the initial configuration. For the further course of this work, we will skip the explicit dependency of variables on the initial configuration and time, thus we will write $\mathbf{u} = \mathbf{u}(\mathbf{X}, t)$. Since φ is bijective, the location can be mapped back to the initial material point position \mathbf{X} with:

$$\mathbf{X} = \varphi^{-1}(\mathbf{x}, t). \quad (2.2)$$

Unless otherwise specified, the initial coordinates and all further quantities, which are related to the initial configuration will be defined by capital letters, the quantities related to the current configuration are defined by lower-case letters.

For the description of the deformation process, the deformation gradient \mathbf{F} is introduced, which maps an infinitesimal material line element of the initial configuration $d\mathbf{X}$ in \mathcal{B}_0 , to a line element of the current configuration $d\mathbf{x}$ in $\mathcal{B}_t = \varphi(\mathcal{B}_0)$ by

$$d\mathbf{x} = \mathbf{F}d\mathbf{X}. \quad (2.3)$$

In order to transform quantities which are defined with respect to the deformed configuration to the reference configuration and vice versa, we define the deformation gradient \mathbf{F} by using equation (2.2) and equation (2.3). It yields:

$$\mathbf{F} = \frac{\partial \mathbf{x}}{\partial \mathbf{X}} = \frac{\partial(\mathbf{X} + \mathbf{u})}{\partial \mathbf{X}} = \mathbf{1} + \frac{\partial \mathbf{u}}{\partial \mathbf{X}} = \mathbf{1} + \nabla_{\mathbf{X}} \mathbf{u} = \mathbf{1} + \mathbf{H}, \quad (2.4)$$

where $\mathbf{1}$ represents the second order unity tensor with respect to the initial configuration and $\mathbf{H} = \nabla_{\mathbf{X}} \mathbf{u}$ the displacement gradient with respect to the initial coordinates. Since the mapping in equation (2.3) has to be a one-to-one mapping, \mathbf{F} can not be singular:

$$J = \det \mathbf{F} \neq 0, \quad (2.5)$$

where J is called the Jacobi determinant. Further, to exclude self penetration of the body, $J > 0$ has to be fulfilled. With equation (2.5), the inverse map of equation (2.3) exists:

$$d\mathbf{X} = \mathbf{F}^{-1}d\mathbf{x}. \quad (2.6)$$

With the use of \mathbf{F} , local transformations of various differential quantities between the initial and current configuration can be done. The transformation between infinitesimal areas is done by using Nanson's formula:

$$d\mathbf{a} = \mathbf{n} da = J \mathbf{F}^{-T} \mathbf{N} dA = J \mathbf{F}^{-T} d\mathbf{A}, \quad (2.7)$$

where \mathbf{n} and \mathbf{N} are the normal vectors and da and dA the infinitesimal areas related to the associated configurations. However, the transformation of an infinitesimal volume element can be obtained by using the Jacobian with:

$$dv = J dV. \quad (2.8)$$

With equation (2.8), the above introduced constrains for J are obvious.

2.1.2 Strain measures

In this section, different strain measures are defined, which will be used throughout the following chapters. Since \mathbf{F} contains rigid body rotations and thus is not objective, it can not be used as a strain measure. To guarantee invariance of constitutive equations with respect to rigid body motions, a polar decomposition can be made for \mathbf{F} , which yields with \mathbf{R} being the rotation tensor:

$$\mathbf{F} = \mathbf{R}\mathbf{U} \quad \text{and} \quad \mathbf{F} = \mathbf{V}\mathbf{R}, \quad (2.9)$$

where \mathbf{U} and \mathbf{V} are the right and left stretch tensors. We further define the right Cauchy-Green tensor with:

$$\mathbf{C} = \mathbf{F}^T \mathbf{F} = \mathbf{U}^T \mathbf{R}^T \mathbf{R} \mathbf{U} = \mathbf{U}^2, \quad (2.10)$$

which is related to the initial configuration and the left Cauchy-Green tensor with:

$$\mathbf{b} = \mathbf{F} \mathbf{F}^T = \mathbf{V} \mathbf{R} \mathbf{R}^T \mathbf{V}^T = \mathbf{V}^2, \quad (2.11)$$

which is defined in the current configuration. Both above introduced tensors \mathbf{C} and \mathbf{b} have their basis vectors fully in their associated configurations. Unlike the before mentioned tensors, the basis vectors of the deformation gradient \mathbf{F} are in both configurations, thus it is called a two-point tensor. By multiplying \mathbf{F} with its transpose, rigid body rotations are excluded, thus the right and left Cauchy-Green tensor can be used as a rotation-independent deformation measure. Further, one can define the Green-Lagrange strain tensor, which is often used in continuum mechanics, as:

$$\mathbf{E} = \frac{1}{2}(\mathbf{F}^T \mathbf{F} - \mathbf{1}) = \frac{1}{2}(\mathbf{C} - \mathbf{1}) = \underbrace{\frac{1}{2}(\mathbf{H}^T + \mathbf{H})}_{\text{geom. linear part}} + \underbrace{\frac{1}{2}(\mathbf{H}^T \mathbf{H})}_{\text{geom. nonlinear part}}. \quad (2.12)$$

For infinitesimal strain theory, the higher order terms in equation (2.12) are neglected by assuming that the gradient of the displacement is of small order, i.e. $\|\mathbf{H}\| \ll 1$, which results in the geometric linear strain tensor:

$$\boldsymbol{\varepsilon} = \frac{1}{2}(\mathbf{H}^T + \mathbf{H}). \quad (2.13)$$

2.1.3 Stress measures

Depending on the formulation in the continuum mechanics framework, different stress measures are used. The most commonly used measure of stress is the Cauchy stress tensor:

$$\boldsymbol{\sigma} = \begin{bmatrix} \sigma_{11} & \sigma_{12} & \sigma_{13} \\ \sigma_{21} & \sigma_{22} & \sigma_{23} \\ \sigma_{31} & \sigma_{32} & \sigma_{33} \end{bmatrix}, \quad (2.14)$$

where the nine components of the stress tensor defines the stress state completely at a point inside a body in the current configuration. The Cauchy stress tensor can be used to relate the force vector \boldsymbol{t} and the associated outward normal \boldsymbol{n} on a plane via the Cauchy Theorem:

$$\boldsymbol{t} = \boldsymbol{\sigma}^T \boldsymbol{n}, \quad (2.15)$$

which implies that \boldsymbol{t} is a linear function of \boldsymbol{n} , see KIENZLER & SCHRÖDER (2019) and ALTENBACH (2018). By multiplying the Cauchy stress tensor with the Jacobian in equation (2.5), the Kirchhoff stress tensor can be introduced:

$$\boldsymbol{\tau} = J \boldsymbol{\sigma}, \quad (2.16)$$

which is defined in the current configuration and is widely used for the description of isochoric plastic deformation processes mostly in metal plasticity, see SIMO & HUGHES (1998). However, various stress measures exist in different configurations, as will be discussed in the following section.

2.2 Balance laws

2.2.1 Balance of mass

In this work, closed systems are considered, where the mass is conserved such that the change of mass has to be zero, i.e. $\dot{m} = 0$. This implies that an infinitesimal mass element in both initial and current configuration has to be equal, which leads:

$$\rho_0 dV = \rho dv, \quad (2.17)$$

where ρ_0 denotes the density in the initial configuration and ρ the density in the current configuration. Combining equation (2.8) and equation (2.17) results in the balance of mass in Lagrangian form:

$$\rho_0 = J \rho, \quad (2.18)$$

where it can be seen that for the incompressible case $J = 1$.

2.2.2 Balance of linear and angular momentum

There are multiple ways to derive balance laws for linear and angular momentum. First, a more illustrative way, the derivation from an infinitesimal volume element will be introduced, see KIENZLER & SCHRÖDER (2019). Fig. 2.2 shows an infinitesimal volume element with normal and shear stresses acting on each face. For simplification, the figure shows only the stresses, which have a contribution to the force equilibrium in x_1 direction. Note that, the use of d'Alembert's principle is made for taking the inertia effects into account.

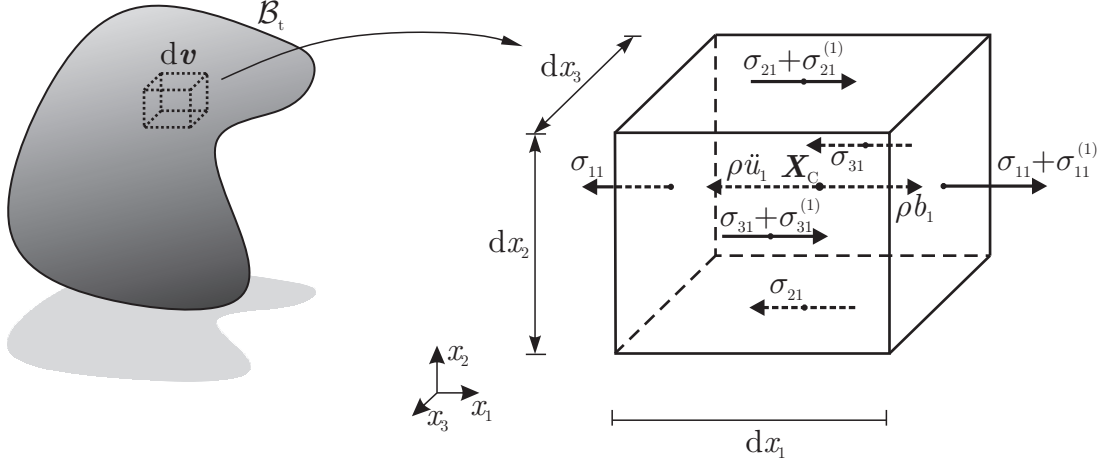


Figure 2.2 – Infinitesimal volume element with stresses, which are relevant for the equilibrium of linear momentum in the direction x_1 .

Since stresses are functions of the coordinates, they change with increasing or decreasing dx_i , thus a Taylor series expansion up to first order is made, which yields in index notation:

$$\bar{\sigma}_{ij} = \sigma_{ij} + \sigma_{ij}^{(1)} \quad \text{with} \quad \sigma_{ij}^{(1)} = \frac{\partial \sigma_{ij}}{\partial x_i} dx_i, \quad (2.19)$$

Truncating the higher order terms is allowed, since dx_i are infinitesimal small, see KIENZLER & SCHRÖDER (2019). In order to derive the balance of linear momentum, the stresses need to be transferred into forces. Forces can be obtained by multiplying the stresses with their associated areas, where they are acting on. Thus the equilibrium equation in x_1 direction yields:

$$\begin{aligned} \sum \mathbf{F}_{x_1} = 0 &= -\sigma_{11} dx_2 dx_3 + \left(\sigma_{11} + \frac{\partial \sigma_{11}}{\partial x_1} dx_1 \right) dx_2 dx_3 \\ &\quad - \sigma_{21} dx_1 dx_3 + \left(\sigma_{21} + \frac{\partial \sigma_{21}}{\partial x_2} dx_2 \right) dx_1 dx_3 \\ &\quad - \sigma_{31} dx_1 dx_2 + \left(\sigma_{31} + \frac{\partial \sigma_{31}}{\partial x_3} dx_3 \right) dx_1 dx_2 \\ &\quad + \rho b_1 dx_1 dx_2 dx_3 - \rho \ddot{u}_1 dx_1 dx_2 dx_3. \end{aligned} \quad (2.20)$$

After some modifications and using the relation $dx_1 dx_2 dx_3 = dv$, equation (2.20) yields:

$$\frac{\partial \sigma_{1j}}{\partial x_j} + \rho b_1 = \rho \ddot{u}_1. \quad (2.21)$$

Note that in equation (2.21), the use of Einstein summation convention is implied. After writing the equilibrium equation for both other directions x_2 and x_3 , equation (2.21) will yield

$$\text{div} \boldsymbol{\sigma}^T + \rho \bar{\mathbf{b}} = \rho \ddot{\mathbf{u}}, \quad (2.22)$$

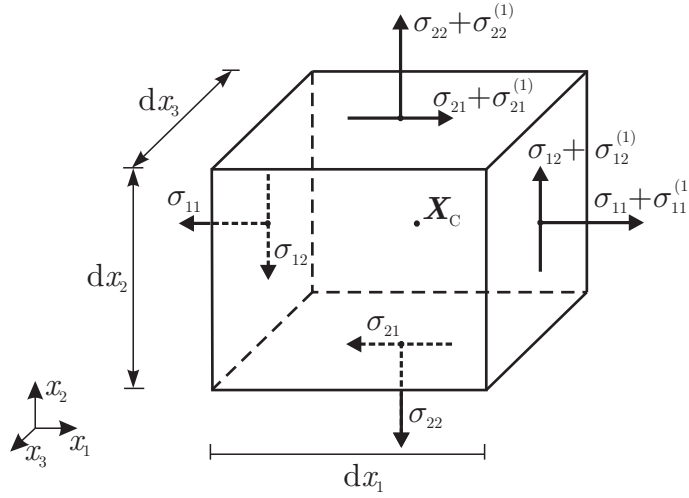


Figure 2.3 – Infinitesimal volume element with stresses, which are relevant for the equilibrium of angular momentum around the x_3 -axis.

which is the local form of balance of linear momentum. The balance of angular momentum can be derived in a similar manner by taking the same infinitesimal volume element as shown in Fig. 2.3. Note, that here also not all stresses are sketched for the three dimensional case. However, by summing up all moments which have a contribution to the x_3 -axis, the equilibrium equation leads:

$$\begin{aligned} \sum M_{x_3} = 0 = & -\sigma_{21} dx_1 dx_3 \frac{dx_2}{2} - \left(\sigma_{21} + \frac{\partial \sigma_{21}}{\partial x_2} dx_2 \right) dx_1 dx_3 \frac{dx_2}{2} \\ & + \sigma_{12} dx_2 dx_3 \frac{dx_1}{2} + \left(\sigma_{12} + \frac{\partial \sigma_{12}}{\partial x_2} dx_2 \right) dx_2 dx_3 \frac{dx_1}{2}. \end{aligned} \quad (2.23)$$

The higher order terms in dx_i are negligibly small and are thus canceled out of equation (2.23), leading to:

$$\sigma_{12} = \sigma_{21}. \quad (2.24)$$

By summing all moments around the other two axis x_1 and x_2 , it can be shown that $\sigma_{13} = \sigma_{31}$ and $\sigma_{23} = \sigma_{32}$ hold too and thus:

$$\boldsymbol{\sigma}^T = \boldsymbol{\sigma}, \quad (2.25)$$

which requires the symmetry of Cauchy stress tensor. The balance equation (2.22) is stated in the current configuration. In some certain cases, it is advantageous to formulate balance laws with respect to the initial configuration. For this purpose, certain quantities need to be transformed back to the initial configuration. This can be done by employing Nanson's formula via equation (2.7) to the integral of equation (2.15) over the current surface:

$$\int_{\Gamma_t} \boldsymbol{\sigma} \mathbf{n} da = \int_{\Gamma_0} J \boldsymbol{\sigma} \mathbf{F}^{-T} \mathbf{N} dA = \int_{\Gamma_0} \mathbf{P} \mathbf{N} dA, \quad (2.26)$$

which defines the first Piola-Kirchhoff stress \mathbf{P} as:

$$\mathbf{P} = J \boldsymbol{\sigma} \mathbf{F}^{-T}, \quad (2.27)$$

where \mathbf{P} is a two point tensor, having its bases in both, the current and the initial configuration. It can be transformed to the second Piola-Kirchhoff stress tensor \mathbf{S} by:

$$\mathbf{S} = \mathbf{F}^{-1} \mathbf{P} = J \mathbf{F}^{-1} \boldsymbol{\sigma} \mathbf{F}^{-T}, \quad (2.28)$$

which has both of its bases in the initial configuration. \mathbf{S} is often used in constitutive modeling, since it is work conjugated to the Green-Lagrange strain tensor in equation (2.12), see WRIGGERS (2008). With equation (2.27), the local form of the balance of linear momentum in the current configuration in equation (2.22) can be recast with respect to the initial configuration as:

$$\text{Div } \mathbf{P} + \rho_0 \bar{\mathbf{b}} = \rho_0 \ddot{\mathbf{u}}, \quad (2.29)$$

where Div denotes the divergence operator with respect to the initial coordinates.

2.2.3 Balance of energy

The conservation of energy in a thermodynamical process is postulated by the first law of thermodynamics, see e.g. HOLZAPFEL (2002) and HAUPT (2002):

$$\dot{E} = \dot{\mathcal{K}} + \dot{U} = \mathcal{P}_{ext} + \mathcal{Q}. \quad (2.30)$$

It states that the rate of total Energy E (sum of kinetic \mathcal{K} and internal U energy) of a thermodynamic system is equal to the external mechanical power \mathcal{P}_{ext} due to volume and surface loads and the heat supply \mathcal{Q} due to surface conduction and inner heat sources with each term being:

$$\mathcal{K} = \int_{\mathcal{B}_t} \frac{1}{2} \rho \dot{\mathbf{u}} \cdot \dot{\mathbf{u}} \, dv, \quad (2.31)$$

$$U = \int_{\mathcal{B}_t} \rho e \, dv, \quad (2.32)$$

$$\mathcal{P}_{ext} = \int_{\mathcal{B}_t} \rho \bar{\mathbf{b}} \cdot \dot{\mathbf{u}} \, dv + \int_{\partial \mathcal{B}_t} \mathbf{t} \cdot \dot{\mathbf{u}} \, da, \quad (2.33)$$

and

$$\mathcal{Q} = \int_{\mathcal{B}_t} \rho r \, dv - \int_{\partial \mathcal{B}_t} \mathbf{q} \cdot \mathbf{n} \, da, \quad (2.34)$$

where the heat supply term is composed of the Cauchy heat flux \mathbf{q} , defined per unit surface area in \mathcal{B}_t and the volumetric head source density ρr . Inserting equations (2.31), (2.32), (2.33) and (2.34) in equation (2.30) and using the balance of mass in (2.17) leads to:

$$\int_{\mathcal{B}_t} \rho \ddot{\mathbf{u}} \cdot \dot{\mathbf{u}} + \rho \dot{e} \, dv = \int_{\mathcal{B}_t} \rho \bar{\mathbf{b}} \cdot \dot{\mathbf{u}} + \rho r \, dv + \int_{\partial \mathcal{B}_t} \mathbf{t} \cdot \dot{\mathbf{u}} - \mathbf{q} \cdot \mathbf{n} \, da. \quad (2.35)$$

By utilizing divergence and Cauchy theorem and the relation from the balance of linear momentum in equation (2.22), the global form of first law of thermodynamics leads to:

$$\int_{\mathcal{B}_t} \rho \dot{e} \, dv = \int_{\mathcal{B}_t} (\boldsymbol{\sigma} \cdot \mathbf{d} + \rho r - \operatorname{div} \mathbf{q}) \, dv. \quad (2.36)$$

The control volume can be arbitrary, thus the local form of the first law of thermodynamics for each material point can be written as:

$$\rho \dot{e} = \boldsymbol{\sigma} \cdot \mathbf{d} + \rho r - \operatorname{div} \mathbf{q}. \quad (2.37)$$

With the Legendre transformation for the internal energy e :

$$\psi = e - \eta \theta, \quad (2.38)$$

equation (2.37) can be rewritten in terms of the specific Helmholtz free energy ψ , the temperature θ and entropy η :

$$\rho \dot{\psi} = \boldsymbol{\sigma} \cdot \mathbf{d} + \rho r - \operatorname{div} \mathbf{q} - \rho \eta \dot{\theta} - \rho \dot{\eta} \theta. \quad (2.39)$$

Equation (2.39) can also be stated in terms of quantities which are referred to the initial configuration with:

$$\rho_0 \dot{\psi} = \mathbf{P} \cdot \dot{\mathbf{F}} + \rho_0 r - \operatorname{Div} \mathbf{Q} - \rho_0 \eta \dot{\theta} - \rho_0 \dot{\eta} \theta, \quad (2.40)$$

where \mathbf{Q} represents the Piola-Kirchhoff heat flux, defined per unit surface area in \mathcal{B}_0 .

2.2.4 Entropy inequality

In the framework of material modeling, i.e. constitutive equations, the second law of thermodynamics needs to be fulfilled. From a phenomenological viewpoint, it can be understood as a directional constraint of energy flow. Energy dissipation during frictional contact can be seen as an example, where energy in terms of mechanical energy (motion) is converted to heat, due to friction. In fact, this energy, which is now preserved as heat, can not be transformed back in to mechanical energy (motion). The second law requires that the entropy production Γ is always larger or equal zero:

$$\Gamma = \dot{\mathcal{S}} - \bar{\mathcal{Q}} \geq 0, \quad (2.41)$$

with $\dot{\mathcal{S}}$ and $\bar{\mathcal{Q}}$ being the entropy change and specific entropy insertion rate respectively:

$$\dot{\mathcal{S}} = \frac{D}{Dt} \int_{\mathcal{B}_t} \rho \eta \, dv \quad \text{and} \quad \bar{\mathcal{Q}} = \int_{\mathcal{B}_t} \frac{\rho r}{\theta} \, dv - \int_{\partial \mathcal{B}_t} \frac{1}{\theta} \mathbf{q} \cdot \mathbf{n} \, dv. \quad (2.42)$$

By combining equation (2.41) and equation (2.42) and applying the divergence theorem, mass continuity, product rule and considering that the control volume can be arbitrary, the local form of second law of thermodynamics leads:

$$\rho \dot{\eta} \geq \frac{\rho r}{\theta} - \operatorname{div} \left(\frac{\mathbf{q}}{\theta} \right). \quad (2.43)$$

By employing again a Legendre transformation with equation (2.38) and using the relation in equation (2.37), the reduced form of the second law of thermodynamics, also known as the Clausius-Duhem inequality, can be written as:

$$\rho \left(\dot{\theta} \eta + \dot{\psi} \right) - \boldsymbol{\sigma} \cdot \mathbf{d} + \frac{1}{\theta} \mathbf{q} \cdot \operatorname{grad} \theta \leq 0, \quad (2.44)$$

where $\mathbf{d} = \frac{1}{2}(\mathbf{l} + \mathbf{l}^T)$ denotes the symmetric part of the spatial velocity gradient with $\mathbf{l} = \dot{\mathbf{F}} \mathbf{F}^{-1}$. Equation (2.44) can also be formulated in the same way with respect to the initial configuration:

$$\rho_0 \left(\dot{\theta} \eta + \dot{\psi} \right) - \mathbf{P} \cdot \dot{\mathbf{F}} + \frac{1}{\theta} \mathbf{Q} \cdot \operatorname{Grad} \theta \leq 0. \quad (2.45)$$

By requiring that heat can only flow against a temperature gradient and using the relationship from equation (2.40), the Clausius-Duhem inequality (2.45) leads to an alternative stronger form, also known as the Clausius-Planck inequality:

$$\mathcal{D}_{int} = \mathbf{P} \cdot \dot{\mathbf{F}} - \rho_0 \dot{e} + \rho_0 \theta \dot{\eta} = \operatorname{Div} \mathbf{Q} - \rho_0 r + \rho_0 \theta \dot{\eta} \geq 0, \quad (2.46)$$

where \mathcal{D}_{int} is denoting the internal dissipation which has to be non-negative. For a pure mechanical problem where an isothermal process is assumed ($\dot{\theta} = 0$) and applying again the Legendre transformation in equation (2.38), the Clausius-Planck inequality reduces to the simple form:

$$\mathcal{D}_{int} = \mathbf{P} \cdot \dot{\mathbf{F}} - \rho_0 \dot{\psi} \geq 0. \quad (2.47)$$

Equation (2.47) says in other words, that the internal mechanical power (stress power) always has to be larger equal the rate of internal energy, which implies that there can not be more energy in the system, than has been inserted in to the system. For reversible processes, where dissipative effects are not considered, equation (2.47) turns to an equality. Equation (2.46) provides the fundamental inequality condition for the construction of constitute equations in a thermodynamically consistent way. It can be used for example to derive flow rules in the concept of maximum plastic dissipation. However, the internal stress power can be expressed by different work conjugated pairs of strain measures and stresses, such as $\mathbf{P} \cdot \dot{\mathbf{F}}$, $\mathbf{S} \cdot \dot{\mathbf{E}}$ or $\boldsymbol{\sigma} \cdot \mathbf{d}$.

2.3 Constitutive equations

In the previous chapters, kinematics and balance laws have been introduced. However, a relation between stresses and strains is missing and a boundary or initial value problem is not solvable yet. This missing gap is filled by constitutive equations, to describe the stress-strain relationship. The material response can be either modeled in a microscopic or macroscopic way. For conventional materials like steel or concrete, which are mainly used in technical applications, a macroscopic material description is sufficient. Thus in this work a microscopic description is omitted. For interested readers, reference is made to ZOHDI & WRIGGERS (2005).

2.3.1 Hyperelasticity

For a hyperelastic material, the constitutive relationship between the stresses and strains can be derived from a strain energy density function $\Psi(\mathbf{F}) = \rho_0 \psi(\mathbf{F})$, also named Green elasticity, see HOLZAPFEL (2002); WRIGGERS (2008). For an ideal elastic material, equation (2.47) turns to an equality and by applying a Coleman-Noll procedure it reads with the chain rule:

$$\mathcal{D}_{int} = \mathbf{P} \cdot \dot{\mathbf{F}} - \dot{\Psi} = \left(\mathbf{P} - \frac{\partial \Psi(\mathbf{F})}{\partial \mathbf{F}} \right) \cdot \dot{\mathbf{F}} = 0, \quad (2.48)$$

where $\dot{\mathbf{F}}$ can be arbitrary and thus it follows:

$$\frac{\partial \Psi}{\partial \mathbf{F}} = \mathbf{P}, \quad (2.49)$$

where \mathbf{P} is often called the thermodynamic force, work conjugated to \mathbf{F} . Depending on the construction of Ψ , other work conjugated pairs can be derived, e.g.:

$$2 \frac{\partial \Psi(\mathbf{C})}{\partial \mathbf{C}} = \frac{\partial \Psi(\mathbf{E})}{\partial \mathbf{E}} = \mathbf{S}. \quad (2.50)$$

There are many different possibilities for the choice of the strain energy density function. A classical geometric nonlinear approach is the choice of a St. Venant-Kirchhoff model with:

$$\Psi = \frac{\lambda}{2} (\text{tr} \mathbf{E})^2 + \mu \text{tr} (\mathbf{E}^2). \quad (2.51)$$

By exchanging \mathbf{E} in equation (2.51) with the small strain tensor $\boldsymbol{\varepsilon}$, the constitutive relationship changes to the geometric linear theory. The St. Venant-Kirchhoff model is limited to deformations with small strains but large displacements and finite rotations, which can appear in the analysis of thin structures, like beams and shells, see WRIGGERS (2008). However, materials which undergo finite deformations tend to have a nonlinear material response, such as rubber-like materials. For those materials, the Neo-Hookean strain energy density function can be used, see CIARLET (1988):

$$\Psi = \frac{\lambda}{4} (J_F^2 - 1 - 2 \ln(J_F)) + \frac{\mu}{2} (I_c - 3 - 2 \ln(J_F)), \quad (2.52)$$

where $J_F = J$ denotes the determinant of the deformation gradient with equation (2.5) and $I_c = \text{tr}(\mathbf{C})$ being the first invariant of the right Cauchy-Green tensor. The Lamé constants can be computed with:

$$\lambda = \frac{E\nu}{(1+\nu)(1-2\nu)} \quad \text{and} \quad \mu = \frac{E}{2(1+\nu)}. \quad (2.53)$$

Equation (2.52) provides a non linear stress strain relationship.

2.3.2 Finite elasto-plasticity

In many engineering applications, such as crash simulations, metal forming or cutting, models for finite plasticity are essential. The model for an elasto-plastic material behavior requires additionally the formulation of a yield function, a hardening law and an evolution equation for the plastic variables. Contrary to small strain plasticity models, where the strains are decomposed in to elastic and plastic parts additively, finite strain models are based on a multiplicative split of the deformation gradient, see SIMO & HUGHES (1998):

$$\mathbf{F} = \mathbf{F}_e \mathbf{F}_p. \quad (2.54)$$

The plastic right and elastic left Cauchy-Green tensor can also be introduced as:

$$\mathbf{b}_e = \mathbf{F}_e \mathbf{F}_e^T = \mathbf{F} \mathbf{C}_p^{-1} \mathbf{F}^T \quad \text{and} \quad \mathbf{C}_p = \mathbf{F}_p^T \mathbf{F}_p. \quad (2.55)$$

For the elastic part of the body, a Neo-Hookean strain energy of the following type can be used:

$$\Psi = \Psi_{vol}(J_e) + \Psi_{iso}(\mathbf{b}_{e,iso}), \quad (2.56)$$

where Ψ_{vol} and Ψ_{iso} are denoting the volumetric and isochoric parts of Ψ as:

$$\Psi_{vol}(J_e) = \frac{\kappa}{4}(J_e^2 - 1 - 2 \ln(J_e)) \quad \text{and} \quad \Psi_{iso}(\mathbf{b}_{e,iso}) = \frac{\mu}{2}(\text{tr}(\mathbf{b}_{e,iso}) - 3). \quad (2.57)$$

Here $\mathbf{b}_{e,iso} = J_e^{-2/3} \mathbf{b}_e$ represents the isochoric part of the elastic left Cauchy-Green tensor and $J_e = \det \mathbf{F}_e = \sqrt{\det(\mathbf{b}_e)}$ the elastic part of the Jacobian. With the definition of the strain energy function Ψ , the Kirchhoff stress can be derived as follows:

$$\boldsymbol{\tau} = 2 \mathbf{b}_e \frac{\partial \Psi}{\partial \mathbf{b}_e}. \quad (2.58)$$

To distinguish between the elastic and plastic regime, a yield function needs to be adopted. For standard J2 plasticity, also known as von Mises plasticity, which is valid for modeling the plastic behavior of metals, the following yield function with nonlinear hardening is adopted:

$$\Phi = \sigma_{vm} - [\sigma_0 + (\sigma_\infty - \sigma_0)(1 - e^{-1/\delta\alpha}) + H\alpha], \quad (2.59)$$

with

$$\sigma_{vm} = \sqrt{\frac{3}{2}} \|\mathbf{s}\| \quad \text{and} \quad \mathbf{s} = \boldsymbol{\tau} - \frac{1}{3} \text{tr}(\boldsymbol{\tau}) \mathbf{1}. \quad (2.60)$$

Here, σ_{vm} denotes the von Mises stress, \mathbf{s} the deviatoric part of the Kirchhoff stress $\boldsymbol{\tau}$, σ_0 and σ_∞ the initial yield limit and infinite yield stress and δ the saturation parameter. H and α represent the hardening modulus and the hardening parameter respectively. For the description of the plastic deformation, an evolution equation is needed. In the case of associative plasticity, the assumption of maximum plastic dissipation leads with the Clausius-Planck inequality in equation (2.46) the associated plastic flow rule in the current configuration:

$$\mathbf{d}_p = \lambda \frac{\partial \Phi}{\partial \boldsymbol{\tau}} \quad \text{and} \quad \dot{\alpha} = \lambda \quad \text{with} \quad \dot{\alpha} \geq 0, \quad (2.61)$$

see SIMO (1992) and KORELC & STUPKIEWICZ (2014). Here \mathbf{d}_p denotes the symmetric part of the plastic spatial velocity gradient, $\mathbf{n} = \frac{\partial \Phi}{\partial \boldsymbol{\tau}}$ the flow direction and λ the plastic Lagrange multiplier. There are many different possibilities for the choice of the internal variable. For example, one could solve for the plastic part of the deformation gradient \mathbf{F}_p in equation (2.55). Here, \mathbf{C}_p^{-1} is chosen to be the internal plastic variable and equation (2.61) can be reformulated by neglecting the plastic spin:

$$\dot{\mathbf{C}}_p^{-1} = -2\lambda \mathbf{F}^{-1} \mathbf{n} \mathbf{F} \mathbf{C}_p^{-1}, \quad (2.62)$$

see KORELC & STUPKIEWICZ (2014). Together with the Karush-Kuhn-Tucker conditions:

$$\Phi \leq 0 \quad , \quad \lambda \geq 0 \quad \text{and} \quad \Phi \lambda = 0, \quad (2.63)$$

and equation (2.62) the setup for the algorithmic treatment of plasticity is well formulated. The solution of equation (2.62) will be discussed in section 4.8.

2.4 Weak form of equilibrium

The before introduced balance of linear momentum, the kinematic relations and constitutive equations form together a system of coupled partial differential equations, which have to be solved. An analytical solution of these systems of nonlinear partial differential equations is only possible for simple problems. Thus, approximation methods like the finite element method, which is based on a variational formulation have to be applied for the solution, see WRIGGERS (2008).

2.4.1 Principle of virtual work

The exact solution \mathbf{u} satisfy the balance of linear momentum in equation (2.29) exactly. However, an approximated solution \mathbf{u}_h will lead to an error and thus the balance of linear momentum will lead to:

$$\text{Div } \mathbf{P}(\mathbf{u}_h) + \rho_0 (\bar{\mathbf{b}} - \ddot{\mathbf{u}}_h) = \mathbf{R}, \quad (2.64)$$

where \mathbf{R} represents the residual due to not satisfying the balance equation exactly. The idea is now to minimize this error in a weak sense. To do so, the residual is multiplied by

a function $\delta \mathbf{u}$, also called virtual displacement or test function and is integrated over the domain:

$$\int_{\mathcal{B}_0} \mathbf{R} \cdot \delta \mathbf{u} \, dV = \int_{\mathcal{B}_0} (\text{Div } \mathbf{P} + \rho_0 (\bar{\mathbf{b}} - \ddot{\mathbf{u}}_h)) \cdot \delta \mathbf{u} \, dV = 0, \quad (2.65)$$

where it has to hold for the approximated solution \mathbf{u}_h and exact solution \mathbf{u} as well. For the sake of clarity, the subscript \square_h will be omitted in the following course of this work. Applying integration by parts to the first term in equation (2.65) and making use of the divergence theorem, together with the Cauchy-theorem in equation (2.15) leads to the weak form of the balance of linear momentum in the initial configuration:

$$G(\mathbf{u}, \delta \mathbf{u}) = \int_{\mathcal{B}_0} \mathbf{P} \cdot \delta \mathbf{F} - \rho_0 (\bar{\mathbf{b}} - \ddot{\mathbf{u}}) \cdot \delta \mathbf{u} \, dV - \int_{\partial \mathcal{B}_0} \mathbf{T} \cdot \delta \mathbf{u} \, dA = 0, \quad (2.66)$$

where $\delta \mathbf{F}$ denotes the variation of the deformation gradient and $\mathbf{T} = \mathbf{P} \mathbf{N}$ the (pseudo) traction vector, also often called Piola-Kirchhoff traction vector, defined in the initial configuration. The first term in equation (2.66) represents the internal virtual work and the last two terms the virtual work of the applied loading. Additionally, the internal virtual work can be recast with different work conjugated pairs, i.e. instead of $\mathbf{P} \cdot \delta \mathbf{F}$ one could also use $\mathbf{S} \cdot \delta \mathbf{E}$, see WRIGGERS (2008).

2.4.2 Hamilton's principle of stationary action

Alternatively, the weak form can be extracted by employing the Hamilton's principle of stationary action. Under the assumption of hyper elastic materials, there exists a strain energy function, which describes the stored elastic energy in a solid. In the geometrically linear theory, the classical principle of the minimum of potential energy can be formulated. However, for finite deformations, only a stationary value of the potential can be obtained, since non-unique deformations can appear. Under the assumption of conservative loads, the following function can be stated:

$$\Pi = \int_{\mathcal{B}_0} \left(\Psi(\mathbf{F}) - \rho_0 \bar{\mathbf{b}} \cdot \mathbf{u} + \int_{t_0}^{t_1} \frac{1}{2} \rho_0 \dot{\mathbf{u}}^2 \, dt \right) \, dV - \int_{\partial \mathcal{B}_0} \mathbf{T} \cdot \mathbf{u} \, dA \quad \text{where} \quad \Pi \rightarrow \text{STAT.} \quad (2.67)$$

To find \mathbf{u} which satisfies the equilibrium equation, the first variation of Π with respect to \mathbf{u} has to be computed with:

$$\delta_{\mathbf{u}} \Pi = \int_{\mathcal{B}_0} \frac{\partial \Psi(\mathbf{F})}{\partial \mathbf{F}} \cdot \delta \mathbf{F} - \rho_0 (\bar{\mathbf{b}} - \ddot{\mathbf{u}}) \cdot \delta \mathbf{u} \, dV - \int_{\partial \mathcal{B}_0} \mathbf{T} \cdot \delta \mathbf{u} \, dA = G(\mathbf{u}, \delta \mathbf{u}), \quad (2.68)$$

where $\frac{\partial \Psi(\mathbf{F})}{\partial \mathbf{F}} = \mathbf{P}$ and thus equation (2.68) and equation (2.66) are equivalent for hyper elastic materials. Again, the internal virtual work can be represented by different work conjugated pairs. Note that, product rule and integration by parts is used to compute the variation of the kinetic energy in (2.68).

2.4.3 Hu-Washizu principle

As an alternative variational principle, a functional based on the Hu-Washizu principle can be adopted. Within this formulation, kinematics and constitutive equations are considered in the functional as additional constraint equations. As a consequence, beside the displacements, strains and stresses occur as additional unknowns.

A special form of the Hu-Washizu principle is widely used for the handling of nearly incompressible material behavior. Based on a volumetric-isochoric split of the deformation as done in equation (2.57), the three field functional can be constructed, see SIMO ET AL. (1985a):

$$\begin{aligned}\Pi &= \Pi_{iso}(\mathbf{C}_{iso}) + \Pi_{vol}(\mathbf{u}, p, \theta) + \Pi_{ext}(\mathbf{u}) \\ &= \int_{\mathcal{B}_0} \Psi_{iso}(\mathbf{C}_{iso}) + \Psi_{vol}(\theta) + p(J - \theta) dV \\ &\quad - \int_{\mathcal{B}_0} \left(\rho_0 \bar{\mathbf{b}} \cdot \mathbf{u} + \int_{t_0}^{t_1} \frac{1}{2} \rho_0 \dot{\mathbf{u}}^2 dt \right) dV - \int_{\partial \mathcal{B}_0} \mathbf{T} \cdot \mathbf{u} dA,\end{aligned}\tag{2.69}$$

$$\tag{2.70}$$

where the isochoric part of the energy is described with $\mathbf{C}_{iso} = J^{-2/3} \mathbf{C}$ representing the isochoric part of the right Cauchy-Green tensor. p and θ are the pressure and dilatation. The variation of Π with respect to the deformation leads to the weak form of equilibrium:

$$\begin{aligned}\delta_{\mathbf{u}} \Pi &= \int_{\mathcal{B}_0} \left(2 \frac{\partial \Psi_{iso}(\mathbf{C}_{iso})}{\partial \mathbf{C}_{iso}} - \frac{1}{3} \left(\frac{\partial \Psi_{iso}(\mathbf{C}_{iso})}{\partial \mathbf{C}_{iso}} \cdot \mathbf{C} \right) \mathbf{C}^{-1} + p J \mathbf{C}^{-1} \right) \cdot \frac{1}{2} \delta \mathbf{C} \\ &\quad - \rho_0 (\bar{\mathbf{b}} - \ddot{\mathbf{u}}) \cdot \delta \mathbf{u} dV - \int_{\partial \mathcal{B}_0} \mathbf{T} \cdot \delta \mathbf{u} dA = 0\end{aligned}\tag{2.71}$$

where the first part in equation (2.71) describes the isochoric part and the second part the volumetric part of the second Piola-Kirchhoff stress:

$$2 \frac{\partial \Psi_{iso}(\mathbf{C}_{iso})}{\partial \mathbf{C}_{iso}} - \frac{1}{3} \left(\frac{\partial \Psi_{iso}(\mathbf{C}_{iso})}{\partial \mathbf{C}_{iso}} \cdot \mathbf{C} \right) \mathbf{C}^{-1} = \mathbf{S}_{iso}\tag{2.72}$$

$$p J \mathbf{C}^{-1} = \mathbf{S}_{vol},\tag{2.73}$$

which illustrates the split into isochoric and volumetric parts, see WRIGGERS (2008). The variation of Π with respect to the additional unknowns leads to the additional constraint condition for $J = \theta$ and the constitutive equation for the pressure p with:

$$\delta_p \Pi = \int_{\mathcal{B}_0} \delta p (J - \theta) dV = 0,\tag{2.74}$$

$$\delta_{\theta} \Pi = \int_{\mathcal{B}_0} \delta \theta \left(\frac{\partial \Psi_{vol}}{\partial \theta} - p \right) dV = 0.\tag{2.75}$$

Chapter 3

Computational contact mechanics

When two (or more) bodies B^α get close to each other, they might come into contact through their surfaces $\Gamma^\alpha = \partial B^\alpha$, where $\alpha \in \{1, 2\}$. During the deformation process, two points, \mathbf{X}^1 and \mathbf{X}^2 , of the two bodies can move, such that they occupy both the same position $\varphi(\mathbf{X}^1, t) = \varphi(\mathbf{X}^2, t)$ in the current configuration, see Fig. 3.1. Here, Γ_D and Γ_N are denoting the Dirichlet and Neumann boundaries. Due to the interaction of both bodies, additional kinematics need to be described. This chapter describes the kinematic relationship and the constraint due to contact in the weak form. All relationships will be introduced for normal contact and friction is not considered. For further details, reference is made to WRIGGERS (2006) and LAURSEN (2003).

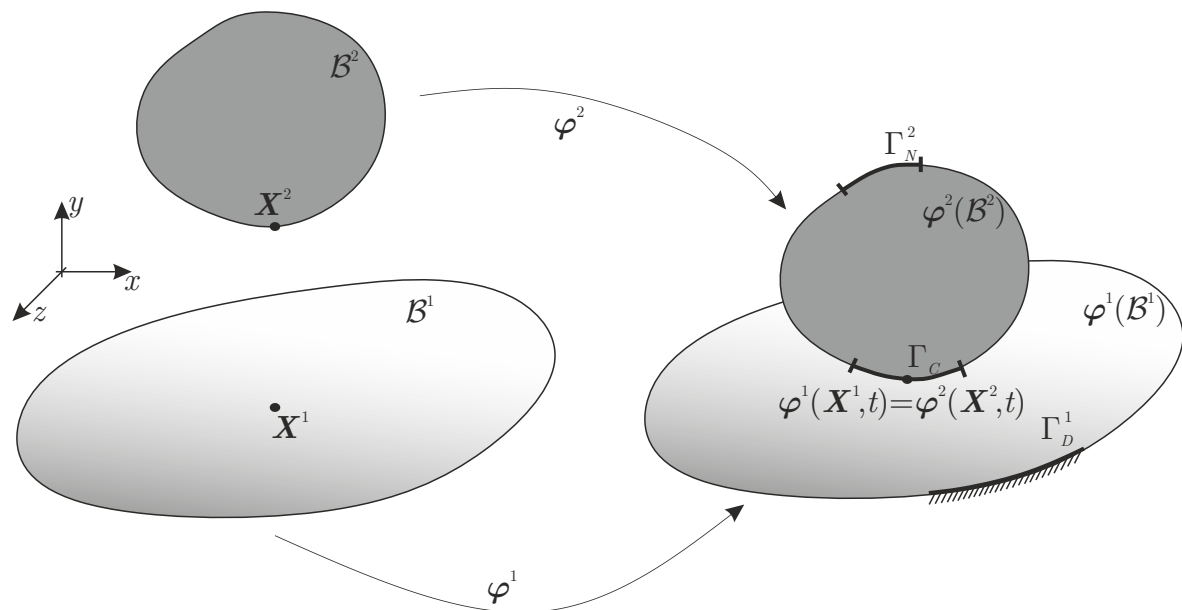


Figure 3.1 – Motion of two body from the initial configuration B^α to the current configuration $\varphi^\alpha(B^\alpha)$.

3.1 Contact kinematics

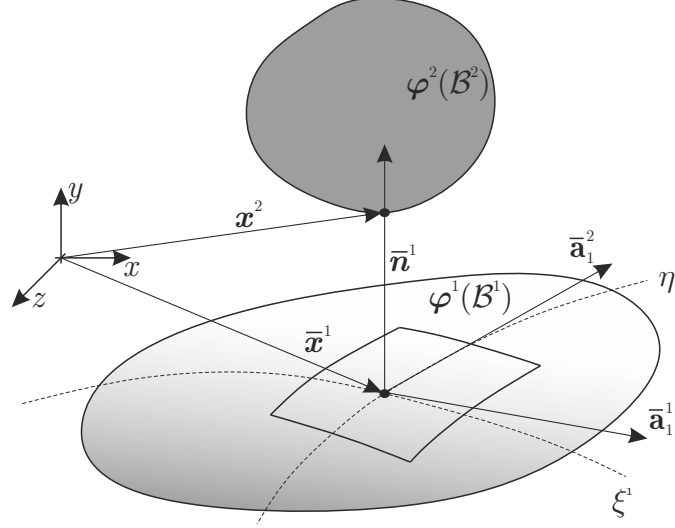


Figure 3.2 – Contact kinematics of two bodies $\varphi^\alpha(\mathcal{B}^\alpha)$ in the current configuration.

To model contact, we assume that two bodies \mathcal{B}^1 and \mathcal{B}^2 approaching each other. The non-penetration condition can be formulated as:

$$(\mathbf{x}^2 - \mathbf{x}^1) \cdot \bar{\mathbf{n}}^1 \geq 0, \quad (3.1)$$

where \mathbf{x}^1 and \mathbf{x}^2 denote points from the surface Γ^1 and Γ^2 of the bodies $\varphi(\mathcal{B}^1)$ and $\varphi(\mathcal{B}^2)$ in the current configuration. For the assumption that the contact boundary Γ_c is at least locally a convex region, every point \mathbf{x}^2 on Γ_2 can be related to a point $\bar{\mathbf{x}}^1 = \bar{\mathbf{x}}^1(\xi_1, \eta_1)$ on Γ_1 via the minimum distance problem, as shown in Fig. 3.2, see WRIGGERS (2006):

$$d^1(\xi_1, \eta_1) = \|\mathbf{x}^2 - \bar{\mathbf{x}}^1\| = \min \|\mathbf{x}^2 - \bar{\mathbf{x}}^1(\xi_1, \eta_1)\| \quad \forall \bar{\mathbf{x}}^1 \subseteq \Gamma^1. \quad (3.2)$$

(ξ_1, η_1) are denoting the parametrization of the boundary Γ_1 . For the parametrization, we can choose simple isoparametric quadrilateral or triangular finite elements, which will be discussed later. The closest point $\bar{\mathbf{x}}^1$ on the master body \mathcal{B}^1 can be computed through:

$$\frac{d}{d(\xi_1, \eta_1)} d^1(\xi_1, \eta_1) = \frac{\mathbf{x}^2 - \bar{\mathbf{x}}^1(\xi_1, \eta_1)}{\|\mathbf{x}^2 - \bar{\mathbf{x}}^1(\xi_1, \eta_1)\|} \cdot \bar{\mathbf{x}}^1_{,\alpha}(\xi_1, \eta_1) = 0 \quad (3.3)$$

or in other words: Find ξ_1 and η_1 , such that $d^1(\xi_1, \eta_1) \rightarrow \min$. Generally this problem can be solved using an inner Newton-Raphson loop and is also known as the local contact problem. Once the closest point $\bar{\mathbf{x}}^1$ is known, the gap g_N in normal direction $\bar{\mathbf{n}}^1$ between the two bodies is given by:

$$g_N = (\mathbf{x}^2 - \bar{\mathbf{x}}^1) \cdot \bar{\mathbf{n}}^1, \quad (3.4)$$

where the normal can be computed from the local tangent vectors $\bar{\mathbf{a}}_1 = \bar{\mathbf{x}}^1_{,\xi_1}$ and $\bar{\mathbf{a}}_2 = \bar{\mathbf{x}}^1_{,\eta_1}$ which yields

$$\bar{\mathbf{n}}^1 = \frac{\bar{\mathbf{a}}_1 \times \bar{\mathbf{a}}_2}{\|\bar{\mathbf{a}}_1 \times \bar{\mathbf{a}}_2\|}. \quad (3.5)$$

Since the contact interface is free of adhesion forces, the normal stress at the interface $\sigma_n = \mathbf{t}^1 \cdot \mathbf{n}^1 = -\mathbf{t}^2 \cdot \mathbf{n}^2$ has to be negative. Beside that, penetration is not allowed. These two conditions can be summarized in the so called Karush-Kuhn-Tucker (KKT) conditions as:

$$g_N \geq 0, \quad \sigma_n \leq 0, \quad g_N \sigma_n = 0, \quad (3.6)$$

where the first inequality constraint describes the non-penetration condition, the second inequality the condition that the contact stresses are always negative and the third equality that at least one quantity the gap g_N or the normal stress σ_n has to be zero. The above introduced KKT conditions can be employed by an active set method to establish the active contact region. The detected constraints can be added to the weak form, introduced in equation (2.4), by using a special form for the contact contribution Π^c with:

$$\Pi = \sum_{\alpha=1}^2 \Pi^{int,\alpha} + \Pi^{ext,\alpha} + \Pi^c. \quad (3.7)$$

3.2 Treatment of contact constraints

Various formulations are possible, like the Lagrange multipliers method, penalty method, Nitsche method, barrier method or the augmented Lagrangian formulation, for details see WRIGGERS (2006).

3.2.1 Penalty method

The easiest way to construct Π^c is to use a penalty formulation. The energy form leads:

$$\Pi^c = \begin{cases} \int_{\Gamma_c} \frac{1}{2} \epsilon_p g_N^2 d\Gamma_c & , \quad \forall g_N \leq 0 \\ 0 & , \quad \forall g_N > 0 \end{cases}, \quad (3.8)$$

where ϵ_p is the penalty parameter. The penalty term Π^c is only added to the system, when the constraint is active ($g_N \leq 0$). However, this method allows penetration of the contact pairs and the right choice of the penalty parameters is a crucial issue. A major disadvantage of this method with the numerical treatment appears when ill-conditioning arises due to the combination of the stiffness of the bodies within the finite element formulation together with the penalty parameter or the stiffness due to constitutive interface laws, see WRIGGERS (2006). For too high penalty parameters, the condition number of the global tangent matrix can become very large, leading to ill-conditioning and thus to unstable and non-unique solutions, see HUNĚK (1993).

3.2.2 Lagrange multiplier method

As an alternative, the Lagrangian multiplier method can be used. Here, the potential form leads:

$$\Pi^c = \begin{cases} \int_{\Gamma_c} \lambda_n g_N d\Gamma_c & , \quad \forall g_N \leq 0 \\ 0 & , \quad \forall g_N > 0 \end{cases}, \quad (3.9)$$

where λ_n is an additional degree of freedom. This method imposes the contact condition exactly but introduces new unknowns with the Lagrange multiplier λ_n . However, this method of enforcing the contact conditions can be too strict in certain cases, see KIKUCHI & ODEN (1988).

3.2.3 Augmented Lagrange method

The augmented Lagrangian formulation is a combination of both aforementioned methods, see KIKUCHI & ODEN (1988) and WRIGGERS (1985). These early works used the Uzawa algorithm. This method provides good algorithmic properties and combines the advantageous properties of the penalty and the Lagrange multiplier formulation, see WRIGGERS (2006) and LAURSEN & SIMO (1993). A full Newton scheme for contact using the augmented Lagrangian method was developed in PIETRZAK & CURNIER (1999). The contact contribution Π^c to the total energy in equation (3.7) is then given by

$$\Pi^c = \begin{cases} \int_{\Gamma_c} (\lambda_n + \frac{\epsilon_p}{2} g_N) g_N \, d\Gamma_c & , \quad \forall \lambda_n \leq 0 \quad (\text{contact}) \\ - \int_{\Gamma_c} \frac{1}{2\epsilon_p} \lambda_n^2 & , \quad \forall \lambda_n > 0 \quad (\text{no contact}) \end{cases} \quad (3.10)$$

where λ_n and ϵ_p are introduced. Since this work focus only on normal contact, the contribution in tangential direction within the contact interface is neglected.

3.3 Contact discretization

For the discretization of the contact area, numerous possibilities can be found in the literature. A detailed overview can be found in LIU ET AL. (2022) and POPP & WALL (2014). Some of the most common used ones are shown in Fig. 3.3. For simplification, the figures are showing two dimensional cases but although the idea is similar for the application to three dimensional problems. The easiest approach is the so called node-to-node contact (as shown in Fig. 3.3c), which was first introduced in the early works by FRANCAVILLA & ZIENKIEWICZ (1975) and HUGHES ET AL. (1976). Aside from the fact that this approach is extremely simple to implement, the main disadvantage is that the contact meshes at the interface must be conforming, which is not always the case. This method enforces the contact conditions nodal wise. However, another frequently used approach is to parametrize the surfaces and find for a surface node on one body, the position of its normal projection on the corresponding surface from the other body. This approach is schematically illustrated in Fig. 3.3a. First implementations can be found in HALLQUIST & LABORATORY (1979) and HUGHES ET AL. (1976) and later extensions to more general cases in SCHWEIZERHOF ET AL. (1992), BATHE & CHAUDHARY and WRIGGERS ET AL. (1990). Generally, a node-to-surface based contact enforcement does not pass the patch test and leads to inconsistent transfer of the contact pressure between the contact bodies, see EL-ABBASI & BATHE (2001). A modified version of node-to-segment based two dimensional contact elements can be found in ZAVARISE & DE LORENZIS. The authors used a modified virtual slave node technique in combination with a specific procedure to correctly compute the contact forces at the master node. This modified node-to-segment contact element passes the

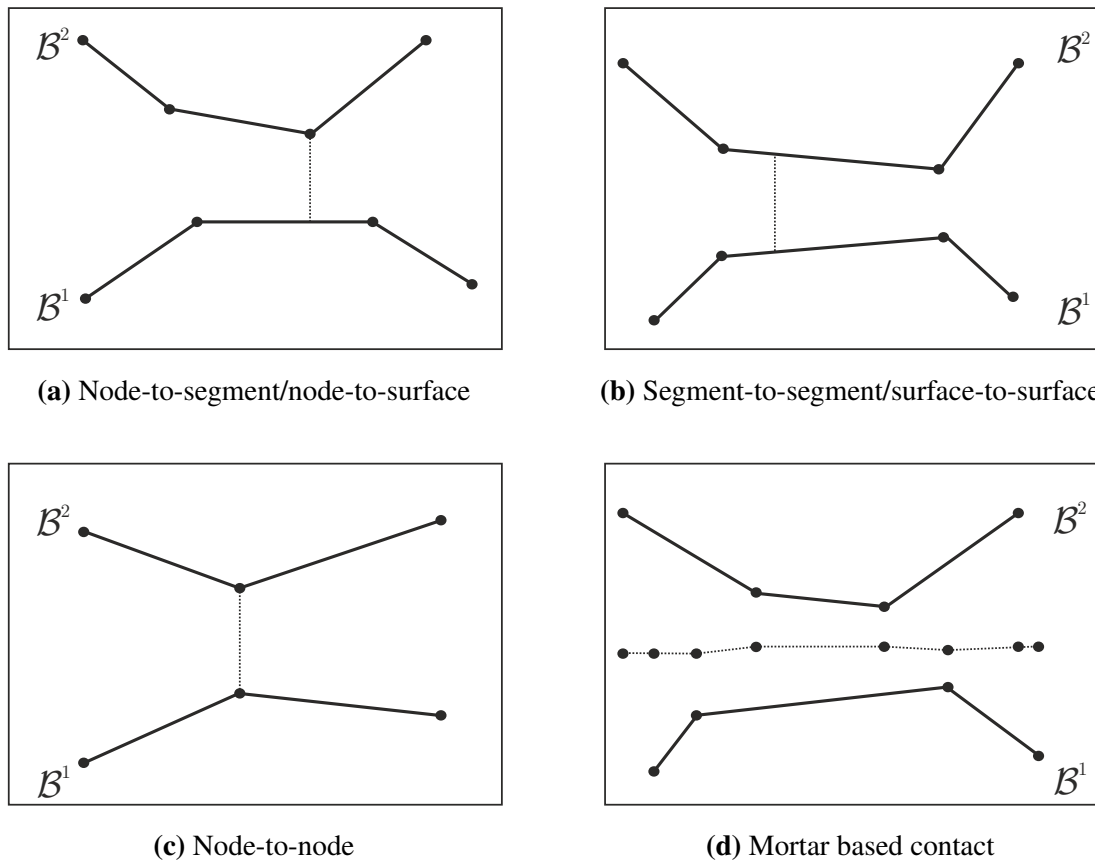


Figure 3.3 – Schematic illustration of different contact discretizations.

patch test at the cost of losing symmetry in the derived contact element tangent. An alternative was first proposed in SIMO ET AL. (1985c) as a segment-to-segment formulation in 2D, as shown in Fig. 3.3b. The idea was to enforce the contact constraint in a weak sense, where the displacement field is interpolated with linear shape functions at the interface, such that the gap function is evaluated in a mean sense. Many further developments of segment-to-segment/surface-to-surface formulations can be found in the literature, for example see ZAVARISE & WRIGGERS (1998) and EL-ABBASI & BATHE (2001). While these methods pass the patch test, they are more difficult to implement. Another alternative method is called mortar method which was first introduced to treat problems involving domain decomposition, see BERNARDI ET AL. (1993). Later, applications to contact problems with non-conforming meshes were realized in two- and three-dimensions in BELGACEM ET AL. (1998), MCDEVITT & LAURSEN (2000), WOHLMUTH, PUSO (2004), PUSO & LAURSEN (2004), FISCHER & WRIGGERS (2005), TUR ET AL. (2009) and TEMIZER (2012). The idea of this method is to enforce the contact conditions weakly on an intermediate mortar surface, as illustratively shown in Fig. 3.3d. However, mortar based contact passes the patch test in general and leads to a higher accuracy than node-to-surface methods. But on the other hand, similarly to surface-to-surface contact, the computer implementation of mortar based methods is complicated and more costly in terms of computation, see FARAH ET AL. (2015). In LIU ET AL. (2022) the authors proposed an enrichment strategy for the displacement terms,

resulting in an augmented node-to-node discretization. Indeed, the possibilities for treating contact are enormous, and the decision is based on whether the treatment is less expensive in terms of computation and implementation or less accurate. Since node-to-node contact is the easiest way for contact treatment in terms of computational costs and implementation aspects, a mesh adaption to reach conforming meshes at the interface would be an efficient alternative, as have been demonstrated in WRIGGERS ET AL. (2016), WRIGGERS & RUST (2019) and RUST (2019) for two dimensional problems.

Chapter 4

Virtual element method

In this chapter, we will shortly introduce very popular and robust techniques, FEM and its extension VEM and outline the differences between them (classical FEM and VEM). The discretization of the weak form and the construction of the virtual element is described for both, static and dynamic case. As the projections in VEM lead to rank deficient tangent matrices, stabilization is needed and thus different stabilization techniques are also given. Beside the usual definition of a purely displacement based formulation, a mixed formulation based on the Hu-Washizu principle is introduced. For all the following integrations over different kind of element shapes, the weights and local coordinates can be found in appendix A.3. Since this work focuses on the virtual element method, a detailed description of the finite element method is omitted and reference is made to different textbooks with WRIGGERS (2008), HUGHES (2012), ZIENKIEWICZ & TAYLOR (2005) and BATHE (2006) which describe the FEM from a more engineering perspective. For the mathematical foundation of the FEM see ODEN & REDDY (2012), CIARLET (2002), BABUŠKA & STROUBOULIS (2001) and BREZZI & FORTIN (2011).

4.1 The concept of discretization

The discretization of the weak form in equation (2.68) can be realized in different ways. So far the theory of continuous mechanics assumed $\mathbf{u}(\mathbf{X})$ is known, however actual analytical solutions are hard to come by and are limited. Thus numerical methods have to be employed e.g. finite difference methods, finite element methods, virtual element methods, finite volume methods and many others, see MAZUMDER (2015), HOFFMAN & FRANKEL (2018) and VASSILEVSKI ET AL. (1999). In this work, different finite and virtual element formulations will be applied, thus the discretization will be discussed based on these two methods. Within both approaches, the exact geometry and primary variables (in our case the displacements) have to be approximated within the body \mathcal{B} . For that purpose, the body \mathcal{B} is discretized using a mesh of n_E finite elements and n_N nodes/vertices which approximate the geometry of the body with (see Fig. 4.1):

$$\mathcal{B} \approx \mathcal{B}_h = \bigcup_{E=1}^{n_E} \Omega_E, \quad (4.1)$$

where $\Omega_E \subset \mathcal{B}_h$ denotes the configuration of one single element, see Fig. 4.1. Note that here Ω_E can represent a finite or virtual element. The first major difference is that within FEM framework a mesh can only consist of certain element shapes (Fig. 4.1a), usually triangles or quadrilaterals of first or higher orders in 2D and tetrahedrons or hexahedrons in 3D, while for VEM any closed polygon/polyhedron can be used as an element (Fig. 4.1b). An exact solution of the problem $\mathbf{u}(\mathbf{X})$ is usually not known and thus the exact solution

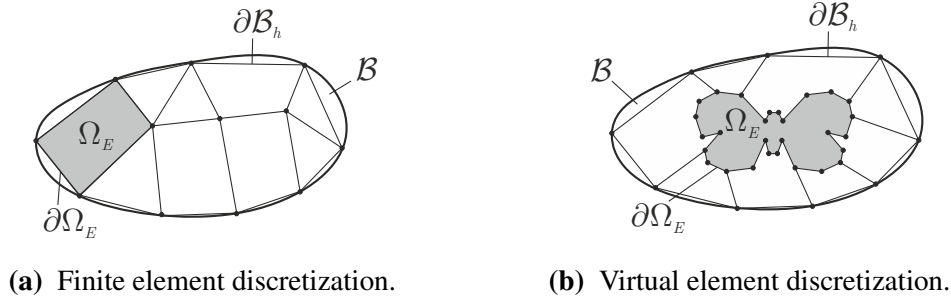


Figure 4.1 – Discretization of the solid.

is only approximated. The ultimate goal is to find the global unknowns \mathbf{u} at given nodes \mathbf{X} . For the solution, various methods can be used. In this work, a global Newton scheme is used, which results in the following linearized system of equations in each iteration:

$$\mathbf{K} \Delta \mathbf{u} + \mathbf{R} = \mathbf{0} \quad \text{with} \quad \mathbf{K} = \mathbf{A} \mathbf{K}_E, \quad \mathbf{R} = \mathbf{A} \mathbf{R}_E, \quad (4.2)$$

where instead of a summation operator \sum , an assembly operator \mathbf{A} is used, to denote a finite element assembly procedure of all local residuals \mathbf{R}_E and tangents \mathbf{K}_E according to the degrees of freedom. Equation (4.2) allows to determine the global primary field of unknowns \mathbf{u} (here displacements), by calculating their linear increment $\Delta \mathbf{u}$ in a classical Newton type iterative solution scheme. Usually in a nonlinear framework, the tangent is a function of the unknowns itself, i.e. $\mathbf{K} = \mathbf{K}(\mathbf{u}^i)$. Thus the solution is searched in incremental steps iteratively and for a converged step the updated vector can be computed with $\mathbf{u}^{i+1} = \mathbf{u}^i + \Delta \mathbf{u}$.

Next step is to find \mathbf{K}_E and \mathbf{R}_E of each element. The residual of one single element can be obtained by computing the first variation of total element potential or pseudo potential (e.g. element integral of strain energy function in equation (2.52)) with respect to the element nodal displacements $\mathbf{u}_E = \{u_1, v_1, w_1, u_2, v_2, w_2, \dots, u_{n_V}, v_{n_V}, w_{n_V}\}$ with:

$$\mathbf{R}_E = \frac{\partial \Pi(\mathbf{u}_E)}{\partial \mathbf{u}_E} \quad \text{and} \quad \mathbf{K}_E = \frac{\partial \mathbf{R}_E(\mathbf{u}_E)}{\partial \mathbf{u}_E}. \quad (4.3)$$

Element nodal unknowns are denoted by \mathbf{p}_E to introduce a more general notation, since additional degrees of freedom would add additional entries in to the vector of unknowns, e.g. $\mathbf{p}_E = \{\mathbf{u}_E, \mathbf{T}_E, \dots\}$, where \mathbf{T}_E can stand for example for temperature degree of freedoms. In the next step, proper functions for nodal variables have to be chosen. Here is where the FEM and VEM start to differ due to the nature of chosen mesh and ansatz functions.

The assembled elements, which result in an approximated geometry, are continuous in the region \mathcal{B} due to compatibility requirements of continuum theory and thus overlapping of elements or gaps between elements are not allowed. In terms of the convergence of the finite element solution to the true solution of the underlying partial differential equation, different requirements for the construction of ansatz functions exist. However, for interested readers, reference is made to WRIGGERS (2008) and HUGHES (2012). The VEM however is more lenient on the choice of geometry as will be discussed later in section 4.4.

4.2 The finite element method and the differences to the virtual element method

Within each finite element Ω_E , nodal quantities can be approximated with ansatz functions N , where the approximated quantities are indicated by the index h in equation (4.4) and (4.1). Generally for a finite element approach, the exact solution of the problem is approximated within a single finite element with interpolation functions by:

$$\mathbf{u}(\mathbf{X})|_{\mathbf{X} \in \Omega_E} \approx \mathbf{u}_h(\mathbf{X}) = \sum_{I=1}^{n_V} N_I(\mathbf{X}) \mathbf{u}_I = \mathbf{N} \mathbf{u}_E, \quad (4.4)$$

where $\mathbf{N} = \{N_1, N_2, \dots, N_I, \dots, N_{n_V}\}$ represents the vector of shape functions for n_V nodes and $\mathbf{u}_E = \{\mathbf{u}_1, \mathbf{u}_2, \dots, \mathbf{u}_I, \dots, \mathbf{u}_{n_V}\}$ is a nodal wise ordered nested list containing the nodal displacements $\mathbf{u}_I = \{u_I, v_I, w_I\}$ of a single element. In a finite element procedure, generally the geometry is interpolated by the same ansatz functions as the variables for both, the initial and current coordinates with:

$$\mathbf{X} = \{X_E, Y_E, Z_E\} = \sum_{I=1}^{n_V} N_I(\Xi) \mathbf{X}_I = \mathbf{N}(\Xi) \mathbf{X}, \quad (4.5)$$

$$\mathbf{x} = \{x_E, y_E, z_E\} = \sum_{I=1}^{n_V} N_I(\Xi) \mathbf{x}_I = \mathbf{N}(\Xi) \mathbf{x}, \quad (4.6)$$

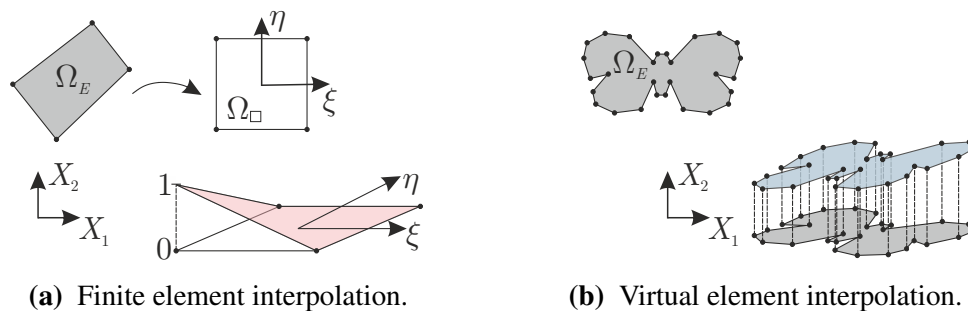
which is known as the isoparametric concept. Similarly to the displacement in equation (4.4), the geometry is approximated and $\mathbf{X} \approx \mathbf{X}_h$. However, for clarity the index h is omitted in the further course of this work. $\Xi = \{\xi, \eta, \zeta\}$ represents the local coordinates in the parametric space. Isoparametric elements are very well suited for nonlinear problems, due to the fact that it makes no difference whether the mapping onto a reference element Ω_\square is made from the initial or spatial configuration. However, this is one of the major differences between the FEM, where all integrations are performed on a reference element and the VEM, where all integrations are performed on the initial coordinates, as depicted in Fig. 4.2. The lack of isoparametric concept indeed increases the integration effort, but on the other hand the VEM is free of shape restrictions during the deformation process, unlike the FEM. Additionally, VEM shape functions are only known at the boundary, leading to polynomials of degree k , while they are not known in the interior and may contain non-polynomial functions. A detailed comparison of both methods is given in table 4.1, see

Table 4.1 – Major differences between FEM and VEM.

Property	FEM	VEM
Meshing	Restricted to certain element topologies, i.e. triangles or quadrilaterals in 2D or tetrahedra, hexahedra,... in 3D. Mesh conformity is needed and hanging nodes need additional treatment.	Free in choice of element shape and number of nodes per element, i.e. arbitrary polygonal shapes, including non-convex shapes with arbitrary number of nodes. Hanging nodes can be added simply by inserting vertices.
Shape functions	Known polynomials.	Implicitly defined. Unknown in the interior but known on element boundaries. Local shape functions contain polynomials and may contain non-polynomial functions.
Local stiffness matrix	Usually isoparametric formulation with Gauss quadrature.	Computed in physical space and thus no mapping. Local stiffness matrix is subdivided into projection part and stabilization part, where the latter requires user-defined stabilization parameter.
Local load vector	Usually isoparametric formulation with Gauss quadrature.	Projection of body forces are required and it depends on polynomial of order k .
Computational cost	Simple computation and assembly thanks to isoparametric concept.	Requires additional effort for the computation of the stiffness matrix. Stabilization part increases computational time.

MENGOLINI ET AL. (2019).

The transformation process is depicted in Fig. 4.3 for a single finite element Ω_E in the initial configuration and an element in the current configuration $\varphi(\Omega_E)$.

**Figure 4.2** – Comparison of interpolation functions for FEM and VEM.

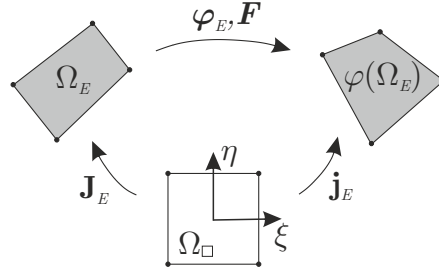


Figure 4.3 – Isoparametric mapping of the deformation of single finite element Ω_E

It can be easily seen that the mapping in Fig. 4.3 from the initial to the current configuration is nothing else then the discrete form of the continuum mechanical description of the motion of a body in Fig. 2.1. The following kinematical quantities can be stated for a single finite element:

$$\mathbf{F} = \mathbf{j}_E \mathbf{J}_E^{-1} \quad \text{and} \quad J_F = \det \mathbf{F} = \frac{\det \mathbf{j}_E}{\det \mathbf{J}_E}, \quad (4.7)$$

where \mathbf{j}_E and \mathbf{J}_E are defined as:

$$\mathbf{j}_E = \frac{\partial \mathbf{x}}{\partial \mathbf{\Xi}} \quad \text{and} \quad \mathbf{J}_E = \frac{\partial \mathbf{X}}{\partial \mathbf{\Xi}}. \quad (4.8)$$

With the relation in equation (4.7) and (4.8) in hand, the computation of gradients related to the initial or current configuration is straightforward.

The discrete solution of partial differential equation can be obtained by different formulations when automatic differentiation is used, see KORELC & WRIGGERS (2016), KORELC (2022) and KORELC (2002). One way is based on the weak form in equation (2.66). Without going to much into detail, this formulation requires the following procedure:

$$\mathbf{u}_h \rightarrow \mathbf{C} \quad \text{and} \quad 2 \frac{\Psi(\mathbf{C})}{\partial \mathbf{C}} = \mathbf{S} \rightarrow \int_{\Omega_E} \frac{1}{2} \mathbf{S} \cdot \delta \mathbf{C} \, d\Omega \rightarrow \mathbf{R}_E \rightarrow \mathbf{K}_E. \quad (4.9)$$

An alternative is the formulation based on the stationarity of a potential with the strain energy and the related kinematic, e.g. \mathbf{F} , together with the element ansatz function \mathbf{u}_h as the only quantities which have to be described. This procedure can be summarized as follows:

$$\mathbf{u}_h \rightarrow \mathbf{C} \rightarrow \int_{\Omega_E} \Psi(\mathbf{C}) \, d\Omega \rightarrow \mathbf{R}_E \rightarrow \mathbf{K}_E. \quad (4.10)$$

The latter is conducted in this work for the computation of the stiffness matrix.

Another possibility is to reformulate the weak form based on equation (4.9) as a pseudo potential using a differentiation exception:

$$\Pi^{ps} = \int_{\Omega_E} \frac{1}{2} \mathbf{S} \cdot \mathbf{C} \, d\Omega \rightarrow \left. \frac{\partial \Pi^{ps}}{\partial \mathbf{u}_E} \right|_{\mathbf{S}=\text{const.}} \delta \mathbf{u}_E \rightarrow \mathbf{R}_E \rightarrow \mathbf{K}_E, \quad (4.11)$$

where Π^{ps} represents a pseudo potential. Therefore weak form formulations can be treated in same manner as potential formulation with proper differentiation exceptions, see KORELC & WRIGGERS (2016) and HUDOBIVNIK & KORELC (2016). In this work, the computation of the mass matrix is based on the aforementioned pseudo potential form, as will be shown later.

Both formulations can either be solved in the current or initial configuration, which leads to four different formulations. However, investigations regarding the code efficiency of various formulations have been analyzed in KORELC & WRIGGERS (2016). In order to compute the residuum, the variational form in equation (2.67) is used. The internal energy part of a single finite element can be formulated as:

$$\int_{\Omega_E} \Psi(\mathbf{C}) \, d\Omega = \sum_{g=1}^{n_g} \Psi(\mathbf{C}(\Xi_g)) \det \mathbf{J}_E(\Xi_g) w_g, \quad (4.12)$$

where the summation denotes the numerical integration over n_g Gauss points for the construction of the element matrices.

The residual of one single element can be obtained by computing the first variation with respect to the nodal unknowns i.e. nodal displacements $\mathbf{u}_E = \{u_1, v_1, w_1, u_2, v_2, w_2, \dots, u_{n_V}, v_{n_V}, w_{n_V}\}$ with:

$$\delta \int_{\Omega_E} \Psi(\mathbf{C}) \, d\Omega \approx \left[\sum_{g=1}^{n_g} \frac{\partial \Psi(\mathbf{C}(\mathbf{u}_E))}{\partial \mathbf{u}_E} J_g w_g \right] \delta \mathbf{u}_E. \quad (4.13)$$

With equation (4.13) the element residual and element tangent leads for a single Gauss point to:

$$\mathbf{R}_g = \frac{\Psi(\mathbf{C}(\mathbf{u}_E))}{\partial \mathbf{u}_E} J_g w_g \quad \text{and} \quad \mathbf{K}_g = \frac{\mathbf{R}_g(\mathbf{u}_E)}{\partial \mathbf{u}_E}, \quad (4.14)$$

where the summation over n_g Gauss points yields the element residual and element tangent:

$$\mathbf{R}_E = \sum_{g=1}^{n_g} \mathbf{R}_g \quad \text{and} \quad \mathbf{K}_E = \sum_{g=1}^{n_g} \mathbf{K}_g. \quad (4.15)$$

4.3 Virtual element space and projection operator

In this work, a low order Ansatz is adopted for the construction of virtual elements, i.e. $k = 1$. The following equations will be derived for the three dimensional case but can be easily adopted to the two dimensional case, see WRIGGERS ET AL. (2017). The domain can be discretized with non overlapping arbitrary shaped polyhedral elements $\Omega_E \in \mathbb{R}^3$. The surface of each element Ω_E consists of polygonal faces $\Gamma_f \in \Gamma_E = \partial\Omega_E$, where Γ_E is a set of all faces of element Ω_E . Each face Γ_f includes linear edges $\gamma_e \in \gamma_f = \partial\Gamma_f$, where γ_f is a set of all edges of face Γ_f . It is a subset in all edges γ_E of element Ω_E with $\gamma_f \in \gamma_E = \partial\Gamma_E$, see Fig. 4.4.

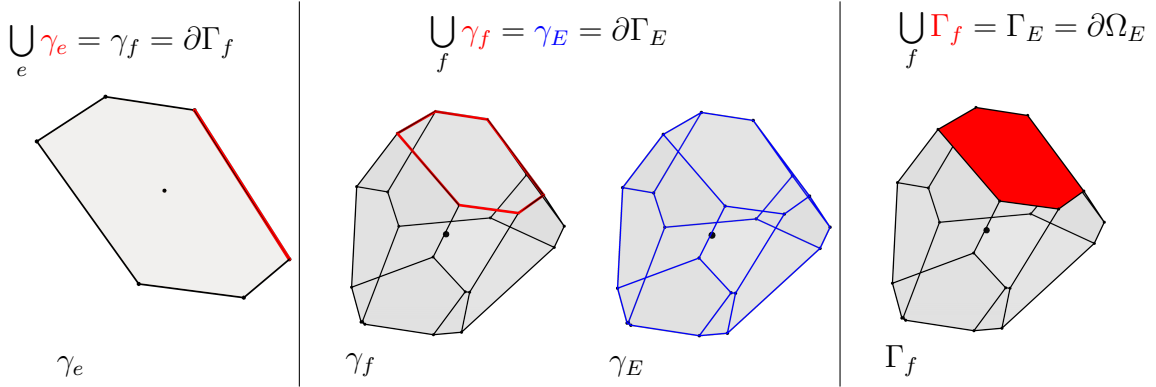


Figure 4.4 – Single three dimensional virtual element with faces and edges.

The virtual element space of each element is defined for admissible displacements \mathbf{u} and its variations $\delta\mathbf{u}$ as:

$$\mathcal{V}_h(\Omega_E) = \{\mathbf{u}_h \in [\mathcal{H}^1(\Omega_E)]^3 : \begin{cases} \Delta\mathbf{u}_h|_{\Omega_E} & \in [\mathcal{P}_{k-2}(\Omega_E)]^3 \\ \mathbf{u}_h|_{\Gamma_f} & \in \mathcal{V}_f(\Gamma_f) \forall \Gamma_f \in \partial\Omega_E \end{cases} \quad (4.16)$$

$$\mathcal{V}_f(\Gamma_f) = \{\mathbf{u}_h \in [\mathcal{H}^1(\Gamma_f) \cap C^0(\Gamma_f)]^3 : \begin{cases} \Delta_f\mathbf{u}_h|_{\Gamma_f} & \in [\mathcal{P}_{k-2}(\Gamma_f)]^3 \\ \mathbf{u}_h|_{\gamma_e} & \in [\mathcal{P}_k(\gamma_e)]^3 \forall \gamma_e \in \partial\Gamma_f, \end{cases} \quad (4.17)$$

where \mathcal{P}_k being the space of polynomials up to order k and Δ_f the Laplacian operator acting in the local face. The space $\mathcal{V}_h(\Omega_E)$ contains harmonic functions, continuous at the boundary of each virtual element and belonging to $\mathcal{V}_f(\Gamma_f)$ on each face. $\mathcal{V}_f(\Gamma_f)$ represents the space, which contains continuous harmonic functions that are piecewise linear at the boundary of the face (edge-by-edge). For $k = 1$, the divergence term vanishes, such that $\Delta\mathbf{u}_h|_{\Omega_E} = 0$ and $\Delta_f\mathbf{u}_h|_{\Gamma_f} = 0$. The main feature of the virtual element method is the projection operator $\tilde{\pi}$. It is defined as an operator onto polynomial space, for $k = 1 \rightarrow \mathcal{P}_1$, $\tilde{\pi} : \mathcal{V}_h(\Omega_E) \rightarrow \mathcal{P}_1(\Omega_E)$, where $\mathcal{V}_h(\Omega_E) := [\mathcal{V}_h(\Omega_E)]^3$ specifies the local VEM shape functions on Ω_E , as defined in equation (4.16). For further details to the mathematical fundamentals of virtual element methods, see BEIRÃO DA VEIGA ET AL. (2014), BEIRÃO DA VEIGA ET AL. (2013a) and CHI ET AL. (2017).

4.4 Construction of the virtual element

The main idea of the virtual element method is the split of the primary variables in to a projection part, denoted by \mathbf{u}_π and a remainder as:

$$\mathbf{u}_h = \mathbf{u}_\pi + (\mathbf{u}_h - \mathbf{u}_\pi). \quad (4.18)$$

For the projected displacements, a low order Ansatz is adopted in this work:

$$\begin{aligned} \tilde{\pi}\mathbf{u}_h &= \mathbf{u}_\pi = (\mathbf{N}_\pi \cdot \mathbf{a}_i) \mathbf{E}_i, \quad i \in \{1, 2, 3\}, \\ \mathbf{N}_\pi &= (1, X, Y, Z), \\ \mathbf{a}_i &= (a_{i1}, a_{i2}, a_{i3}, a_{i4}), \end{aligned} \quad (4.19)$$

where \mathbf{a} represents 12 unknown parameters $\mathbf{a} = \bigcup_{i=1}^{n_{dim}} \mathbf{a}_i$ of the virtual element formulation which have to be determined. In the two dimensional case with only displacements as primary variables, these virtual parameters are reduced to 6, while additional primary unknowns increase the amount of parameters, see ALDAKHEEL ET AL. (2019). Alternatively to the polynomial \mathbf{N}_π in equation (4.19), a scaled Ansatz can be used as interpolation function, for details see e.g. ARTIOLI ET AL. (2017a). The key for the computation of the map between the nodal degrees of freedom and the virtual parameters is the requirement that the remainder $(\mathbf{u}_h - \mathbf{u}_\pi)$ is orthogonal to any polynomial of first order \mathbf{p} and further that the gradient of the remainder $(\nabla \mathbf{u}_h - \nabla \mathbf{u}_\pi)$ is orthogonal to the gradient of any polynomial of first order $\nabla \mathbf{p}$, see BEIRÃO DA VEIGA ET AL. (2013b, 2014):

$$\int_{\Omega_E} \mathbf{p} \cdot (\mathbf{u}_\pi - \mathbf{u}_h) \, d\Omega = 0 \quad \text{and} \quad \int_{\Omega_E} \nabla \mathbf{p} \cdot (\nabla \mathbf{u}_\pi - \nabla \mathbf{u}_h) \, d\Omega = 0, \quad \forall \mathbf{p} \in \mathcal{P}_1. \quad (4.20)$$

Since linear ansatz functions are used, $\nabla \mathbf{p}$ and $\nabla \mathbf{u}_\pi$ are constant at the element domain Ω_E which yields for equation (4.20)₂

$$\nabla \mathbf{u}_\pi = \frac{1}{|\Omega_E|} \int_{\Omega_E} \nabla \mathbf{u}_h \, d\Omega = \frac{1}{|\Omega_E|} \int_{\Gamma_E} \mathbf{u}_h \otimes \mathbf{N} \, d\Gamma, \quad (4.21)$$

where divergence theorem is applied to shift the volume integral to the boundary of the element. Here \mathbf{N} denotes the normal vector on the reference boundary Γ_E of the domain Ω_E , which belongs to a virtual element E .

By employing the linear ansatz space in equation (4.19), the left hand side of equation (4.21) takes the simple form

$$\nabla \mathbf{u}_\pi = \begin{bmatrix} a_{12} & a_{13} & a_{14} \\ a_{22} & a_{23} & a_{24} \\ a_{32} & a_{33} & a_{34} \end{bmatrix}. \quad (4.22)$$

In the next step, the integral in equation (4.21) has to be computed. In 2D, it is straight forward, since \mathbf{u}_h is linear at the edges of the polygon. For the solution, a linear ansatz with one dimensional linear shape function can be adopted, see WRIGGERS ET AL. (2016) and WRIGGERS ET AL. (2017). However, in the 3D case, various methods are available for the integration. An integration scheme is presented in GAIN ET AL. (2014), where the faces of an element are subdivided into quadrilateral elements. The corners of the quadrilateral elements have specific positions and the evaluation of the integral is performed on those quadrilateral elements. In the next sections, two alternatives will be presented.

4.4.1 Integration over triangles

In the 3D case, element boundary consists of polygonal faces. Therefore the evaluation of the integral in equation (4.21) is not straight forward. One way is to subdivide the element faces into 3 noded triangles. The integration is then carried out over the triangles of the polygonal faces by using the standard ansatz functions for a linear triangle and Gauss integration:

$$\mathbf{N}_h^\mathcal{T} = (\xi, \eta, 1 - \xi - \eta) \quad (4.23)$$

$$\mathbf{u}_h^\mathcal{T} = \mathbf{N}_h^\mathcal{T} \mathbf{u}^\mathcal{T} \quad \text{where} \quad \mathbf{u}^\mathcal{T} = \bigcup_I \mathbf{u}_I \quad \forall I \in \mathcal{T}, \quad (4.24)$$

as outlined in HUDOBIVNIK ET AL. (2018). Here $\mathbf{u}_h^\mathcal{T}$ denotes the linear ansatz for the displacements at each triangle of the polygonal faces. $\mathbf{u}^\mathcal{T}$ is a list which contains the three nodal displacement vectors \mathbf{u}_I of the triangle \mathcal{T} . ξ and η are local dimensionless coordinates at the triangle level. Finally the right hand side of equation (4.21) can be computed. Using

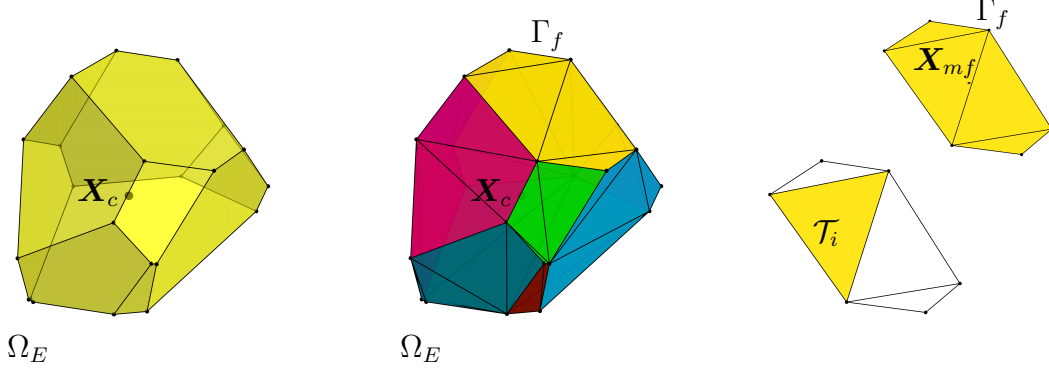


Figure 4.5 – Virtual element with polygonal faces, subdivided into triangles.

equation (4.24), the integral in (4.21) takes the form:

$$\frac{1}{|\Omega_E|} \int_{\Gamma_E} \mathbf{u}_h \otimes \mathbf{N} \, d\Gamma = \frac{1}{|\Omega_E|} \sum_{f=1}^{n_f} \int_{\Gamma_f} \mathbf{u}_h \otimes \mathbf{N}^f \, d\Gamma \quad (4.25)$$

$$= \frac{1}{|\Omega_E|} \sum_{f=1}^{n_f} \sum_{\mathcal{T}=1}^{n_{\mathcal{T}}} \int_{\mathcal{T}} \mathbf{u}_h^\mathcal{T} \otimes \mathbf{N}^\mathcal{T} \, d\Gamma \quad (4.26)$$

$$= \frac{1}{|\Omega_E|} \sum_{f=1}^{n_f} \sum_{\mathcal{T}=1}^{n_{\mathcal{T}}} \sum_{g=1}^{n_g^\mathcal{T}} w_g^\mathcal{T} J_g^\mathcal{T} \mathbf{u}_{hg}^\mathcal{T} \otimes \mathbf{N}^\mathcal{T}, \quad (4.27)$$

where n_f is the number of element faces, $n_{\mathcal{T}}$ the number of triangles on face f and n_g the number of integration points per triangle. \square_g denotes quantities which are evaluated at the Gauss points of the triangle. For an integration over triangles with linear shape functions in equation (4.23) one point quadrature with $n_g^\mathcal{T} = 1$ Gauss point and $w_g^\mathcal{T} = 1/2$ Gauss weight with the local coordinates $\xi = 1/3$ and $\eta = 1/3$ is sufficient. The normal vector $\mathbf{N}^\mathcal{T}$ and the Jacobian of the isoparametric mapping $J^\mathcal{T}$ are evaluated as follows:

$$\mathbf{X}_h^\mathcal{T} = \mathbf{N}_h^\mathcal{T} \mathbf{X}^\mathcal{T} \quad \text{where} \quad \mathbf{X}^\mathcal{T} = \bigcup_I \mathbf{X}_I \quad \forall I \in \mathcal{T}, \quad (4.28)$$

$$\mathbf{G}_\xi = \frac{\partial \mathbf{X}_h^\mathcal{T}}{\partial \xi}, \quad \mathbf{G}_\eta = \frac{\partial \mathbf{X}_h^\mathcal{T}}{\partial \eta}, \quad \mathbf{G}_\zeta = \mathbf{G}_\xi \times \mathbf{G}_\eta, \quad (4.29)$$

$$J^\mathcal{T} = \|\mathbf{G}_\zeta\|, \quad \mathbf{N}^\mathcal{T} = \frac{\mathbf{G}_\zeta}{J^\mathcal{T}}. \quad (4.30)$$

All quantities are related to the initial configuration. Comparing equation (4.22) and (4.27),

the unknown virtual parameters $a_{ij}|_{i \in (1,2,3) \wedge j \in (2,3,4)}$ can be obtained by inspection, for further details see e.g. WRIGGERS ET AL. (2017).

Usually, it is sufficient to compute the linear part of the virtual parameters only for the computation of the stiffness matrix. However, for partial differential equations, where the primary field appears with its zeroth derivative, the computation of the virtual parameters, which are related to the constant part are required, e.g. for computing the mass matrix. The constant part of the projection $a_{i1}|_{i \in (1,2,3)}$ can be obtained from equation (4.20)₁. This L^2 -projection is evaluated at the nodal points which yields for each virtual element Ω_E

$$\sum_{I=1}^{n_V} \mathbf{u}_\pi(\mathbf{X}_I) = \sum_{I=1}^{n_V} \mathbf{u}_h(\mathbf{X}_I), \quad (4.31)$$

where n_V is the total number of element nodes and \mathbf{X}_I is the coordinate of nodal point I in the initial configuration. By substituting equation (4.19) and (4.22) in (4.31) the missing three parameters can be expressed in terms of the nodal displacements and known projection gradient $\nabla \mathbf{u}_\pi$:

$$(a_{11}, a_{21}, a_{31}) = \frac{1}{n_V} \sum_{I=1}^{n_V} (\mathbf{u}_I - \nabla \mathbf{u}_\pi \mathbf{X}_I). \quad (4.32)$$

Finally with equation (4.27) and (4.32) the ansatz function \mathbf{u}_π of the virtual element is completely defined in terms of the element unknowns, i.e. nodal displacements $\mathbf{u}_E = \{\mathbf{u}_1, \mathbf{u}_2, \dots, \mathbf{u}_{n_V}\}$. The parameters a_{ij} in equation (4.22) and (4.32) can be related by a linear mapping to the nodal displacements and equation (4.19) can be rewritten

$$\mathbf{a} = \tilde{\pi} \mathbf{u}_E \quad \longrightarrow \quad \mathbf{u}_\pi = \mathbf{H}(\mathbf{X}) \tilde{\pi} \mathbf{u}_E, \quad (4.33)$$

where $\mathbf{H}(\mathbf{X})$ is the matrix representation of the ansatz functions \mathbf{N}_π and $\tilde{\pi}$ denotes the matrix representation of the projection operator $\tilde{\pi}$. For a detailed computation of $\tilde{\pi}$, see WRIGGERS ET AL. (2016). In our framework, where automatic differentiation is used, it is explicitly expressed with the help of equation (4.21). Having the virtual parameters in hand, now all kinematic quantities can be expressed in terms of the projection function.

4.4.2 Integration over edges

Alternatively equation (4.21) can be computed on edges of an element in 3D directly by applying the divergence theorem again (see equation (A.1)) and shift the integral $\frac{1}{|\Omega_E|} \int_{\Gamma_E} \mathbf{u}_h \otimes \mathbf{N} \, d\Gamma$ in equation (4.21) over element surface Γ_E to an integral over the edge γ_E , as introduced in ANTONIETTI ET AL. (2018) and CHIN ET AL. (2015). Such formulation does not require any additional triangulation of each face and thus the bias of triangle choice is eliminated. By applying the divergence theorem again and summing up over all edges n_e

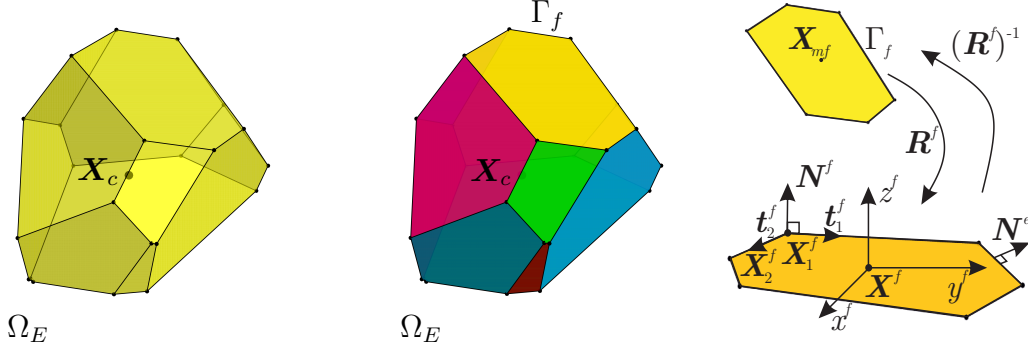


Figure 4.6 – Virtual element with polygonal faces.

and assuming that N^f is constant over the face, equation (4.21) leads:

$$\nabla \mathbf{u}_\pi = \frac{1}{|\Omega_E|} \sum_{f=1}^{n_f} \int_{\Gamma_f} \mathbf{u}_h \otimes N^f d\Gamma \quad (4.34)$$

$$= \frac{1}{|\Omega_E|} \sum_{f=1}^{n_f} \int_{\Gamma_f} \mathbf{u}_h d\Gamma \otimes N^f \quad (4.35)$$

$$= \frac{1}{|\Omega_E|} \sum_{f=1}^{n_f} \sum_{e=1}^{n_e} \left(\frac{1}{2} \int_{\gamma_e} \left[\int \mathbf{u}_h dX^f \right] \cdot \mathbf{R}^f \cdot \mathbf{N}^e d\gamma \right) \otimes N^f \quad (4.36)$$

The divergence theorem is applied locally on each face, which explains the rotation of the edge normal to get the locally defined normal of the edge $\mathbf{R}^f \cdot \mathbf{N}^e = \mathbf{N}_{loc}^e$. Equation (4.36) can only be integrated if \mathbf{u}_h is known on the face. However, due to arbitrary shape of polygon, the ansatz function associated to it is not easily constructed. Thus equation (4.36) has to be reformulated, such that the integral is solvable. Considering that N^f is constant over the face, only the integral of \mathbf{u}_h is needed. However, the integral over a face of \mathbf{u}_π^f and \mathbf{u}_h has to be identical:

$$\int_{\Gamma_f} \mathbf{u}_h d\Gamma = \int_{\Gamma_f} \mathbf{u}_\pi^f d\Gamma, \quad (4.37)$$

and equation (4.36) can be rewritten as:

$$\nabla \mathbf{u}_\pi = \frac{1}{|\Omega_E|} \sum_{f=1}^{n_f} \left(\sum_{e=1}^{n_e} \frac{1}{2} \int_{\gamma_e} \left[\int \mathbf{u}_\pi^f dX^f \right] \cdot \mathbf{R}^f \cdot \mathbf{N}^e d\gamma \right) \otimes N^f, \quad (4.38)$$

where \mathbf{u}_π^f represents a new two dimensional virtual element Ansatz on each face in three dimensional space. It is defined as:

$$\begin{aligned} \mathbf{u}_\pi^f &= \left(\mathbf{N}_\pi^f \cdot \mathbf{a}_i^f \right) \mathbf{E}_i, \quad i \in \{1, 2, 3\}, \\ \mathbf{N}_\pi^f &= (1, X^f, Y^f), \\ \mathbf{a}_i^f &= \left(a_{i1}^f, a_{i2}^f, a_{i3}^f \right). \end{aligned} \quad (4.39)$$

This procedure requires to find new projection coefficients \mathbf{a}_i^f for every face. The integral of \mathbf{u}_π^f with respect to \mathbf{X}^f is known on the whole face, which requires simple integration of polynomials. The integrands have to be expressed in the local coordinate system of a face by using the rotation matrix \mathbf{R}^f i.e. $\in \mathbb{R}^3 \otimes \mathbb{R}^3$ with the origin at the coordinate mean \mathbf{X}_{mf} of each face:

$$\mathbf{X}_{mf} = \frac{1}{n_V^f} \sum_{I=1}^{n_V^f} \mathbf{X}_I^f, \quad (4.40)$$

where n_V^f is the number of nodes at face Γ_f . The coordinate system is transformed by:

$$\square(\mathbf{X}) \rightarrow \square(\mathbf{X}(\mathbf{X}^f)), \text{ where } \mathbf{X}^f = \mathbf{R}^f(\mathbf{X} - \mathbf{X}_{mf}) \quad \text{and} \quad \mathbf{R}^f = \begin{bmatrix} \mathbf{t}_1^f \\ \mathbf{t}_2^f \end{bmatrix}, \quad (4.41)$$

where \mathbf{t}_1^f and \mathbf{t}_2^f are the orthonormal base vectors of the face. They can be simply calculated as:

$$\mathbf{t}_1^f = \frac{\mathbf{X}_2^f - \mathbf{X}_1^f}{\|\mathbf{X}_2^f - \mathbf{X}_1^f\|}, \quad \mathbf{t}_2^f = \mathbf{N}^f \times \mathbf{e}_X^f, \quad (4.42)$$

$$\mathbf{N}^{f,0} = (\mathbf{X}_1^f - \mathbf{X}_{mf}) \times (\mathbf{X}_2^f - \mathbf{X}_{mf}), \quad \mathbf{N}^f = \frac{\mathbf{N}^{f,0}}{\|\mathbf{N}^{f,0}\|}, \quad (4.43)$$

where $\mathbf{N}^{f,0}$ and \mathbf{N}^f are the non-normalized and normalized normal vector of the face. The projection $\nabla \mathbf{u}_\pi^f$ of a face f of a single virtual element is defined from the averaged gradient on the face $\nabla \mathbf{u}_h^f$. Utilizing the divergence theorem leads to an integral on the edge γ_f of face f . Summing up over all edges n_e reads:

$$\begin{bmatrix} a_{12}^f & a_{13}^f \\ a_{22}^f & a_{23}^f \\ a_{32}^f & a_{33}^f \end{bmatrix} = \nabla \mathbf{u}_\pi^f = \frac{1}{\Omega_f} \int_{\Gamma_f} \nabla_f \mathbf{u}_h^f d\Gamma = \frac{1}{\Omega_f} \int_{\gamma_f} \mathbf{u}_h \otimes \mathbf{R}^f \mathbf{N}^e d\gamma \quad (4.44)$$

$$= \frac{1}{|\Omega_f|} \sum_{e=1}^{n_e} \int_{\gamma_e} \mathbf{u}_h^e \otimes \mathbf{R}^f \mathbf{N}^e d\gamma \quad (4.45)$$

$$= \frac{1}{|\Omega_f|} \sum_{e=1}^{n_e} \sum_{g=1}^{n_g^e} w_g^e J_g^e \mathbf{u}_{h,g}^e \otimes \mathbf{N}_{loc}^e, \quad (4.46)$$

where \mathbf{N}_{loc}^e is the normal of edge e in the local coordinate system of the corresponding face, $\nabla_f = \frac{\partial(\cdot)}{\partial \mathbf{X}^f}$ being the gradient operator with respect to the local face coordinates and \mathbf{u}_h^e is a one dimensional linear ansatz on the edge with:

$$\mathbf{N}_h^e = (\xi, 1 - \xi) \quad (4.47)$$

$$\mathbf{u}_h^e = \mathbf{N}_h^e \mathbf{u}^e \quad \text{where} \quad \mathbf{u}^e = \bigcup_I \mathbf{u}_I \quad \forall I \in \gamma, \quad (4.48)$$

$$\mathbf{X}_h^e = \mathbf{N}_h^e \mathbf{X}^e \quad \text{where} \quad \mathbf{X}^e = \bigcup_I \mathbf{X}_I \quad \forall I \in \gamma, \quad (4.49)$$

$$\mathbf{G}_\xi = \frac{\partial \mathbf{X}_h^e}{\partial \xi}, \quad J^e = \|\mathbf{G}_\xi\|, \quad \mathbf{N}^e = \frac{\mathbf{G}_\xi}{J^e}. \quad (4.50)$$

By applying the divergence theorem to a local gradient operator, the local edge normal will appear on the right hand side of equation (4.44), which explains the need of \mathbf{R}^f . It is a similar procedure as in equation (4.36). The virtual parameters related to the constant part can be computed with equation (4.31):

$$\left(a_{11}^f, a_{21}^f, a_{31}^f \right) = \frac{1}{n_V^f} \sum_{I=1}^{n_V^f} \left(\mathbf{u}_I^f - \nabla \mathbf{u}_\pi^f \mathbf{X}_I^f \right) = \frac{1}{n_V^f} \sum_{I=1}^{n_V^f} \mathbf{u}_I^f. \quad (4.51)$$

Note that the term $\frac{1}{n_V^f} \sum_{I=1}^{n_V^f} \mathbf{X}_I^f = \mathbf{0}$ vanishes, since the origin of local coordinates is at the face center \mathbf{X}_{m_f} . The projected quantity $\mathbf{u}_\pi^f(\mathbf{X}^f)$ at any element point is then given by the ansatz in equation (4.39). Since $\mathbf{u}_\pi^f(\mathbf{X}^f)$ is now known, equation (4.38) can be evaluated to find the original virtual parameters of the three dimensional element $\nabla \mathbf{u}_\pi$. The computation of the constant parts is not necessarily needed for the computation of the stiffness matrix. However, in some cases, such as dynamics, the constant parts are needed and can be simply evaluated by equation (4.32). The integration over the edges to obtain the virtual parameters is a procedure, which requires flat faces of the virtual element.

4.5 Construction of the potential function

4.5.1 Time discretization

For the computation of the accelerations, an implicit time stepping method is chosen. The implicit Newmark method as outlined in NEWMARK (1959) and WOOD (1990) is used. The equations for the velocity $\dot{\mathbf{u}} = \mathbf{v}$ and acceleration $\ddot{\mathbf{u}} = \mathbf{a}$ at time step t_{n+1} are given as

$$\dot{\mathbf{u}}(\mathbf{u}) = \dot{\mathbf{u}}_{n+1}(\mathbf{u}_{n+1}) = \frac{\gamma_N}{\zeta_N \Delta t} (\mathbf{u}_{n+1} - \mathbf{u}_n) - \left(\frac{\gamma_N}{\zeta_N} - 1 \right) \dot{\mathbf{u}}_n - \left(\frac{\gamma_N}{\zeta_N} - 1 \right) \Delta t \ddot{\mathbf{u}}_n \quad (4.52)$$

$$\ddot{\mathbf{u}}(\mathbf{u}) = \ddot{\mathbf{u}}_{n+1}(\mathbf{u}_{n+1}) = \frac{1}{\zeta_N \Delta t^2} (\mathbf{u}_{n+1} - \mathbf{u}_n) - \frac{1}{\zeta_N \Delta t} \dot{\mathbf{u}}_n - \left(\frac{1}{2\zeta_N} - 1 \right) \ddot{\mathbf{u}}_n, \quad (4.53)$$

where γ_N and ζ_N are the so called Newmark parameters. \square_n are the known quantities from the previous time step t_n . $\Delta t = t_{n+1} - t_n$ is the time step. The Newmark parameters are chosen as $\zeta_N = 1/4$ and $\gamma_N = 1/2$ which yields a solution without numerical damping, see e.g. WOOD (1990) and WOOD ET AL. (1981).

4.5.2 Displacement based formulation

As introduced in section 4.4, the formulation of a virtual element undergoing large deformations is based on a split of the energy into a constant part and an associated stabilization term. The nodal degrees of freedom of an element are in each element projected to a polynomial projection function. Further each displacement component is approximated with the same interpolation function, but having unique set of \mathbf{a}_i parameters each. Thus the consistency part does not lead to a stable formulation, when the virtual element has more than 3 nodes in 2D and 4 nodes in 3D and thus a stabilization term is required. Two different stabilization techniques can be found in the literature on virtual element technologies, which work well for classical solid mechanics problems. For the construction of the virtual element method the potential function in equation (2.67) is used. After summing up all element contributions for the n_E virtual elements, the following expression is obtained:

$$\Pi(\mathbf{u}) = \mathbf{A}_{E=1}^{n_E} [\Pi_p^E(\mathbf{u}_\pi) + \Pi_{stab}^E(\mathbf{u}_h - \mathbf{u}_\pi)] \quad (4.54)$$

Consistency part

For the consistency part, the projection \mathbf{u}_π as introduced in section 4.4 is used in the total potential (2.67), thus the first part of equation (4.54) is given by

$$\begin{aligned} \Pi_p(\mathbf{u}_\pi) &= \Pi_p^{stat}(\mathbf{u}_\pi) + \Pi_p^{ext}(\mathbf{u}_\pi) + \Pi_p^{dyn}(\mathbf{u}_\pi) \\ &= \int_{\Omega_E} [\Psi(\mathbf{u}_\pi) - \bar{\mathbf{b}} \cdot \mathbf{u}_\pi] d\Omega - \int_{\Gamma_E^N} \mathbf{T} \cdot \mathbf{u}_\pi d\Gamma + \int_{\Omega_E} \rho \ddot{\mathbf{u}}_\pi \cdot \mathbf{u}_\pi d\Omega, \end{aligned} \quad (4.55)$$

where $\Pi_p^{stat} = \Pi_p^{int}$ denoting the internal energy. Here, it is denoted by the superscript \square^{stat} to represent the difference to the dynamic part. The external part $\Pi_p^{ext}(\mathbf{u}_\pi)$ will be discussed later in section 4.6. To simplify the notation, the subscript E , is omitted in the following, since all formulations are formulated for one single virtual element. The gradient of the projection $\nabla \mathbf{u}_\pi$ is constant on the entire domain Ω_E thus all kinematic quantities, that stem from it, e.g. $\mathbf{F}_\pi = \mathbf{1} + \nabla \mathbf{u}_\pi$ are constant as well. Hence the integration of the strain energy function can be simplified as:

$$\int_{\Omega_E} \Psi(\mathbf{C}_\pi) d\Omega = \Psi(\mathbf{C}_\pi) |\Omega_E|, \quad (4.56)$$

which is still nonlinear with respect to the unknown nodal degrees of freedom.

The acceleration can be evaluated from equation (4.53) as $\ddot{\mathbf{u}}_\pi = \ddot{\mathbf{u}}(\mathbf{u}_\pi)$. Since the projected displacement \mathbf{u}_π is linear, the pseudo potential $\Pi^{dyn}(\mathbf{u}_\pi)$ in equation (4.55) is a quadratic function and can be computed in various ways as demonstrated next. The function to be integrated takes the form:

$$\int_{\Omega_E} \rho \ddot{\mathbf{u}}_\pi \cdot \mathbf{u}_\pi d\Omega = \mathbf{u}_e (\tilde{\boldsymbol{\pi}})^T \int_{\Omega_E} \rho \mathbf{H}^T \mathbf{H} d\Omega \tilde{\boldsymbol{\pi}} \ddot{\mathbf{u}}_e \quad (4.57)$$

1. The first possibility is to evaluate the integral at the centroid \mathbf{X}_c of the polygon in 2D and of the polyhedra in 3D. The displacements and the accelerations are then evaluated at the centroid and multiplied by the area (2D) or the volume (3D) of the element, which is an approximation (due to under-integration):

$$\int_{\Omega_E} \rho \ddot{\mathbf{u}}_\pi \cdot \mathbf{u}_\pi \, d\Omega = \rho \ddot{\mathbf{u}}_\pi(\mathbf{X}_c) \cdot \mathbf{u}_\pi(\mathbf{X}_c) |\Omega_E|. \quad (4.58)$$

2. Another possibility is to introduce a sub-triangulation of the polygon and again use Gauss integration which yields an evaluation at the integration points \mathbf{X}_g of each triangle \mathcal{T} in 2D:

$$\int_{\Omega_E} \rho \ddot{\mathbf{u}}_\pi \cdot \mathbf{u}_\pi \, d\Omega = \rho \sum_{\mathcal{T}=1}^{n_{\mathcal{T}}} \sum_{g=1}^{n_g^{\mathcal{T}}} w_g^{\mathcal{T}} J_g^{\mathcal{T}} \ddot{\mathbf{u}}_\pi(\mathbf{X}_g) \cdot \mathbf{u}_\pi(\mathbf{X}_g), \quad (4.59)$$

or to use a submesh of tetrahedrons \mathfrak{T} in 3D:

$$\int_{\Omega_E} \rho \ddot{\mathbf{u}}_\pi \cdot \mathbf{u}_\pi \, d\Omega = \rho \sum_{\mathfrak{T}=1}^{n_{\mathfrak{T}}} \sum_{g=1}^{n_g^{\mathfrak{T}}} w_g^{\mathfrak{T}} \det \mathbf{J}_g^{\mathfrak{T}} \ddot{\mathbf{u}}_\pi(\mathbf{X}_g) \cdot \mathbf{u}_\pi(\mathbf{X}_g), \quad (4.60)$$

where $\mathbf{J}^{\mathfrak{T}}$ is the standard Jacobian for a three dimensional finite element tetrahedron, see equation (4.72) and $J^{\mathcal{T}}$ being the Jacobian of a two dimensional finite element triangle, see equation (4.30). Since the integral contains quadratic terms of X , Y and in 3D additionally of Z , the integration above approximates the integral when using one Gauss point, i.e. $n_g^{\mathcal{T}} = n_g^{\mathfrak{T}} = 1$. However, by using a higher order Gauss integration, the integral can be computed exactly.

3. As a third option, the integral can be exactly computed using the nodal coordinates at the boundary via divergence theorem, see SINGER (1993); PETERSEN (2013):

$$\int_{\Omega_E} \rho \ddot{\mathbf{u}}_\pi \cdot \mathbf{u}_\pi \, d\Omega = \mathbf{u}_e(\tilde{\boldsymbol{\pi}})^T \left(\int_{\Omega_E} \rho \overbrace{\mathbf{H}^T \mathbf{H}}^{f(\mathbf{X})} \, d\Omega \right) \tilde{\boldsymbol{\pi}} \ddot{\mathbf{u}}_e \quad (4.61)$$

$$\int_{\Omega_E} f(\mathbf{X}) \, d\Omega = \frac{1}{n_{dim}} \int_{\Gamma_E} \overbrace{\left[\int f(\mathbf{X}) \, dX \int f(\mathbf{X}) \, dY \int f(\mathbf{X}) \, dZ \right]}^{f_{int}} \cdot \mathbf{N} \, d\Gamma$$

integration over $n_{\mathcal{T}}$ triangles \mathcal{T} in 3D:

$$\stackrel{3D}{=} \frac{1}{n_{dim}} \sum_{f=1}^{n_f} \sum_{\mathcal{T}=1}^{n_{\mathcal{T}}} \sum_{g=1}^{n_g^{\mathcal{T}}} w_g^{\mathcal{T}} J_g^{\mathcal{T}} \mathbf{f}_{int,g} \cdot \mathbf{N}^{\mathcal{T}} \quad (4.62)$$

integration over n_V edges e in 2D:

$$\stackrel{2D}{=} \frac{1}{n_{dim}} \sum_{k=1}^{n_V} \sum_{g=1}^{n_g^e} w_g^e J_g^e \mathbf{f}_{int,g} \cdot \mathbf{N}^e \quad (4.63)$$

Note that, the expression which has to be integrated f_{int} is for $k = 1$ cubic on the surface in 3D or edge in 2D which requires an appropriate order of Gauss integration. However, in the three dimensional case the integral can be computed on the edges, similarly as have been done for the virtual parameters in section 4.4.2. This would require appropriate order of a linear ansatz on the edge, since cubic functions appear.

4.5.3 Stabilization techniques

The consistency term is computable but leads to a rank deficient tangent, when the virtual element has more than 3 vertices in 2D and 4 vertices in 3D and thus needs to be stabilized. There are different ways to stabilize the method. Various stabilization techniques can be found in the literature on virtual element technologies, which work well for classical solid mechanics problems. The two most commonly used stabilization techniques will be briefly introduced in the following.

Stabilization based on the degrees of freedom

The first stabilization depends on the degrees of freedom. A point wise error measure between the nodal quantities \mathbf{u}_I and the approximation function \mathbf{u}_π evaluated at the vertices \mathbf{X}_I is introduced, see e.g. BEIRÃO DA VEIGA ET AL. (2013a, 2015) and CHI ET AL. (2017). The stabilization energy is taken as the difference of nodal and projected quantities at each node as

$$\Pi_{stab} = \frac{\gamma}{2} \sum_I^{n_V} \Delta \mathbf{u}_I \cdot \Delta \mathbf{u}_I \quad \text{with} \quad \Delta \mathbf{u}_I = \mathbf{u}_I - \mathbf{u}_\pi(\mathbf{X}_I) \quad (4.64)$$

The parameter γ can be computed using the constitutive or tangent element matrix, see CHI ET AL. (2017) and BEIRÃO DA VEIGA ET AL. (2015).

$$\gamma = \frac{\alpha}{n_{dof}} \sqrt{\sum_i^{n_{dof}} K_{\pi,ii}^2} \quad \text{or} \quad \gamma = \alpha \frac{tr \mathbf{K}_\pi}{4n_{dof}} = \frac{\alpha}{4n_{dof}} \sum_i^{n_{dof}} K_{\pi,ii} \quad (4.65)$$

Equation (4.65)₂ is adopted in this work. $n_{dof} = 3n_V$ is the number of degrees of freedom of the element. The parameter $\alpha \in \mathcal{R}$ with $\alpha > 0$ is not necessarily required but was introduced for a generalization and to adjust energies for higher order modes, see ARTIOLI ET AL. (2017a); GAIN ET AL. (2014). It is a user-defined parameter and can be chosen according to the problem. For linear elastic problems, α can be set to 1/2, see MENGOLINI ET AL. (2019); ARTIOLI ET AL. (2017a). In GAIN ET AL. (2014) it has been shown, that the optimal value of α is around 1 but can have a wide range for irregular shaped, distorted polyhedrons with small edges. Later in this work, the virtual element method will be used to model contact. However, due to a novel projection algorithm for the modeling of node-to-node contact at non-conforming contact interfaces, highly irregular shaped virtual elements with small edges and faces can appear. Thus in this work, $\alpha = 2$ will be used, which leads to satisfying results.

Energy stabilization

The idea of the energy stabilization is to introduce a new positive definite energy $\hat{\Pi}$, with the help of which the stabilization term is redefined, as introduced in WRIGGERS ET AL. (2017):

$$\Pi_{stab}(\mathbf{u}_h - \mathbf{u}_\pi) = \hat{\Pi}(\mathbf{u}_h) - \hat{\Pi}(\mathbf{u}_\pi) \quad (4.66)$$

Such a stabilization was also used in KRYSL (2015b) for stabilized mean strain formulations of finite elements. Thus the $\hat{\Pi}$ is chosen to be $\beta\Pi_p$ resulting finally in the total energy of the form:

$$\Pi_{stab}(\mathbf{u}_h - \mathbf{u}_\pi) = \beta (\Pi_p(\mathbf{u}_h) - \Pi_p(\mathbf{u}_\pi)) , \quad (4.67)$$

where the factor $\beta^{stat} \in (0, 1]$ defines the ratio between the projection part and finite element internal mesh approximation part. It can be obtained from an analytical solution for bending of one finite element, as discussed in KRYSL (2015b,a).

By combining equation (4.67) and (4.54) the final form of the total potential energy function follows:

$$\Pi(\mathbf{u}) = \mathbf{A}_{E=1}^{n_E} (1 - \beta^{stat})\Pi_p^E(\mathbf{u}_\pi) + \beta^{stat}\Pi_p^E(\mathbf{u}_h) . \quad (4.68)$$

The consistency part in equation (4.68) can be computed in a similar way as described in section 4.5.2. The stabilization part needs an approximation, see e.g. WRIGGERS ET AL. (2017). For the three dimensional case, the displacement field is approximated by introducing an internal submesh of 4 noded tetrahedrons with linear ansatz functions $\mathbf{N}_h^{\mathfrak{T}}$ as:

$$\mathbf{N}_h^{\mathfrak{T}} = (1 - \xi - \eta - \zeta, \xi, \eta, \zeta) \quad (4.69)$$

$$\mathbf{u}_h^{\mathfrak{T}} = \mathbf{N}_h^{\mathfrak{T}} \mathbf{u}^{\mathfrak{T}} \quad \text{where} \quad \mathbf{u}^{\mathfrak{T}} = \bigcup_I \mathbf{u}_I \quad \forall I \in \mathfrak{T}, \quad (4.70)$$

$$\mathbf{X}_h^{\mathfrak{T}} = \mathbf{N}_h^{\mathfrak{T}} \mathbf{X}^{\mathfrak{T}} \quad \text{where} \quad \mathbf{X}^{\mathfrak{T}} = \bigcup_I \mathbf{X}_I \quad \forall I \in \mathfrak{T}, \quad (4.71)$$

$$\mathbf{J}^{\mathfrak{T}}(\xi, \eta, \zeta) = \left[\frac{\partial \mathbf{X}_h^{\mathfrak{T}}}{\partial \xi}, \frac{\partial \mathbf{X}_h^{\mathfrak{T}}}{\partial \eta}, \frac{\partial \mathbf{X}_h^{\mathfrak{T}}}{\partial \zeta} \right], \quad \mathbf{J}^{\mathfrak{T}} = \det(\mathbf{J}^{\mathfrak{T}}), \quad (4.72)$$

where $\mathbf{u}_h^{\mathfrak{T}}$ denotes the ansatz for the displacements at each tetrahedron of the virtual element, see Fig. 4.7. The matrix $\mathbf{u}^{\mathfrak{T}}$ contains the four nodal displacement vectors \mathbf{u}_I of the tetrahedron \mathfrak{T} . ξ , η and ζ are the local dimensionless coordinates at the element level. The nodes of the generated submesh belong to the set of nodes defining the virtual element ($\mathbf{u}^{\mathfrak{T}} \subset \mathbf{u}_E$), hence no additional nodes have to be introduced. In 2D, 3 noded linear finite element triangles would be used. A Gauss point integration yields:

$$\Pi_p^E(\mathbf{u}_h) = \sum_{\mathfrak{T}=1}^{n_{\mathfrak{T}}} \sum_{g=1}^{n_g^{\mathfrak{T}}} w_g^{\mathfrak{T}} J_g^{\mathfrak{T}} \Psi(\mathbf{u}_{h,g}^{\mathfrak{T}}) . \quad (4.73)$$

The stabilization parameter $0 < \beta^{stat} \leq 1$ can be chosen freely. For $\beta^{stat} = 1$ the total energy is calculated using only the stabilization part and thus is purely based on the FEM mesh. For $\beta^{stat} = 0$ a rank deficient tangent is generated and thus it is not allowed. The choice for the stabilization parameter β was analyzed in HUDOBIVNIK ET AL. (2018); ALDAKHEEL ET AL. (2018) and it has been shown that the optimal value is in the range $\beta^{stat} \in [0.2, 0.6]$. Both stabilization techniques are utilized in this work.

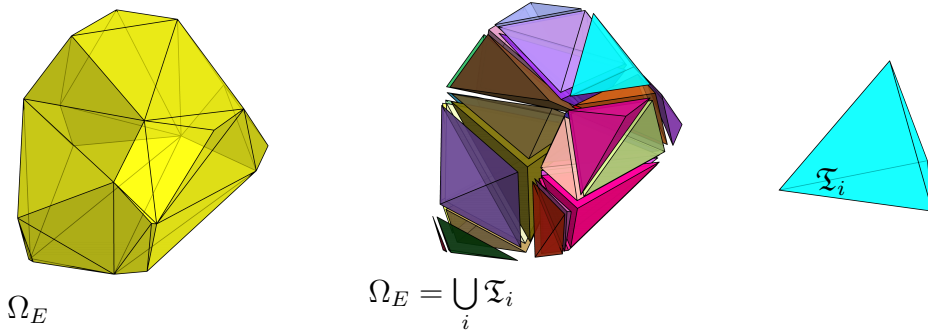


Figure 4.7 – Virtual element with polygonal faces, subdivided into tetrahedrons.

4.5.4 Mixed formulation

While the VEM ansatz for the displacements \mathbf{u}_π is linear, the pressure p_π and the dilatation Θ_π are considered to be constant over the entire element, see Fig. 4.8. To obtain a locking

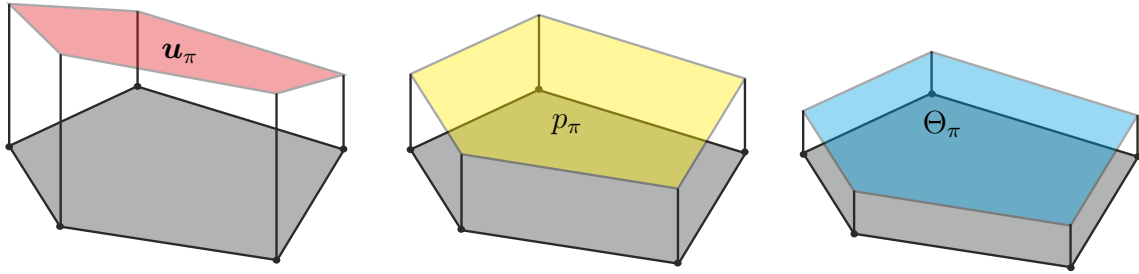


Figure 4.8 – VEM shape functions for displacements \mathbf{u}_π , pressure p_π and dilatation Θ_π .

free behavior in the framework of J_2 -plasticity, the Hu-Washizu functional in equation (2.70) is adopted for the virtual element formulation, see WASHIZU (1975). Several mixed formulations were already discussed for virtual elements in WRIGGERS ET AL. (2017), applied to finite strain hyperelastic solids. Here, based on the classical formulations in the context of finite element methods for finite strain plasticity, see SIMO ET AL. (1985b), the following Hu-Washizu functional is employed

$$\Pi_p^{stat,HW}(\mathbf{u}_\pi, \Theta_\pi, p_\pi) = \int_{\Omega} \Psi^{iso}(\mathbf{u}_\pi) + \Psi^{p\Theta}(\mathbf{u}_\pi, \Theta_\pi, p_\pi) + \Psi^{vol}(\Theta_\pi) \, d\Omega \quad (4.74)$$

with

$$\Psi^{iso}(\mathbf{u}_\pi) = \frac{\mu}{2} (J_e^{-\frac{2}{3}} \operatorname{tr} \mathbf{b}_{\pi,e} - 3), \quad (4.75)$$

$$\Psi^{p\Theta}(\mathbf{u}_\pi, \Theta_\pi, p_\pi) = p_\pi (J_e - \Theta_\pi), \quad (4.76)$$

$$\Psi^{vol}(\Theta_\pi) = \frac{\kappa}{4} (\Theta_\pi^2 - 1 - 2 \ln \Theta_\pi). \quad (4.77)$$

In this formulation, the energy is split into an isochoric and volumetric part. In addition to that, a constraint associated with the volumetric deformation is added to the potential. Within this framework, the pressure p and the volume dilatation Θ occur as additional independent variables.

For the Hu-Washizu formulation, the same potential as in equation (4.55) is used as well, but it is only necessary to use the mixed formulation only for the consistency part of the virtual element. Thus the consistency part is exchanged by the Hu-Washizu potential in equation (4.74). By inserting the projected quantities in to the consistency part, the total energy yields:

$$\Pi(\mathbf{u}_h, \mathbf{u}_\pi, p_\pi, \Theta_\pi) = (1 - \beta^{stat})\Pi_p^{stat,HW}(\mathbf{u}_\pi, \Theta_\pi, p_\pi) + \beta^{stat}\Pi_p^{stat}(\mathbf{u}_h) \quad (4.78)$$

Note that the derivative of equation (4.78) needs to be taken with respect to all variables. Looking at equation (4.78), it is clear that the Hu-Washizu virtual element is based only on the projection part of the mixed terms. The stabilization is constructed purely on the displacement potential. Test computations have demonstrated that a stabilization of the mixed part is not necessary and additionally such a reduced formulation leads to a more efficient element since the mixed variables need not to be treated within the internal triangular mesh. This leads to an element tangent $\mathbf{K}_{\pi,E}$ and element residual $\mathbf{R}_{\pi,E}$ with the structure:

$$\mathbf{K}_{\pi,E} = \begin{bmatrix} \mathbf{K}_{uu} & 0 & \mathbf{K}_{up} \\ 0 & \mathbf{K}_{\Theta\Theta} & \mathbf{K}_{\Theta p} \\ \mathbf{K}_{up}^T & \mathbf{K}_{\Theta p}^T & \mathbf{0} \end{bmatrix} \quad \text{and} \quad \mathbf{R}_{\pi,E} = \begin{bmatrix} \mathbf{R}_u \\ \mathbf{R}_\Theta \\ \mathbf{R}_p \end{bmatrix}. \quad (4.79)$$

Since p_π and Θ_π are constant over the entire virtual element, static condensation can be applied to eliminate these constant variables at element level, see GUYAN (1965). This yields the condensed element residual $\mathbf{R}_{\pi,E}^{cond}$ and condensed element tangent $\mathbf{K}_{\pi,E}^{cond}$:

$$\mathbf{K}_{\pi,E}^{cond} = \mathbf{K}_{uu} - \begin{bmatrix} \mathbf{K}_{u\theta} \\ \mathbf{K}_{up} \end{bmatrix}^T \mathbf{h}_a \quad (4.80)$$

$$\mathbf{R}_{\pi,E}^{cond} = \mathbf{R}_u + \begin{bmatrix} \mathbf{K}_{u\theta} \\ \mathbf{K}_{up} \end{bmatrix}^T \mathbf{h}_b, \quad (4.81)$$

where \mathbf{h}_a is a matrix and \mathbf{h}_b a vector defined as:

$$\mathbf{h}_a = \begin{bmatrix} \mathbf{K}_{\Theta\Theta} & \mathbf{K}_{\Theta p} \\ \mathbf{K}_{\Theta p}^T & \mathbf{0} \end{bmatrix}^{-1} \begin{bmatrix} \mathbf{K}_{u\theta} \\ \mathbf{K}_{up} \end{bmatrix} \quad \mathbf{h}_b = - \begin{bmatrix} \mathbf{K}_{\Theta\Theta} & \mathbf{K}_{\Theta p} \\ \mathbf{K}_{\Theta p}^T & \mathbf{0} \end{bmatrix}^{-1} \begin{bmatrix} \mathbf{R}_\Theta \\ \mathbf{R}_p \end{bmatrix}. \quad (4.82)$$

4.6 Load approximation

The approximation of $\Pi^{ext}(\mathbf{u})$ depends on the construction of the tangent. Depending on which integration scheme was used for the computation of the virtual parameters and which stabilization technique was used, the approximation of the external force potential needs to be chosen properly. In the next study, "s1" denotes the energy stabilization and "s2" the

stabilization based on the degrees of freedom. "TI" represents the computation of the virtual parameters based on the integration over triangles, as introduced in section 4.4.1 and "EI" stands for the integration over the edges, as shown in section 4.4.2 respectively. β^l is a scalar factor, which weights the load between the one which is computed on linear finite element triangles with:

$$\Pi_p^{ext}(\mathbf{u}_h) = \int_{\Gamma^N} \mathbf{T} \cdot \mathbf{u}_h \, d\Gamma = \sum_{\mathcal{T}=1}^{n_{\mathcal{T}}} \sum_{g=1}^{n_g^{\mathcal{T}}} w_g^{\mathcal{T}} J_g^{\mathcal{T}} \mathbf{u}_{hg}^{\mathcal{T}} \cdot \mathbf{T}, \quad (4.83)$$

and the one computed via the projection:

$$\Pi_p^{ext}(\mathbf{u}_{\pi}) = \int_{\Gamma^N} \mathbf{T} \cdot \mathbf{u}_{\pi}^f \, d\Gamma = \sum_{f=1}^{n_f} \sum_{e=1}^{n_e} \sum_{g=1}^{n_g^e} w_g^e J_g^e \left[\int \mathbf{u}_{\pi}^f \, dX^f \right] \cdot \mathbf{N}_{loc}^e \cdot \mathbf{T}, \quad (4.84)$$

leading to the total force potential:

$$\Pi^{ext}(\mathbf{u}) = (1 - \beta^l) \Pi_p^{ext}(\mathbf{u}_{\pi}) + \beta^l \Pi_p^{ext}(\mathbf{u}_h). \quad (4.85)$$

Not that the integral in equation 4.84 is solved on the edge, similarly as already been done for the virtual parameters. However, it can be solved alternatively on a submesh, consisting of linear finite element triangles (same way as in equation (4.83)), which would lead to the same result. For testing purpose, a patch test with all different kind of combinations is analyzed in Fig. 4.9 for H1 element topology and in Fig. 4.10 for voronoi shaped elements. As a consequence of the study, the following combinations can be used and any other combination will lead to wrong results and thus will not pass the patch test:

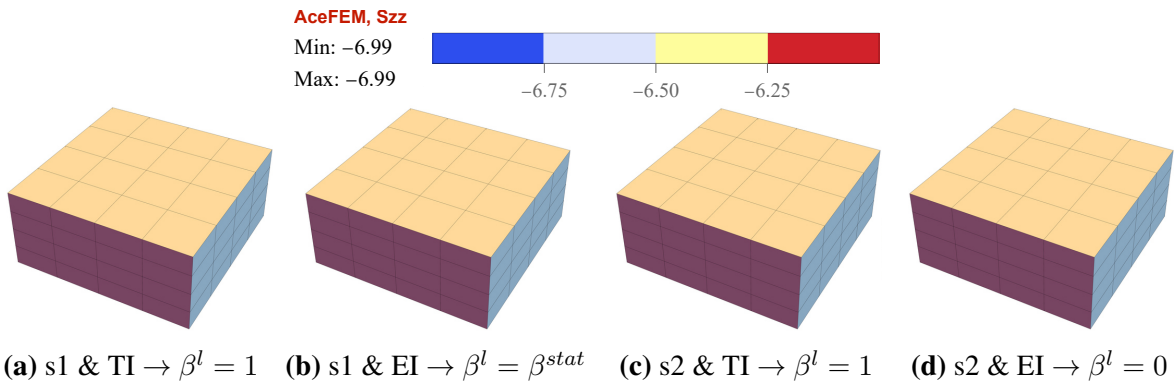


Figure 4.9 – Contourplots showing stresses S_{zz} for patch test with H1 shaped virtual elements and different stabilizations, integration schemes for the virtual parameters and load parameters.

1. When using the energy stabilization "s1" in combination with the construction of the virtual parameters via the triangles "TI", the load term needs to be fully computed on the triangle part with $\beta^l = 1$.

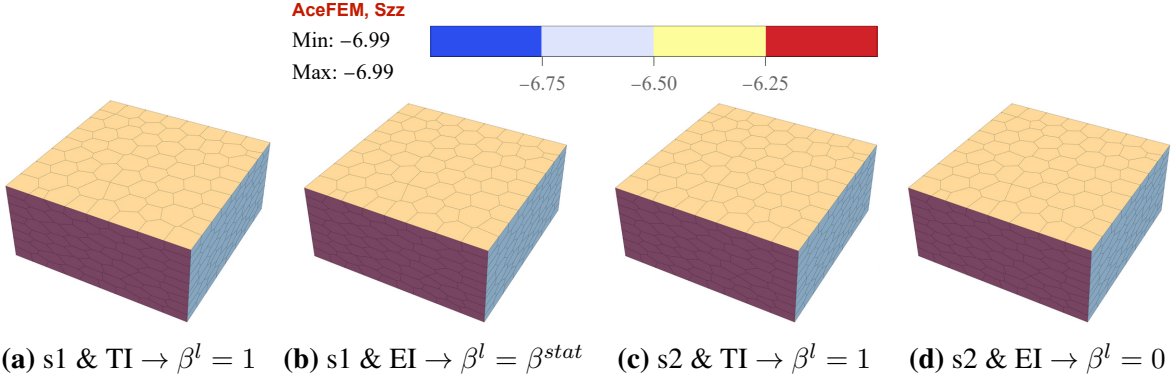


Figure 4.10 – Contourplots showing stresses S_{zz} for patch test with VO shaped virtual elements and different stabilizations, integration schemes for the virtual parameters and load parameters.

2. When using the energy stabilization "s1" in combination with the construction of the virtual parameters via the edges "EI", the load term needs to be computed as a combination of both, projected and triangle part with $\beta^l = \beta^{stat}$.
3. When using the stabilization based on the degrees of freedom "s2" in combination with the construction of the virtual parameters via the triangles "TI", the load term needs to be fully computed on the triangle part with $\beta^l = 1$.
4. When using the stabilization based on the degrees of freedom "s2" in combination with the construction of the virtual parameters via the edges "EI", the load term needs to be computed fully on the projection part with $\beta^l = 0$.

Note that the above introduced equations can be used analogously for the computation of the body forces $\bar{\mathbf{b}}$ in the weak form of equilibrium.

4.7 Solution scheme and linearization of static and dynamic formulation

To obtain the element residual vector \mathbf{R}_E and effective element tangent matrix \mathbf{K}_E in equation (4.2), the first and second derivative of the total energy $\Pi(\mathbf{u}_h)$ have to be computed with respect to the element unknowns \mathbf{u}_E . In the first step the residual is obtained by:

$$\begin{aligned}
 \mathbf{R}_E &= (1 - \beta^{stat}) \left. \frac{\partial \Pi_p^{stat}(\mathbf{u}_\pi)}{\partial \mathbf{u}_E} \right|_{\ddot{\mathbf{u}}_E = const.} + (1 - \beta^{dyn}) \left. \frac{\partial \Pi_p^{dyn}(\mathbf{u}_\pi)}{\partial \mathbf{u}_E} \right|_{\ddot{\mathbf{u}}_E = const.} \\
 &+ \beta^{stat} \left. \frac{\partial \Pi_p^{stat}(\mathbf{u}_h)}{\partial \mathbf{u}_E} \right|_{\ddot{\mathbf{u}}_E = const.} + \beta^{dyn} \left. \frac{\partial \Pi_p^{dyn}(\mathbf{u}_h)}{\partial \mathbf{u}_E} \right|_{\ddot{\mathbf{u}}_E = const.} \\
 &= (1 - \beta^{stat}) \mathbf{R}_{\pi,E}^{stat} + (1 - \beta^{dyn}) \mathbf{R}_{\pi,E}^{dyn} + \beta^{stat} \mathbf{R}_{h,E}^{stat} + \beta^{dyn} \mathbf{R}_{h,E}^{dyn}
 \end{aligned} \tag{4.86}$$

Note that \mathbf{u}_E has to be kept constant when evaluating the dynamic pseudo potential. This procedure is in the same manner as shown in equation 4.11 by using the weak form in a pseudo potential formulation with proper differentiation exception.

With equation (4.33), the projected displacement, velocity and acceleration are:

$$\mathbf{u}_\pi = \mathbf{H}\tilde{\boldsymbol{\pi}}\mathbf{u}_E, \quad \dot{\mathbf{u}}_\pi = \mathbf{H}\tilde{\boldsymbol{\pi}}\dot{\mathbf{u}}_E \quad \text{and} \quad \ddot{\mathbf{u}}_\pi = \mathbf{H}\tilde{\boldsymbol{\pi}}\ddot{\mathbf{u}}_E \quad (4.87)$$

and equivalently for the ansatz \mathbf{u}_h^ξ for the sub mesh (triangles in 2D or tetrahedrons in 3D) with equation (4.70):

$$\mathbf{u}_h^\xi = \mathbf{N}_h^\xi \mathbf{u}^\xi, \quad \dot{\mathbf{u}}_h^\xi = \mathbf{N}_h^\xi \dot{\mathbf{u}}^\xi \quad \text{and} \quad \ddot{\mathbf{u}}_h^\xi = \mathbf{N}_h^\xi \ddot{\mathbf{u}}^\xi. \quad (4.88)$$

Inserting equation (4.87) into Π^{dyn} in (4.55) and using the procedure in equation (4.86) yields the explicit form of the dynamic part of the residual for the Newmark time integration with equation (4.52) and (4.53) for the projected part:

$$\mathbf{R}_{\pi,E}^{dyn} = (\tilde{\boldsymbol{\pi}})^T \int_{\Omega} \rho \mathbf{H}^T \mathbf{H} \, d\Omega \, \tilde{\boldsymbol{\pi}} \left[\frac{1}{\zeta \Delta t^2} \mathbf{u}_{E,n+1} - \ddot{\mathbf{u}}_{E,n} \right], \quad (4.89)$$

with $\ddot{\mathbf{u}}_{E,n} = \frac{1}{\zeta \Delta t^2} \mathbf{u}_{E,n} + \frac{1}{\zeta \Delta t} \dot{\mathbf{u}}_{E,n} + \left(\frac{1}{2\zeta} - 1 \right) \ddot{\mathbf{u}}_{E,n}$. In the same way the residual is obtained for the discretization in equation (4.88):

$$\mathbf{R}_{h,E}^{dyn} = \mathbf{A}_{\xi=1}^{n_\xi} \int_{\Omega_\xi} \rho (\mathbf{N}_h^\xi)^T \mathbf{N}_h^\xi \, d\Omega_\xi \left[\frac{1}{\zeta \Delta t^2} \mathbf{u}_{n+1}^\xi - \ddot{\mathbf{u}}_n^\xi \right], \quad (4.90)$$

with $\ddot{\mathbf{u}}_n^\xi = \frac{1}{\zeta \Delta t^2} \mathbf{u}_n^\xi + \frac{1}{\zeta \Delta t} \dot{\mathbf{u}}_n^\xi + \left(\frac{1}{2\zeta} - 1 \right) \ddot{\mathbf{u}}_n^\xi$.

The projection and stabilization part of the total element tangent for the dynamic part takes the form, note that differentiation is only performed with respect to nodal displacements at time t_{n+1} :

$$\mathbf{K}_{\pi,E}^{dyn} = \frac{\partial \mathbf{R}_{\pi,E}^{dyn}}{\partial \mathbf{u}_E} = \mathbf{M}_{\pi,E} \frac{1}{\zeta \Delta t^2} \quad (4.91)$$

$$\text{with} \quad \mathbf{M}_{\pi,E} = (\tilde{\boldsymbol{\pi}})^T \int_{\Omega} \rho \mathbf{H}^T \mathbf{H} \, d\Omega \, \tilde{\boldsymbol{\pi}}$$

$$\mathbf{K}_{h,E}^{dyn} = \frac{\partial \mathbf{R}_{h,E}^{dyn}}{\partial \mathbf{u}_E} = \mathbf{M}_{h,E} \frac{1}{\zeta \Delta t^2} \quad (4.92)$$

$$\text{with} \quad \mathbf{M}_{h,E} = \mathbf{A}_{\xi=1}^{n_\xi} \mathbf{M}_{h,E}^\xi = \mathbf{A}_{\xi=1}^{n_\xi} \int_{\Omega_\xi} \rho \mathbf{N}_h^{\xi T} \mathbf{N}_h^\xi \, d\Omega_\xi$$

The total element tangent includes static and dynamic parts of the projection and stabilization:

$$\mathbf{K}_E = (1 - \beta^{stat}) \mathbf{K}_{\pi,E}^{stat} + (1 - \beta^{dyn}) \mathbf{K}_{\pi,E}^{dyn} + \beta^{stat} \mathbf{K}_{h,E}^{stat} + \beta^{dyn} \mathbf{K}_{h,E}^{dyn}. \quad (4.93)$$

All differentiations leading to the residual and tangent of the elasto-dynamic virtual element were obtained with the software tool *AceGen*, see KORELC & WRIGGERS (2016). It provides the most efficient element routines when a potential formulation is used. Let us note that the exact weak form follows from Π^{stat} and from the pseudo potential Π^{dyn} for fixed accelerations and thus the derivation above is equivalent to using the weak form directly. With equations (4.52), (4.53), (4.86) and (4.93) at hand the global tangent matrix \mathbf{K} and residual vector \mathbf{R} can be assembled in equation (4.2).

It is sufficient to use the consistency term alone (i.e. $\beta^{dyn} = 1$) for the construction of the dynamic part, without any stabilization, if the problem is not reaction dominated, as shown in BEIRÃO DA VEIGA ET AL. (2014) and AHMAD ET AL. (2013).

The presented tangent matrix \mathbf{K}_E in equation (4.93) includes the mass matrix implicitly through the Newmark algorithm: $\mathbf{K}_E = \mathbf{K}_E^{stat} + \frac{1}{\zeta \Delta t^2} \mathbf{M}_E$. Thus the rank deficiency of mass is not a major factor in the simulation as will be shown in examples. Its calculation is not needed for transient boundary and initial value problems, it is however needed for the eigenvalue analysis, which is also shown in the examples. Different ways of how to integrate the mass matrix $\mathbf{M}_{\pi,E}$ were shown in section 4.5.2.

4.8 Solution scheme and linearization of plasticity

The discretized form with an exponential map approach of the evolution equation for \mathbf{C}_p^{-1} in equation (2.62) follows from KORELC & STUPKIEWICZ (2014) and SIMO (1998) and yields together with equation (2.63) the local residual:

$$\mathbf{Q}_E = \mathbf{F} \mathbf{C}_p^{-1} - \exp[-2(\alpha - \alpha_n) \mathbf{n}] \mathbf{F} \mathbf{C}_{p,n}^{-1} = 0 \quad \text{and} \quad \Phi = 0. \quad (4.94)$$

Here, \mathbf{C}_p^{-1} and α_n are the converged history variables from the previous step and therefore given. Equation (4.94) contains one equation for each of the six unique components of $\mathbf{C}_{p,n}^{-1}$ and one additional equation for the hardening variable α . For $\Phi < 0$, a pure elastic step follows and therefore the history variables, \mathbf{h}_E , will remain the same as from the previous time step, i.e. $\mathbf{C}_p^{-1} = \mathbf{C}_{p,n}^{-1}$ and $\alpha = \alpha_n$. If $\Phi > 0$, the set of equations (4.94) needs to be solved locally at the centroid of virtual element Ω_E which yields to an updated history field array $\mathbf{h}_E = \{\mathbf{C}^{p-1}, \alpha\}$. The resulting equations, which need to be solved at the centroid of each virtual element Ω_E , are the residual $\mathbf{Q}_E = \{\mathbf{Q}_E, \Phi\}$ which stem from the plastic routine and the residual \mathbf{R}_E resulting from the first variation of the pseudo potential in equation (4.54):

$$\mathbf{Q}_E(\mathbf{F}, \mathbf{h}_E, \mathbf{h}_{E,n}) = 0 \quad (4.95)$$

$$\mathbf{A}_{E=1}^{n_E} \mathbf{R}_E(\mathbf{u}_E, \mathbf{h}_E, \mathbf{h}_{E,n}) = 0 \longrightarrow \mathbf{R}(\mathbf{u}, \mathbf{h}, \mathbf{h}_n) = 0 \quad (4.96)$$

The above equations are solved in a nested algorithm, where first equation (4.95) needs to be solved locally at the element level in a inner Newton-Raphson loop for a fixed \mathbf{u}_E to update the plastic history variables \mathbf{h}_E for the current time step $t = t_{n+1}$. The summary of the finite

<p>Given: \mathbf{F}, \mathbf{C}_{pn}^{-1}, α_n Find: \mathbf{C}_p^{-1}, α ;</p> <hr/> <p>$\mathbf{b}_e = \mathbf{F} \mathbf{C}_{pn}^{-1} \mathbf{F}^T$; $J_e = \sqrt{\det \mathbf{b}_e}$; $\Psi_e = \frac{\kappa}{4}(J_e^2 - 1 - 2 \ln J_e) + \frac{\mu}{2}(J_e^{-\frac{2}{3}} \text{tr} \mathbf{b}_e - 3)$; $\boldsymbol{\tau}_e = 2 \mathbf{b}_e \frac{\partial \Psi_e}{\partial \mathbf{b}_e}$; $\mathbf{s}_e = \boldsymbol{\tau}_e - \frac{1}{3} \text{tr} \boldsymbol{\tau}_e \mathbf{1}$; $\Phi = \sqrt{\frac{3}{2}} \ \mathbf{s}_e\ - [Y_0 + (Y_\infty - Y_0)(1 - e^{-\delta \alpha}) + H \alpha]$; $\mathbf{n} = \frac{\partial \Phi}{\partial \mathbf{s}_e}$; $\mathbf{Q}_E = \mathbf{F} \mathbf{C}_p^{-1} - \exp[-2(\alpha - \alpha_n) \mathbf{n}] \mathbf{F} \mathbf{C}_{pn}^{-1}$;</p> <hr/> <p>$\mathbf{Q}_E = \{\mathbf{Q}_E, \Phi\} = \{Q_{11}, Q_{22}, Q_{33}, Q_{12}, Q_{13}, Q_{23}, \Phi\}^T$; $\mathbf{h}_E = \{\mathbf{C}^{p-1}, \alpha\} = \{C_{11}^{p-1} - 1, C_{22}^{p-1} - 1, C_{33}^{p-1} - 1, C_{12}^{p-1}, C_{13}^{p-1}, C_{23}^{p-1}, \alpha\}^T$;</p>
--

Algorithm 1: Summary of the finite strain elasto-plastic material model

strain plasticity model, that leads to \mathbf{Q}_E is given in box (1). Thus the local tangent matrix for the inner loop yields:

$$\mathbf{A}_E = \frac{\partial \mathbf{Q}_E(\mathbf{F}, \mathbf{h}_E, \mathbf{h}_{E,n})}{\partial \mathbf{h}_E} \quad (4.97)$$

Next, the outer Newton-Raphson loop is solved globally by using standard Newton-Raphson iteration procedure: $\mathbf{K} \Delta \mathbf{u} = \mathbf{R}$. The residual \mathbf{R}_E and tangent matrix \mathbf{K}_E at each virtual element Ω_E are obtained by utilizing *AceGen*'s automatic differentiation techniques, which will yield to the residual and tangent of the virtual element:

$$\mathbf{R}_{\pi,E} = \left. \frac{\partial \Pi_p(\mathbf{u}_\pi, \mathbf{h}_E, \mathbf{h}_{E,n})}{\partial \mathbf{u}_E} \right|_{\frac{D\mathbf{h}_E}{D\mathbf{F}}=0; \dot{\mathbf{u}}_E=const.} \quad (4.98)$$

$$\mathbf{K}_{\pi,E} = \left. \frac{\partial \mathbf{R}_{\pi,E}(\mathbf{u}_\pi, \mathbf{h}_E, \mathbf{h}_{E,n})}{\partial \mathbf{u}_E} \right|_{\frac{D\mathbf{h}_E}{D\mathbf{F}} = -\mathbf{A}_E^{-1} \frac{\partial \mathbf{Q}_E}{\partial \mathbf{F}}} \quad (4.99)$$

Note that residual $\mathbf{R}_{\pi,E}$ is obtained by holding history variables \mathbf{h}_E constant during differentiation procedure. Additionally, when deriving the tangent $\mathbf{K}_{\pi,E}$ with respect to the primary variables \mathbf{u}_E , providing the dependency $\frac{D\mathbf{h}_E}{D\mathbf{F}}$ is necessary to ensure a consistent linearization. For further details see KORELC & STUPKIEWICZ (2014). For plasticity, we choose the approach from ALDAKHEEL ET AL. (2019) and HUDOBIVNIK ET AL. (2018), where the stabilization parameter β^{stat} was chosen as a function of the accumulated plastic strains. Thus, with increasing amount of plastic deformation, the stabilization parameter decreases. β^{stat} is redefined as:

$$\beta^{stat} = \min \left[0.4, \max \left[\frac{\sigma_{vM}}{E\alpha}, \eta \right] \right], \quad (4.100)$$

where $\eta = 10^{-3}$ denotes the minimum amount of stabilization, see Fig. 4.11 and $\sigma_{vM} = \sqrt{\frac{3}{2}} \|\mathbf{s}_e\|$ the von Mises stress. Without η , the stabilization parameter would decrease during the simulation and tend to be zero, which would result in a rank deficient tangent.

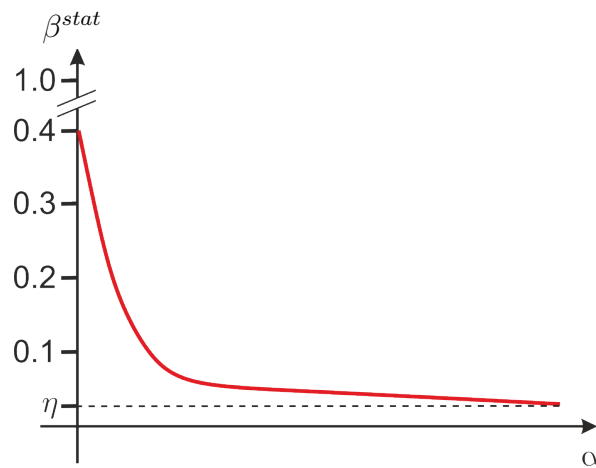


Figure 4.11 – Stabilization parameter β^{stat} as a function of the plastic deformation α .

4.9 Validation

In this chapter, basic tests, such as the classical patch test and comparison of local tangents of single elements are investigated. Note that for the following tests the energy stabilization is used. However, the stabilization based on the degrees of freedom in section 4.5.3 will reproduce equivalent results.

4.9.1 Patch test

The first test is the well known patch test, see ZIENKIEWICZ & TAYLOR (1997). The aim is to obtain a constant stress state and linear displacement field by applying a constant pressure or constant displacement field on the face of the body. For the test, an unit cube with $h = \ell = b = 1$ and the material properties $E = 1$ and $\nu = 0.3$ is chosen. The cube is fixed at $X = 0$ in X -direction, $Y = 0$ in Y -direction and $Z = 0$ in Z -direction. A constant displacement boundary condition with $\bar{u}_z = 0.2$ is applied at the top face at $Z = 1$, see Fig. 4.12a. The discretization is realized with three dimensional virtual elements, including non-convex shapes, see Fig. 4.12b. Figure Fig. 4.12 shows the contour plots for the displacements in the X -, Y - and Z -direction. It can be seen, that the displacements are linear in all direction and thus reproduce a correct displacement field. The stresses are shown in figure Fig. 4.13. Similar results are obtained. The stresses in the X - and Y -direction are zero, while the stresses in the Z -direction, where the displacement boundary condition is applied, are constant over the entire body. This shows, that the virtual element formulation works well and can be used for further investigations.

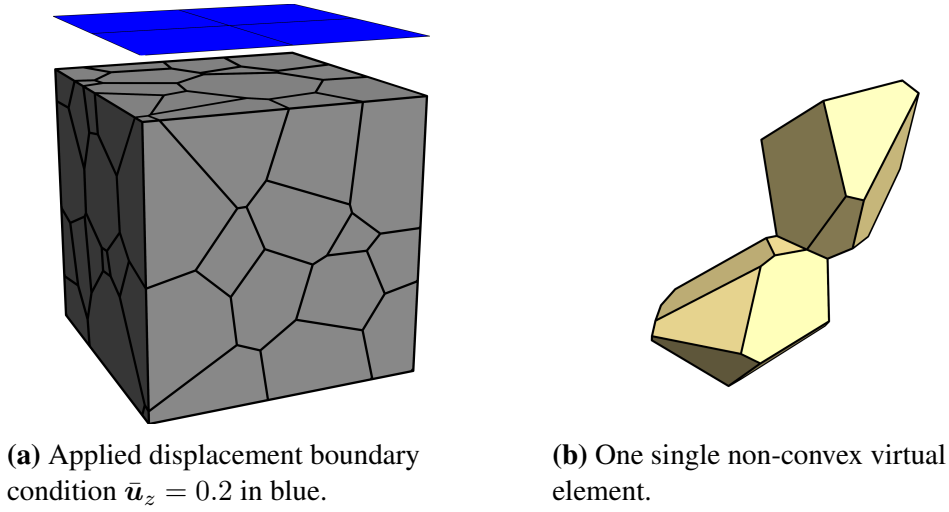


Figure 4.12 – Patch test with applied displacement boundary condition at the upper face.

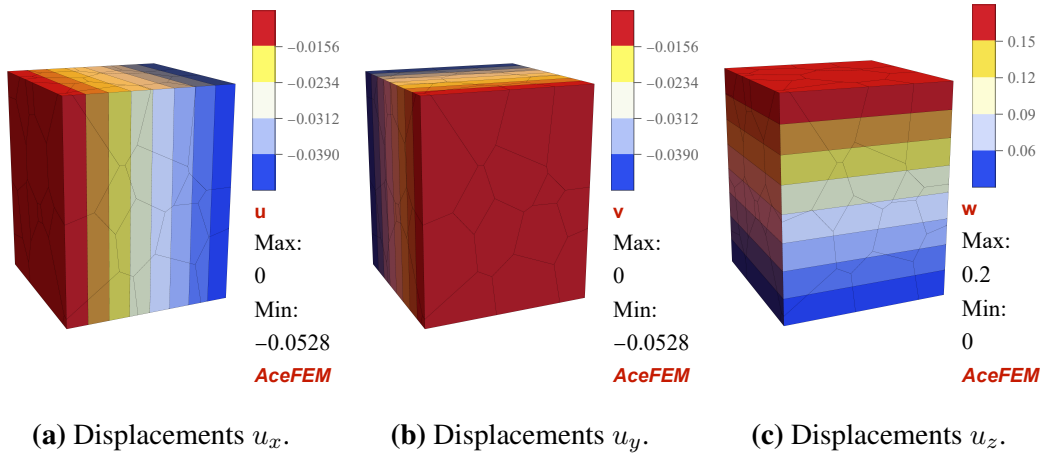


Figure 4.13 – Deformation plot showing the displacements in X -, Y - and Z -direction.

4.9.2 Projection test

Due to the properties of the virtual element space, the projection part must be able to recover a linear displacement field. For testing purpose, a cube with four elements is substituted to a linear displacement field at the upper face with:

$$\bar{\mathbf{u}} = \begin{bmatrix} 0.2 X \\ 0.15 Y \\ 0 \end{bmatrix}, \quad (4.101)$$

where the other Dirichlet boundary conditions are the same as in the previous example in section 4.9.1. The body is fixed at $X = 0$ in X -direction, $Y = 0$ in Y -direction and $Z = 0$ in Z -direction. The displacement field which is applied at the top is shown in Fig. 4.15a in blue. The deformation is depicted in Fig. 4.15b. Fig. 4.15c shows the projection \mathbf{u}_π at the corresponding face, where the Dirichlet boundary condition is applied. It can be seen, that

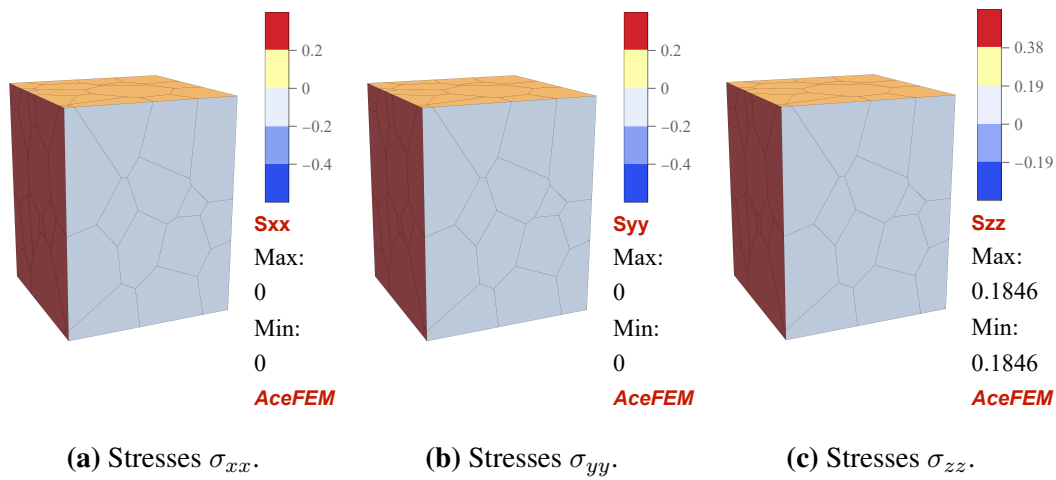


Figure 4.14 – Deformation plot showing the stresses in X -, Y - and Z -direction.

the projection is exactly capturing the linear displacement field in equation (4.101).

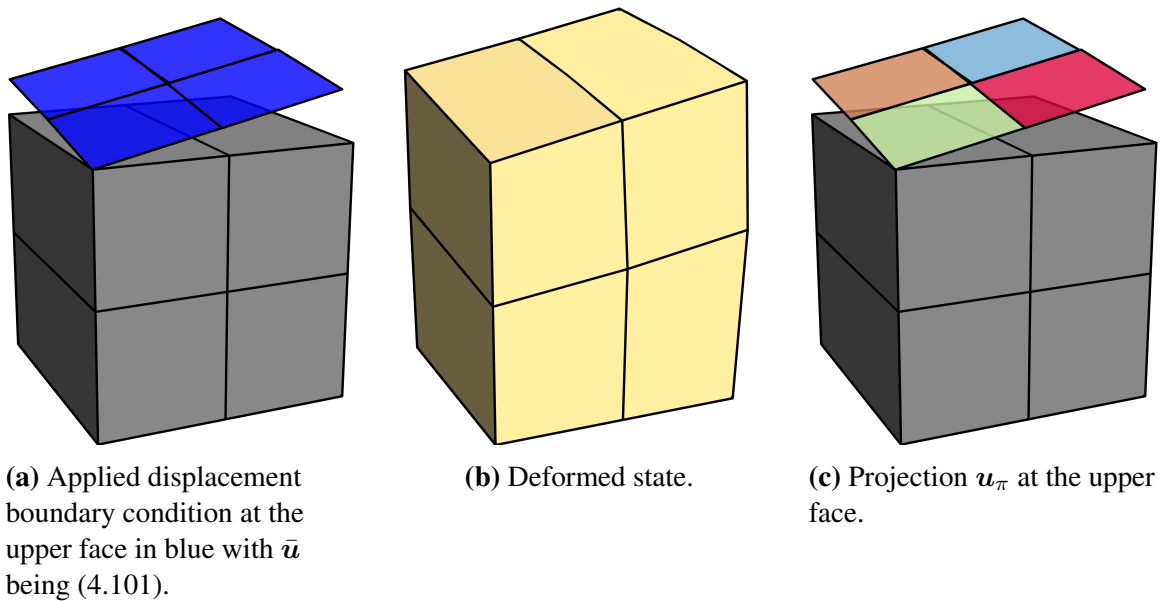


Figure 4.15 – Projection test of a simple block.

4.9.3 Eigenvalue and tangent comparison of finite and virtual element method

Simple triangular element

In this small example, the linear triangular finite element is compared to a linear virtual element with triangular shape. Clearly, both elements have the same shape and node ordering, see Fig. 4.16. The nodes are located at $\{0, 0\}$, $\{1, 0\}$ and $\{0, 1\}$ and material parameters are

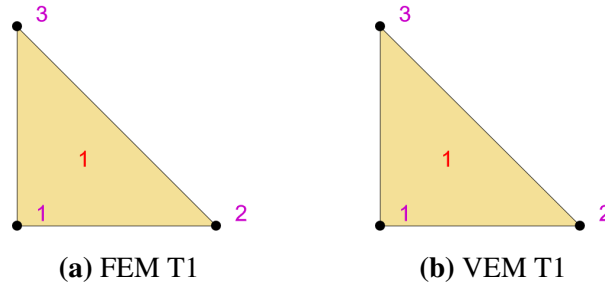


Figure 4.16 – Single triangular finite and virtual element.

set to $E = 1 \frac{\text{kN}}{\text{mm}^2}$ and $\nu = 0.25$. From the shape of the virtual element ansatz in equation (4.19), it is clear that for triangular shaped virtual elements with three nodes in 2D, the shape functions are identically equal to a linear triangular finite element and thus the local element tangents and the corresponding eigenvalues are identical too, see equation (4.102) and equation (4.103). Thus the coded virtual element is verified. Note here, that the same has to hold for three dimensional tetrahedral elements. Furthermore, since VEM has no isoparametric mapping, the shape functions of the finite element have to be mapped to the physical space to be comparable with the shape functions of the virtual element.

$$\mathbf{K}_{FEM}^{T1} = \begin{bmatrix} 0.8 & 0.4 & -0.6 & -0.2 & -0.2 & -0.2 \\ 0.4 & 0.8 & -0.2 & -0.2 & -0.2 & -0.6 \\ -0.6 & -0.2 & 0.6 & 0 & 0 & 0.2 \\ -0.2 & -0.2 & 0 & 0.2 & 0.2 & 0 \\ -0.2 & -0.2 & 0 & 0.2 & 0.2 & 0 \\ -0.2 & -0.6 & 0.2 & 0 & 0 & 0.6 \end{bmatrix}, \quad \lambda_{FEM}^{T1} = \begin{bmatrix} 1.8928 \\ 0.8 \\ 0.5072 \\ 0 \\ 0 \\ 0 \end{bmatrix}. \quad (4.102)$$

$$\mathbf{K}_{VEM}^{T1} = \begin{bmatrix} 0.8 & 0.4 & -0.6 & -0.2 & -0.2 & -0.2 \\ 0.4 & 0.8 & -0.2 & -0.2 & -0.2 & -0.6 \\ -0.6 & -0.2 & 0.6 & 0 & 0 & 0.2 \\ -0.2 & -0.2 & 0 & 0.2 & 0.2 & 0 \\ -0.2 & -0.2 & 0 & 0.2 & 0.2 & 0 \\ -0.2 & -0.6 & 0.2 & 0 & 0 & 0.6 \end{bmatrix}, \quad \lambda_{VEM}^{T1} = \begin{bmatrix} 1.8928 \\ 0.8 \\ 0.5072 \\ 0 \\ 0 \\ 0 \end{bmatrix}. \quad (4.103)$$

Simple quadrilateral element

The next example is the test of one single quadrilateral finite element with an quadrilateral shaped virtual element. Fig. 4.17a and Fig. 4.17b are depicting the quadrilateral finite and virtual element, which are again identical in shape and node numbering. Fig. 4.17c shows the internal submesh, consisting of two linear finite element triangles. Equation (4.107) is the local element tangent of the finite element Q1 and can be seen as a reference tangent. Equation (4.106) depicts the tangent, which results from the internal sub mesh and thus it is a simple assembled tangent of two linear triangular finite elements. The local element tangent, stemming from the projection is given in equation (4.105), which is obviously rank deficient. However, the different colors are depicting the deviation from the reference finite element Q1. Equation (4.108) has a full rank after the stabilization with equation (4.106)

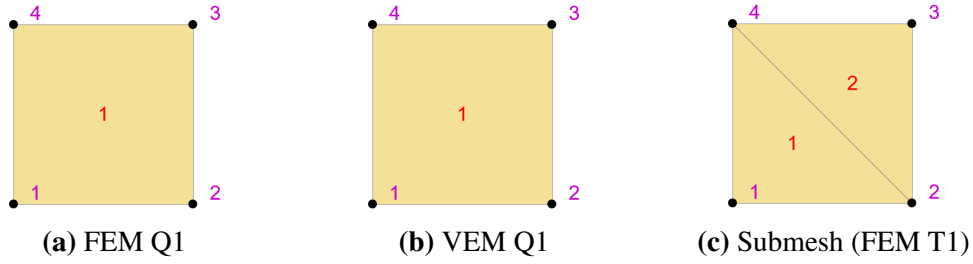


Figure 4.17 – Single quadrilateral finite and virtual element in (a) and (b) and the internal submesh of the virtual element with linear finite element triangles in (c).

which can be simply obtained by employing equation (4.93) with $\beta^{stat} = 0.4$ and neglecting the dynamic parts as:

$$\mathbf{K}_E = 0.6 \mathbf{K}_{\pi,E}^{stat} + 0.4 \mathbf{K}_{h,E}^{stat}, \quad (4.104)$$

where $\mathbf{K}_{h,E}^{stat}$ denotes the assembled tangent of the sub mesh in Fig. 4.17c.

$$\mathbf{K}_{\pi,E}^{stat} = \begin{bmatrix} 0.4 & 0.2 & -0.2 & 0 & -0.4 & -0.2 & 0.2 & 0 \\ 0.2 & 0.4 & 0 & 0.2 & -0.2 & -0.4 & 0 & -0.2 \\ -0.2 & 0 & 0.4 & -0.2 & 0.2 & 0 & -0.4 & 0.2 \\ 0 & 0.2 & -0.2 & 0.4 & 0 & -0.2 & 0.2 & -0.4 \\ -0.4 & -0.2 & 0.2 & 0 & 0.4 & 0.2 & -0.2 & 0 \\ -0.2 & -0.4 & 0 & -0.2 & 0.2 & 0.4 & 0 & 0.2 \\ 0.2 & 0 & -0.4 & 0.2 & -0.2 & 0 & 0.4 & -0.2 \\ 0 & -0.2 & 0.2 & -0.4 & 0 & 0.2 & -0.2 & 0.4 \end{bmatrix}. \quad (4.105)$$

$$\mathbf{K}_{h,E}^{stat} = \begin{bmatrix} 0.8 & 0.4 & -0.6 & -0.2 & 0 & 0 & -0.2 & -0.2 \\ 0.4 & 0.8 & -0.2 & -0.2 & 0 & 0 & -0.2 & -0.6 \\ -0.6 & -0.2 & 0.8 & 0 & -0.2 & -0.2 & 0 & 0.4 \\ -0.2 & -0.2 & 0 & 0.8 & -0.2 & -0.6 & 0.4 & 0 \\ 0 & 0 & -0.2 & -0.2 & 0.8 & 0.4 & -0.6 & -0.2 \\ 0 & 0 & -0.2 & -0.6 & 0.4 & 0.8 & -0.2 & -0.2 \\ -0.2 & -0.2 & 0 & 0.4 & -0.6 & -0.2 & 0.8 & 0 \\ -0.2 & -0.6 & 0.4 & 0 & -0.2 & -0.2 & 0 & 0.8 \end{bmatrix}. \quad (4.106)$$

$$\mathbf{K}_{FEM}^{Q1} = \begin{bmatrix} 0.53 & 0.2 & -0.33 & 0 & -0.27 & -0.2 & 0.07 & 0 \\ 0.2 & 0.53 & 0 & 0.07 & -0.2 & -0.27 & 0 & -0.33 \\ -0.33 & 0 & 0.53 & -0.2 & 0.07 & 0 & -0.27 & 0.2 \\ 0 & 0.07 & -0.2 & 0.53 & 0 & -0.33 & 0.2 & -0.27 \\ -0.27 & -0.2 & 0.07 & 0 & 0.53 & 0.2 & -0.33 & 0 \\ -0.2 & -0.27 & 0 & -0.33 & 0.2 & 0.53 & 0 & 0.07 \\ 0.07 & 0 & -0.27 & 0.2 & -0.33 & 0 & 0.53 & -0.2 \\ 0 & -0.33 & 0.2 & -0.27 & 0 & 0.07 & -0.2 & 0.53 \end{bmatrix}. \quad (4.107)$$

$$\mathbf{K}_E = \begin{bmatrix} 0.56 & 0.28 & -0.36 & -0.08 & -0.24 & -0.12 & 0.04 & -0.08 \\ 0.28 & 0.56 & -0.08 & 0.04 & -0.12 & -0.24 & -0.08 & -0.36 \\ -0.36 & -0.08 & 0.56 & -0.12 & 0.04 & -0.08 & -0.24 & 0.28 \\ -0.08 & 0.04 & -0.12 & 0.56 & -0.08 & -0.36 & 0.28 & -0.24 \\ -0.24 & -0.12 & 0.04 & -0.08 & 0.56 & 0.28 & -0.36 & -0.08 \\ -0.12 & -0.24 & -0.08 & -0.36 & 0.28 & 0.56 & -0.08 & 0.04 \\ 0.04 & -0.08 & -0.24 & 0.28 & -0.36 & -0.08 & 0.56 & -0.12 \\ -0.08 & -0.36 & 0.28 & -0.24 & -0.08 & 0.04 & -0.12 & 0.56 \end{bmatrix}. \quad (4.108)$$

Note that the stabilization parameter β^{stat} has a strong influence on the entries of the tangent matrix. By increasing or decreasing the parameter, lower modes are increased or decreased such that the ordering of eigenmodes can change. By choosing $\beta^{stat} = 0.4$, especially bending modes are captured well, see WRIGGERS ET AL. (2017). It is clear, that the standard Q1 finite element does not represent the benchmark but the comparison is just to show the difference between those elements.

Chapter 5

Contact modeling via the virtual element method

The discretization of the contact interface can be performed in different ways, for an overview, see WRIGGERS (2006). The virtual element method has the advantage of being able to add nodes to an element during the computation. In this chapter, three different contact discretizations will be introduced, namely node-to-surface, node-to-node and surface-to-surface. Note that in this chapter, indices which were used as superscripts in the previous chapters are used here as subscripts, since superscripts are needed to distinguish between the different contact bodies, i.e. $\square^\alpha \forall \alpha \in \{1, 2\}$.

5.1 Node-to-surface approach

The interface of the bodies in contact is parametrized using the node-to-surface approach. When virtual elements are employed for the spatial discretization of the bodies, the surfaces can be subdivided into non overlapping triangles, in the same way as for the computation of the virtual parameters, see section 4.4.1. The triangles discretize the contact interface, as shown in Fig. 5.1. For the discretization, we choose linear triangular finite elements with shape functions:

$$N_1^\alpha = 1 - \xi^\alpha - \eta^\alpha \quad N_2^\alpha = \xi^\alpha \quad N_3^\alpha = \eta^\alpha, \quad (5.1)$$

where ξ^α and η^α denote the local coordinates in the parametric space.

This approach is illustrated in Fig. 5.2, where contact node i of body \mathcal{B}^2 is in contact with the triangle related to body \mathcal{B}^1 . Here the nodes $k-1$, k and $k+1$ define the triangle. The location of the contact points ξ^α and η^α and the gap g_N follow from the solution of the local contact problem also known as closest point projection, see equation (3.3). Thus an additional set of equations has to be solved

$$[\mathbf{x}^2 - \bar{\mathbf{x}}^1(\bar{\xi}^1, \bar{\eta}^1)] \cdot \bar{\mathbf{a}}_k = \left[\mathbf{x}^2 - \sum_{I=1}^3 N_I^1(\bar{\xi}^1, \bar{\eta}^1) \mathbf{x}_I^1 \right] \cdot \bar{\mathbf{a}}_k = 0, \quad (5.2)$$

where $\bar{\mathbf{a}}_k$ denotes the tangent vectors, defined as

$$\bar{\mathbf{a}}_1 = \mathbf{x}_2^1 - \mathbf{x}_1^1 \quad \text{and} \quad \bar{\mathbf{a}}_2 = \mathbf{x}_3^1 - \mathbf{x}_1^1. \quad (5.3)$$

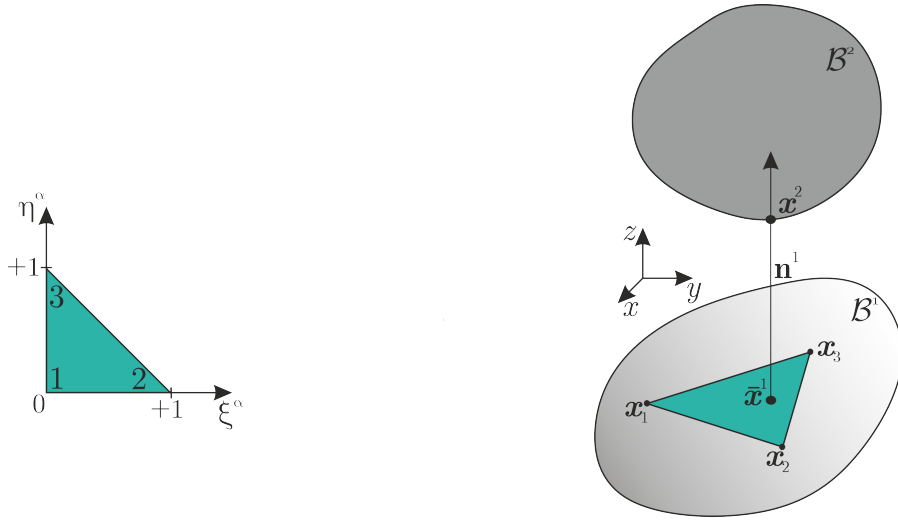


Figure 5.1 – Triangle in parametric space (left) and 3D Euclidian space (right).

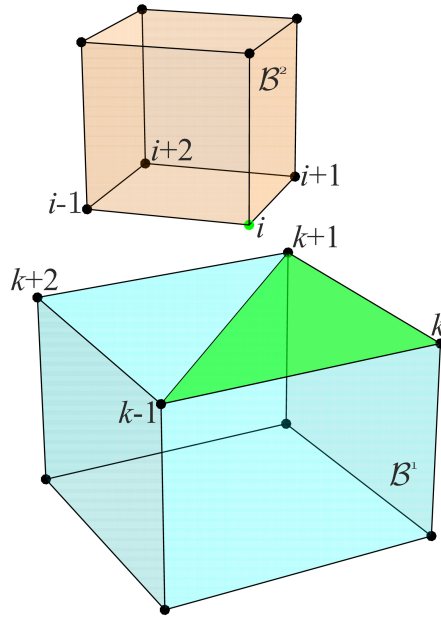


Figure 5.2 – Node-to-surface discretization.

Equation (5.2) yields the equation system

$$\begin{Bmatrix} \bar{\xi}^1 \\ \bar{\eta}^1 \end{Bmatrix} = \begin{bmatrix} \bar{\mathbf{a}}_1 \cdot \bar{\mathbf{a}}_1 & \bar{\mathbf{a}}_1 \cdot \bar{\mathbf{a}}_2 \\ \bar{\mathbf{a}}_2 \cdot \bar{\mathbf{a}}_1 & \bar{\mathbf{a}}_2 \cdot \bar{\mathbf{a}}_2 \end{bmatrix}^{-1} \begin{Bmatrix} (\mathbf{x}^2 - \mathbf{x}_1^1) \cdot \bar{\mathbf{a}}_1 \\ (\mathbf{x}^2 - \mathbf{x}_1^1) \cdot \bar{\mathbf{a}}_2 \end{Bmatrix} \quad (5.4)$$

and can be solved directly for $\bar{\xi}^1$ and $\bar{\eta}^1$. For surface discretization with higher order triangles or Bezier surfaces an additional set of nonlinear equations has to be solved:

$$\mathbf{Q}_i = \bar{\mathbf{x}}_i^1(\bar{\xi}_i^1, \bar{\eta}_i^1) + g_{N,i} \bar{\mathbf{n}}_i^1 - \mathbf{x}_i^2 = \mathbf{0}. \quad (5.5)$$

Equation (5.5) represents a steady-state locally coupled problem and is solved similarly as in section 4.8 for the treatment of plasticity in an inner Newton-Raphson loop for a fixed \mathbf{u} ,

leading to the linearization of the inner problem residual:

$$\mathbf{A}_i^j = \frac{\partial \mathbf{Q}_i^j}{\partial \mathbf{h}_i^j}, \quad \mathbf{A}_i^j \Delta \mathbf{h}_i^j + \mathbf{Q}_i^j = 0, \quad \mathbf{h}_i^{j+1} := \mathbf{h}_i^j + \Delta \mathbf{h}_i^j, \quad (5.6)$$

where \mathbf{A}_i^j denotes the local tangent of contact element i and step j and $\mathbf{h}_i^j = (\bar{\xi}^1, \bar{\eta}^1, g_N)_i^j$ the unknown vector. Once the local coordinates are known, the gap g_N can be computed with equation (3.4) and the contact contribution to the weak form in equation (3.7) can be formulated for the augmented Lagrangian approach as:

$$\Pi_{AL}^c = \begin{cases} \int_{\Gamma_c} (\lambda_n + \frac{\epsilon_p}{2} g_N) g_N \, d\Gamma_c = \sum_{i=1}^{n_c} (\lambda_{ni} + \frac{\epsilon_p}{2} g_{Ni}) g_{Ni} A_i & , \forall \lambda_{ni} \leq 0 \text{ (contact)} \\ - \int_{\Gamma_c} \frac{1}{2\epsilon_p} \lambda_n^2 \, d\Gamma_c = \sum_{i=1}^{n_c} \frac{1}{2\epsilon_p} \lambda_{ni}^2 A_i & , \forall \lambda_{ni} > 0 \text{ (no contact)} \end{cases} \quad (5.7)$$

where A_i is the area of the corresponding contact surface, related to the contact node i and n_c is the total number of contact pairs.

The global residual and tangent follow from the first and second derivative of the potential in equation (5.7) with respect to the unknowns $\mathbf{p}_i = \{\mathbf{u}_i, \lambda_{ni}\}$:

$$\mathbf{R}_i^c = \left. \frac{\partial \Pi^c(\mathbf{u}_i, \mathbf{h}_i)}{\partial \mathbf{p}_i} \right|_{\frac{D\mathbf{h}_i}{D\mathbf{p}_i} = -\mathbf{A}_i^{-1} \frac{\partial \mathbf{Q}_i}{\partial \mathbf{p}_i}} \quad (5.8)$$

$$\mathbf{K}_i^c = \frac{\partial \mathbf{R}_i^c(\mathbf{u}_i, \mathbf{h}_i)}{\partial \mathbf{p}_i}, \quad (5.9)$$

where $\frac{D\mathbf{h}_i}{D\mathbf{p}_i} = -\mathbf{A}_i^{-1} \frac{\partial \mathbf{Q}_i}{\partial \mathbf{p}_i}$ is an AD (automatic differentiation) exception, which has to be considered when using automatic differentiation tool AceGen. This exception appears, due to the implicit dependence of \mathbf{h} on the degrees of freedom \mathbf{u} through the local problem solution. To avoid the differentiation of the whole inner Newton-Raphson loop, this exception has to be taken in to account, when differentiating the total potential to obtain the total tangent with the dependency:

$$\frac{D\mathbf{h}}{D\mathbf{p}} = - \left[\frac{\partial \mathbf{Q}}{\partial \mathbf{h}} \right]^{-1} \frac{\partial \mathbf{Q}}{\partial \mathbf{p}}. \quad (5.10)$$

Note that the AD exception for the computation of the residual in equation (5.8) only needs to be taken in to account, when equation (5.5) is used for the computation of unknowns. If the parametrization is linear, as it is in this node-to-surface formulation (linear triangles), equation (5.4) can be used instead and no AD exception needs to be taken in to account, see KORELC ET AL. (2006) and LENGIEWICZ ET AL. (2011).

5.2 Node-to-node approach

To be able to use a node-to-node contact formulation, the interfaces between the contact bodies need to be conformal in terms of the nodes, which is in general not the case. A way out is to perform a node insertion procedure. Here the framework of virtual elements offers a great advantage, since virtual elements can handle arbitrary number of nodes and arbitrary element shapes. The idea of node insertion was first presented in WRIGGERS ET AL. (2016)

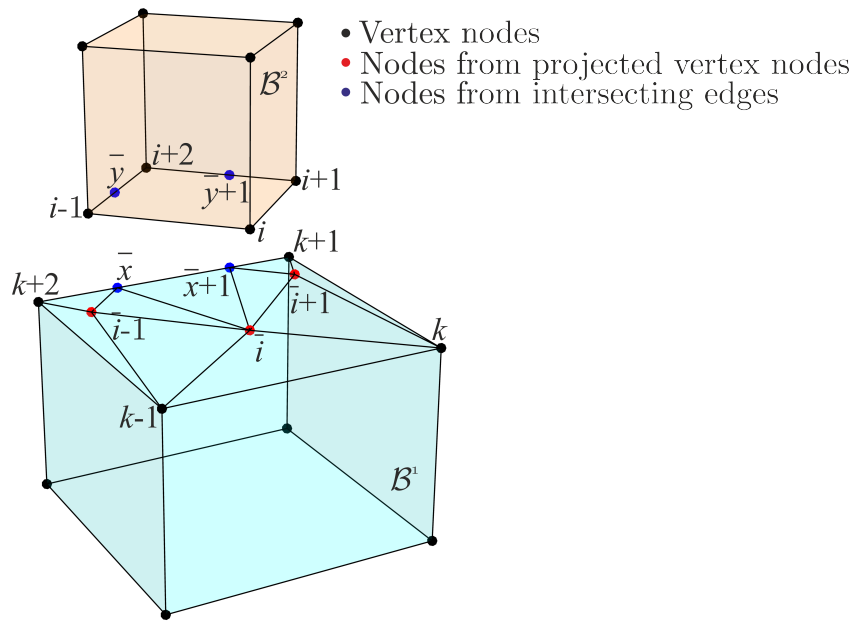


Figure 5.3 – Node-to-node discretization using node insertion.

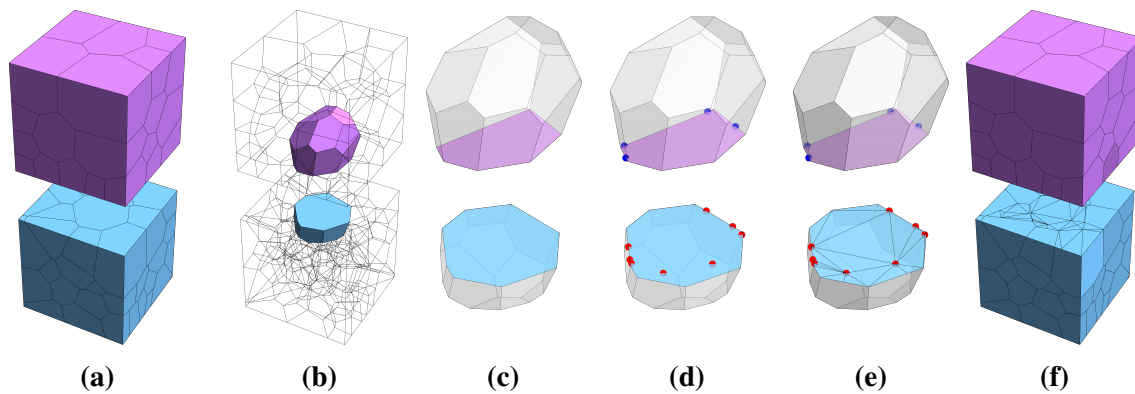


Figure 5.4 – Node insertion from B^1 to B^2 and vice versa with a) initial mesh, b) two particular elements from B^1 and B^2 , c) faces of this two elements, which get projected to each other, d) nodes which will be inserted due to intersecting edges and vertices, e) nodes which are inserted and new faces of elements and f) new final mesh with conforming nodes.

for geometrically linear problems and was extended to nonlinear problems in WRIGGERS & RUST (2019). It is now adopted to three dimensional problems in this work.

The node insertion procedure starts with a projection of each element face from B^1 to B^2 and vice versa, which results in two different types of projected nodes. The first type are nodes stemming from existing vertex nodes of the opposite body, denoted by red nodes in Fig. 5.3. The second type of nodes appear due to edge-to-edge intersections of two element faces, denoted by blue nodes in Fig. 5.3. Nodes which are inserted in to edges are inserted quite easily. These nodes only have to be added in to the corresponding faces, which are associated with the edge. A special treatment have to be considered for nodes, which are

added in to existing faces of elements. For this, the element face with an inserted node can be subdivided in to triangular faces, see Fig. 5.4. This approach is the easiest way to introduce these new nodes. However, this treatment is not the only way to insert nodes in to faces. One could also think about creating new faces via convex hulls of new nodes, leading to new polygonal faces. The node insertion procedure works in the same manner as for the node-to-surface approach, but additionally the nodes are physically inserted into the virtual element. Thus, element connectivity and number of degrees of freedom of the total system change within each simulation step.

Once the nodes are inserted, the integral is evaluated using equation (5.7) for each nodal contact pair. Note that the area A_i in equation (5.7) can be neglected or is hidden in the penalty parameter, see WRIGGERS (2006). However, the physical meaning of the Lagrange multiplier will either be a force or pressure when neglecting or including the area. Note that the area A_i is weighting each contact pair with respect to the corresponding area. If the area is neglected, the stiffness of all contact pairs are constant, which however, did not change the overall results in our test cases.

5.2.1 Algorithmic treatment of node-to-node contact

For the treatment of contact problems, generally a global search needs to be performed to find contacting pairs. The global search algorithm is based on a purely geometrical approach and makes use of basic geometrical functions and sorting algorithms, for details see e.g. LAURSEN (2003) and WRIGGERS (2006). Here we restrict ourselves to local contact which acts close to element level. The following steps describe the methodology to detect contact pairs for node-to-node contact at each simulation step. We define \mathcal{B}^α as master body and its surface Γ^α as master surface which defines the contact normals.

Algorithm:

1. Find all surface faces \mathcal{F}_i^α , of the surface of each body \mathcal{B}^α , i.e. $\bigcup \mathcal{F}_i^\alpha = \Gamma^\alpha$.
2. For each face \mathcal{F}_i^α find the closest subset of faces $\tilde{\mathcal{F}}_\alpha^\beta$ ($\alpha \neq \beta$) from the other body in the deformed configuration which have an orientation towards \mathcal{F}_i^α and which are located within a given gap tolerance.
3. Project face \mathcal{F}_i^α to $\tilde{\mathcal{F}}_\alpha^\beta$ for each body pair, e.g. $\{\alpha, \beta\} = \{1, 2\}$ and $\{\alpha, \beta\} = \{2, 1\}$ via the normal \mathbf{n}^α to find a projection point $\varphi(\bar{\mathcal{P}}_\alpha^\beta)$. This point is either (a) an intersection of each edge of the subset $\tilde{\mathcal{F}}_\alpha^\beta$ or (b) a node within the interior of face $\tilde{\mathcal{F}}_\alpha^\beta$, under the assumption of flat faces.
4. Since $\varphi(\bar{\mathcal{P}}_\alpha^\beta)$ is a point in the current configuration, with its location described by the convective coordinates (ξ, η) , it has to be transformed back to the initial point $\bar{\mathcal{P}}_\alpha^\beta$:
 - (a) Edge γ_i^α to edge γ_j^β intersection initial position, $\bar{\mathcal{P}}_\alpha^\beta$ is defined by the local coordinate of the edge $\bar{\mathcal{P}}_\alpha^\beta = \mathbf{X}_1^{\gamma_i^\alpha} (1 - \xi) + \mathbf{X}_2^{\gamma_j^\beta} \xi$. The same point exists also on Γ^α as γ_j^α , thus $\bar{\mathcal{P}}_\alpha^\beta = \mathbf{X}_1^{\gamma_j^\alpha} (1 - \xi) + \mathbf{X}_2^{\gamma_i^\alpha} \xi$. The local coordinate ξ is found by an intersection of two lines in 2D.

(b) Node $\bar{\mathcal{P}}_\alpha^\beta$ to face projection: $\bar{\mathcal{P}}_\alpha^\beta$ is found by evaluating $\bar{\mathcal{P}}_\alpha^\beta = \mathbf{X}_1^{\mathcal{T}_j^\beta} \xi + \mathbf{X}_2^{\mathcal{T}_j^\beta} \eta + (1 - \xi - \eta) \mathbf{X}_3^{\mathcal{T}_j^\beta}$ using the coordinates ξ and η from the current configuration. Insertion of the point \mathcal{P}^α on Γ^α is not required since this pairing node is already known.

5. A check is made for each projection point if a node already exists at the same coordinate (intersection on edge end, or projecting on triangle corner). If not $\bar{\mathcal{P}}_\alpha^\beta$ has to be inserted to all elements that contain the cut edge or triangle. In case of node to face projection, a face has to be re triangulated with new nodes included.
6. All the node-to-node pairs are gathered containing indices of projection $\bar{\mathcal{P}}_\alpha^\beta$ and its origin \mathcal{P}^α . The number of contact elements is modified to match the number of pairs, furthermore the related node indices are updated. Thus the size of global tangent changes in every load/time step. In case of node to face projection, a face has to be re triangulated with new nodes included.
7. *Remark: Nodes, which are not active in the current step are removed from the current mesh and thus are deactivated; hence they have no contribution to the local/global tangent.*

Once the nodes of the contacting bodies are matching at the interface, the gap can be evaluated by applying equation (3.4) for each nodal pair at the contact interface. In the work on two-dimensional contact, see WRIGGERS ET AL. (2016), a special stabilization was introduced that penalized contact nodes being close to each other. This was especially necessary when treating contact problems with friction since nodes being close to each other can result in oscillations of the normal stresses. A similar procedure could also be employed for the three-dimensional case. Due to the fact that large oscillation were not observed in the examples the special stabilization was not introduced, but will be considered in an upcoming paper.

5.2.2 Algorithmic treatment of the global search for node-to-surface contact

Similarly as node-to-node, contact pairs of node and the triangle it projects to have to be constructed. The procedure is similar, except that the actual intersection positions aren't required, but only the triangle and node pairs have to be constructed. To find these pairs, a standard global search algorithm is adopted. For further details, see WRIGGERS (2006).

5.2.3 Implementation aspects

The history (in our case the displacements) needs to be interpolated to assign interpolated displacements to the new nodes, since the projection is done in the current configuration and node insertion in the initial configuration. This interpolation can be performed with linear one dimensional shape functions on edges and linear two dimensional shape functions on

triangles, see Fig. 5.5. The local coordinates which are found from the projection are used to compute the interpolated displacements \mathbf{u}^* with the help of the shape functions and are used to map the new points back to the initial configuration. In the next step, the nodes are inserted, as introduced before. As a last step, the displacements are again used to compute the current configuration. Inserting a node in to an edge needs a manipulation of the following

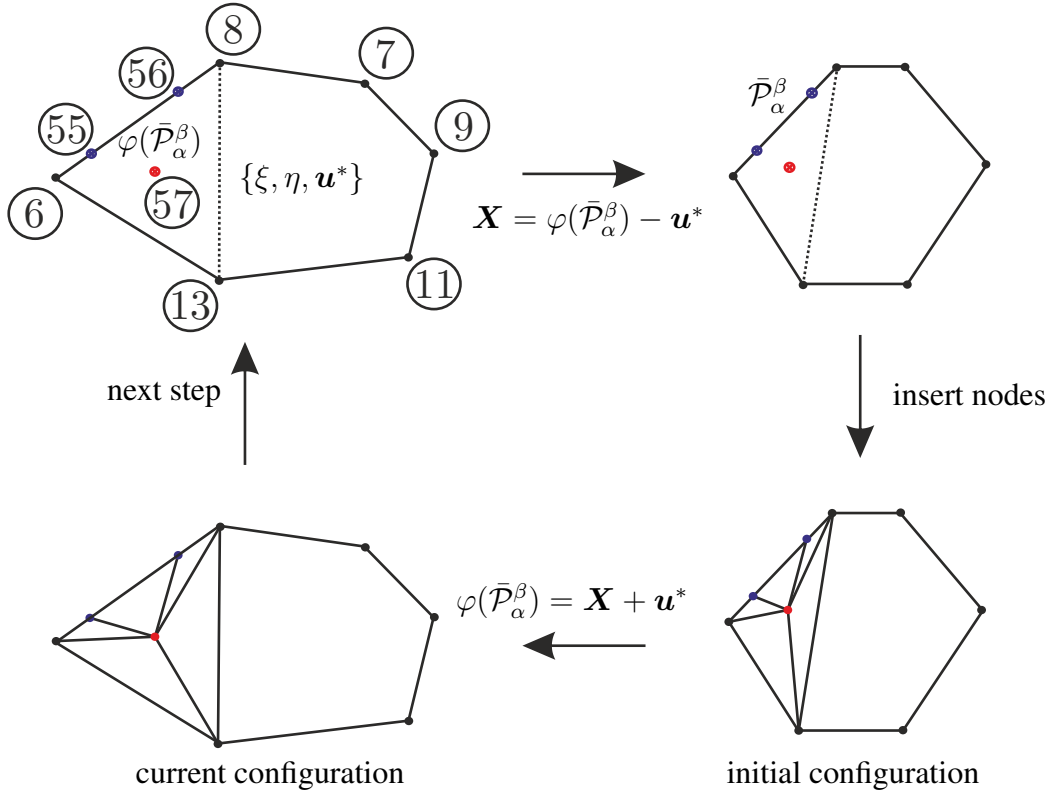


Figure 5.5 – Update of history field and mapping between current and initial configuration

data array of one element E :

$$\{E, \mathbf{n}_E, \{\mathbf{n}_{f=1}, \mathbf{n}_{f=2}, \dots, \mathbf{n}_{f=n_f}\}\}, \quad (5.11)$$

where E is the element id and \mathbf{n}_E is a list which contains the node indices of element E . $\mathbf{n}_{f=i}$ represents a list, which contains node indices of face i . Lets assume, face $f = 3$ with global nodes $\{6, 8, 7, 9, 11, 13\}$ has to be modified, as shown in the left upper part of Fig. 5.5. First, new global nodes $\{55, 56\}$ need to be inserted by:

$$\mathbf{n}_{f=3} = \{6, 13, 11, 9, 7, 8\} \rightarrow \mathbf{n}_{f=1}^+ = \{6, 13, 11, 9, 7, 8, \mathbf{56}, \mathbf{55}\}. \quad (5.12)$$

Of course these nodes also have to be inserted reversely with $\{55, 56\}$ in to the face, which shares the edge $\{6, 8\}$. So far, the insertion of new edge nodes was simple. However, the insertion of global node $\{57\}$ will need more effort. The modification of the new face $\mathbf{n}_{f=3}^+$

leads:

$$\mathbf{n}_{f=3}^+ = \{6, 13, 11, 9, 7, 8, \mathbf{56}, \mathbf{55}\} \rightarrow \begin{cases} \mathbf{n}_{f=3}^{+1} = \{13, 11, 9, 7, 8\} \\ \mathbf{n}_{f=3}^{+2} = \{8, \mathbf{56}, \mathbf{57}\} \\ \mathbf{n}_{f=3}^{+3} = \{\mathbf{56}, \mathbf{55}, \mathbf{57}\} \\ \mathbf{n}_{f=3}^{+4} = \{\mathbf{55}, 6, \mathbf{57}\} \\ \mathbf{n}_{f=3}^{+5} = \{6, 13, \mathbf{57}\} \\ \mathbf{n}_{f=3}^{+6} = \{13, 8, \mathbf{57}\} \end{cases}, \quad (5.13)$$

where six new faces (five triangles + one polygon) are introduced, see right bottom in Fig. 5.5. Alternatively one could create only 2 polygonal faces without triangulization. But this would need more effort. Further one has to ensure that new triangles have to be compatible between both bodies at the interface. Face $\mathbf{n}_{f=3}^+$ needs to be replaced with the new faces $\mathbf{n}_{f=3}^{+m} \forall m \in \{1, 2, \dots, 6\}$. An update of \mathbf{n}_E has to be performed by joining the old face nodes \mathbf{n}_E with new nodes $\{55, 56, 57\}$. The actual node insertion is performed in local coordinates but was explained here in terms of global coordinates for simplification. It is very important to note, that the projection of nodes is carried out in the current configuration but using the initial mesh. If the current mesh would be used, a special treatment of old nodes would be required, e.g. erasing or shifting those nodes. However, by using the old mesh, the number of nodes due to node insertion will not dramatically increase. But it would be the case if current mesh would be used.

5.3 Surface-to-surface approach

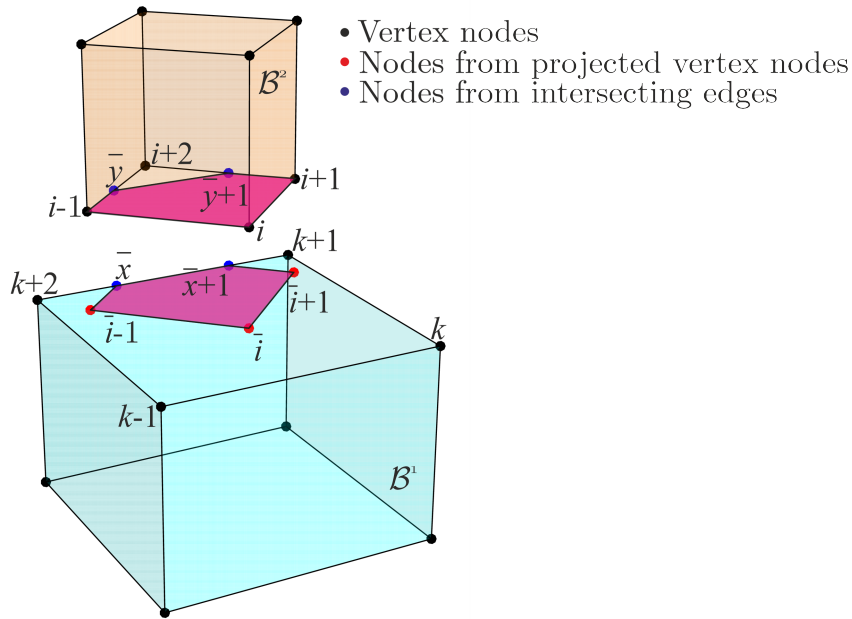


Figure 5.6 – Surface-to-surface discretization using node insertion.

The surface to surface contact is a novel approach, where the gap function in equation (3.4) is defined as a function of the projected displacements. For that, the body is discretized at

the contact interface with virtual contact elements, as can be seen in Fig. 5.7. For the contact

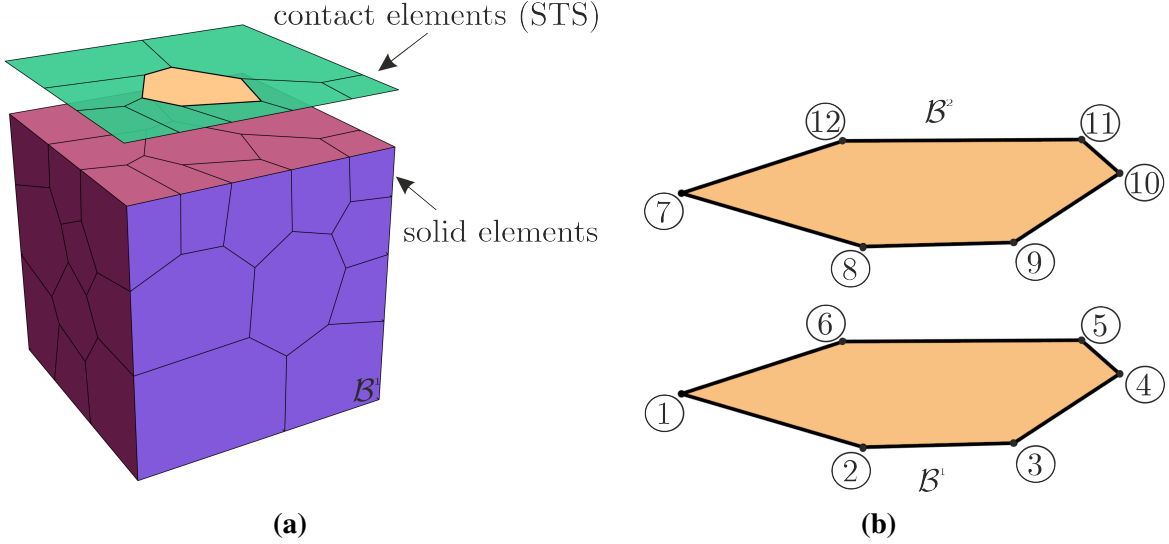


Figure 5.7 – Body B^1 discretized with solid elements and contact interface discretized with contact elements based on a surface-to-surface contact formulation in (a) and contact element with polygon pairs from both bodies B^1 and B^2 with node numbering in (b).

elements, a two dimensional Ansatz in three dimensional space is made with:

$$\begin{aligned} \mathbf{u}_\pi^\alpha &= (\mathbf{N}_\pi^\alpha \cdot \mathbf{a}_i^\alpha) \mathbf{E}_i, \quad i \in \{1, 2, 3\}, \\ \mathbf{N}_\pi^\alpha &= (1, X^\alpha, Y^\alpha), \\ \mathbf{a}_i^\alpha &= (a_{i1}^\alpha, a_{i2}^\alpha, a_{i3}^\alpha). \end{aligned} \quad (5.14)$$

Note that \mathbf{N}_π^α is a two dimensional function but the element is still in the three dimensional space. For that, some of the equations in section 4.4 need to be modified. The computation of the virtual parameters has to be done in local coordinates, since no three dimensional information is given for the two dimensional element. Thus the coordinates need to be transformed from the global coordinate system to a local coordinate systems, similarly to equation (4.41) as shown in Fig. 5.8.

The local coordinates \mathbf{X}^f are defined as:

$$\mathbf{X}^f = \mathbf{R}^f (\mathbf{X} - \mathbf{X}_{mf}), \quad (5.15)$$

with \mathbf{R}^f being the rotation matrix:

$$\mathbf{R}^f = \begin{bmatrix} \mathbf{t}_1^f \\ \mathbf{t}_2^f \\ \mathbf{N}^f \end{bmatrix}, \quad (5.16)$$

constructed as the base of the face with \mathbf{t}_1^f and \mathbf{t}_2^f being the local tangent vectors of the face

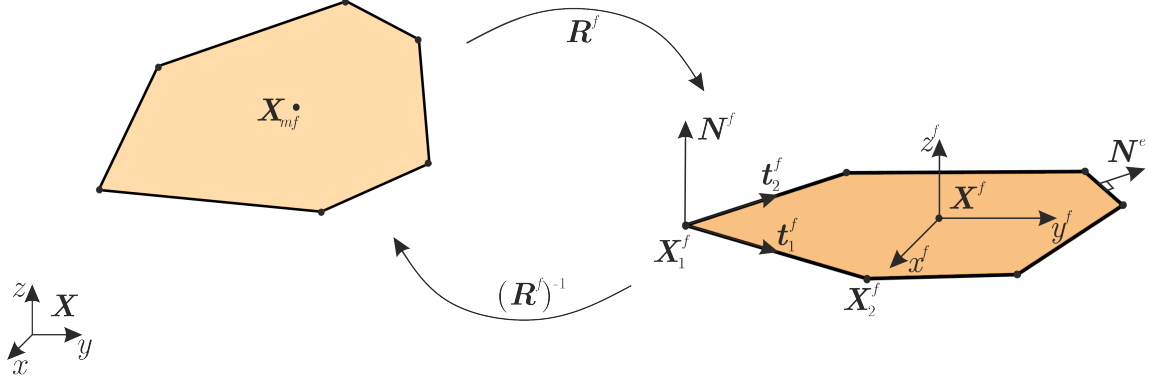


Figure 5.8 – Rotation of polygonal face.

and $N^{f,0}$ the face normal with:

$$\mathbf{t}_1^f = \frac{\mathbf{X}_2^f - \mathbf{X}_1^f}{\|\mathbf{X}_2^f - \mathbf{X}_1^f\|}, \quad \mathbf{t}_2^f = \mathbf{N}^f \times \mathbf{e}_X^f, \quad (5.17)$$

$$\mathbf{N}^{f,0} = (\mathbf{X}_1^f - \mathbf{X}_{mf}) \times (\mathbf{X}_2^f - \mathbf{X}_{mf}), \quad \mathbf{N}^f = \frac{\mathbf{N}^{f,0}}{\|\mathbf{N}^{f,0}\|}, \quad (5.18)$$

where \mathbf{X}_{mf} is denoting the coordinate mean of the associated face and can be computed with equation (4.40). The above equations are identical with equation (4.43). The gradient of the projected displacements $\nabla \mathbf{u}_\pi^\alpha$ consists of six virtual parameters, since the Ansatz is made in two dimensions:

$$\nabla \mathbf{u}_\pi^\alpha = \begin{bmatrix} a_{12}^\alpha & a_{13}^\alpha \\ a_{22}^\alpha & a_{23}^\alpha \\ a_{32}^\alpha & a_{33}^\alpha \end{bmatrix}. \quad (5.19)$$

For the computation of the virtual parameters with a three dimensional ansatz, we used equation (4.21). This equation has to be modified to be solved, since local coordinates are used. The integration can be done in two different ways. The first way is to apply divergence theorem and integrate equation (4.21) over the element edges:

$$\begin{aligned} \nabla \mathbf{u}_\pi^\alpha &= \frac{1}{|\Gamma_f|} \int_{\Gamma_f} \nabla_f \mathbf{u}_h \, d\Gamma \stackrel{Edge}{=} \frac{1}{|\Gamma_f|} \int_{\gamma_f} \mathbf{u}_h \otimes \mathbf{N}_{loc}^e \, d\gamma \\ &= \frac{1}{|\Gamma_f|} \sum_{e=1}^{n_e} \int_{\gamma_e} \mathbf{u}_h^e \otimes \mathbf{N}_{loc}^e \, d\gamma, \quad (5.20) \\ &= \frac{1}{|\Gamma_f|} \sum_{e=1}^{n_e} \sum_{g=1}^{n_g^e} w_g^e J_g^e \mathbf{u}_{h,g}^e \otimes \mathbf{N}_{loc}^e \end{aligned}$$

where the Jacobian is defined as:

$$J^e = \left\| \frac{\partial \mathbf{X}^f}{\partial \xi} \right\|. \quad (5.21)$$

However, this integration is only exact under the condition, that the faces are flat and remain flat. Thus for small deformations, this way is valid. The second way for the integration is to integrate again on triangles, as have been done in equation (4.27):

$$\begin{aligned} \nabla \mathbf{u}_\pi^\alpha &= \frac{1}{|\Gamma_f|} \int_{\Gamma_f} \nabla_f \mathbf{u}_h \, d\Gamma \stackrel{Trig}{=} \frac{1}{|\Gamma_f|} \sum_{\mathcal{T}=1}^{n_{\mathcal{T}}} \int_{\Gamma_{\mathcal{T}}} \nabla_f \mathbf{u}_h^{\mathcal{T}} \, d\Gamma \\ &= \frac{1}{|\Gamma_f|} \sum_{\mathcal{T}=1}^{n_{\mathcal{T}}} \sum_{g=1}^{n_g^{\mathcal{T}}} w_g^{\mathcal{T}} J_g^{\mathcal{T}} \nabla_f \mathbf{u}_{h,g}^{\mathcal{T}} \end{aligned} \quad (5.22)$$

where the Jacobian is same as in equation (4.30) with:

$$J^{\mathcal{T}} = \|\mathbf{G}_\zeta\|. \quad (5.23)$$

Since the integration of the constant part in equation (5.20) or equation (5.22) is performed in local coordinates, the right term in equation (4.32) vanishes leading to:

$$(a_{11}^\alpha, a_{21}^\alpha, a_{31}^\alpha) = \frac{1}{n_V} \sum_{I=1}^{n_V} \mathbf{u}_I. \quad (5.24)$$

This is valid, since the right term in equation (4.32) is already considered by using the gradient with respect to the local coordinates $\nabla_f \mathbf{u}_h$.

Once the virtual parameters are computed, the gap function can be constructed, according to equation (3.4):

$$g_{N\pi} = (\mathbf{x}_\pi^2 - \mathbf{x}_\pi^1) \cdot \mathbf{n}^1, \quad (5.25)$$

with:

$$\mathbf{x}_\pi^\alpha = \mathbf{X}_{\mathcal{T}}^\alpha + \mathbf{u}_\pi^\alpha, \quad (5.26)$$

where $\mathbf{X}_{\mathcal{T}}$ denotes the initial coordinates of the triangles with:

$$\mathbf{X}_{\mathcal{T}} = \mathbf{N}_{\mathcal{T}} \mathbf{X}_{\mathcal{T}} \quad \text{where} \quad \mathbf{X}_{\mathcal{T}} = \bigcup_I \mathbf{X}_I \quad \forall I \in \mathcal{T}. \quad (5.27)$$

The normal \mathbf{n}^1 in equation (5.25) can be simply computed with equation (5.18). The decision regarding which face normal to take, depends on the master/slave setup. However, when a face becomes non flat during the deformation process, a mean normal of the associated face could be used. The shape functions $\mathbf{N}_{\mathcal{T}}$ in equation (5.27) are simple linear finite element triangle shape functions, as introduced in equation (4.23). Constructing the contact potential based on a penalty formulation with equation (3.8) and using the definition of the projected gap function in equation (5.24) leads to:

$$\Pi_{\pi,E}^c = \int_{\Gamma_c} \frac{\epsilon_p}{2} g_{N\pi}^2 \, d\Gamma = \sum_{\mathcal{T}=1}^{n_{\mathcal{T}}} \sum_{g=1}^{n_g^{\mathcal{T}}} w_g^{\mathcal{T}} J_g^{\mathcal{T}} \frac{\epsilon_p}{2} g_{N\pi,g}^2, \quad (5.28)$$

where the integration is similar to equation (4.27). However, since the argument in equation (5.28) is a quadratic function, three Gauss-points per triangle are needed. Fig. 5.9 is showing the projection \mathbf{u}_π^α of both contact pairs, the projected gap $g_{N\pi}$ and the resulting function which needs to be integrated. The Jacobian $J^{\mathcal{T}}$ is computed according to equation (4.30).

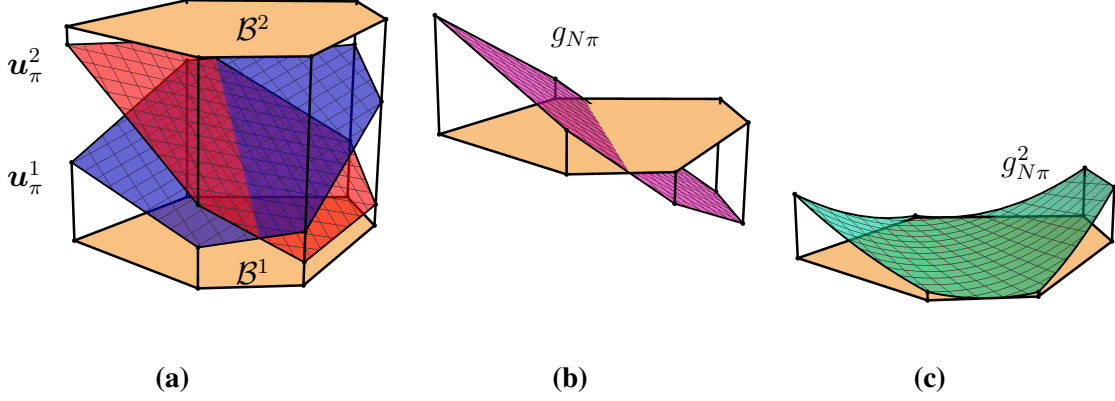


Figure 5.9 – Projected displacements \mathbf{u}_π^1 and \mathbf{u}_π^2 from both contact pairs in (a), projected gap function $g_{N\pi}$ in (b) and the function $g_{N\pi}^2$ in (c) which has to be integrated in equation (5.28).

The projection part solely results in a rank deficient contact tangent and thus needs to be stabilized. For the stabilization of the contact tangent, the same idea as for stabilization of the solid is introduced by:

$$\Pi_E^c = (1 - \beta^c)\Pi_{\pi,E}^c + \beta^c\Pi_{h,E}^c, \quad (5.29)$$

where β^c has a similar definition as in equation (4.67). The motivation of β^c is purely numerical and not as have been introduced for the solid part. Thus the choice has to be done according to the geometry of the contact element. Increasing the amount of nodes will lead to a higher rank deficiency and thus β^c has to be increased.

The approximation of equation (5.29) can be done similar as for the solid formulation in section 4.5.3 by reformulating the gap function for each triangle of the sub mesh with:

$$g_{NT} = (\mathbf{x}_T^2 - \mathbf{x}_T^1) \cdot \mathbf{n}^1, \quad (5.30)$$

where the current coordinate is defined as:

$$\mathbf{x}_T^\alpha = \mathbf{X}_T^\alpha + \mathbf{u}_T^\alpha. \quad (5.31)$$

By introducing linear triangular finite element shape functions for the approximation of the displacements:

$$\mathbf{u}_T = \mathbf{N}_T \mathbf{u}_T \quad \text{where} \quad \mathbf{u}_T = \bigcup_I \mathbf{u}_I \quad \forall I \in \mathcal{T}, \quad (5.32)$$

the stabilization contact potential leads:

$$\Pi_{h,E}^c = \int_{\Gamma_c} \frac{\epsilon_p}{2} g_{NT}^2 d\Gamma = \sum_{T=1}^{n_T} \sum_{g=1}^{n_g^T} w_g^T J_g^T \frac{\epsilon_p}{2} g_{NT,g}^2, \quad (5.33)$$

where the Jacobian J^T is the same as in equation (4.30). Since the argument is of order two, three Gauss-point integration is done per triangle.

The total contact residual and contact tangent can be obtained by taking the first and second derivative of the total potential with respect to the unknowns, leading to:

$$\begin{aligned}\mathbf{R}_E^c &= (1 - \beta^c) \frac{\partial \Pi_{\pi,E}^c(\mathbf{u}_\pi)}{\partial \mathbf{u}_E} + \beta^c \frac{\partial \Pi_{h,E}^c(\mathbf{u}_h)}{\partial \mathbf{u}_E} \\ &= (1 - \beta^c) \mathbf{R}_{\pi,E}^c + \beta^c \mathbf{R}_{h,E}^c\end{aligned}\quad (5.34)$$

$$\mathbf{K}_{\pi,E}^c = \frac{\partial \mathbf{R}_{\pi,E}^c}{\partial \mathbf{u}_E} \quad \mathbf{K}_{h,E}^c = \frac{\partial \mathbf{R}_{h,E}^c}{\partial \mathbf{u}_E} \quad (5.35)$$

$$\mathbf{K}_E^c = (1 - \beta^c) \mathbf{K}_{\pi,E}^c + \beta^c \mathbf{K}_{h,E}^c \quad (5.36)$$

Chapter 6

Numerical examples

6.1 Comparison of edge-integration and trig-integration

In section 4.4.1 and 4.4.2, the evaluation of the integral in equation (4.21) was discussed. In this chapter, the performance of each integration scheme for the computation of the virtual parameters will be analyzed by means of the Cook's membrane problem. Later in section 6.5, each formulation is applied to the contact patch test.

6.1.1 3D Cook's membrane

In this example, the well known Cook's membrane is analyzed. The material parameters are set to $E = 10 \frac{\text{kN}}{\text{mm}^2}$ and $\nu = 0.3$. The geometrical setup can be taken from Fig. 6.1, where the dimensions are $H_1 = 44 \text{ mm}$, $H_2 = 16 \text{ mm}$, $B = 10 \text{ mm}$ and $L = 48 \text{ mm}$. The Cook's membrane is loaded with $p_0 = 0.5 \text{ kN}$. The deflection of the tip is shown in Fig.

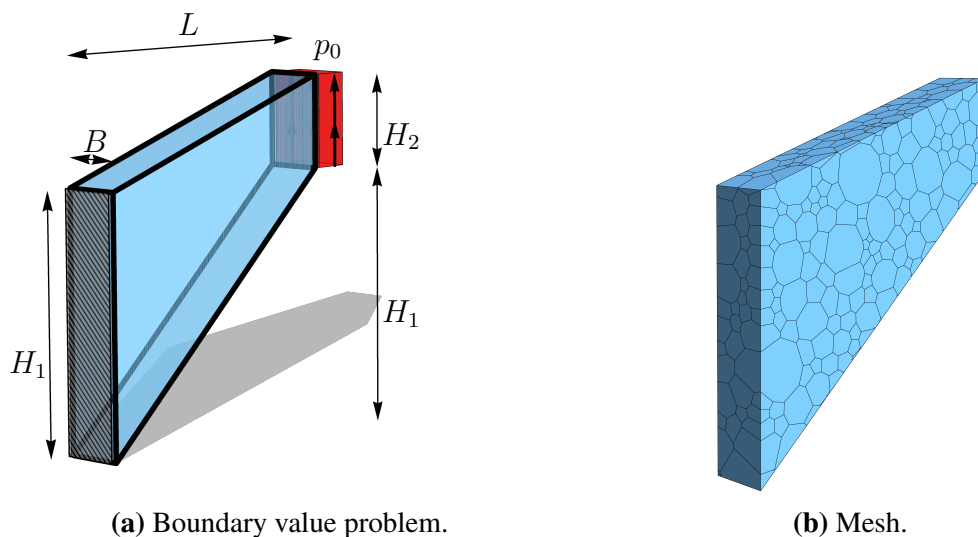


Figure 6.1 – 3D Cook's membrane for testing of different integration schemes for the computation of the virtual parameters.

6.2 for different element geometries and different mesh densities. The reference solution is obtained with an TSCG12 *enhanced assumed strain (EAS)* element, which is based on a Taylor series expansion of shape function derivatives, introduced in KORELC ET AL. (2010) with around 32768 elements which is equivalent to 107712 degrees of freedom. Elements with edge integration are denoted by "EI", while elements, which are computed via a triangle integration are represented by "TI". "s1" represents the energy stabilization and "s2" the stabilization based on the degrees of freedom, see section 4.5.3. It can be seen, that the edge integration converges faster to the reference solution, than the integration based on a sub tessellation. This results is reproduced by all type of element shapes, but more significantly for H2S shaped virtual elements, see Fig. 6.2c. Another important observation shows, that the edge integration has a significant effect on the overall results for the DOF stabilization, but has a less effect, when energy stabilization is used. However, all type of stabilizations and integration schemes are converging to the reference solution. The choice of which stabilization and which integration scheme is used, depends on the application. A more detailed discussion will be made in section 6.5, where both integration schemes are compared for contact applications.

For completeness, the deformation, including contour plots with stresses σ_{zz} are shown in Fig. 6.3, Fig. 6.4 and Fig. 6.5 for all kind of variations and element shapes. Note here, that finer mesh densities for voronoi shaped virtual elements were not converging. This is due to poor mesh quality and results from distorted triangles and tetrahedrons, leading to tiny edges. A detailed mesh manipulation would lead to convergence but is not the focus of this work.

6.2 Dynamics

In this section, the performance of the derived 2D and 3D virtual element formulations for dynamic problems at finite deformations are demonstrated. For comparison purposes results of the standard finite element method (FEM) are included. The material parameters used in this chapter are the same for all examples and provided in table 6.1.

Table 6.1 – Material parameters used for the numerical examples

No.	Parameter	Label	Value	Unit
1	Elastic modulus	E	210	kN/mm ²
2	Poisson ratio	ν	0.3	–
3	Density	ρ	2.7	kg/mm ³

In this chapter, the following mesh types with low order virtual element discretizations are introduced. Different evaluations of the mass matrix $\mathbf{M}_{\Pi,E}$ in section 4.5.2 are employed with the following element types:

- VEM \square : The argument of the integral is evaluated at the centroid of the polygon in 2D or polyhedron in 3D and is multiplied by the area or volume of the element respectively. The mass matrix is computed using only the projection part with $\beta^{dyn} = 0$. This

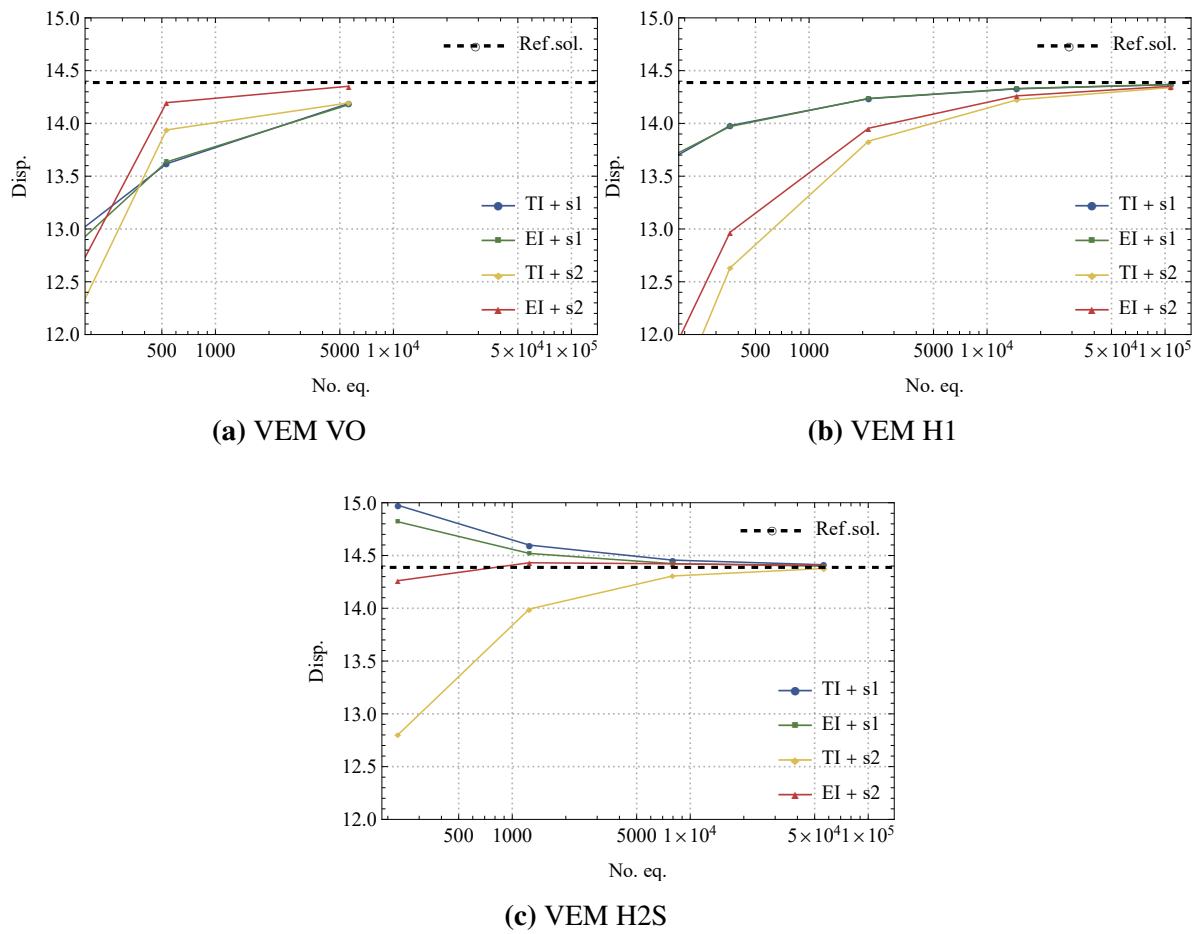


Figure 6.2 – 3D Cook’s membrane - Convergence study for edge integration (EI) and triangle integration (TI) with stabilization based on an internal energy (s1) and stabilization based on the degrees of freedom (s2).

represents the evaluation with equation (4.58). The \square denotes the element topology with:

- Q1: A mesh consisting of regular 2D quadrilateral elements with 4 nodes.
 - Q2S: A mesh consisting of serendipity 2D quadrilateral elements with 8 nodes.
 - VO: A mesh consisting of voronoi type 2D/3D elements with arbitrary number of nodes and arbitrary shape.
 - H1: A mesh consisting of regular 3D hexahedral elements with 8 nodes.
 - H2S: A mesh consisting of serendipity 3D hexahedral elements with 20 nodes.
- VEM \square Stab: Elements which are additionally denoted with "Stab" have a stabilized mass matrix with $\beta^{dyn} = 0.4$, where the mass matrix is stabilized, as introduced in equation (4.7).
 - VEM \square BI: Elements which are additionally denoted with "BI" are using equation (4.63) to evaluate the mass matrix exactly on the boundary.

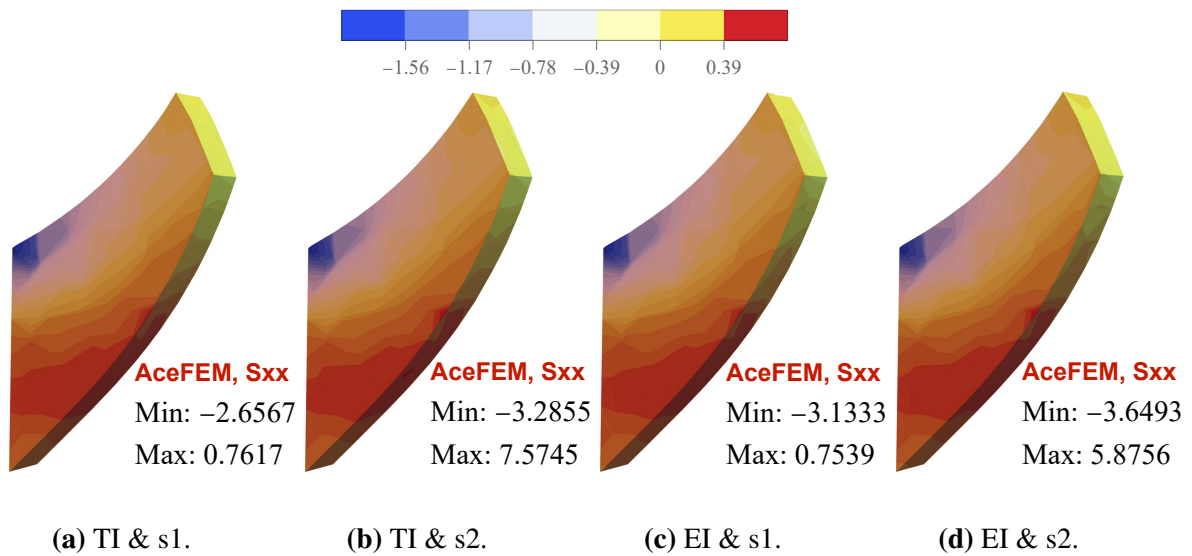


Figure 6.3 – 3D Cook's membrane - Contourplots showing stresses S_{xx} with voronoi shaped virtual elements.

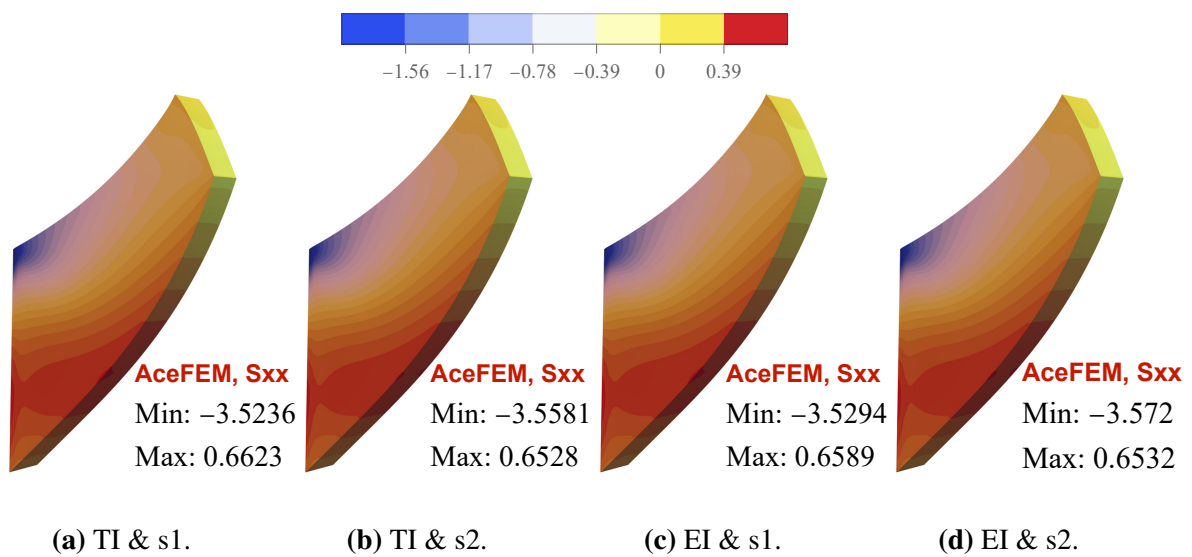


Figure 6.4 – 3D Cook's membrane - Contourplots showing stresses S_{xx} with H1 shaped virtual elements.

- VEM \square -I: Elements which are additionally denoted with "I" are using equation (4.59) to evaluate the mass matrix on the internal sub mesh.
- VEM \square -II: Elements which are additionally denoted with "II" are computed with $\beta^{dyn} = 1$, which result in a pure finite element mass matrix, using equation (4.92).

For a representative comparison, the following finite element formulations were selected:

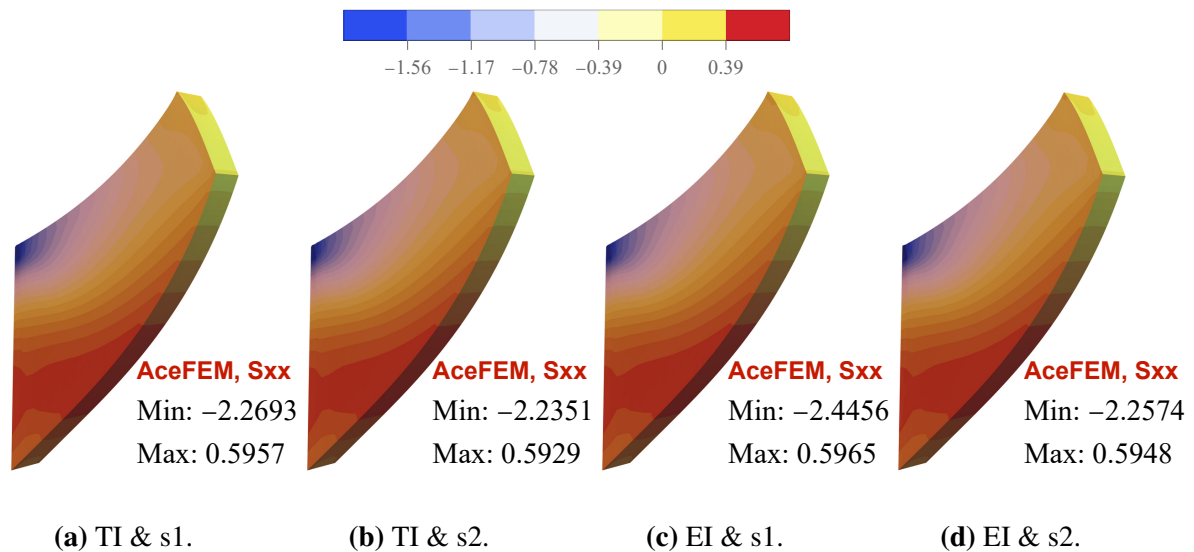


Figure 6.5 – 3D Cook's membrane - Contourplots showing stresses S_{xx} with H2S shaped virtual elements.

- FEM T1: A mesh consisting of regular 2D first order triangular finite elements with 3 nodes.
- FEM Q1: A mesh consisting of regular 2D first order quadrilateral finite elements with 4 nodes.
- FEM Q2: A mesh consisting of regular 2D second order quadrilateral finite elements with 9 nodes.
- FEM H1: A mesh consisting of regular 3D first order quadrilateral finite elements with 8 nodes.
- FEM H2: A mesh consisting of regular 3D second order quadrilateral finite elements with 27 nodes.

The stabilization parameter of the *static part* was chosen as $\beta^{stat} = 0.4$ for all the simulations in this section.

6.2.1 Eigenvalue analysis

In this subsection, different virtual element formulations are compared to classical finite elements with regards to eigenfrequencies and eigenmodes of single elements and structural systems to check the correctness of the formulations.

Single element analysis

The eigenfrequencies of a single quadrilateral element which has a free-free boundary condition are shown in table 6.6. Here eigenfrequencies related to rigid body motions are ex-

cluded. To investigate the effect of the stabilization parameters β^{stat} and β^{dyn} on the eigenfrequencies, both stabilization parameters have been varied. It can be observed, that both stabilization parameters have an influence the eigenfrequencies of the element. In previous publications, an optimal stabilization parameter β^{stat} for the static part was found to be in the range 0.2 – 0.4, see WRIGGERS ET AL. (2017). Thus for transient analysis, $\beta^{stat} = 0.4$ is chosen as well which lead to results close to the one obtained with a linear finite element FEM Q1. The results obtained with VEM Q1 Stab (evaluating the mass matrix at the centroid) are slightly stiffer when compared with FEM Q1 and VEM Q1 BI Stab.

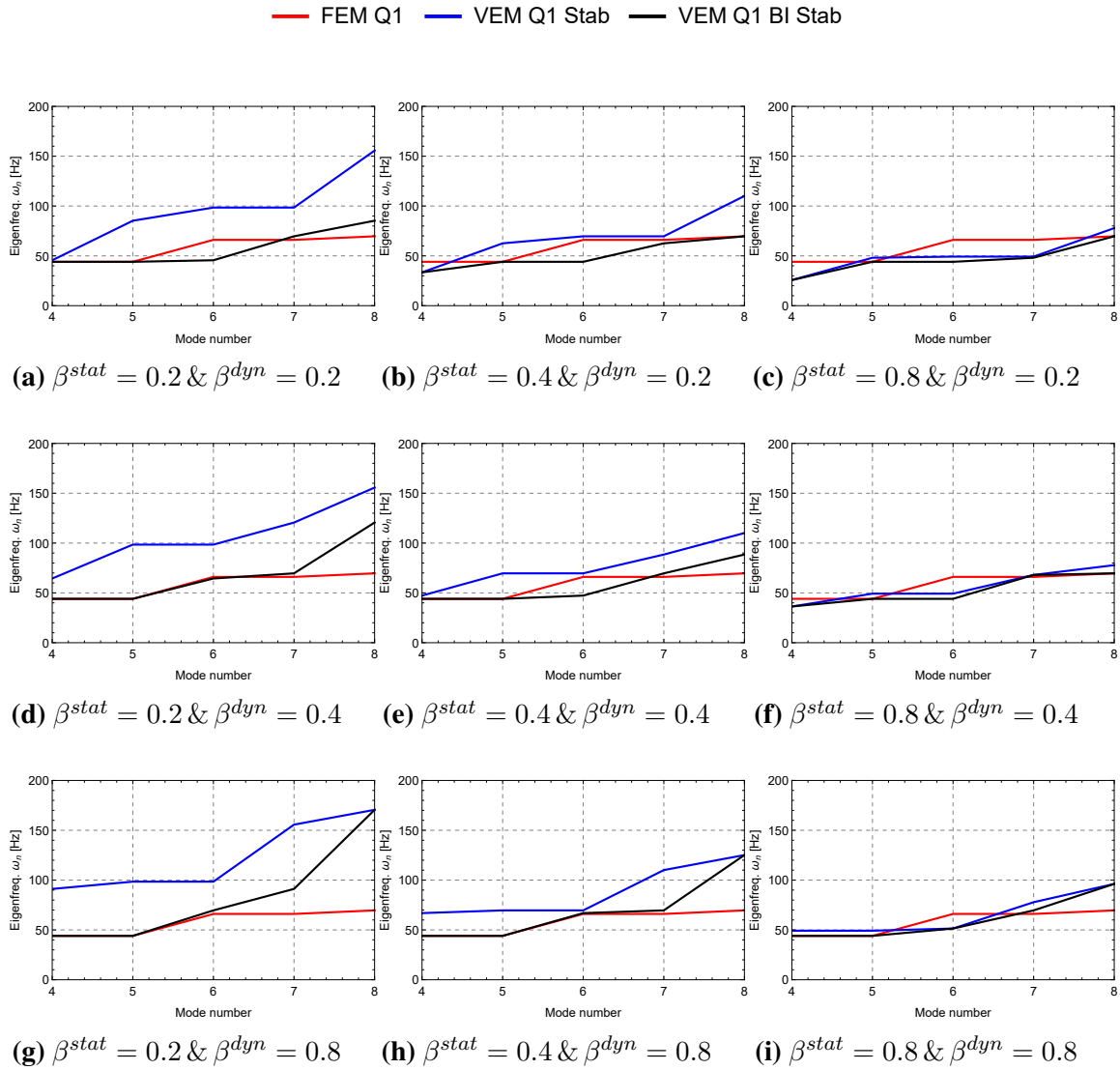


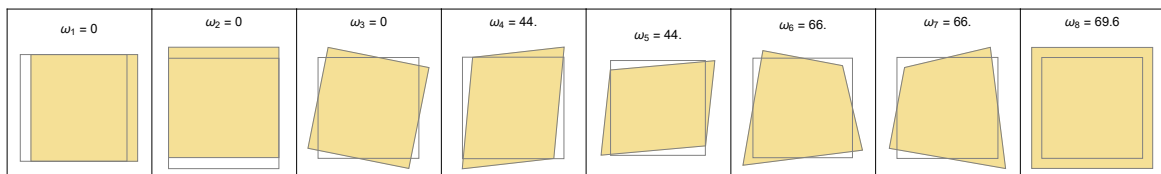
Figure 6.6 – Eigenfrequencies ω_n in Hz of a single element (free-free) for different stabilization parameters β^{stat} and β^{dyn} .

For $\beta^{stat} = \beta^{dyn} = 0.4$, the first eight eigenfrequencies and eigenmodes are depicted in Fig. 6.7. The elements used in this analysis are:

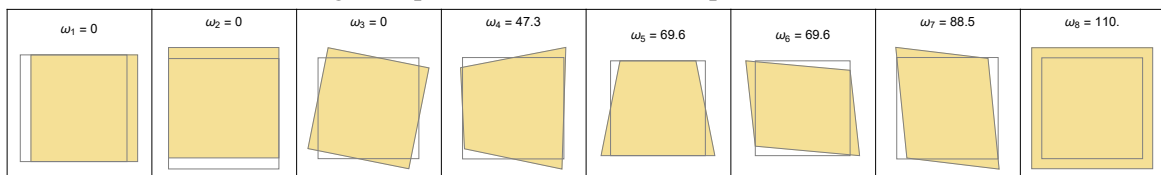
- The first order finite element FEM Q1 in Fig. 6.7a.

- The virtual element VEM Q1 Stab in Fig. 6.7b, evaluating the mass matrix at the centroid.
- The virtual element VEM Q1 BI Stab in Fig. 6.7c, evaluating the mass matrix exactly on the boundary.
- The virtual element VEM Q1-I Stab in Fig. 6.7d, evaluating the mass matrix on the submesh.

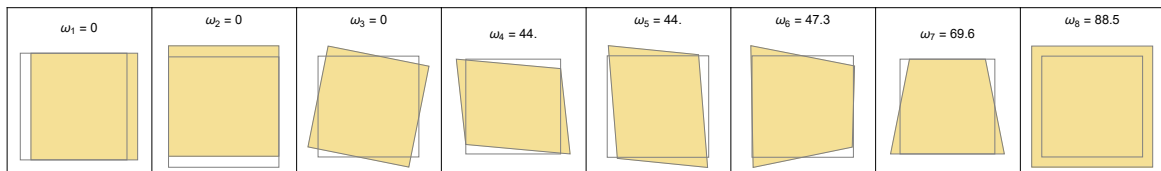
Note that all these virtual elements have a stabilized mass matrix, since the computation of eigenfrequencies with rank deficient mass matrix is not possible for a single element.



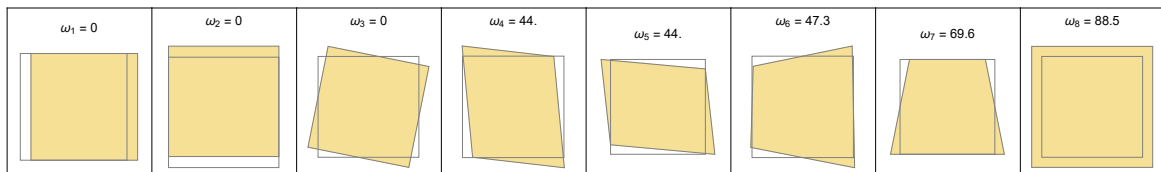
(a) Eigenfrequencies ω_n and modeshapes for FEM Q1.



(b) Eigenfrequencies ω_n and modeshapes for VEM Q1 Stab.



(c) Eigenfrequencies ω_n and modeshapes for VEM Q1 BI Stab.



(d) Eigenfrequencies ω_n and modeshapes for VEM Q1-I Stab.

Figure 6.7 – Eigenfrequencies ω_n and modeshapes for single element with free-free boundary condition and stabilization parameters $\beta^{stat} = \beta^{dyn} = 0.4$.

Structural analysis

In this analysis, an eigenvalue study of the mass and stiffness matrix for the computation of a specific initial boundary value problems is performed. A cantilever beam, which is clamped at one side and free at the other side (C-F) is considered. The material parameters can be taken from table 6.1. The dimensions of the beam are set to $l = 30$ mm and $h = 0.3$ mm. In

this study the stabilization parameters for the static and the dynamic part are set to $\beta^{stat} = \beta^{dyn} = 0.4$.

Fig. 6.8 shows the eigenvalues with respect to the mode numbers, obtained with FEM Q1 and VEM Q1 Stab. In all figures no distinction is made between the mode types. The eigenvalues are computed with a discretization that has 360 unknowns. The eigenvalues of the stiffness and mass matrix computed with VEM are very close to the eigenvalues obtained by FEM. Note that a mass matrix which is based purely on the projection part ($\beta^{dyn} = 0$) will yield in a rank deficient mass matrix and thus the eigenvalues are not computable. Nevertheless it will be shown later that mass matrices with $\beta^{dyn} = 0$ and $\beta^{dyn} > 0$ yield good results when applying them to transient initial boundary value problems.

Table 6.2 depicts the eigenfrequencies which are corresponding to the first six longitudinal (L) and transversal (T) modes for two different mesh densities. The graphical representation of this results are depicted in Fig. 6.9. For the longitudinal modes, the eigenfrequencies computed with VEM Q1 Stab are nearly the same when compared to the eigenfrequencies obtained with FEM Q1. For the bending modes, the eigenfrequencies have some shift, but they are in a good agreement. However, it is interesting, that increasing the number of nodes per virtual element from 4 to 8 nodes (changing the element topology from Q1 to Q2S topology), increases the quality of the computed eigenfrequencies for the virtual element significantly. The order of the ansatz is still a linear one, i.e. $k = 1$. Note that the eigenvalues are converging to the analytical solution for all element types for refined meshes.

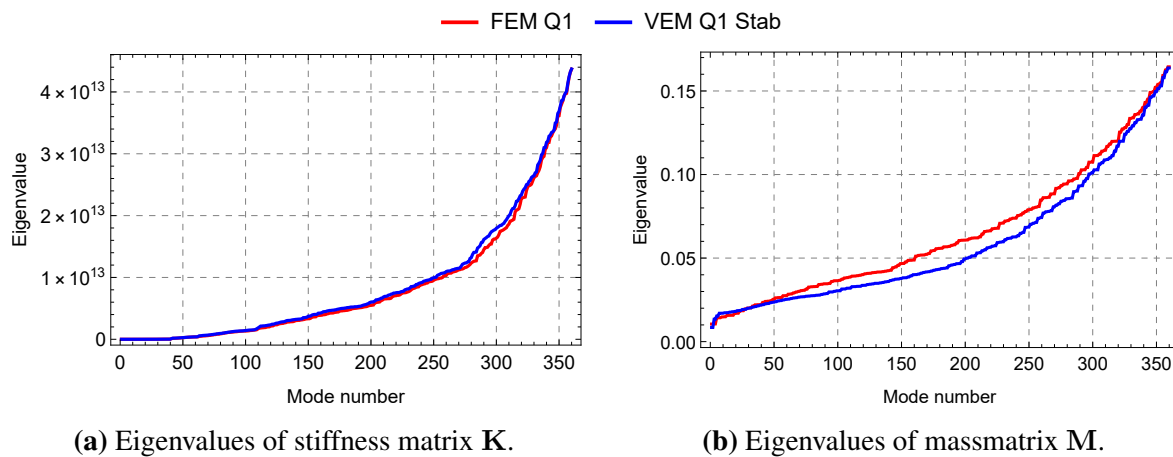


Figure 6.8 – Eigenvalues of stiffness and mass matrix for 2D beam (C-F).

6.2.2 Wave propagation in longitudinal beams

This example deals with wave propagation in longitudinal beams. The geometric setup and the loading conditions of the specimen are depicted in Fig. 6.10. Table 6.1 provides the material parameters. The height of the beam is chosen to be $H = 0.3$ mm and the length $L = 30$ mm. The boundary conditions are set, such that the degrees of freedom in longitudinal direction are fixed on the right side. Due to the high frequencies which appear in this specific example, the time increment is set to $\Delta t = 0.001 \mu s$. The initial velocity of

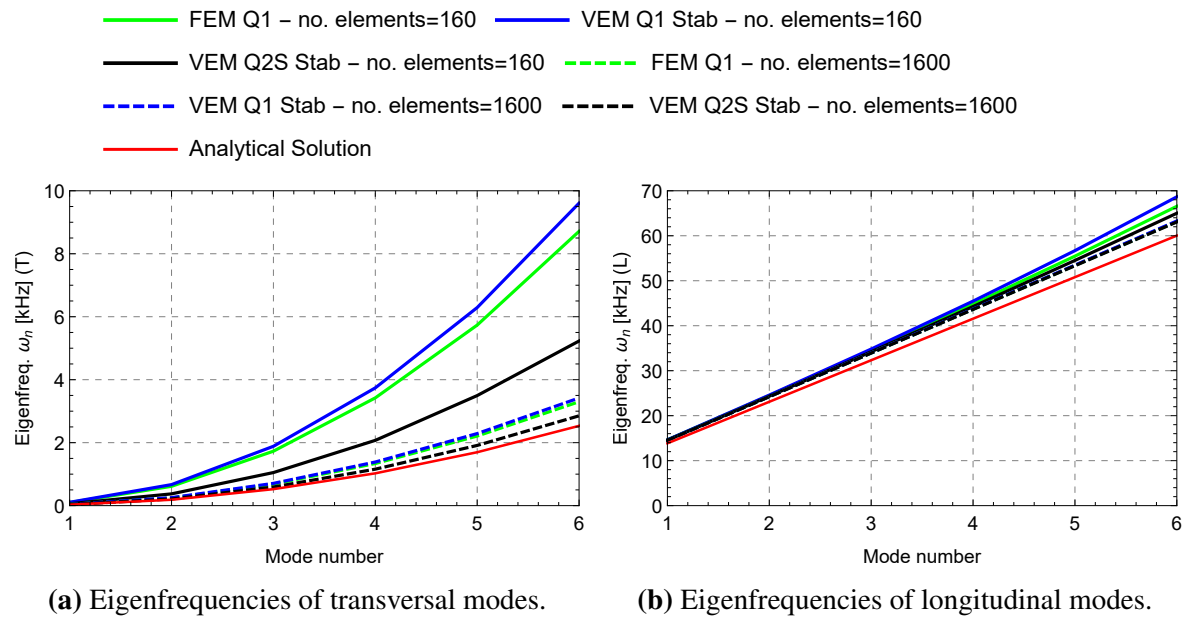


Figure 6.9 – Eigenfrequencies for 2D beam (C-F).

Table 6.2 – Eigenfrequencies ω_n in Hz for 2D beam (C-F) with 1600 elements for modetype: T=Transversal and L=Longitudinal.

Element type	Mode no. (type)					
	1 (T)	2 (T)	3 (T)	4 (T)	5 (T)	6 (T)
FEM Q1	38.94	243.99	682.94	1337.76	2210.41	3300.27
VEM Q1 Stab	40.31	252.54	706.96	1385.06	2289.1	3418.76
VEM Q1 BI Stab	40.26	252.25	706.25	1382.9	2284.79	3410.94
VEM Q1-I Stab	40.26	252.25	706.25	1382.9	2284.79	3410.94
VEM Q2S Stab	33.74	211.38	591.50	1158.09	1912.27	2852.76
VEM Q2S BI Stab	33.72	211.23	590.97	1156.72	1909.34	2847.17
VEM Q2S-I Stab	33.72	211.23	590.97	1156.72	1909.34	2847.17
Analytical	29.84	186.99	523.48	1026.01	1696.06	2533.62
	1 (L)	2 (L)	3 (L)	4 (L)	5 (L)	6 (L)
FEM Q1	14524.3	24214.1	33914.2	43628.8	53362.0	63118.0
VEM Q1 Stab	14525.7	24220.4	33931.5	43665.5	53429.2	63229.3
VEM Q1 BI Stab	14524.4	24214.5	33915.4	43631.3	53366.6	63125.6
VEM Q1-I Stab	14524.4	24214.5	33915.4	43631.3	53366.6	63125.6
VEM Q2S Stab	14523.4	24209.8	33902.4	43603.6	53315.9	63041.7
VEM Q2S BI Stab	14522.1	24204.0	33886.4	43569.6	53253.8	62939.3
VEM Q2S-I Stab	14522.1	24204.0	33886.4	43569.6	53253.8	62939.3
Analytical	13853.1	23088.5	32324.0	41559.4	50794.8	60030.2

all nodes is set to $v_{0,X} = 20 \frac{\text{m}}{\text{s}}$. The virtual element method is compared with the finite element method and the analytical solution which can be obtained with equation (6.2) by solving the wave equation (6.1). Fig. 6.11a and Fig. 6.11b are showing the wave propagation through the elastic body. The displacement over time response for different VEM and FEM formulations is compared with analytical results. The FEM results are computed for 4×200 elements, where the virtual element results are computed for 4×100 elements. We observe a good agreement of VEM compared with FEM solution and the analytical solution. In terms of the period and the amplitude of the wave, the virtual elements shows results that are close to the analytical solution. Furthermore, the time history of the displacements is nearly the same for both elements VEM Q2S Stab and VEM Q2S with stabilized and non stabilized mass matrix. This shows, that even a rank deficient mass matrix leads to sufficient accurate results.

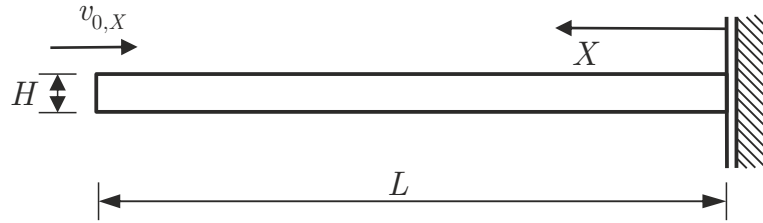


Figure 6.10 – Wave propagation in longitudinal beams - Boundary value problem.

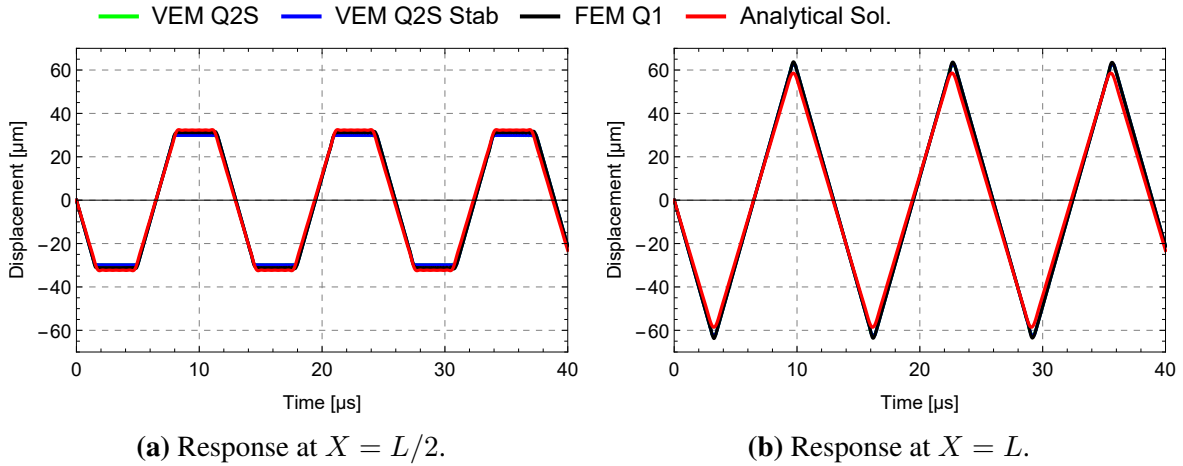


Figure 6.11 – Wave propagation in longitudinal beams - Displacement over time response.

$$\frac{\partial^2 u}{\partial t^2} = c^2 \frac{\partial^2 u}{\partial x^2} \quad \text{where} \quad c = \sqrt{\frac{E}{\rho}} \quad (6.1)$$

$$u(X, t) = \sum_{n=0}^{\infty} \frac{2 v_0 c}{L \omega_n^2} \sin\left(\frac{\omega_n X}{c}\right) \sin(\omega_n t) \quad \text{with} \quad \omega_n = \frac{(2n+1)\pi c}{2L}. \quad (6.2)$$

For both virtual elements VEM Q2S and VEM Q2S Stab the integral for the dynamic part in equation (4.55) is evaluated at the centroid of the element with equation (4.58), hence this simple and efficient scheme seems to be sufficient.

6.2.3 Transversal beam vibration

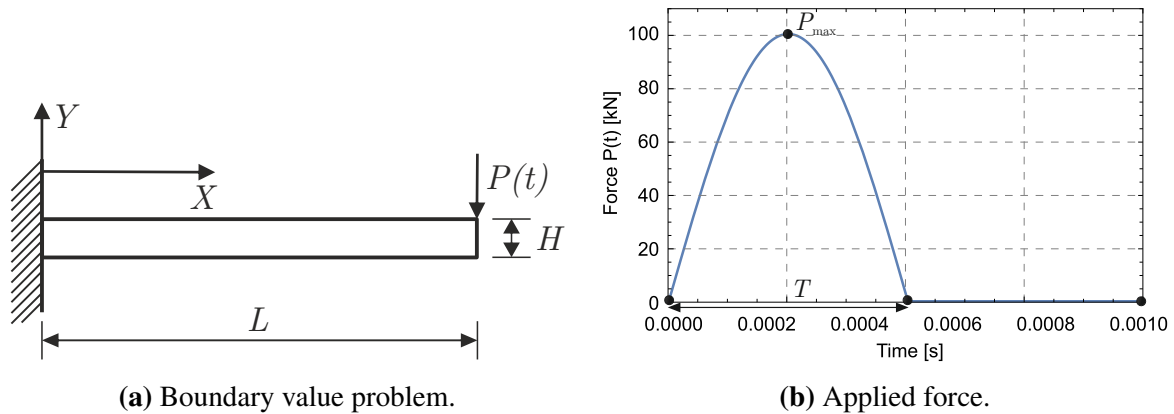


Figure 6.12 – Transversal beam vibration.

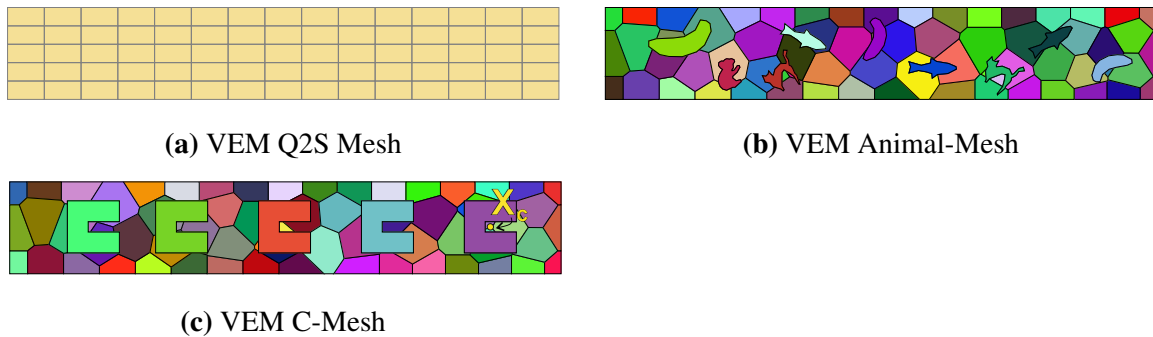


Figure 6.13 – Transversal beam vibration - Different meshes.

The next example is concerned with the analysis of transversal vibrations in beams. The geometric setup and the loading conditions of the cantilever beam are depicted in Fig. 6.12a. For the material parameters see table 6.1. The length of the bar is set to $L = 30$ mm and the height is $H = 5$ mm. The force is applied transversal as a point load at the upper corner at $X = L$ as shown in Fig. 6.12b. The temporal course of the force is given by a half sine, where the maximum of the force is set to $P_{\max} = 100$ kN. The time period T of the applied force is adjusted to the bending stiffness of the beam and is defined as:

$$T = \frac{3.5156}{2\pi L^2} \sqrt{\frac{12\rho}{E L H^3}}. \quad (6.3)$$

In order to analyze the effect of the element shape (convex or concave) on evaluating the integral of the dynamic part, different type of meshes are used, which can be seen in Fig.

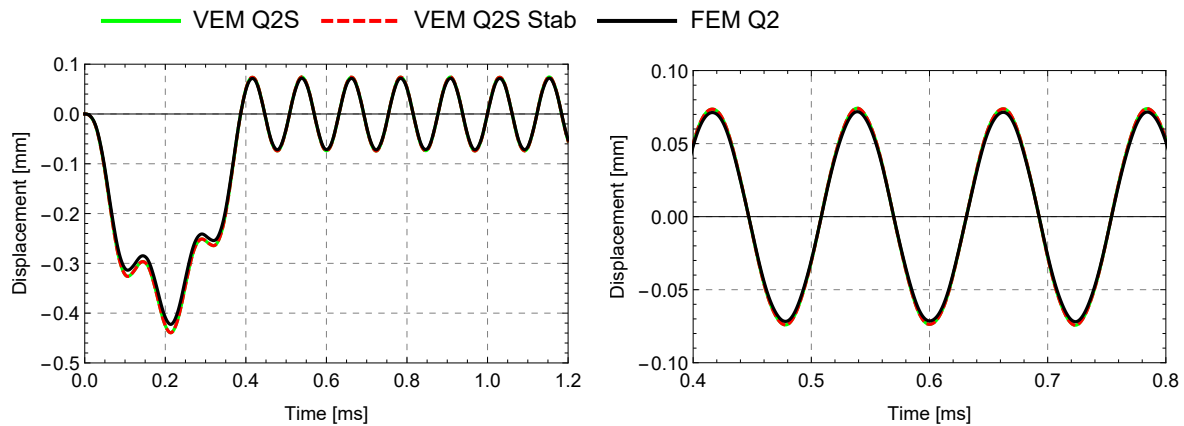


Figure 6.14 – Transversal beam vibration - Displacement over time response at $X = L$ (1).

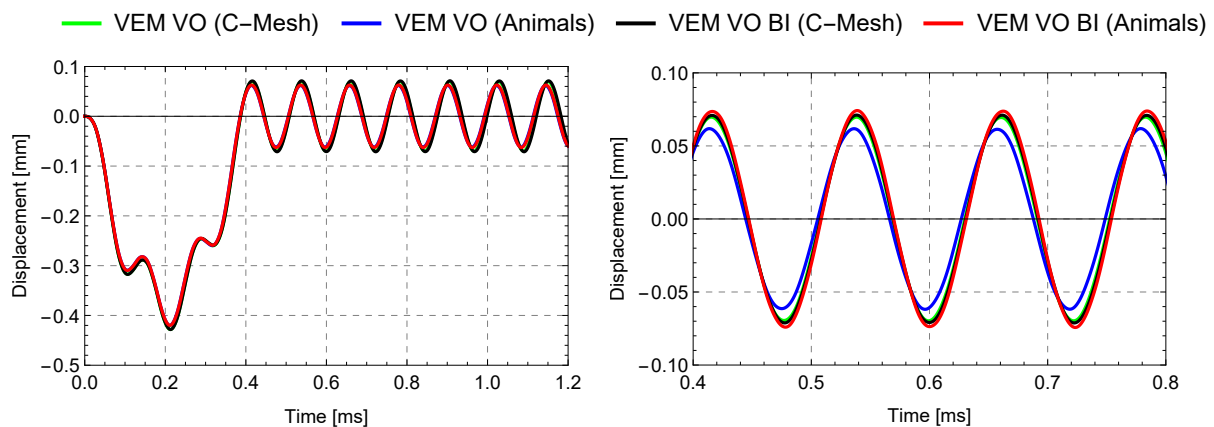


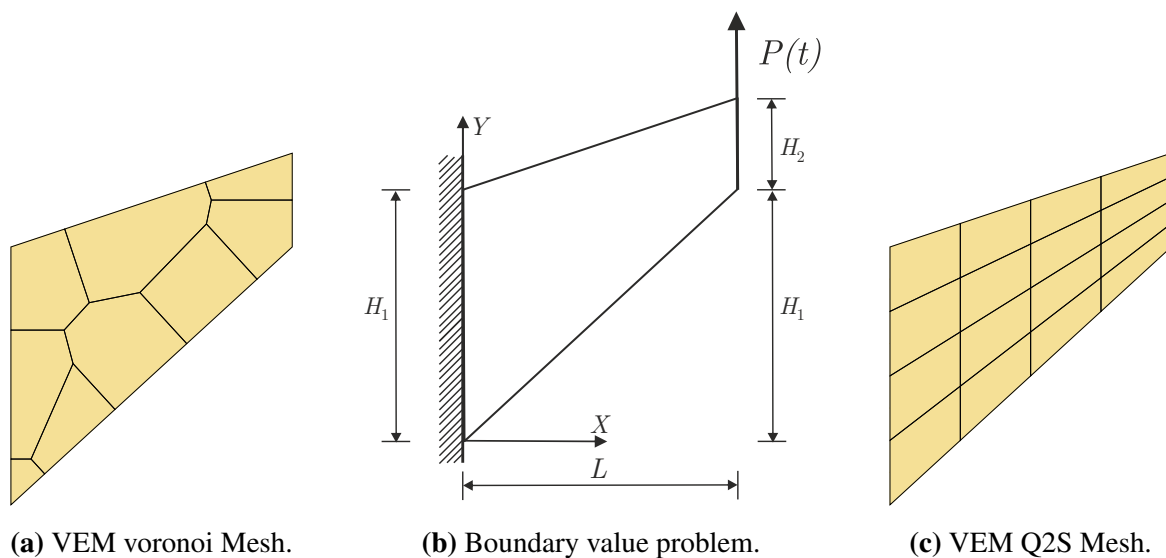
Figure 6.15 – Transversal beam vibration - Displacement over time response at $X = L$ (2).

6.13. The "animal" mesh (Fig. 6.13b) includes concave elements. To see the effect of using concave elements where the centroid of the element is outside of the element domain, a special mesh with C-shaped elements is used, where the centroid of the C-element is outside of the element domain (Fig. 6.13c).

Fig. 6.14 and Fig. 6.15 are showing the displacement over time response in the center at $X = L/2$ and at the end of the beam at $X = L$. The finite element solution is computed for 1000 elements, whereas VEM results are obtained with 100 virtual elements. The comparison of the virtual elements VO and VO BI shows that it makes no difference if the integral of the dynamic part in equation (4.55) is evaluated approximately on the centroid of the element or exactly on the boundary using the moments of area. Furthermore, it can be seen that the displacements in the center of the beam are slightly higher for VEM than the results obtained with FEM. However the period fits very well compared with results obtained with FEM. In general the virtual element results are in a good agreement with the compared finite element results. Furthermore the elements VEM Q2S and VEM Q2S Stab are reproducing nearly the same response. Thus almost identical results can be reproduced with a non stabilized mass matrix.

The comparison of the different meshes shows, that the C-mesh yields a higher deflection, compared to the other results, see Fig. 6.15. Nevertheless qualitatively the shape of the displacement over time response fits very well the finite element FEM Q2 results and the virtual element VEM Q2S results. Again, the evaluation of the integral at the centroid of the element compared to computing the integral at the boundary exactly using the moments of area does not affect the overall results.

6.2.4 2D Cook's membrane problem



(a) VEM voronoi Mesh.

(b) Boundary value problem.

(c) VEM Q2S Mesh.

Figure 6.16 – 2D Cook's membrane problem.

In this example, the Cook's membrane problem in 2D is investigated. Here as well, the virtual element performance will be compared with the finite element results. The geometrical setup and boundary conditions can be taken from Fig. 6.16b, where $H_1 = 44$ mm, $H_2 = 16$ mm and $L = 48$ mm. In this test a force driven scenario is applied at the right edge as a line load as depicted in Fig. 6.16b. The force is applied as shown in Fig. 6.12b with $P_{max} = 10000 \frac{\text{kN}}{\text{mm}}$. The VEM VO mesh and regular VEM Q2S mesh are also plotted in Fig. 6.16a and Fig. 6.16c, respectively. The material properties are provided in table 6.1. The contour plots of the von Mises stress distribution for different element formulations at the time $t = 0.035$ ms are shown in Fig. 6.17. Both elements VEM Q2S and VEM Q2S Stab, which use the stabilized and non stabilized mass matrix, result in nearly the same von Mises stress distribution. The nonlinear behavior is clearly observed in the deformation process due to the dynamic effects at finite strains. Fig. 6.18 shows a mesh refinement study with the element division of 2^N for $N = 1, 2, 3, 4$. For $N = 3$ and higher the solution converges. A comparison with FEM depicts that the results are in a very good agreement.

This study shows again, that the evaluation of the integral of the dynamic part in equation (4.55) at the element centroid is absolutely sufficient to compute the mass matrix and that an element with a rank deficient mass matrix reproduces almost identical responses.

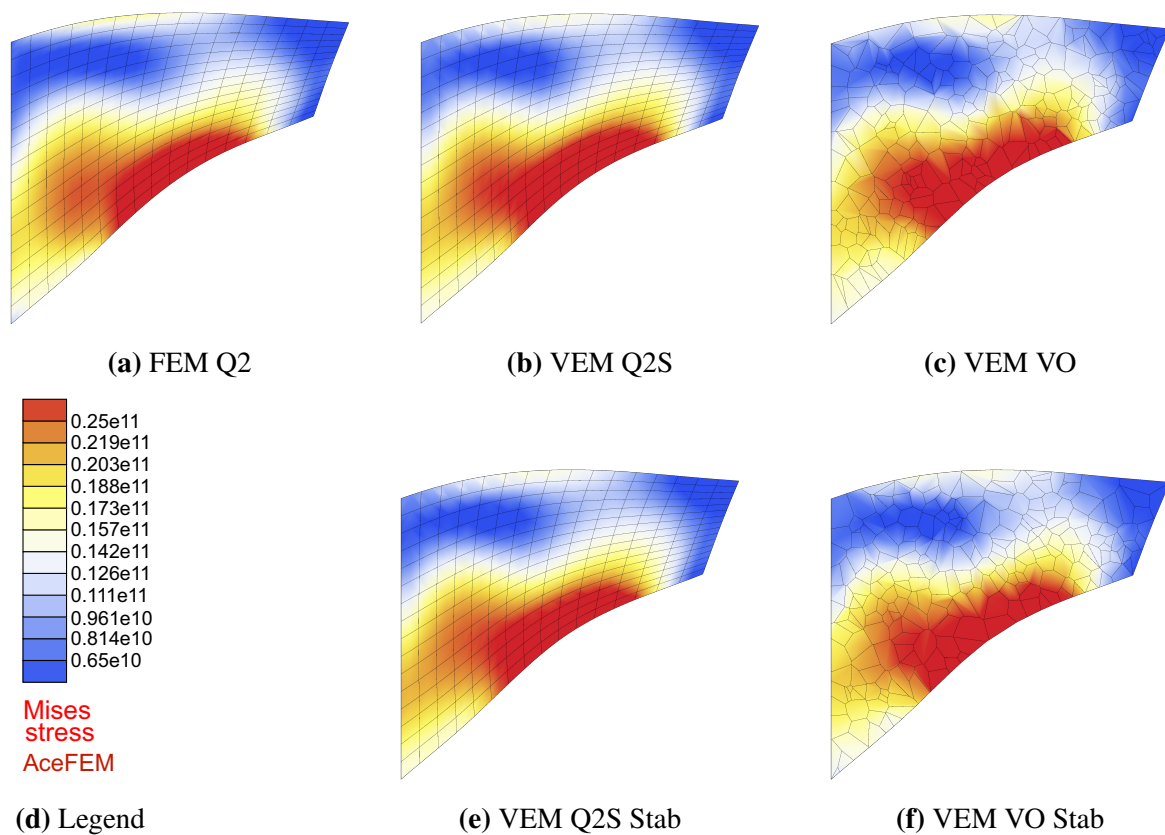


Figure 6.17 – 2D Cook’s membrane problem - Von Mises stress distribution at time $t = 0.035$ ms for different elements at same scale.

6.2.5 Wave propagation in a bar

The previously introduced 2D model of a bar is here extended to the third dimension. The length of the bar is set to $L = 30$ mm and the height is equal to the width with $H = B = 5$ mm. An initial velocity of $v_{0,X} = 20 \frac{\text{m}}{\text{s}}$ is applied to all nodes in longitudinal direction. The material parameters can be taken from table 6.1 and the time increment is set to $\Delta t = 0.01 \mu\text{m}$. The virtual element results are obtained using 400 elements, were the finite element results were obtained with 4320 elements. In this example the virtual elements VEM H2S, VEM H2S Stab, VEM H2S-I and VEM H2S-II are compared with the finite element FEM H1 and the analytical solution which was obtained for the 1D case in equation (6.2). As already introduced before, the variable β^{dyn} indicates how the dynamic part is going to be evaluated. For $\beta^{dyn} = 0$, the dynamic part is calculated using only the projection part. Whereas for $\beta^{dyn} = 1$ the computation of the dynamic part is carried out using the stabilization part. Fig. 6.19 depicts the displacement over time response in longitudinal direction at $X = L$ and $X = L/2$. The computation of the dynamic part using VEM H2S-I and VEM H2S-II results in a very similar response. Further the computation using the projected part and evaluating the integral of the dynamic part in equation (4.55) at the element centroid (i.e. VEM H2S) produces nearly the same results as the finite element H1 and the analytical solution. However, looking at Fig. 6.19c, it can be seen that for high

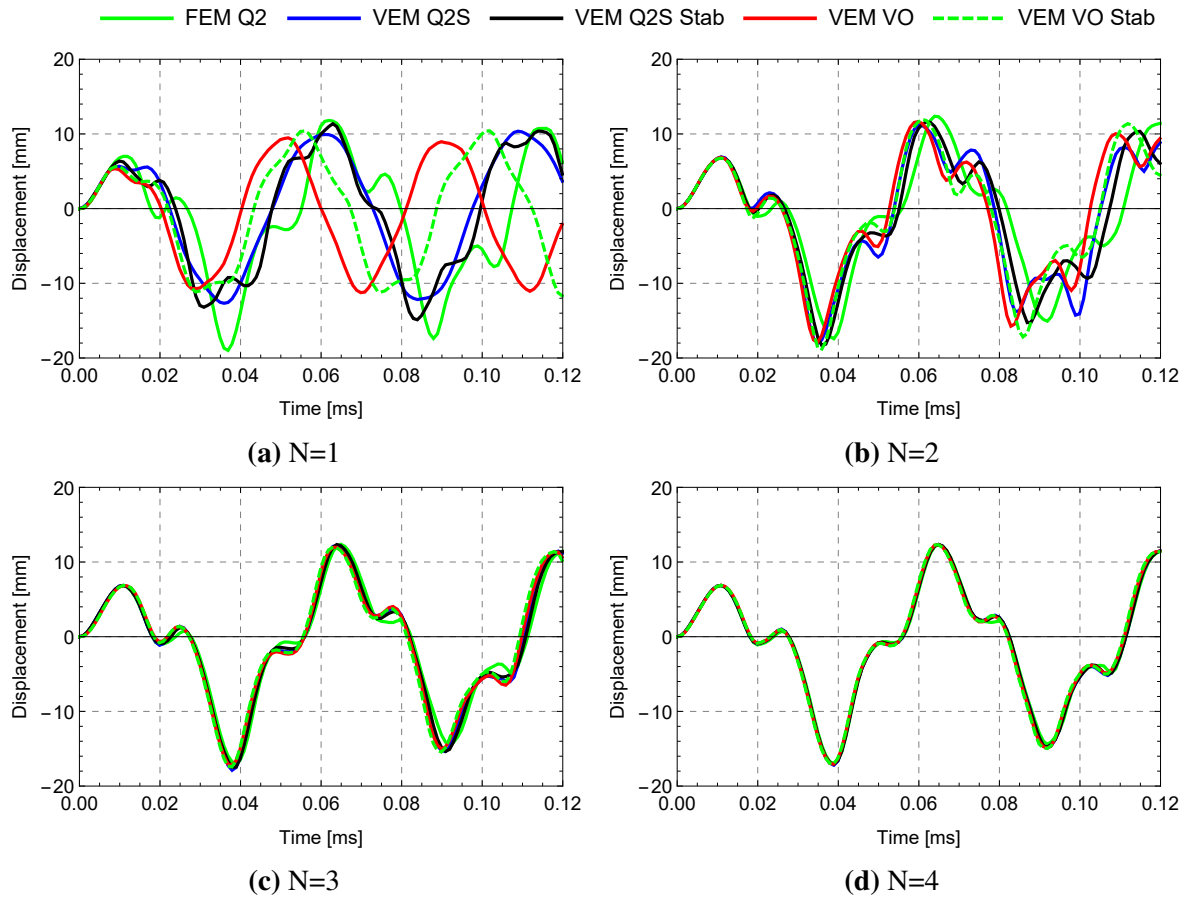


Figure 6.18 – 2D Cook's membrane problem - Displacement over time response at the tip with element division 2^N , where N increases from (a) to (d).

oscillations, the results are not identical with the analytical results. Nevertheless, an highly refined mesh would lead to similar results.

6.2.6 Transversal vibration of a thick beam

In this benchmark test a 3D cantilever beam is investigated. The geometric setup and the loading conditions of the specimen are depicted in Fig. 6.20. Here a line load is applied along the upper edge at the end of the beam with $P_{max} = 6 \frac{\text{kN}}{\text{mm}}$. The temporal course of the force is again given by a half sine, as shown in Fig. 6.12b. In this example, the same material parameters as in the previous examples are used, see table 6.1. Furthermore, similar to the 2D case, the beam length is set to $L = 30 \text{ mm}$ with equal height and width as $H = B = 5 \text{ mm}$. The virtual elements VEM H1, VEM H2S and VEM VO with non-stabilized mass matrix and VEM H1 Stab, VEM H2S Stab and VEM VO Stab with stabilized mass matrix are compared with the finite elements FEM H1 and FEM H2. For this purpose a mesh refinement is employed from 8, 32, 128 to 1024 elements ($N = 1, 2, 3, 4$). The FEM H2 solution is computed with 3200 elements and can be seen as a reference solution. The maximum deformation state is sketched in Fig. 6.21b, representing the deflection w . Here

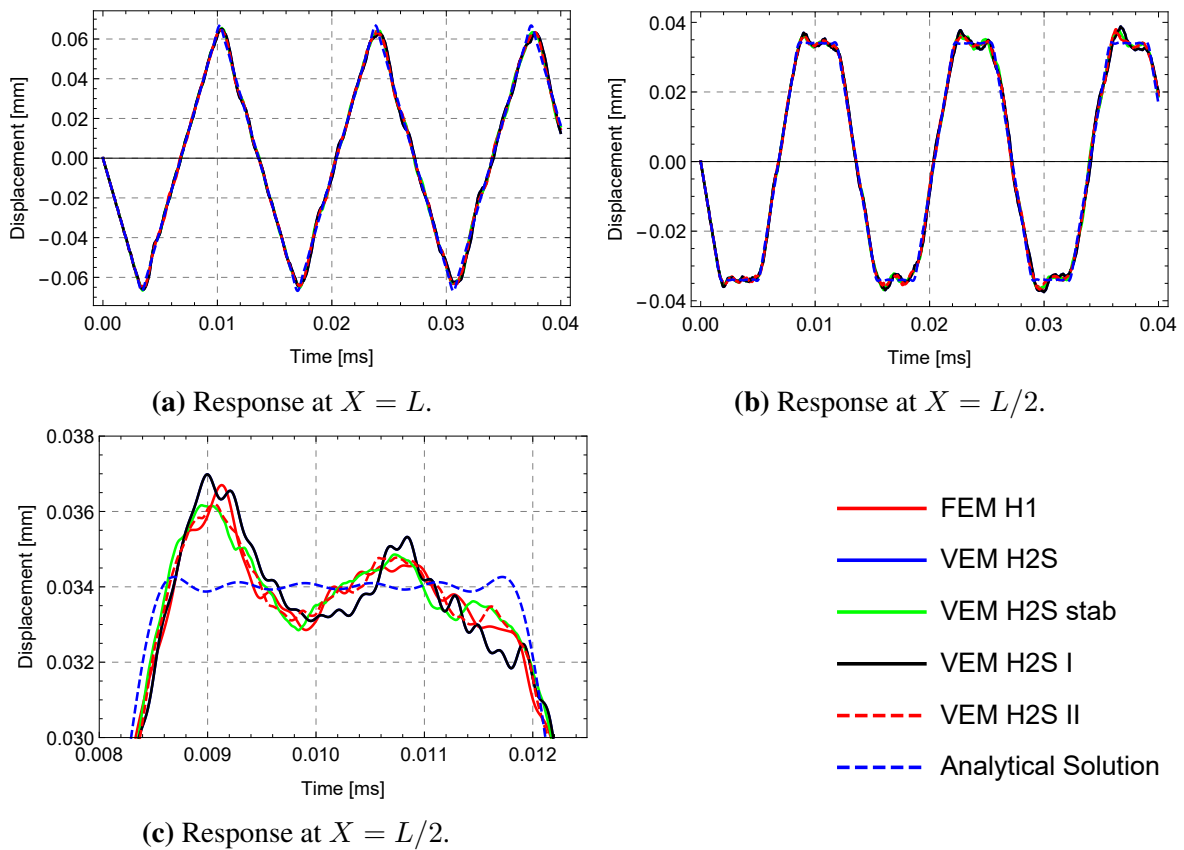


Figure 6.19 – Wave propagation in a bar - Displacement over time response with initial velocity of $v_{0,x} = 20 \frac{\text{m}}{\text{s}}$.

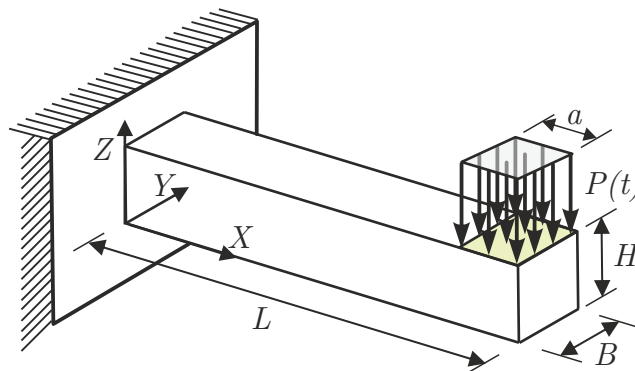
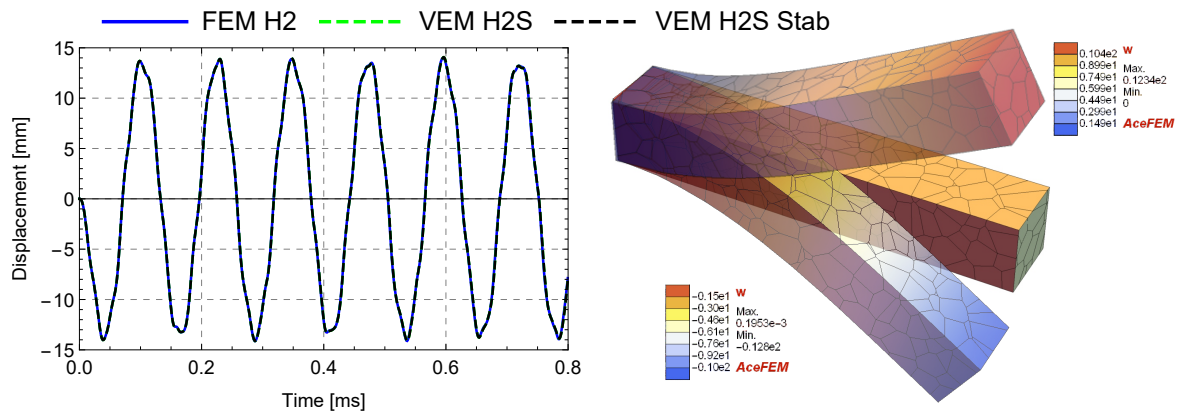


Figure 6.20 – Transversal vibration of a thick beam - Boundary value problem.

the nonlinear behavior is clearly observed due to the dynamic effects at finite strains. Fig. 6.23 illustrates the displacement over time response at $X = L$ for the mesh refinement study. This response is plotted for the center of the cross section. It can be observed that both, VEM and FEM results are converging to the reference solution for increasing number of elements.

However, there is a shift with increasing time, this is due to the less accuracy of VEM/FEM H1 element compared with the FEM H2 with quadratic ansatz function.



(a) Displacement over time response at $X = L$. (b) Undeformed and maximal deformed mesh.

Figure 6.21 – Transversal vibration of a thick beam.

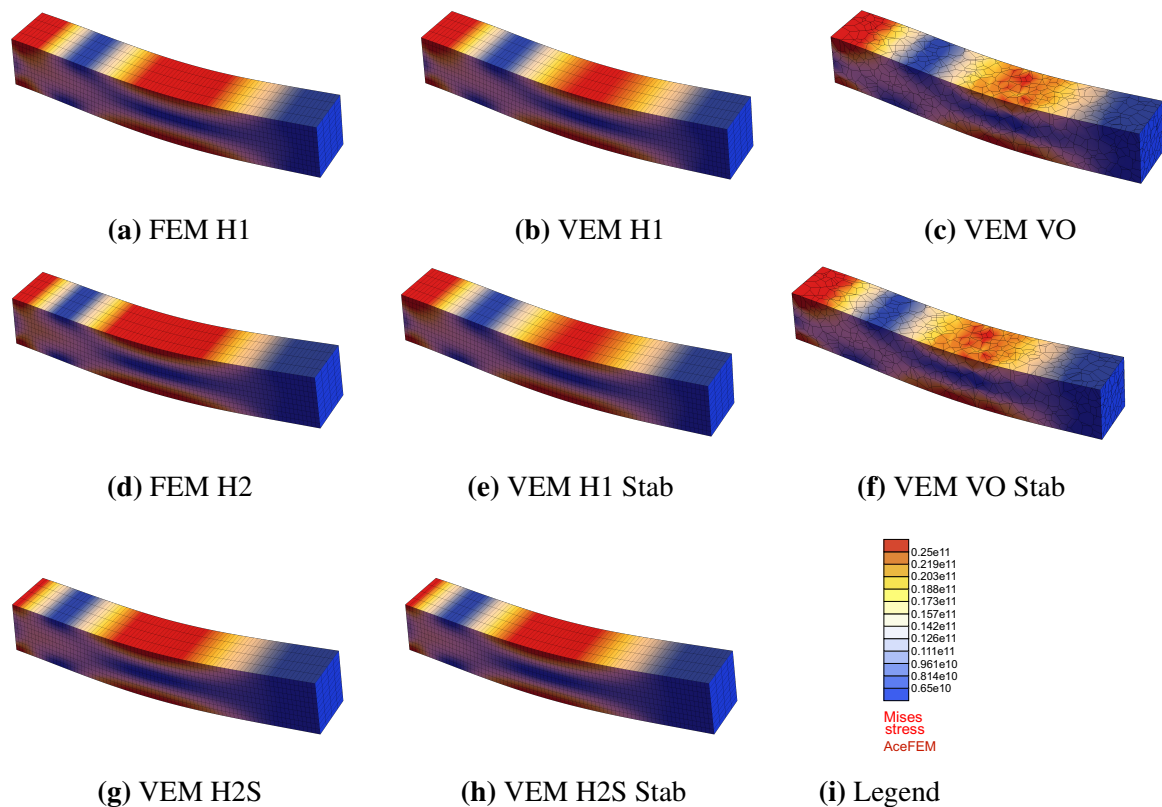


Figure 6.22 – Transversal vibration of a thick beam - Von Mises stress distribution at time $t = 0.1$ ms with different element types.

Additionally, the virtual element VEM H2S is employed and the result obtained with 256 elements is shown in Fig. 6.21a and compared with the reference solution (FEM H2 with

3200 elements). It is interesting to note that despite the use of linear ansatz functions VEM H2S produces nearly the same results as the reference solution. This is due to the fact that the stabilization uses the bending modes. In conclusion, the presented formulation depicts very good results also in the 3D case. This test also confirms that evaluating the integral of the dynamic part in equation (4.55) for the computation of the mass matrix only at the centroid of the polygon/polyhedra is absolutely enough to get satisfying results. Furthermore, the virtual elements with stabilized and non-stabilized mass matrix lead to similar results. This again shows, that a rank deficient mass matrix can also be employed to use this virtual elements for elasto-dynamic problems. However, for higher frequencies, further investigations need to be done. Since the resulting stresses play an important role in engineering applications, Fig. 6.22 shows the von Mises stress distribution at time $t = 0.1$ ms. The distribution of the von Mises stress shows a good agreement between all elements. Due to the inhomogeneous distribution of the voronoi elements VEM VO and VEM VO Stab, the stresses are slightly lower but show a qualitatively similar distribution, compared to all other virtual and finite elements.

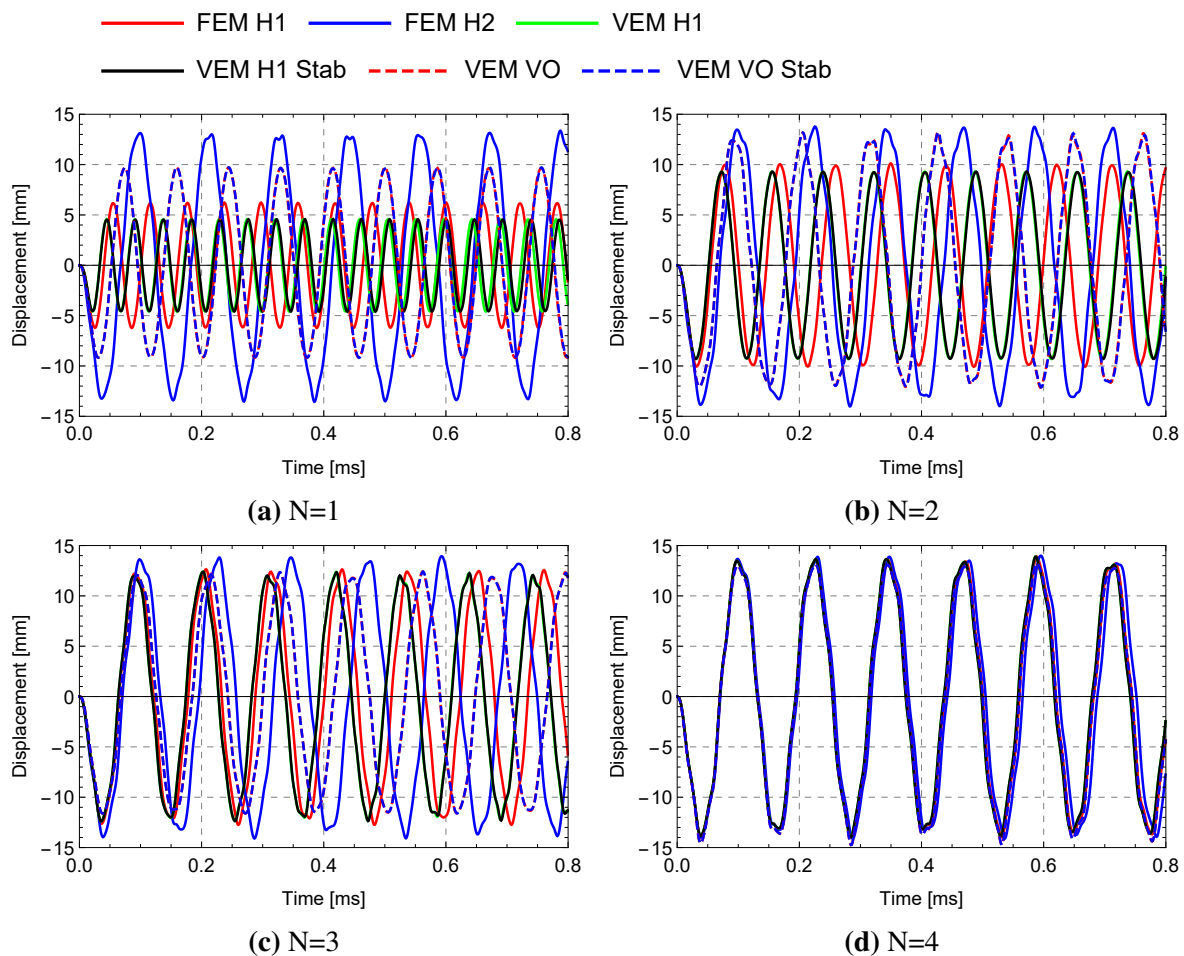


Figure 6.23 – Transversal vibration of a thick beam - Displacement over time response with element division 2^N , where N increases from (a) to (d).

6.2.7 Vibration of a thick plate

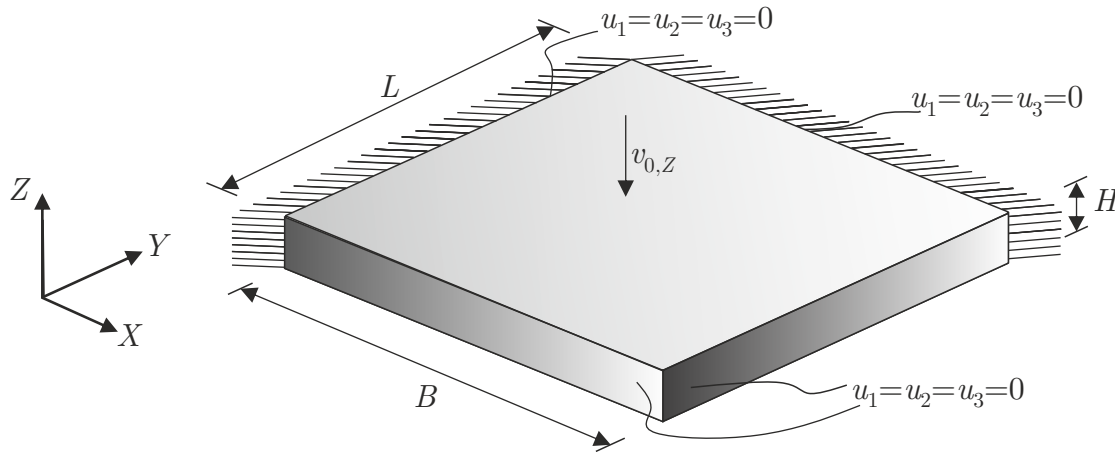


Figure 6.24 – Vibration of a thick plate - Boundary value problem.

The last example of this section is related to the vibration of a thick plate which is discretized using three-dimensional elements. The plate has a length $L = 30$ mm, a thickness $H = 5$ mm and a width $B = 30$ mm as shown in Fig. 6.24. The material parameters are the same as in the previous examples, see table 6.1. The initial velocity of all nodes is set to $v_{0,Z} = 200 \frac{\text{m}}{\text{s}}$, see Fig. 6.24. Fig. 6.26 is showing the evolution of the displacement in the Z -direction for different deformation states using the VEM VO element. Herein a nonlinear response undergoing large deformation is observed due to the elasto-dynamic behavior. In Fig. 6.25 the vertical displacement over time response is plotted at the center of the plate at the thickness $Z = H/2$. A good match between the virtual element results and the finite element results is observed. Here, in addition to regular shaped elements, voronoi shaped elements which have an arbitrary number of nodes and element shapes are used. The computation is performed with 1024 virtual elements of type H1/H1 Stab, H2S/H2S Stab, VO/VO Stab and the finite elements H1 and H2. The reference solutions is obtained with 6400 FEM H2 elements. Again one can observe that the computation of the mass matrix using only the projection part and evaluating the integral of the dynamic part in equation (4.55) at the centroid of the element yields sufficiently accurate results. Further, as already observed in previous examples, the virtual elements with stabilized and non-stabilized mass matrix result in similar responses.

6.2.8 Summary and conclusions

In this section, numerical examples for an efficient low order virtual element formulation for nonlinear elasto-dynamics was presented. The presented contribution does not consider the effect of damping, which can be included in future works. However, it could also be included as numerical damping in a modified Newmark-method, see WOOD ET AL. (1981). A formulation that derives single tangent matrix of dynamics problem was derived. The Newmark time discretization was performed on the local element level. Thus the only unknowns of our problem are nodal displacements whereas the mass matrix is not explicitly required

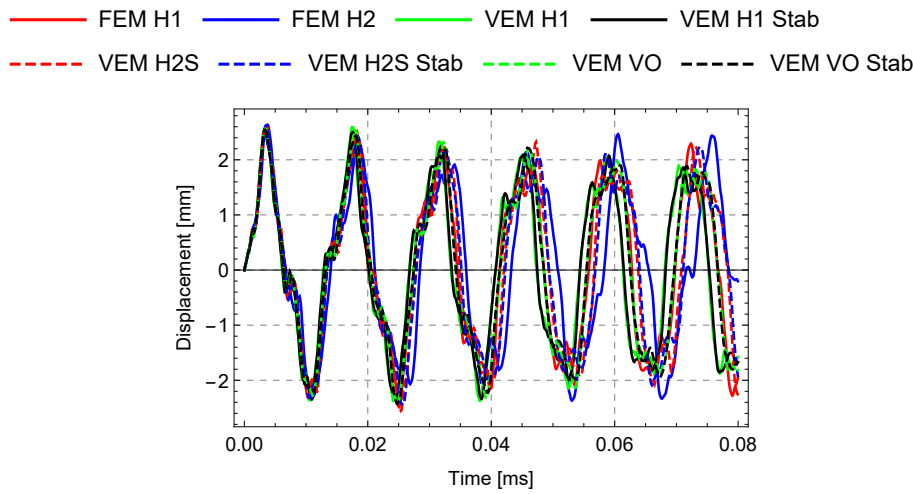


Figure 6.25 – Vibration of a thick plate - Vertical displacement over time response at the center of the plate.

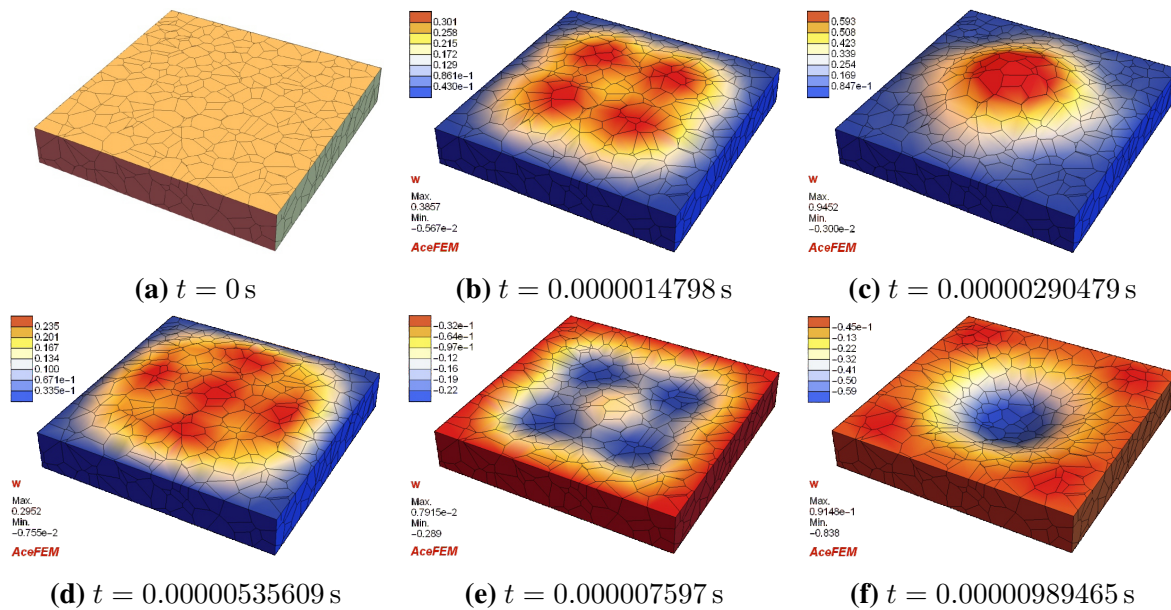


Figure 6.26 – Vibration of a thick plate - Evolution of the displacement in the Z -direction with different deformation states.

for solving simulations. However, the mass matrix can simply be exported, for eigenvalue analysis if required. Further solving the elasto-dynamics problem, employing the Newmark time integration on a global level will lead to similar results. Various schemes to integrate the dynamic part were shown, with and without stabilization. It was shown that the dynamic part does not need to be stabilized for the correctness and convergence of the procedure, unless eigenvalue analysis is needed. The virtual element results show a very good match with finite elements and analytical results for boundary and initial value problems. Arbitrary shaped elements with a various number of nodes could be used successfully for the simula-

tions.

It shows that within this framework, the stabilization of the mass matrix is not needed. This is valid only for problems, where the equations are not reaction dominated, see BEIRÃO DA VEIGA ET AL. (2014) and AHMAD ET AL. (2013). To compute the integral of the dynamic part in equation (4.55), the argument can be evaluated at the element centroid. This is sufficiently accurate as shown in the examples. Hence, there is no need to perform any sub-triangulation of the element or use the moment of areas in equation (4.63) for the computation of the mass matrix.

6.3 Elasto-plasto dynamics

In this section, the elasto-dynamic formulation is coupled with plastic material behavior. The proposed mixed virtual element formulation will be investigated. For comparison purposes, results of the standard finite element method (FEM) are also included. The material parameters used in this chapter are the same for all examples and are provided in table 6.3, unless it is otherwise specified. The potential used in this examples is based on a Hu-Washizu principle which was introduced in section 4.5.4 for the consistency part and a pure displacement formulation for the stabilization part leading to:

$$\begin{aligned} \Pi(\mathbf{u}_h, \mathbf{u}_\pi, \mathbf{h}_E, p_\pi, \Theta_\pi) = & (1 - \beta^{stat}) \Pi_p^{stat, HW}(\mathbf{u}_\pi, \Theta_\pi, p_\pi, \mathbf{h}_E) \\ & + \beta^{stat} \Pi_p^{stat}(\mathbf{u}_h, \mathbf{h}_E) + (1 - \beta^{dyn}) \Pi_p^{dyn}(\mathbf{u}_\pi) + \beta^{dyn} \Pi_p^{dyn}(\mathbf{u}_h). \end{aligned} \quad (6.4)$$

The following mesh types for first order virtual element discretizations are used:

- VEM H1: A regular shaped 3D virtual element with 8 nodes and linear ansatz. Pure displacement formulation, based on equation (4.68).
- VEM H1JP: A regular shaped 3D virtual element with 8 nodes. This element is using a Hu-Washizu formulation with a linear ansatz for the displacement, constant pressure p and constant dilatation Θ as additional degrees of freedom, see equation (6.4).
- VEM VO: A 3D voronoi shaped virtual element with arbitrary number of nodes and linear ansatz. Pure displacement formulation, based on equation (4.68).

Table 6.3 – Material parameters used for the numerical examples

No.	Parameter	Label	Value	Unit
1	Elastic modulus	E	210	kN/mm ²
2	Poisson ratio	ν	{0.3, 0.499999}	–
3	Density	ρ	0.0027	g/mm ³
4	yield stress	Y_0	0.45	kN/mm ²
5	infinite yield stress	Y_∞	1.165	kN/mm ²
6	hardening coefficient	H	0.13	kN/mm ²
7	saturation exponent	δ	16.93	–

- VEM VOJP: A 3D voronoi shaped virtual element with arbitrary number of nodes. This element is using a Hu-Washizu formulation with a linear ansatz for the displacement, constant pressure p and constant dilatation Θ as additional degrees of freedom, see equation (6.4).

For a representative comparison, the following finite element formulations are selected:

- FEM H1: A regular shaped 3D finite element with 8 nodes and linear ansatz based on a pure displacement formulation.
- FEM H1JP: A regular shaped 3D finite element with 8 nodes. This element is using a Hu-Washizu formulation with a linear ansatz for the displacement, constant pressure p and constant dilatation Θ as additional degrees of freedom.
- FEM H2: A regular shaped 3D finite element with 27 nodes and quadratic ansatz based on a pure displacement formulation.

The stabilization parameter of the static part β^{stat} is computed in all the simulation with equation (4.100), unless it is otherwise specified. For the dynamic part the mass matrix is computed according to equation (4.58) without any stabilization. Therefore, equations (4.86) and (4.93) simplify to:

$$\mathbf{R}_E = (1 - \beta^{stat}) \frac{\partial \Pi_p^{stat, HW}(\mathbf{u}_\pi, \Theta_\pi, p_\pi, \mathbf{h}_E)}{\partial \mathbf{u}_E} + \left. \frac{\partial \Pi_p^{dyn}(\mathbf{u}_\pi)}{\partial \mathbf{u}_E} \right|_{\ddot{\mathbf{u}}_E = const.} + \beta^{stat} \frac{\partial \Pi_p^{stat}(\mathbf{u}_h, \mathbf{h}_E)}{\partial \mathbf{u}_E} \quad (6.5)$$

$$\mathbf{K}_E = (1 - \beta^{stat}) \mathbf{K}_{\pi, E}^{stat} + \mathbf{K}_{\pi, E}^{dyn} + \beta^{stat} \mathbf{K}_{h, E}^{stat} \quad (6.6)$$

6.3.1 Necking problem

In the first numerical example the proposed element formulations will be tested and compared for the quasi static case. Necking of cylindrical bar due to prescribed displacements along axial direction is considered, see HUDOBIVNIK ET AL. (2018). This example serves to illustrate the robustness of the mixed virtual element method for localization of plastic strains in the necking area.

The geometrical setup and the boundary conditions of the cylindrical bar with diameter $D = 1$ mm and length $L = 10$ mm is depicted in Fig. 6.27. The material parameters can be taken from table 6.3.

Fig. 6.28 depicts the load-displacement curves for two different mesh discretization. The prescribed displacement is applied at the center of the cross section. It can be observed that all elements give nearly the same force response until the necking appears. Thereafter at about $\bar{u}_z = 0.7$ mm, the FEM H1 element reproduces stiffer results compared to all other elements due to an expected locking behaviour. However, the similar, displacement based virtual elements (i.e. VEM H1 & VEM VO) performs much better but still not as good as the reference FEM H2 element with a quadratic ansatz. In this regard, the newly developed

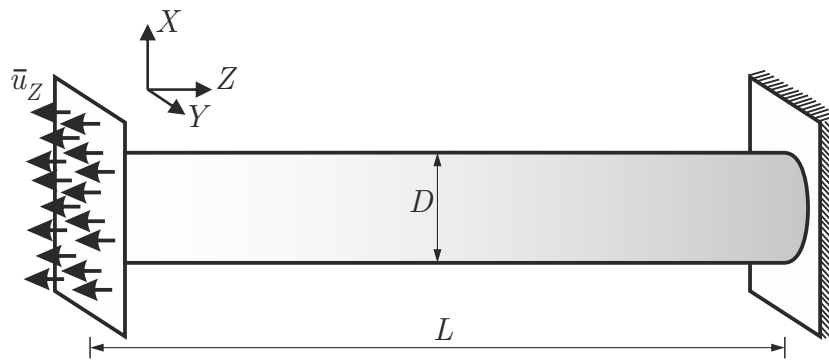


Figure 6.27 – Necking problem - Boundary value problem.

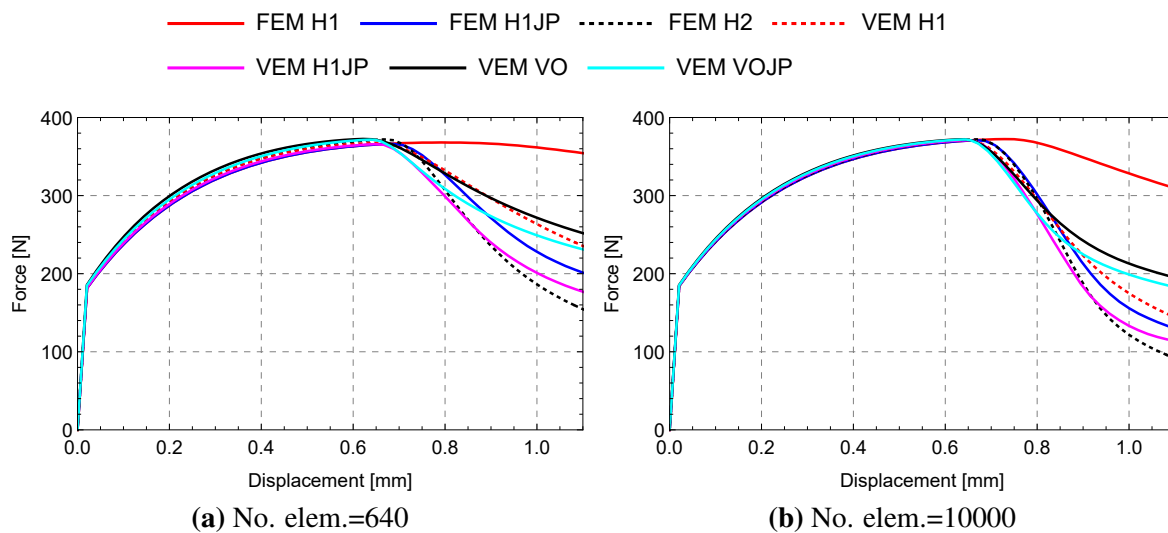


Figure 6.28 – Necking problem - Force-displacement response with two different mesh densities.

mixed VEM formulation produces very good results that compare with the higher order FEM H2 element. The results are even better than the ones using the mixed FEM H1JP element as shown in Fig. 6.28 for both, coarser and finer meshes. The accumulated plastic strain contour plots are given in Fig. 6.29.

6.3.2 3D beam

In the second example a three-dimensional beam is dynamically loaded by a surface load $P(t)$ at the end of the beam, as illustrated in Fig. 6.20. The geometrical setup is the same as in the example, which was introduced in section 6.2.6. The load is applied as a half sine function with the time period $T_0 = 0.0008$ s and an amplitude of $45 \frac{\text{N}}{\text{mm}^2}$. Thereafter, the force is released and the beam is oscillating around its new position of rest. The time increment is

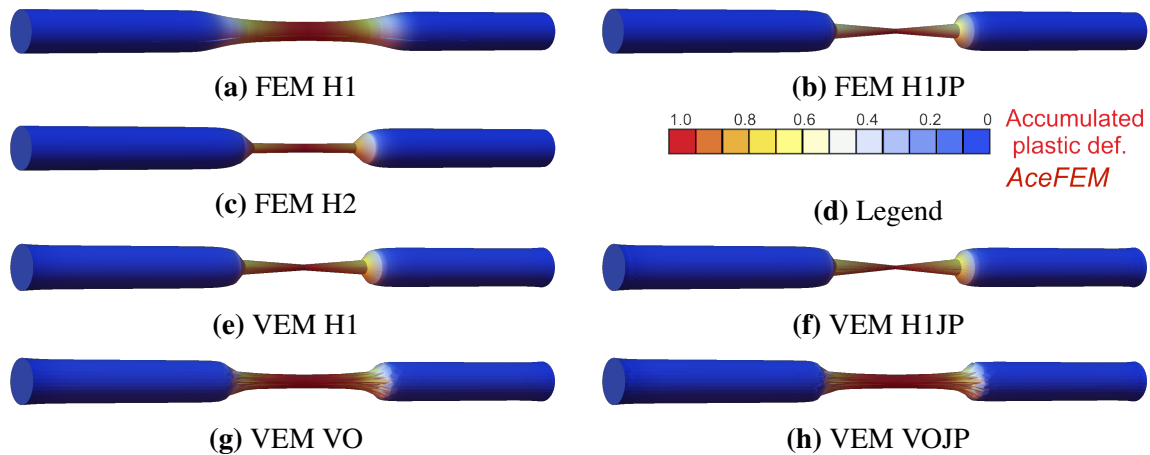


Figure 6.29 – Necking problem - Deformation state with different elements, showing the accumulated plastic strain.

set to $\Delta t = 1\mu s$.

The key goal of this investigation is to demonstrate the performance of the Hu-Washizu formulation for compressible and nearly incompressible material behavior. Different Poisson’s ratios are chosen with $\nu = \{0.3, 0.45, 0.49, 0.499, 0.4999, 0.49999, 0.499999\}$. The material parameters used in the simulations are listed in table 6.3.

Fig. 6.30 shows the time history of the displacement at the tip of the beam. For a compressible material (i.e. $\nu = 0.3$ outlined in Fig. 6.30 a–c), the bending of the beam converges with increasing node numbers to nearly $u = 70$ mm, see Fig. 6.30c).

Nevertheless, the finite and virtual elements, which are based on a pure displacement formulation H1/VO, tend to provide stiffer responses after getting into the plastic regime. Such an observation is in line with the artificial stiffening due to volumetric locking. Since this example is bending dominated bending locking can also appear. By increasing the Poisson’s ratio up to a nearly incompressible material (i.e. $\nu = 0.499999$ outlined in Fig. 6.30 d–f), a strongly stiffer response is observed for the pure displacement elements in comparison with the stable and robust mixed finite and virtual element formulations. Thus the Hu-Washizu based finite and virtual elements produce a much softer response and hence can handle incompressible material behaviour well.

For a representative comparison between all elements, the relative error of the maximum displacement (related to Fig. 6.30) is plotted in Fig. 6.31 for different elements and Poisson ratios. Hereby, the error is computed with respect to an overkill solution, that is obtained from the mixed finite element FEM H1JP using 100000 elements. In Fig. 6.31a (for $\nu = 0.3$), the error is remarkably reduced by increasing the number of element for all types. In this regard, the pure displacement elements H1/VO demonstrate a high error in comparison with mixed FEM and VEM formulations in the case of coarse meshes. When increasing the Poisson’s ratio, the error of the pure displacement elements is further increased, reaching its maximum for $\nu = 0.499999$. The mixed finite and virtual elements stay nearly constant and are not effected by any kind of locking phenomena. This illustrates the importance of using a mixed formulation for virtual element, when it comes to elastic and plastic incompressibility.

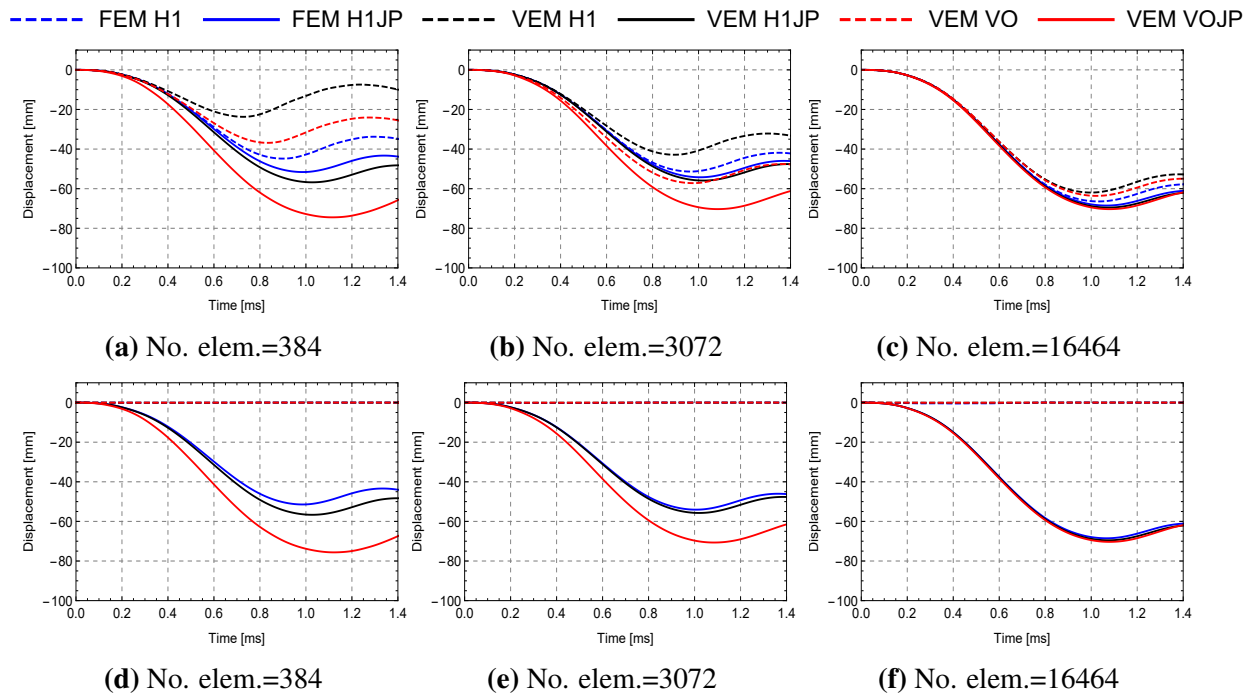


Figure 6.30 – 3D Beam - Displacement over time response for different element types and mesh discretization in (a) to (c) with $\nu=0.3$ and (d) to (f) with $\nu = 0.499999$.

6.3.3 Taylor Anvil test

The next example presents the Taylor-Anvil problem, which is widely used to test the dynamic behavior of metals but it is also a validation test for discretization schemes that simulate finite strains elasto-plasticity undergoing dynamic loadings, see SIMO (1992) and TAYLOR (1948). Within this framework, a rod impacts at high velocity a rigid plate. This is modeled by fixing one side of the rod in longitudinal direction and by prescribing an initial velocity to all other parts of the body, as depicted in Fig. 6.32a.

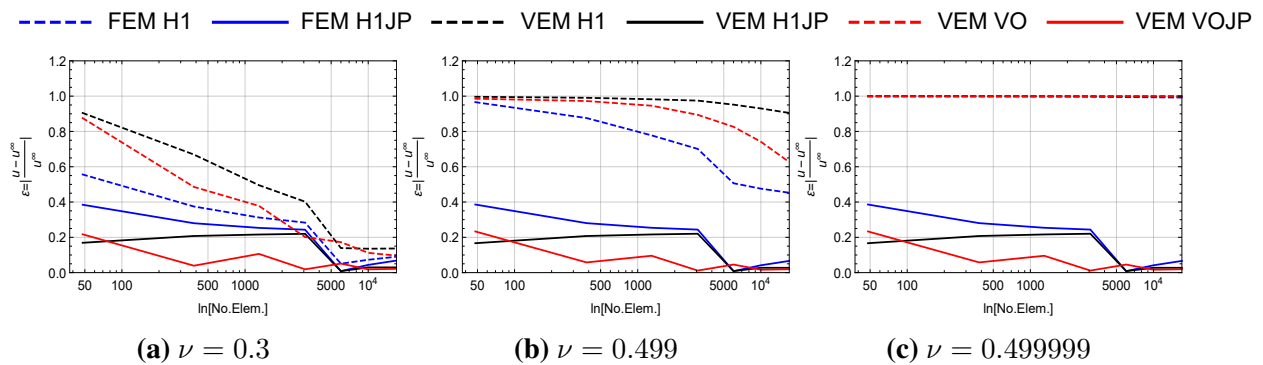


Figure 6.31 – 3D Beam - Error of the maximum displacement over time for different element types and various Poisson's ratios in (a) to (c).

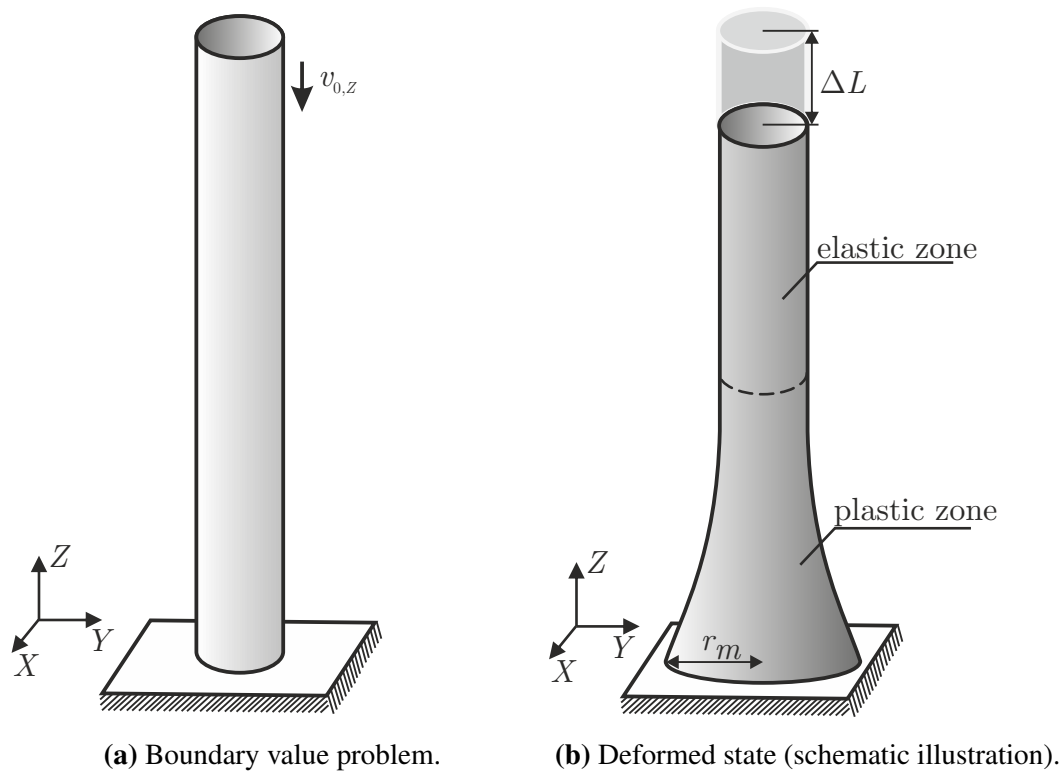


Figure 6.32 – Taylor Anvil test.

Table 6.4 – Material parameters used for the Taylor Anvil test

No.	Parameter	Label	Value	Unit
1	Elastic modulus	E	117	kN/mm^2
2	Poisson ratio	ν	0.35	–
3	Density	ρ	8930	g/mm^3
4	yield stress	Y_0	0.400	kN/mm^2
6	hardening coefficient	H	0.100	kN/mm^2
7	saturation exponent	δ	0	–

The material parameters for the simulations, which are summarized in table 6.4, are taken from the literature, see KAMOULAKOS (1990), ZHU & CESCOTTO (1995), CAMACHO & ORTIZ (1997), LI ET AL. (2010) and KUMAR ET AL. (2019). Hereby, the saturation parameter is set to zero ($\delta = 0$), hence the exponential term in equation (2.59) disappears and the model is reduced to linear hardening. The initial velocity is set to $v_{0,z} = 227 \frac{\text{m}}{\text{s}}$. The time increment for the dynamic simulation is $\Delta t = 0.01 \mu\text{s}$. During the impact a plastic front develops and moves upwards leading to a deformed state as shown in Fig. 6.32b.

The equivalent plastic strain at the final deformation state for all element formulations is depicted in Fig. 6.33 and is obtained with 10000 elements. As expected large plastic deformations are observed at the end of the rod, as well documented in the literature, see TAYLOR (1948), KUMAR ET AL. (2019) and TAYLOR & PAPADOPOULOS (1993). This is due to the

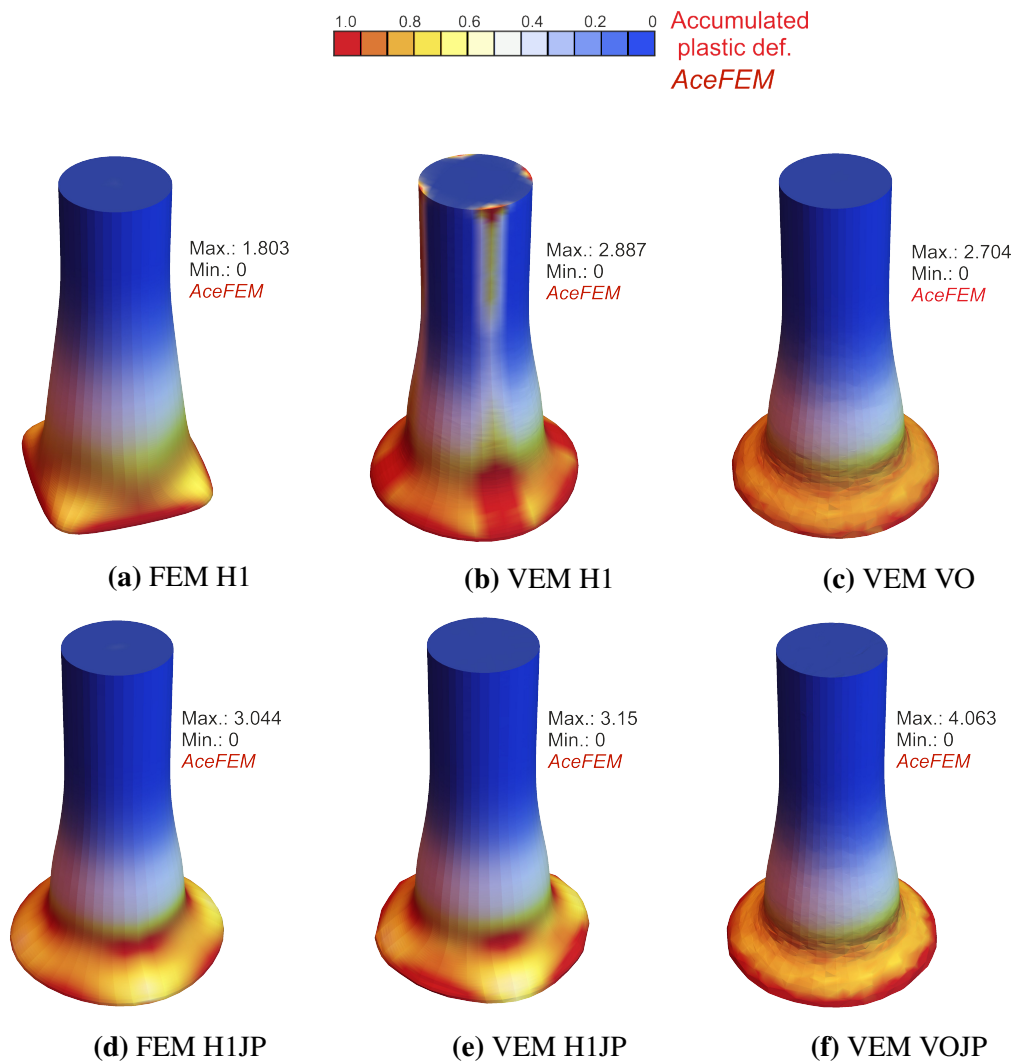


Figure 6.33 – Taylor Anvil test - Deformation state for different elements, showing the accumulated plastic strain.

influence of the kinetic energy resulting in high stresses at the front of the rod where the essential boundary condition is applied. When a certain energy is dissipated, the stresses are not reaching the yield stress anymore. Therefore some elastic energy is still stored in the upper part of the rod as shown in Fig. 6.33. The contour plots show that all elements yield similar results except the stiffer FEM H1 element. Fig. 6.34 shows the length change over time for different element formulations and two mesh discretization. All element types show nearly the same displacement curves over time. Locking effects for this impact test occur only for the FEM H1 discretization. For all formulations a small oscillation with low frequency can be observed which is due to the elastic response at the upper part of the rod.

Fig. 6.35 depicts the development of the mushroom radius at the lower part ($Z = 0$). Good agreement between all element formulations – besides the FEM H1 – is also observed. Again the mixed formulation converges for finite and virtual elements (FEM/VEM H1JP) and re-

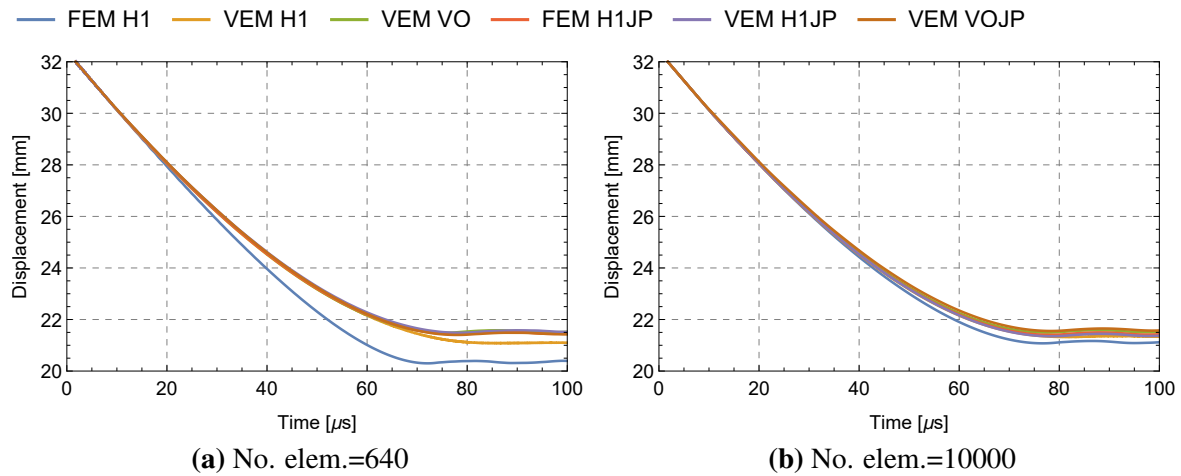


Figure 6.34 – Taylor Anvil test - Length change over time for different mesh densities and element formulations.

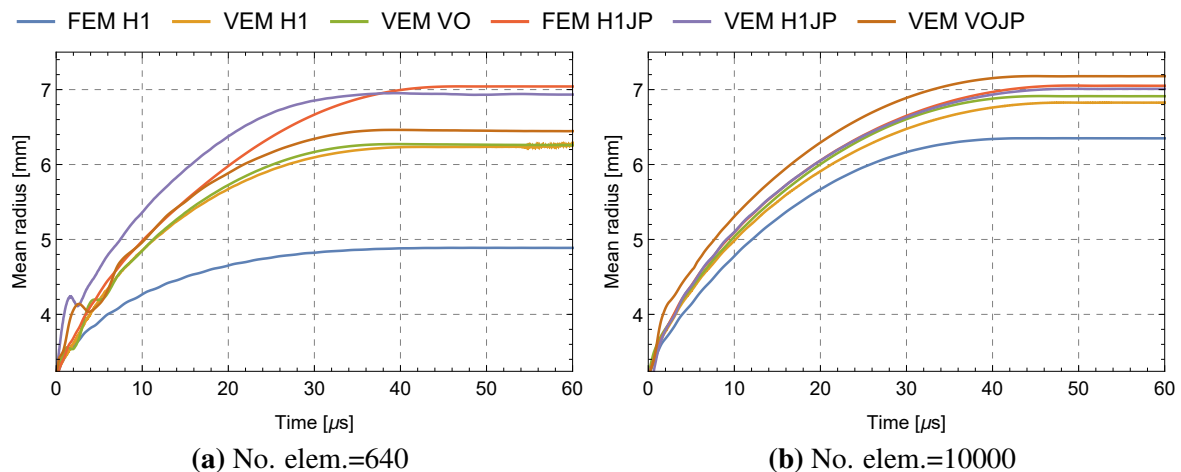


Figure 6.35 – Taylor Anvil test - Evolution of the mushroom radius r_m for different mesh densities and element formulations.

sults in the best coarse mesh accuracy, see Fig. 6.35a. Next, table 6.5 presents the results obtained by different authors with different methods. The results are compared with the values from the current work, depicted in table 6.6. Good agreement is achieved for the proposed mixed virtual element formulation.

6.3.4 Punch problem

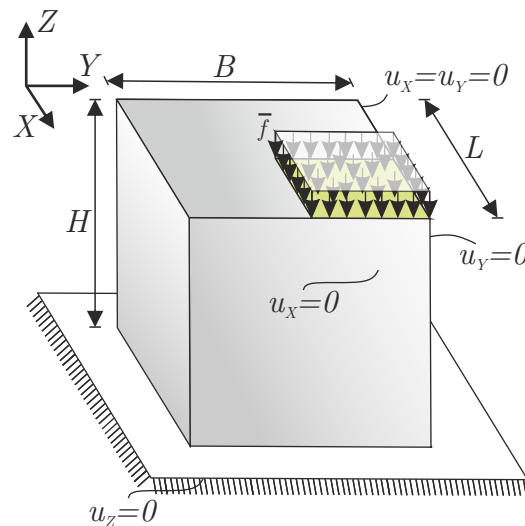
The last example in this section is again concerned with the capability of the proposed mixed VEM formulations to solve dynamic elastic-plastic problems. For this purpose, a punch problem is selected which is subjected to high compression loading. A surface load is ap-

Table 6.5 – Taylor Anvil test - Comparison of different results obtained in the literature.

Source	Method	Max. acc. plastic strain	Final height (mm)	Final mushroom radius (mm)
KAMOULAKOS (1990)	FEM	2.47-3.24	21.47-21.66	7.02-7.12
ZHU & CESCOTTO (1995)	FEM	2.75-3.03	21.26-21.49	6.89-7.18
CAMACHO & ORTIZ (1997)	FEM	2.97-3.25	21.42-21.44	7.21-7.24
LI ET AL. (2010)	OTM	3.0	21.43	6.8
KUMAR ET AL. (2019)	OTM	2.69	21.45	6.84
BELYTSCHKO ET AL. (2000)	EFG	3.33	21.46	7.13
BODE (2021)	PBG	3.35	21.54	7.28

Table 6.6 – Taylor Anvil test - Comparison of results for different element types.

Element	Max. acc. plastic strain	Final height (mm)	Final mushroom radius (mm)
FEM H1	1.803	21.09-21.17	6.34-6.35
VEM H1	2.887	21.32-21.36	6.81-6.83
VEM VO	2.704	21.51-21.59	6.89-6.91
FEM H1JP	3.04	21.41-21.5	7.04-7.05
VEM H1JP	3.15	21.36-21.45	6.99-7.01
VEM VOJP	4.063	21.56-21.65	7.17-7.18

**Figure 6.36** – Punch problem - Boundary value problem.

plied on one quarter of the block with the geometrical properties $H = B = L = 50$ mm. The boundary and loading conditions can be taken from Fig. 6.36. For a comprehensive comparison, a convergence study is performed where the number of elements is set

to $\{64, 512, 1728, 4096, 10648, 21952, 39304\}$. The load is applied in time as a half-sine function with a time period of $T_0 = 0.4$ ms and an amplitude of $2.5 \frac{\text{kN}}{\text{mm}^2}$. Similar to the previous examples, the force is released after a half sine. The material parameters used for the numerical simulations are same as in the previous examples, see table 6.3. The time increment used in this example is $\Delta t = 1 \mu\text{s}$.

Fig. 6.37 illustrates the accumulated plastic strain α at the end of the simulation. As expected the pure displacement formulations H1 of FEM and VEM underestimate the large deformation behavior due to locking phenomena, resulting in low maximum values of α , see Fig. 6.37a and 6.37b. For VEM VO with voronoi shaped element, the locking phenomena is even more significant as depicted in Fig. 6.37c. This non-physical behavior is overcome for both, FEM and VEM elements, by the mixed Hu-Washizu type formulation as shown in Fig. 6.37d-6.37f.

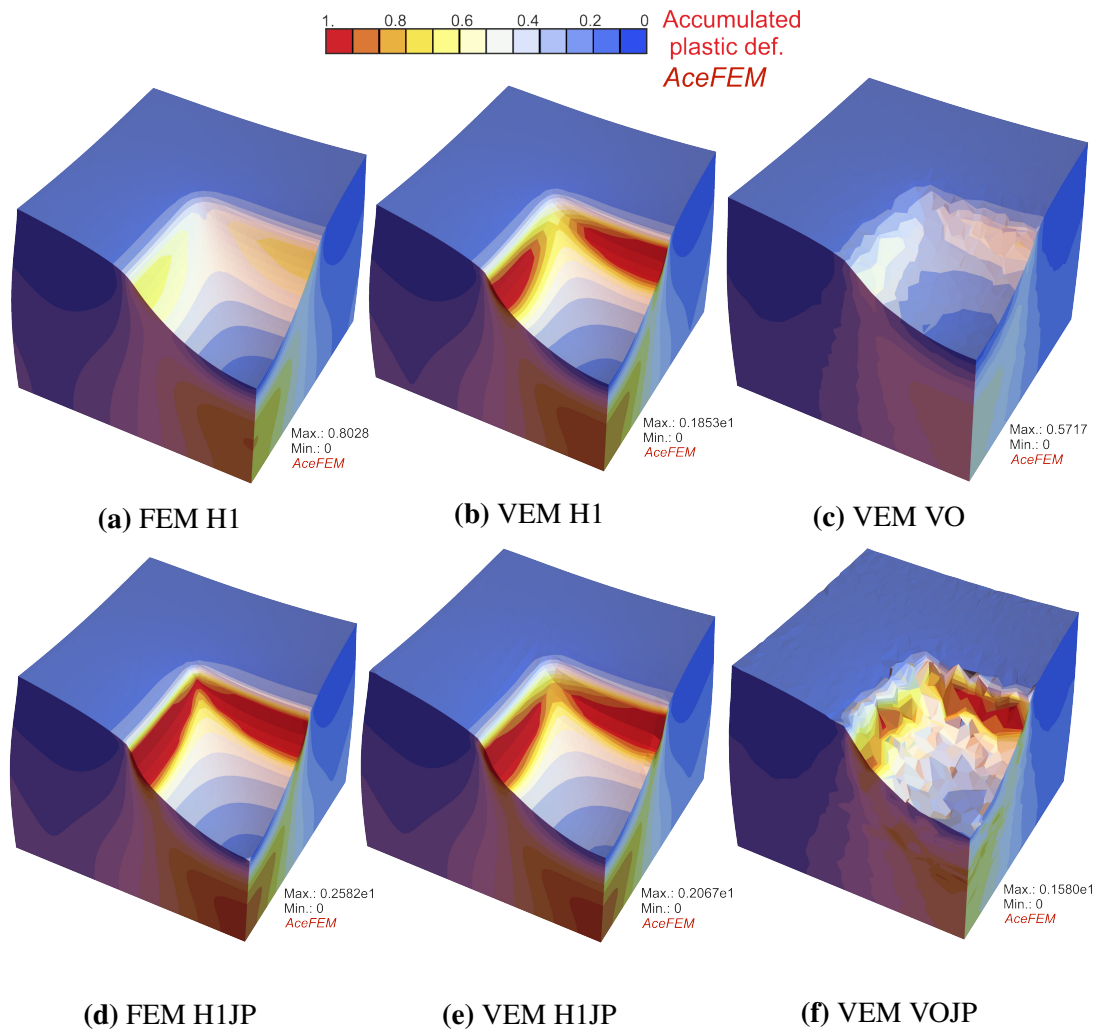


Figure 6.37 – Punch problem - Deformation state for different elements, showing the accumulated plastic strain.

Fig. 6.38a depicts the time history of the displacement at the corner of the block, where the

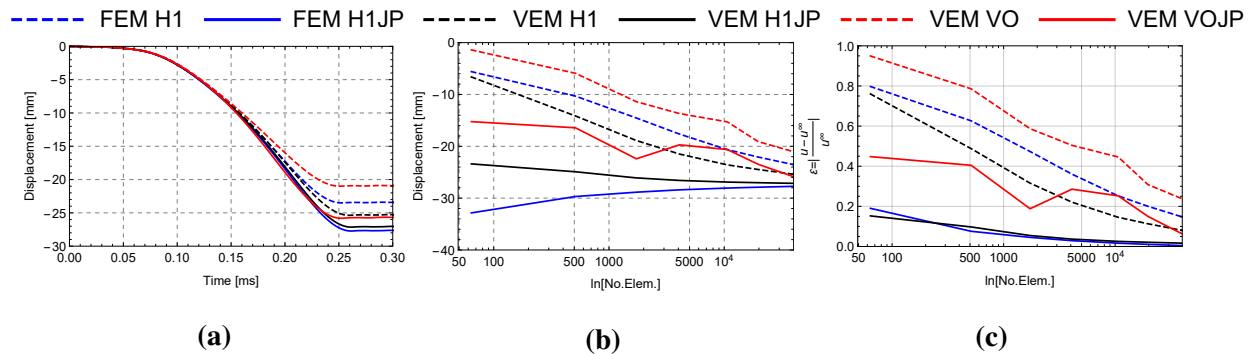


Figure 6.38 – Punch problem - Time history of maximum displacement at the tip in (a), error of the maximum displacement over number of elements in (b) and maximum displacement over number of elements in (c).

maximum displacement appears. The presented curves are obtained with 40000 elements. It can be seen, that the mixed finite element FEM H1JP leads to the largest deformation followed by the mixed virtual element VEM H1JP. Those elements illustrate a much softer response compared with the pure displacement finite and virtual elements which is related to their locking free behavior. The same can be seen in Fig. 6.38b and 6.38c, which is showing the maximum displacement at the corner and its relative error for different numbers of elements. The reference solution for the error analyses is computed with the mixed finite element FEM H1JP, using around 100000 elements.

A closer look reveals, that the mixed finite and virtual elements are providing a much softer response, compared to the pure displacement elements. Especially for coarse mesh, the mixed elements behave softer and thus are not affected by volumetric locking phenomena.

6.3.5 Summary and conclusions

A mixed low order virtual element formulation for three-dimensional dynamic elasto-plasticity was analyzed in this section. The mixed approach is based on a three field Hu-Washizu potential function, which leads to a softer response of the body undergoing large deformations. This yields also for virtual elements a superior coarse grid accuracy in comparison with pure displacement elements. The presented formulation is based on a minimization of a specific pseudo-potential, considering the dynamic behavior of the solid. The treatment of VEM for elasto-plasticity in this contribution is in line with previous works in the literature, see ALDAKHEEL ET AL. (2019) and HUDOBIVNIK ET AL. (2018). The extension towards dynamic problems was performed using a fast and simple computation of the mass matrix which was shown in the previous section.

It has been shown that the mixed formulation for virtual elements, can prevent volumetric locking under elastic and plastic incompressibility conditions, especially for voronoi shaped virtual elements. However, a pure displacement based virtual element formulation has already a softer behavior than compared with pure displacement finite elements. Nevertheless it behaves stiffer than a mixed finite element and thus despite this, a mixed virtual element

formulation is needed.

6.4 Node-to-node contact

Dynamic and plastic material behavior was analyzed in the previous sections. To model impact problems properly, contact needs to be taken in to account additionally. This section deals with three dimensional contact problems. More precisely speaking, the projection algorithm which was introduced in subsection 5.2 is applied to get conforming meshes at the contact interface. Various examples are computed to show the performance of this method.

6.4.1 Contact patch test

In the first example, the three dimensional contact patch test is considered. As illustrated in Fig. 6.39, both bodies \mathcal{B}^1 and \mathcal{B}^2 are fixed in X -direction at $X = 0$ and in Y -direction at $Y = 0$. Body \mathcal{B}^2 is fixed in Z -direction at $Z = 0$. The body \mathcal{B}^1 is loaded at the upper face with the surface load $p_0 = 1 \cdot 10^7 \frac{\text{N}}{\text{m}^2}$. The material parameters are set to $E_1 = E_2 = 4 \cdot 10^8 \frac{\text{N}}{\text{m}^2}$ and $\nu_1 = \nu_2 = 0.3$. Both bodies are discretized using an irregular shaped voronoi mesh which does not match at the contact interface, see the contact pair at the right side of Fig. 6.39.

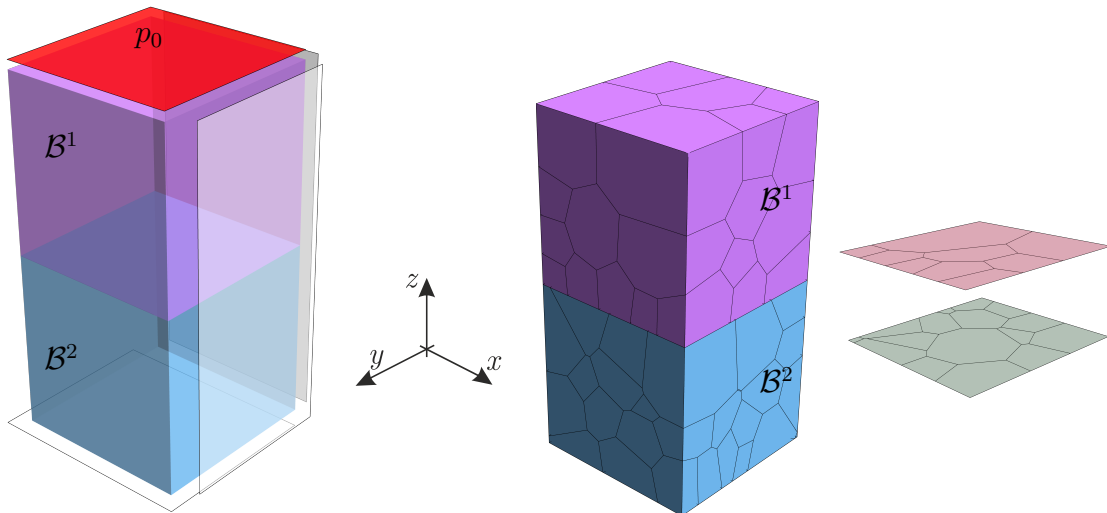


Figure 6.39 – Contact patch test - Boundary value problem with mesh at contact interface.

Fig. 6.40 shows the stress σ_{zz} in the direction of the load. It can be easily seen, that the node insertion scheme leading to a node-to-node discretization reproduces a homogeneous stress state (Fig. 6.40 (a) and (c)). A node-to-surface contact enforcement does not lead to correct contact forces and thus to a non homogeneous stress state in the contact bodies, as can be seen in Fig. 6.40 (b) and (d). This shows the advantage of the node insertion strategy and which is possible when using the virtual element method. However, looking at Fig. 6.40b, the patch test is not fulfilled exactly, since the stresses have some deviations. This is due to non matching triangles and tetrahedrons at the contact interface. To demonstrate

this behaviour, a small study is performed, as depicted in Fig. 6.41 and Fig. 6.42. The two blocks have a non-conforming mesh at the contact interface, consisting of regular shaped hexahedral virtual elements. The upper block is pushed down with a displacement boundary condition at the upper face. As can be seen in Fig. 6.41a, the triangles for the evaluation of equation (4.27) are non-matching at the contact interface and thus leading to deviations in terms of the stresses, see Fig. 6.41c. Using matching triangles as in Fig. 6.42a, the contact patch test is fulfilled exactly, see Fig. 6.42c.¹

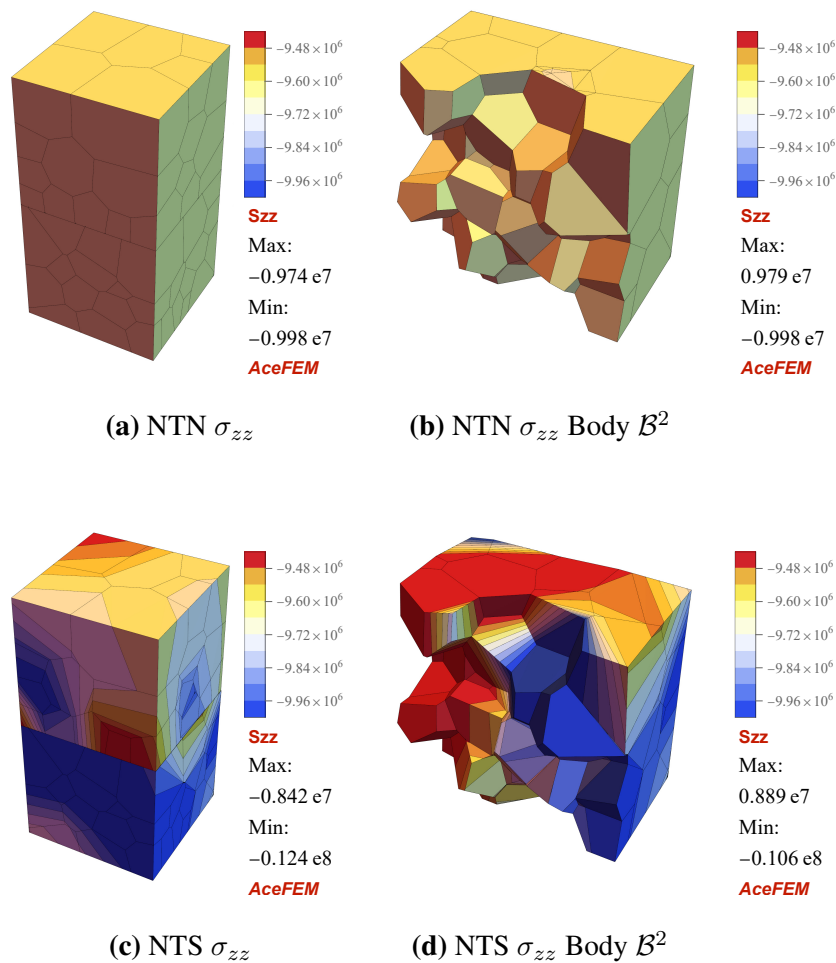


Figure 6.40 – Contact patch test - Deformed state showing the stresses σ_{zz} for node-to-node (NTN) and node-to-surface (NTS) contact.

6.4.2 Hertzian problem

Next, the Hertzian contact of a sphere and a block is analyzed. For this example, voronoi type elements, denoted by VO and regular shaped hexahedral elements, denoted by H1 are

¹Note that, taking care of the triangles and tetrahedrons at the interface is not needed when the integration scheme based on the edges to evaluate equation (4.27) as well as the stabilization based on degrees of freedom is used, as will be shown in section 6.5.

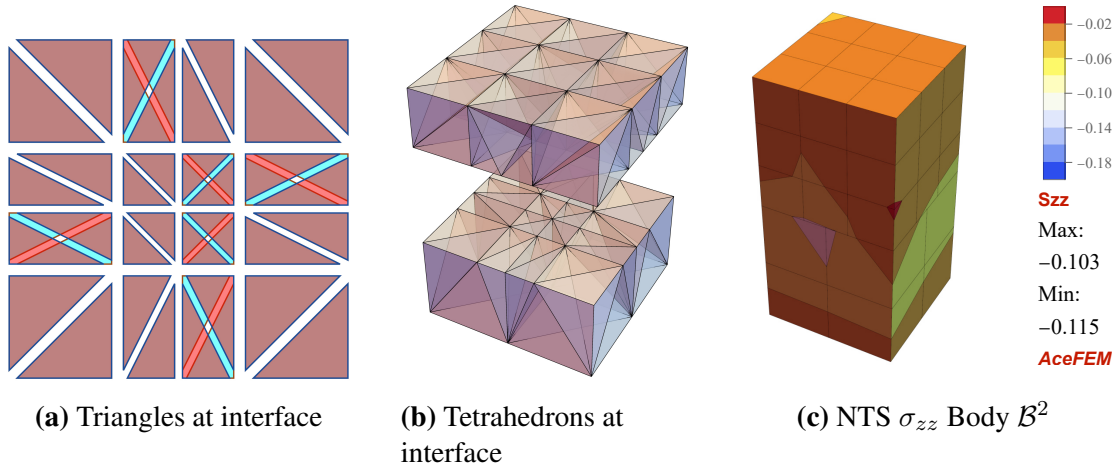


Figure 6.41 – Node-to-node contact with non-matching triangles and tetrahedrons at the contact interface.

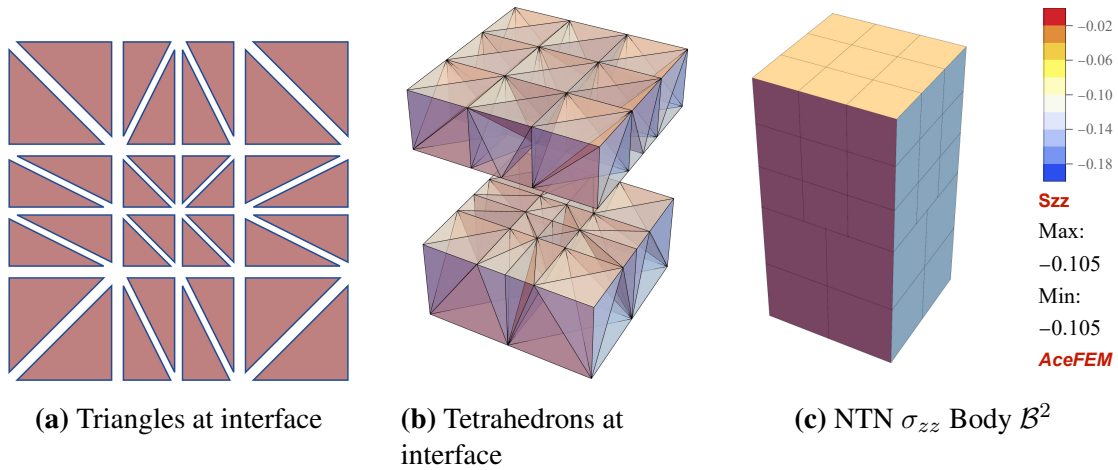


Figure 6.42 – Node-to-node contact with matching triangles and tetrahedrons at the contact interface.

used. For small deformations, the analytical results can be obtained, see POPOV ET AL. (2019). The stress in normal direction can be expressed as a function of the radius r :

$$S_{zz}(r) = \frac{2E^*}{\pi R} \sqrt{a^2 - r^2}, \quad (6.7)$$

where R is the radius of the sphere, a the contact width and E^* the effective modulus, see HERTZ (1882). The contact width a , the effective Young's modulus E^* and the force F follow as:

$$E^* = \left(\frac{1 - \nu_1^2}{E_1} + \frac{1 - \nu_2^2}{E_2} \right)^{-1}, \quad a = \left(\frac{3FR}{4E^*} \right)^{\frac{1}{3}}, \quad F = p\pi R^2 \quad (6.8)$$

In order to avoid high computing times, the discretized model is reduced to a quarter, see Fig. 6.43. Symmetry boundary conditions are used to capture the whole model behavior.

The setup of the numerical model is shown in Fig. 6.43. The sphere is loaded at the upper face by a pressure p_0 . The inner boundaries (faces) are fixed in normal directions. To avoid rigid body motions, the bottom face is additionally fixed in normal direction. Fig. 6.44 depicts the normal stress distribution along the surface. The contact stresses are obtained from the actual stress $\sigma_{zz} = (\boldsymbol{\sigma}\mathbf{n}) \cdot \mathbf{n}$.

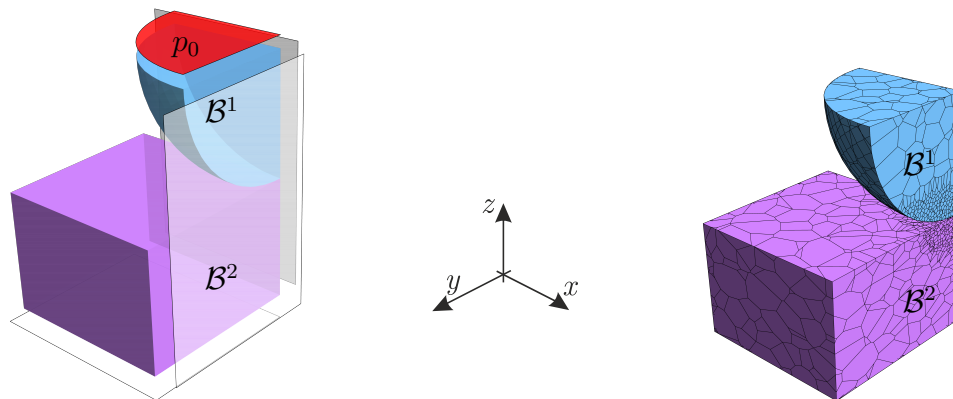


Figure 6.43 – Hertzian contact - Boundary value problem.

The node-to-node contact based on node insertion leads to better results as the node-to-surface formulation. Both solutions are compared to the analytical solution. Oscillations of the stresses are stronger for node-to-surface contact and reduced for the node-to-node contact. For voronoi meshes, this effect is also reduced, but constant stress segments are obtained. This is due to the properties of the virtual element ansatz, which leads to constant stresses within each virtual element. Introducing new nodes per element results in the same stresses on this nodes, as computed for existing nodes in the initial mesh. Clearly a refinement of the mesh is needed to obtain more accurate results.

6.4.3 Rotating blocks

The last example deals with two elastic blocks which are placed on top of each other. While the lower one is fixed at the bottom, the upper one is first pushed down with a prescribed displacement. When the final prescribed displacement is reached, the upper block starts to rotate around its center axis. This example is chosen to show the smoothness of the reaction forces. The material parameters for both blocks are identical and set to $E = 1.0$ and $\nu = 0.3$. In the first step, the upper block is loaded with a prescribed displacement $\bar{u}_z = -0.1$. The node-to-node contact enforcement results in a smooth distribution of the reaction forces, see Fig. 6.47. However, the different stabilization strategies yield slightly different results. This is due to a different behavior in the total stiffness of the bodies. Furthermore, the energy stabilization does not converge for certain rotation angles. A rotation angle close to 90 degrees causes a divergence. This is due to very small edges and faces, which appear as a results of the projection. The DOF stabilization works robust and smooth. The results are shown in Fig. 6.47 for a rotation increment of $\Delta\theta = 2^\circ$. Fig. 6.48 depicts the reaction force related to the rotation for a larger rotation increment of $\Delta\theta = 5^\circ$. This increment

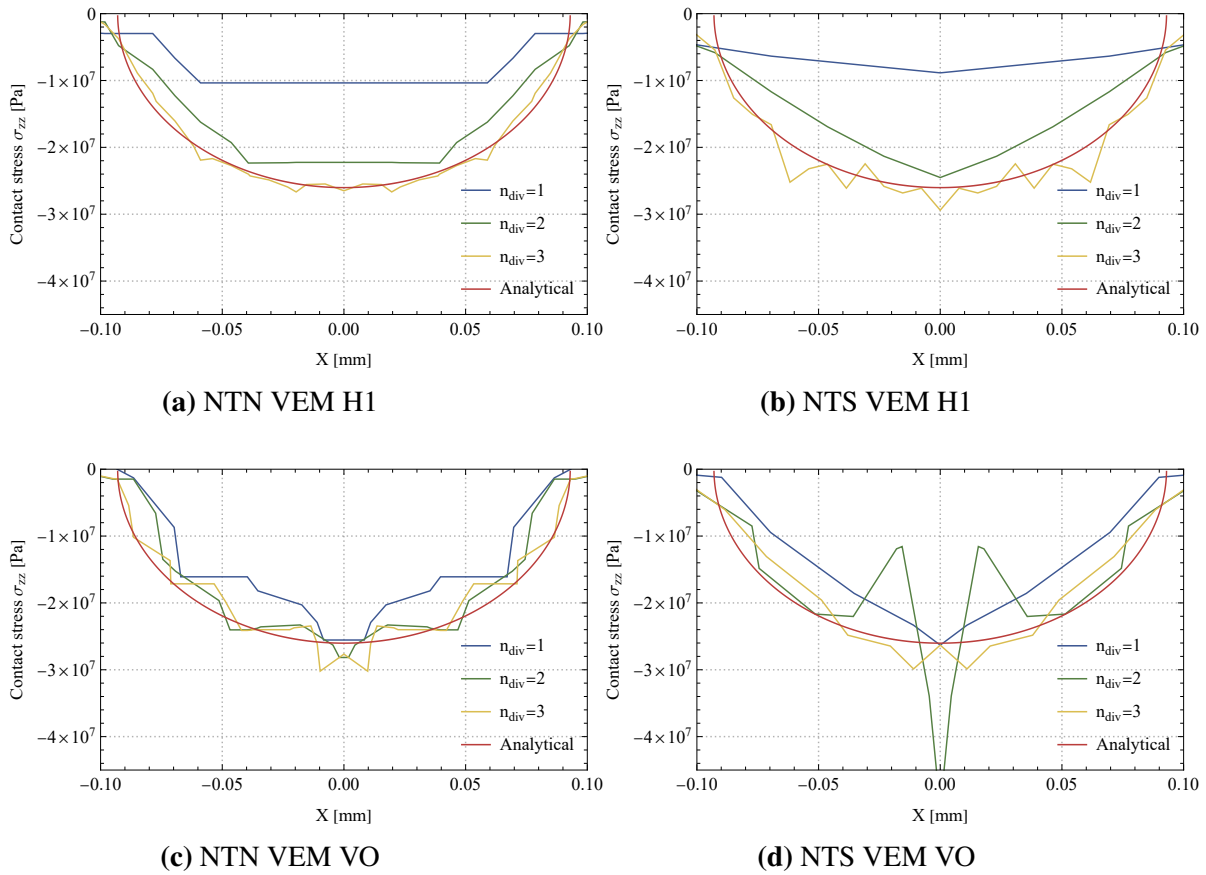


Figure 6.44 – Hertzian contact - Stress distributions in normal direction defined as $\sigma_{zz} = (\boldsymbol{\sigma}\mathbf{n}) \cdot \mathbf{n}$ with node-to-node in (a, c) and node-to-surface contact in (b, d).

was selected to obtain fair comparison with the results by Weißenfels et al. in DZIEWIECKI ET AL. (2015). The results match very well. For this example, the Saint Venant-Kirchhoff strain energy function in equation (2.51) was adopted.

This choice is justified by the fact, that the linearized strain tensor in equation (2.13) can not capture rigid body rotations. However, this example is still undergoing small strains. The results obtained in this example are in good agreement with different existing results for the rotating block test, see DZIEWIECKI ET AL. (2015) and PUSO & LAURSEN (2004). However, the jump in the reaction forces, obtained by Weißenfels et al. in DZIEWIECKI ET AL. (2015) is not present in the virtual element results. This is due to the coarse mesh, in which the bending of the bodies for a 45 degree rotation angle is not modeled correctly. Indeed, using a finer mesh, will reproduce this effect as well.

The variation of the stabilization parameter α for the stabilization based on the degrees of freedom in Fig. 6.48 shows, that the reaction forces fit well for $\alpha = 2$ with the results using the energy stabilization and observed by Weißenfels in DZIEWIECKI ET AL. (2015).

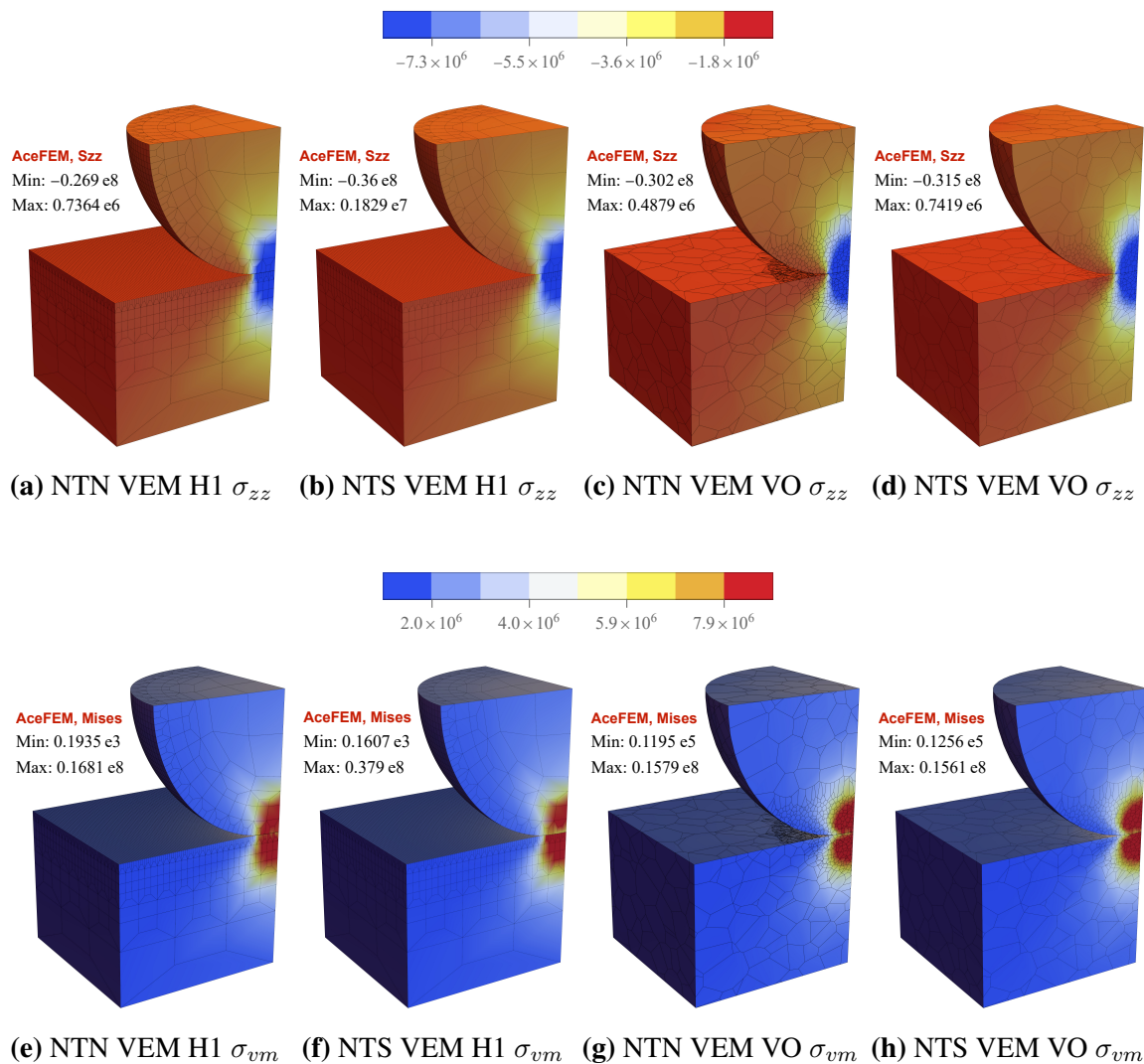


Figure 6.45 – Hertzian contact - Stress distributions in deformed configuration with actual stress in normal direction σ_{zz} in (a, b, c, d) and von Mises stress σ_{vm} in (e, f, g, h).

6.4.4 Summary and conclusion

In this section, the new methodology to obtain matching meshes at contact interfaces for node-to-node contact was analyzed in the framework of the virtual element method in 3D. Node-to-node contact is in the context of VEM more accurate than classical node-to-surface approaches. The patch test is fulfilled for node-to-node contact but results in non-homogeneous stress states for node-to-surface contact. However, small deviations appear due to non-matching triangles and tetrahedrons at the contact interface. Beside having conforming meshes, regarding the nodes at the interface, matching triangles and tetrahedrons are needed to fulfill the patch test exactly, when energy stabilization is used.

Although energetic stabilization generally improves overall results, the DOF stabilization is more suitable for changing meshes during the simulation. This effect can be explained by the fact, that energy stabilization is sensitive to internal mesh quality. Especially during contact

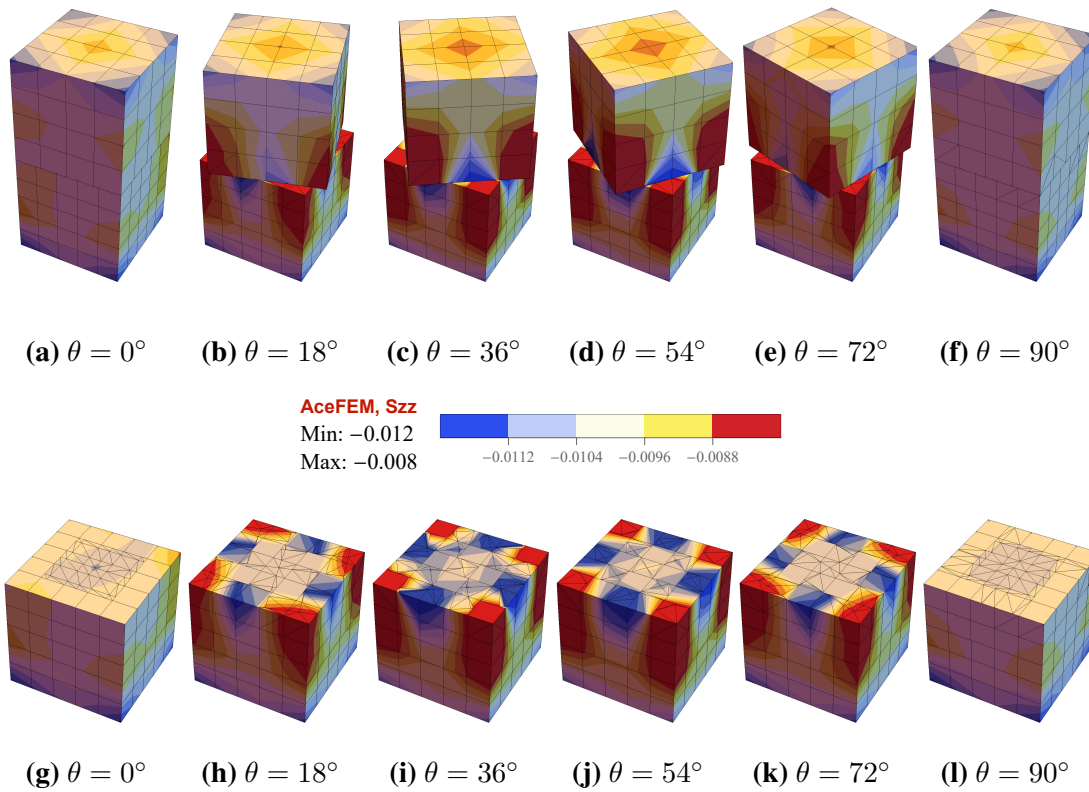


Figure 6.46 – Rotating blocks - Stress distributions σ_{zz} for different rotation angles from a) to f) showing both bodies and g) to l) showing the lower block with $\theta \in \{0, 18, 36, 54, 72, 90\}$.

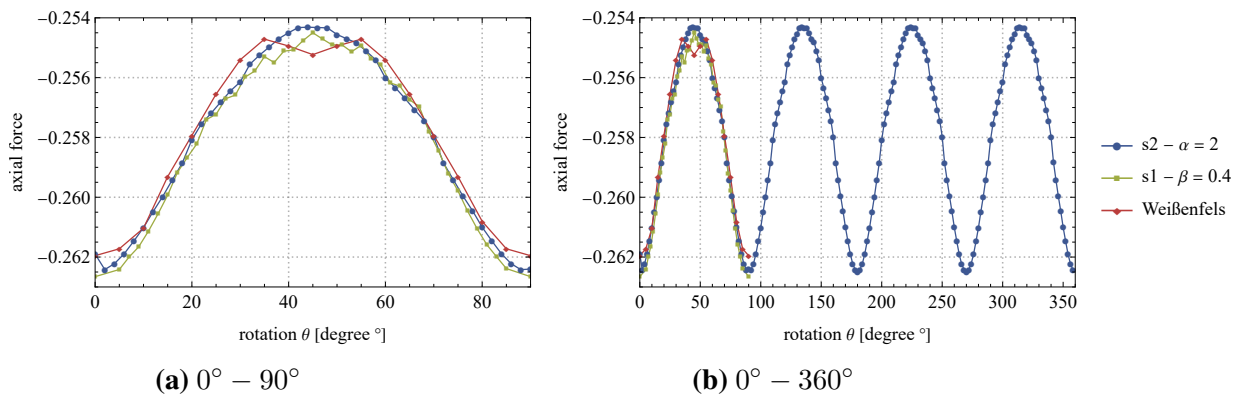


Figure 6.47 – Rotating blocks - Reaction forces over rotation angle with rotation increment $\Delta\theta = 2^\circ$.

in some certain cases small edges and faces appear, which can cause numerical issues when computing the inverse of the Jacobian of internal tetrahedrons.

The extension to large deformation contact is possible but will result in non constant normals. Further, the normals for the contact elements need to be smoothed across the contact surface, such that vertices will have unique normals. For this purpose, smoothing strategies, such as

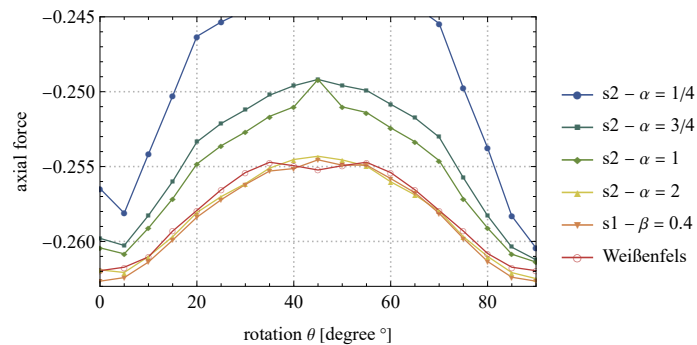


Figure 6.48 – Rotating blocks - Reaction forces over rotation angle with rotation increment $\Delta\theta = 5^\circ$. Comparison with Weißenfels et al. DZIEWIECKI ET AL. (2015).

the construction of Bezier surfaces could be employed, to construct C1 continuous normals, see KRSTULOVIĆ-OPARA ET AL. (2002). Alternatively, an easier way would be averaging the normals at each node by taking the mean value of the neighboring faces.

6.5 Surface-to-surface contact

In the previous section, node-to-node contact was analyzed. However, another way to treat non conforming contact pairs is to treat the contact pairs as polygonal pairs. This approach results in the surface-to-surface contact formulation, introduced in section 5.3. Beside the contact patch test, a comparison with node-to-node contact for both before introduced stabilization techniques and various interface meshes are presented.

6.5.1 Contact patch test

In this example, the surface-to-surface contact formulation is used for analyzing the classical contact patch test. Fig. 6.49 is showing the interface mesh of the contact bodies and the contact elements at the contact interface. Here, compared to the node-to-node formulation from section 6.4, an additional sub triangulation of the interface mesh after inserting the nodes is not made. Note that this is also not necessary for the node-to-node formulation but was done due to simple implementation aspects. However, in this example, both cubes have unit dimensions and the material parameters for both bodies are chosen to be $E = 1.0$ and $\nu = 0.3$. The upper block is pushed down with a displacement boundary condition $\bar{u}_z = 0.5$. Fig. 6.50 shows the contour plots for σ_{zz} . While the contact formulation with $\beta^c = 0$ leads to slightly non homogeneous stresses, a small stabilization with $\beta^c = 0.1$ leads to homogeneous stresses, such that the contact patch test is fulfilled. The rank deficiency of the contact element tangent will be higher by increasing the amount of nodes, i.e. having polygonal surface-to-surface contact elements with more than four nodes. As an out coming result, it can be noted that both contact formulations node-to-node and surface-to-surface are passing the contact patch test, see Fig. 6.50.

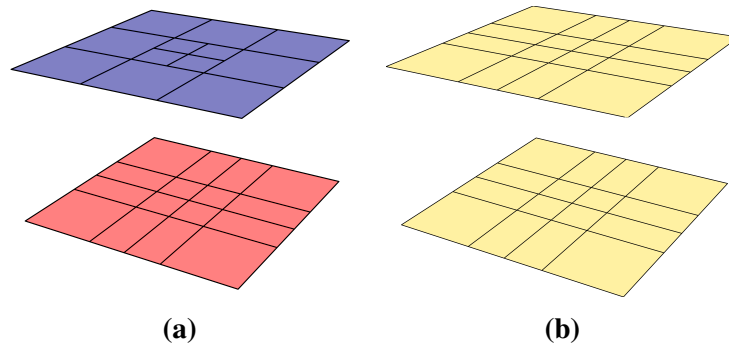


Figure 6.49 – Mesh at the interface of both contact pairs in (a) and contact elements at the interface in (b).

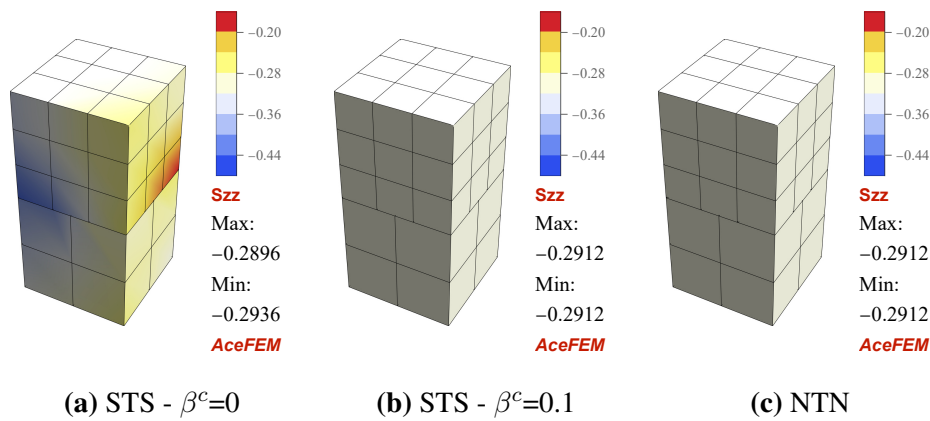


Figure 6.50 – Contourplots for S_{zz} for the contact patch test with regular shaped virtual elements showing different contact formulations.

6.5.2 Comparison of surface-to-surface and node-to-node contact

In this example, the surface-to-surface contact formulation is compared for the two different stabilization techniques with the node-to-node contact formulation. Furthermore, the influence of the interface mesh on the results will be analyzed. The geometrical setup and material parameters for this example are the same as in the previous example in section 6.5.1. Fig. 6.51 and Fig. 6.52 are showing the contour plots for σ_{zz} and the interface meshes for surface-to-surface and node-to-node contact formulations. As already mentioned before, "s1" represents the energy stabilization and "s2" the stabilization based on the degrees of freedom. As a first main outcome of this study, one can see that both stabilizations and both integration schemes in all its variations are passing the contact patch test and can be used for contact modeling with surface-to-surface contact elements, see Fig. 6.51. However, using the integration over triangles gives more flexibility for the choice of the interface mesh. The reason is that for the edge integration, polygonal pairs need to be constructed between the bodies, see Fig. 6.51b, Fig. 6.51d, Fig. 6.51f and Fig. 6.51h. At the contact interface, whether the edges or the triangles need to match, depending on the integration scheme which is used. On the other hand, the same analysis is done for the node-to-node formulation, see

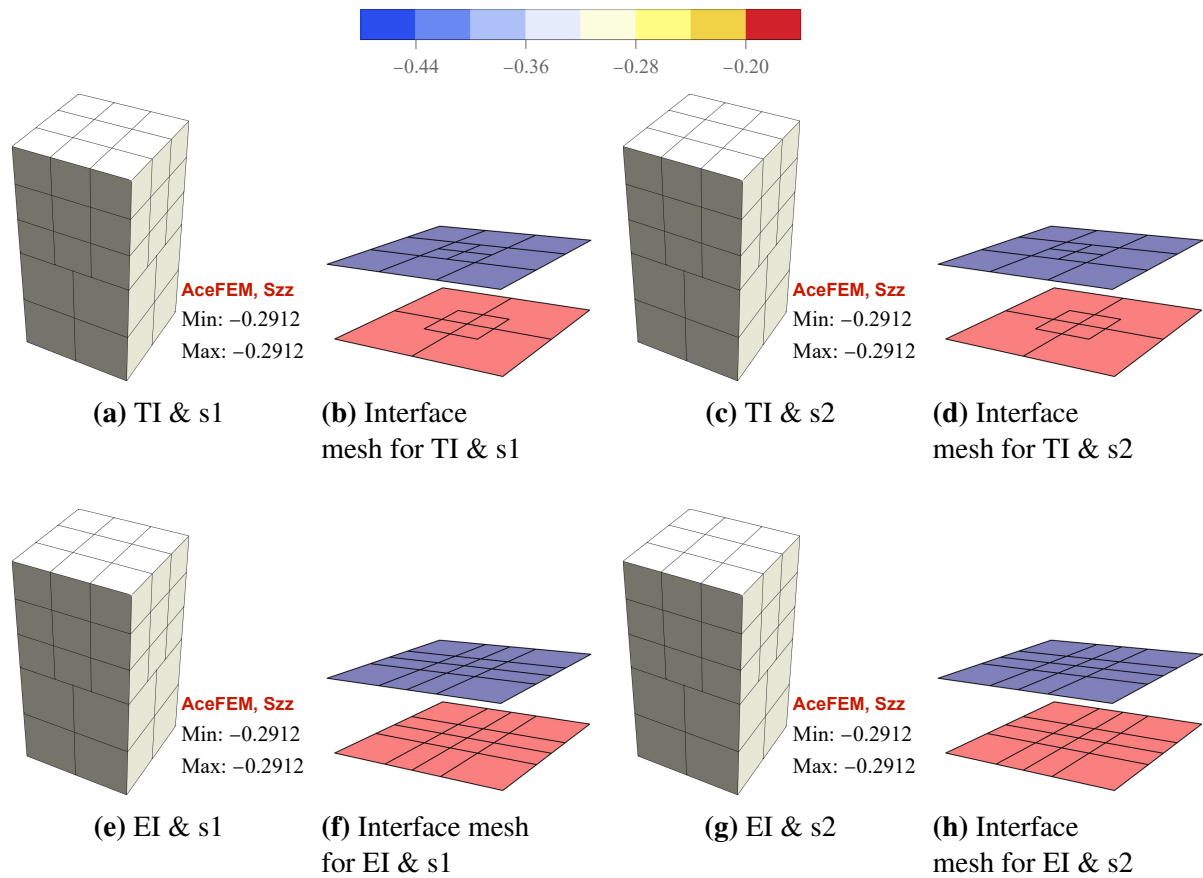


Figure 6.51 – Contourplots for S_{zz} for the contact patch test with regular shaped virtual elements and surface-to-surface contact formulation.

Fig. 6.52. One can see here that similarly to the surface-to-surface contact formulation, both stabilization and both integration schemes can be used to pass the contact patch test. However, similarly to the surface-to-surface contact formulation, the interface mesh needs to have conforming polygons, when edge integration is used for the computation of the virtual parameters, see Fig. 6.52i, Fig. 6.52j, Fig. 6.52k and Fig. 6.52l.

6.5.3 Summary and conclusion

A three dimensional surface-to-surface contact formulation in terms of the virtual element method was analyzed in this section. The introduced formulation treats the contact pairs as polygonal pairs and reproduces similar results, compared to node-to-node contact. The patch test is fulfilled, similarly to node-to-node contact. However, within this framework, polygons need to match at the interface, which is a different restriction as for node-to-node contact.

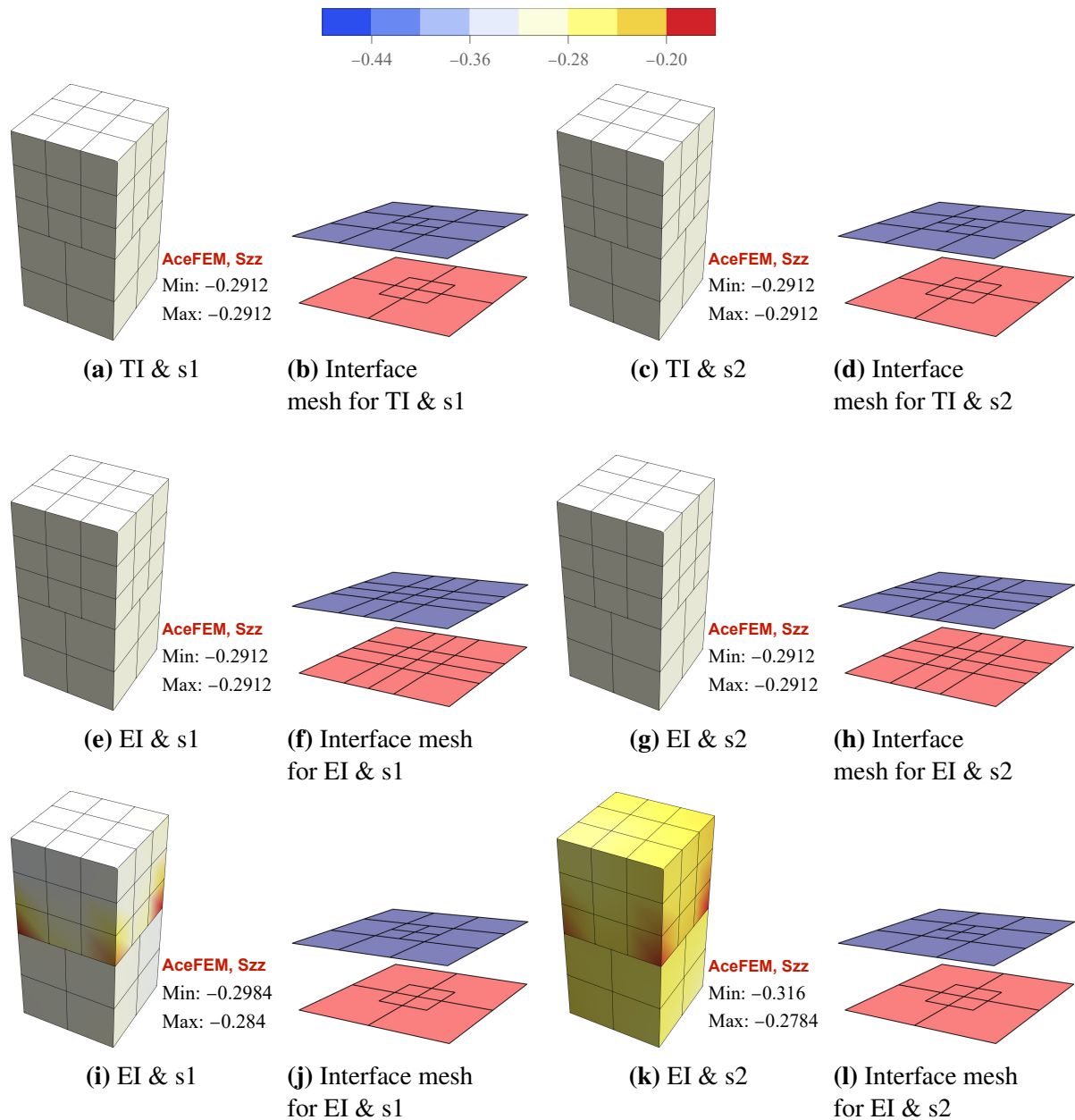


Figure 6.52 – Contourplots for S_{zz} for the contact patch test with regular shaped virtual elements and node-to-node contact formulation.

6.6 Coupled Taylor Anvil impact

The last section of this work deals with the Taylor Anvil test which was analyzed in section 6.3.3. The dimensions of the specimen and all material parameters can be taken from table 6.7. Instead of fixing the degrees of freedom at the lower part as have been done in section 6.3.3, real contact is modeled via the node-to-node contact modeling procedure, which was

presented in the previous sections. The aim was to choose a test case, where the specimen comes multiple times in to contact. For this purpose, gravity is introduced, such that the body forces (accelerations) can compensate the acceleration of the rod after the impact. The numerical parameters for this example can be taken from table 6.7. Contact is modeled via

Table 6.7 – Numerical parameters used for coupled Taylor Anvil contact example.

No.	Parameter	Label	Value	Unit
1	Elastic modulus of rod	E^1	29.25	N/mm ²
1	Elastic modulus of cube	E^2	58.5	N/mm ²
2	Poisson ratio	ν	0.35	–
3	Density	ρ	7800	kg/m ³
4	Yield stress	Y_0	0.65	N/mm ²
6	Hardening coefficient	H	3.1	N/mm ²
7	Saturation exponent	δ	0	–
8	Velocity	v_z	1.39	m/s
9	Gravity	g_z	10	m/s ²
10	Height of rod	h_0	32.4	cm
11	Radius of rod	r_0	3.2	cm

the node-to-node formulation with the help of the node insertion algorithm. However, the mesh is not adaptive, such that the initial mesh is manipulated only once. This is valid, since the deformation at contact is small and normals remain constant. Modeling large deformation contact would need an adaptive mesh where nodes are projected in each step, as have been done for the rotating blocks example in Fig. 6.47. Fig. 6.53 is showing different energies over time, including the kinetic energy, potential energy, internal energy of both bodies and the sum of all, the total energy. The energies are normalized with respect to the initial total energy. Two different test cases are simulated, where Fig. 6.53a is showing the purely elastic case and Fig. 6.53b the elasto-plastic case. It can be seen, that the energy conservation over time is fulfilled and energy is transferred correctly between both bodies. However, for the elasto-plastic case, the total energy decreases after the first and second impact due to plastic dissipation, see Fig. 6.53b. Fig. 6.54 is showing the contour plots of the accumulated plastic strains at different time steps for the plastic simulation.

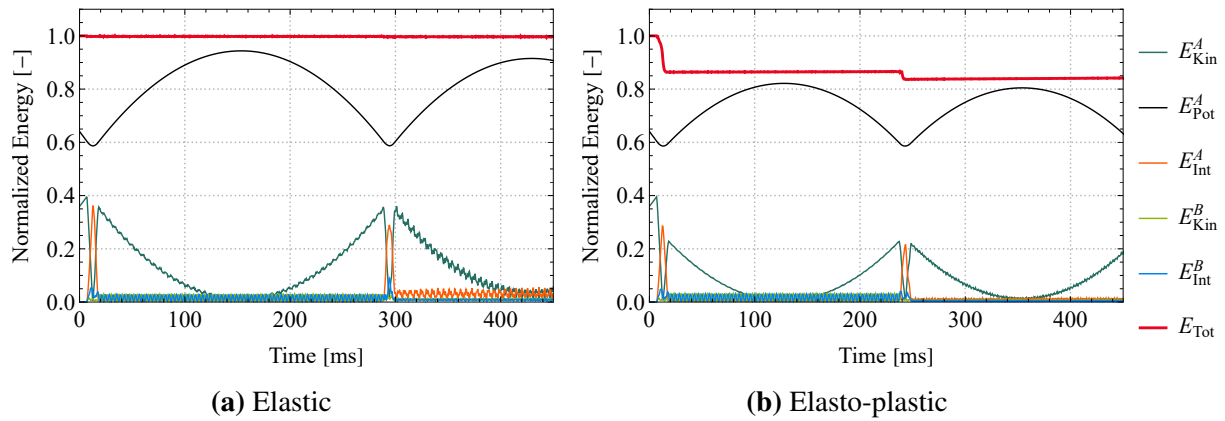


Figure 6.53 – Coupled Taylor Anvil impact - Different energies over time responses for.

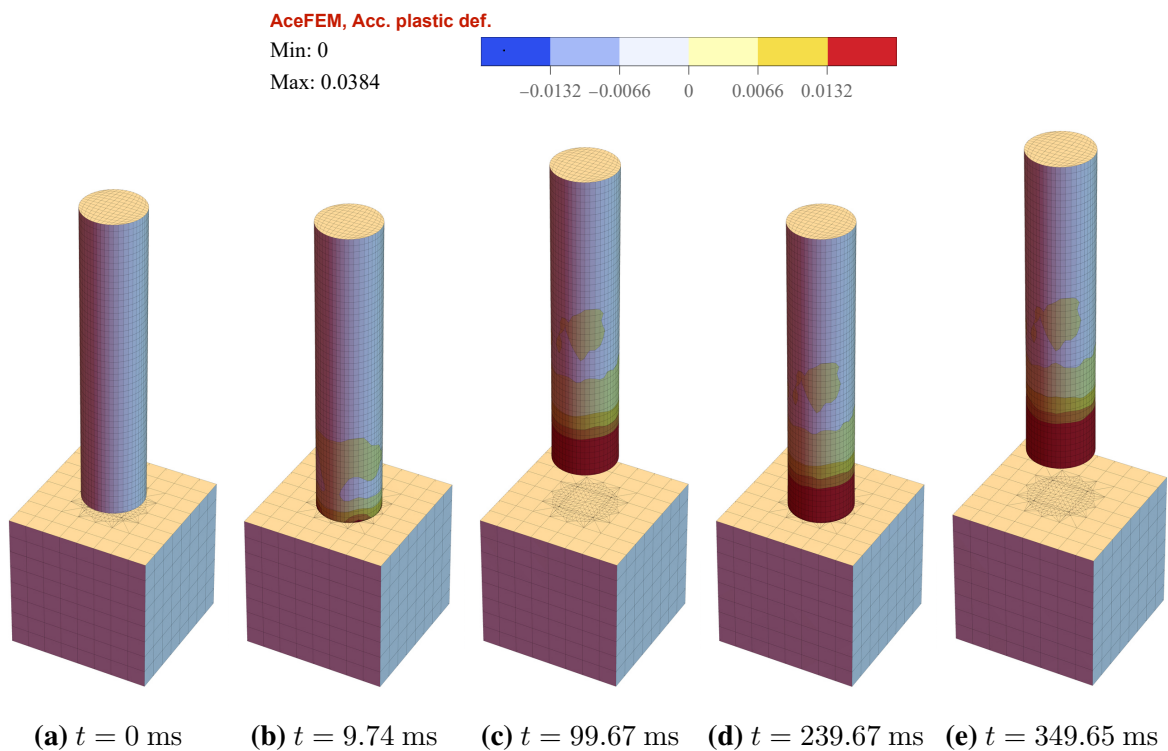


Figure 6.54 – Coupled Taylor Anvil impact - Deformed state showing the accumulated plastic deformation distributions at different time from a) to e).

Chapter 7

Conclusions

7.1 Achievements

The essential outcome of this work can be divided into three major parts. The first part discusses a virtual element formulation considering dynamic effects by using a pseudo potential. Proper integration schemes, including the exact integration of the mass matrix are introduced and differences in evaluating the mass matrix regarding the response of specific benchmark problems are analyzed. A novel stabilization scheme for the mass matrix, based on the ideas of stabilizing the stiffness matrix in WRIGGERS ET AL. (2017), is employed. It could be shown that the computation of the mass matrix with and without stabilization leads to similar results for elasto-dynamic problems in two and three dimensions.

The second part shows a coupling of the aforementioned elasto-dynamic formulation with a von Mises plasticity model to simulate finite strain plastic material behavior within dynamical responses. For the treatment of elastic and plastic incompressibility, a mixed virtual element formulation is adopted based on a Hu-Washizu functional. Various numerical examples, including the Taylor-Anvil test, are computed showing results that are in a good agreement with results from the literature.

In the third part, two novel contact formulations in three dimensions are introduced. The first one is based on the ideas introduced in WRIGGERS ET AL. (2016) for the two dimensional case and makes use of the advantageous properties of the virtual element method. A projection algorithm detects possible contact pairs between the contact bodies and projects surfaces to each other to find new nodes stemming from different intersections, which get inserted into the existing mesh, leading to a very simple node-to-node contact formulation. It could be demonstrated that this formulation passes the patch test and improves the overall results for different benchmark problems. However, as a major drawback, beside having nodal pairs, is that triangles and tetrahedrons of the sub mesh have to be continuous due to compatibility requirements, depending on the stabilization technique for the stiffness matrix. This increases the computational effort. Using a different stabilization technique, which does not require any sub mesh eliminates this drawback.

As a further outcome, a new treatment of contact is introduced by means of treating the

contact pairs as polygonal pairs, such that a surface-to-surface contact element can be formulated. This novel formulation shows promising results and passes the patch test as well. Indeed, a mesh manipulation, like for the node-to-node contact, needs to be performed. Thus matching polygons can be generated at the contact interface. In this formulation, the projected displacements are used to define the gap function, leading to a projected gap function, which has a similar linear form as the virtual element ansatz. It could be proven that the integration of the contact energy can be realized in different ways, namely the integration on the edges of a polygon or using an integration scheme on a sub mesh consisting of triangles. This way of contact treatment yields similar results, compared to the node-to-node contact formulation and passes the patch test as well. However, the integration scheme for the computation of the virtual parameters influences the choice of the interface mesh.

The final achievement of this work is the development of a coupled impact simulation, taking dynamic effects, plastic material behavior and contact into account. This example is calculated for a very simple problem just to show the possibilities of the developed models. Energy is correctly conserved during impact, additionally a plastic impact is simulated. To sum up, the different models of this work can model impact problems and can be used for example for crash simulations. However, the final impact simulation in this work is modeled for small strains and is restricted due to the projection algorithm. The latter needs to be extended to large deformation contact. For the extension, the node projection algorithm needs to be applied at each step.

7.2 Outlook

For the virtual element method, further research is required to progress from basic testings to a reliable prediction tool. To make the virtual element method usable in commercial software, further developments need to be achieved including stabilization free formulations, see e.g. BERRONE ET AL. (2023) and CHEN & SUKUMAR (2023).

However, with respect to the presented work, further investigations could be:

- Extension of the node-to-node contact formulation to large deformations. This needs an extension of the node projection algorithm.
- Extension of the surface-to-surface contact formulation to large deformations.
- Extension of both, node-to-node and surface-to-surface contact, towards frictional contact.
- Extension to large deformation impact simulations, which needs the projection of contact pairs in each time step.

More generally speaking, to take advantage of the benefits of the virtual element method it can be applied to various fields, for example to:

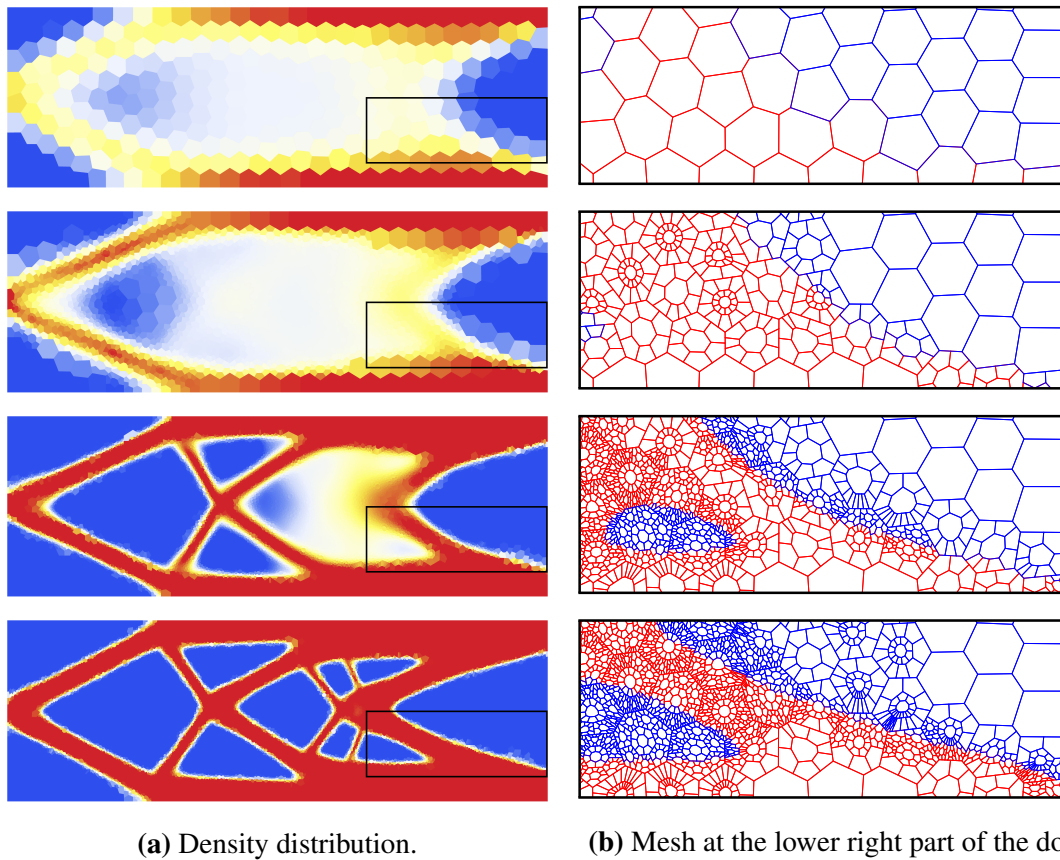


Figure 7.1 – Topology optimization of a beam which is under bending. Different optimization steps from top to bottom with Voronoi elements as initial mesh and refinement of the mesh.

- Virtual elements for 3D discrete crack propagation, based on the ideas presented in HUSSEIN ET AL. (2019) and HUSSEIN ET AL. (2020) for two dimensional problems.
- Topology optimization where the main advantage of VEM lies in simple treatment of mesh refinement and mesh coarsening due to simple handling of hanging nodes.

The latter was already implemented and first ideas have been formulated. Fig. 7.1 shows the thermodynamically consistent topology optimization of a beam under bending conditions, following the work by JANTOS ET AL. (2019) and JUNKER & BALZANI (2021). The initial discretization is realized with Voronoi shaped virtual elements. During the optimization procedure the density distribution is evolving and according to the interface between material and void, a mesh refinement algorithm refines the mesh at the interface. This simple example is implemented to show the possibilities and power of the virtual element method in dealing with hanging nodes, see mesh refinement in Fig. 7.1. This lead to a consistent C^0 -continuous mesh.

Appendix A

A.1 Divergence theorem

General form of the divergence theorem used, applied on arbitrary element face in \mathbb{R}^3 domain $\Gamma_f \in \{X, Y, Z\}$:

$$\int_{\Gamma_f} \phi d\Gamma = \frac{1}{2} \int_{\gamma_f} \begin{bmatrix} \int \phi dX^f \\ \int \phi dY^f \end{bmatrix} \cdot \begin{bmatrix} \mathbf{e}_X^f \\ \mathbf{e}_Y^f \end{bmatrix} \cdot \mathbf{N}_e d\gamma \quad (\text{A.1})$$

The integrand $\phi(X, Y, Z) \leftarrow \phi^f(X^f, Y^f)$ has to be expressed first with local coordinate system of a face $\mathbf{X}^f = (X^f, Y^f) = \mathbf{R}^f(\mathbf{X} - \mathbf{X}_m)$. Applied twice on whole domain leads:

$$\begin{aligned} \int_{\Omega} \phi d\Omega &= \frac{1}{3} \int_{\Gamma} \begin{bmatrix} \int \phi dX \\ \int \phi dY \\ \int \phi dZ \end{bmatrix} \cdot \mathbf{N}_f d\Gamma = \\ &= \frac{1}{6} \sum_{f=1}^{n_f} \int_{\gamma_f} \begin{bmatrix} \int \phi dXdX^f \mathbf{e}_X^f \cdot \mathbf{N}_e + \int \phi dXdY^f \mathbf{e}_Y^f \cdot \mathbf{N}_e \\ \int \phi dYdX^f \mathbf{e}_X^f \cdot \mathbf{N}_e + \int \phi dYdY^f \mathbf{e}_Y^f \cdot \mathbf{N}_e \\ \int \phi dZdX^f \mathbf{e}_X^f \cdot \mathbf{N}_e + \int \phi dZdY^f \mathbf{e}_Y^f \cdot \mathbf{N}_e \end{bmatrix} d\gamma \cdot \mathbf{N}_f \quad (\text{A.2}) \end{aligned}$$

Note that above is a general form.

A.2 Finite element shape functions

A.2.1 One-Dimensional shape functions

Linear shape functions:

$$N_1(\xi) = \frac{1}{2}(1 - \xi) \quad N_2(\xi) = \frac{1}{2}(1 + \xi) \quad (\text{A.3})$$

Quadratic shape functions:

$$N_1(\xi) = \frac{1}{2}\xi(1 - \xi) \quad N_2(\xi) = (1 - \xi)^2 \quad N_3(\xi) = \frac{1}{2}\xi(1 + \xi) \quad (\text{A.4})$$

A.2.2 Two-Dimensional shape functions

Linear shape functions for a triangle:

$$N_1 = 1 - \xi - \eta \quad N_2 = \xi \quad N_3 = \eta \quad (\text{A.5})$$

Quadratic shape functions for a triangle:

$$\begin{aligned} N_1 &= \lambda(2\lambda - 1) & N_2 &= \xi(2\xi - 1) & N_3 &= \eta(2\eta - 1) \\ N_4 &= 4\xi\lambda & N_5 &= 4\xi\eta & N_6 &= 4\eta\lambda, \end{aligned} \quad (\text{A.6})$$

where $\lambda = 1 - \xi - \eta$.

A.2.3 Three-Dimensional shape functions

Linear shape functions for a tetrahedron:

$$N_1 = 1 - \xi - \eta - \zeta \quad N_2 = \xi \quad N_3 = \eta \quad N_4 = \zeta \quad (\text{A.7})$$

Quadratic shape functions for a tetrahedron:

$$\begin{aligned} N_1 &= \lambda(2\lambda - 1) & N_2 &= \xi(2\xi - 1) & N_3 &= \eta(2\eta - 1) & N_4 &= \zeta(2\zeta - 1) \\ N_5 &= 4\xi\lambda & N_6 &= 4\xi\eta & N_7 &= 4\eta\lambda & N_8 &= 4\zeta\lambda & N_9 &= 4\xi\zeta & N_{10} &= 4\eta\zeta, \end{aligned} \quad (\text{A.8})$$

where $\lambda = 1 - \xi - \eta - \zeta$.

A.3 Gauss-Integration

Table A.1 – One-dimensional Gauss-Integration.

n_g^e	\mathbf{g}	ξ_g^e	w_g^e
1	{1}	{0}	{2}
2	{1,2}	$\{\frac{1}{\sqrt{3}}, \frac{1}{\sqrt{3}}\}$	{1,1}
3	{1,2,3}	$\{-\sqrt{\frac{3}{5}}, 0, \sqrt{\frac{3}{5}}\}$	$\{\sqrt{\frac{5}{9}}, \sqrt{\frac{8}{9}}, \sqrt{\frac{5}{9}}\}$

Table A.2 – Two-dimensional Gauss-Integration for triangular elements.

n_g^T	\mathbf{g}	ξ_g^T	η_g^T	w_g^T
1	{1}	$\{\frac{1}{3}\}$	$\{\frac{1}{3}\}$	$\{\frac{1}{2}\}$
3	{1,2,3}	$\{\frac{1}{2}, 0, \frac{1}{2}\}$	$\{\frac{1}{2}, \frac{1}{2}, 0\}$	$\{\frac{1}{6}, \frac{1}{6}, \frac{1}{6}\}$

Table A.3 – Three-dimensional Gauss-Integration for tetrahedral elements.

$n_g^{\bar{x}}$	\mathbf{g}	$\xi_g^{\bar{x}}$	$\eta_g^{\bar{x}}$	$\zeta_g^{\bar{x}}$	$w_g^{\bar{x}}$
1	{1}	$\{\frac{1}{4}\}$	$\{\frac{1}{4}\}$	$\{\frac{1}{4}\}$	$\{\frac{1}{6}\}$
5	{1,2,3,4,5}	$\{\frac{1}{4}, \frac{1}{6}, \frac{1}{6}, \frac{1}{6}, \frac{1}{2}\}$	$\{\frac{1}{4}, \frac{1}{6}, \frac{1}{6}, \frac{1}{2}, \frac{1}{6}\}$	$\{\frac{1}{4}, \frac{1}{6}, \frac{1}{2}, \frac{1}{6}, \frac{1}{6}\}$	$\{-\frac{2}{15}, \frac{3}{40}, \frac{3}{40}, \frac{3}{40}, \frac{3}{40}\}$

Bibliography

- AHMAD B., ALSAEDI A., BREZZI F., MARINI L. ET AL. Equivalent projectors for virtual element methods. *Computers & Mathematics with Applications*, 66 (2013) (3): 376–391.
- ALDAKHEEL F., HUDOBIVNIK B., ARTIOLI E., BEIRÃO DA VEIGA L. ET AL. Curvilinear virtual elements for contact mechanics. *Computer Methods in Applied Mechanics and Engineering*, 372 (2020): 113–139.
- ALDAKHEEL F., HUDOBIVNIK B., HUSSEIN A. & WRIGGERS P. Phase-field modeling of brittle fracture using an efficient virtual element scheme. *Computer Methods in Applied Mechanics and Engineering*, 341 (2018).
- ALDAKHEEL F., HUDOBIVNIK B. & WRIGGERS P. Virtual elements for finite thermo-plasticity problems. *Computational Mechanics*, (2019).
- ALTENBACH H. *Kontinuumsmechanik: Einführung in die materialunabhängigen und materialabhängigen Gleichungen*, volume 3. 2018.
- ANTONIETTI P., HOUSTON P. & PENNESI G. Fast numerical integration on polytopic meshes with applications to discontinuous galerkin finite element methods. *Journal of Scientific Computing*, 77 (2018).
- ARTIOLI E., BEIRÃO DA VEIGA L., LOVADINA C. & SACCO E. Arbitrary order 2D virtual elements for polygonal meshes: part i, elastic problem. *Computational Mechanics*, 60 (2017a) (3): 355–377.
- ARTIOLI E., VEIVA L., LOVADINA C. & SACCO E. Arbitrary order 2d virtual elements for polygonal meshes: Part ii, inelastic problem. *Computational Mechanics*, 60 (2017b).
- BABUŠKA I. & STROUBOULIS T. *The Finite Element Method and Its Reliability*. Numerical Mathematics and Scie. Clarendon Press, 2001.
- BATHE K. *Finite Element Procedures*. Prentice Hall, 2006.
- BATHE K.J. & CHAUDHARY A. A solution method for planar and axisymmetric contact problems. *International Journal for Numerical Methods in Engineering*, 21 () (1): 65–88.
- BELGACEM F.B., HILD P. & LABORDE P. The mortar finite element method for contact problems. *Mathematical and Computer Modelling*, 28 (1998): 263–271.

- BELYTSCHKO T., GUO Y., KAM LIU W. & PING XIAO S. A unified stability analysis of meshless particle methods. *International Journal for Numerical Methods in Engineering*, 48 (2000) (9): 1359–1400.
- BERNARDI C., MADAY Y. & PATERA A.T. *Domain Decomposition by the Mortar Element Method*, pages 269–286. Springer Netherlands, Dordrecht, 1993.
- BERRONE S., BORIO A., MARCON F. & TEORA G. A first-order stabilization-free virtual element method. *Applied Mathematics Letters*, 142 (2023): 108 641.
- BODE T. Peridynamic galerkin methods for nonlinear solid mechanics. *PhD Thesis*, (2021).
- BREZZI F. & FORTIN M. *Mixed and Hybrid Finite Element Methods*. Springer Series in Computational Mathematics. Springer New York, 2011.
- BREZZI F., LIPNIKOV K. & SHASHKOV M. Convergence of the mimetic finite difference method for diffusion problems on polyhedral meshes. *SIAM J. Numerical Analysis*, 43 (2005a): 1872–1896.
- BREZZI F., LIPNIKOV K. & SIMONCINI V. A family of mimetic finite difference methods on polygonal and polyhedral meshes. *Mathematical Models and Methods in Applied Sciences*, 15 (2005b).
- CAMACHO G. & ORTIZ M. Adaptive lagrangian modelling of ballistic penetration of metallic targets. *Computer Methods in Applied Mechanics and Engineering*, 142 (1997): 269–301.
- CANGIANI A., GEORGOULIS E. & HOUSTON P. Hp-version discontinuous galerkin methods on polygonal and polyhedral meshes. *Mathematical Models and Methods in Applied Sciences*, 24 (2014).
- CHEN A. & SUKUMAR N. Stabilization-free serendipity virtual element method for plane elasticity. *Computer Methods in Applied Mechanics and Engineering*, 404 (2023): 115 784.
- CHI H., BEIRÃO DA VEIGA L. & PAULINO G. Some basic formulations of the virtual element method (VEM) for finite deformations. *Computer Methods in Applied Mechanics and Engineering*, 318 (2017): 148–192.
- CHIN E., LASSERRE J.B. & SUKUMAR N. Numerical integration of homogeneous functions on convex and nonconvex polygons and polyhedra. *Computational Mechanics*, 56 (2015).
- CHOI H., CHI H. & PARK K. Virtual element method for mixed-mode cohesive fracture simulation with element split and domain integral. *International Journal of Fracture*, 240 (2023): 1–20.
- CIARLET P. *Mathematical elasticity i: three-dimensional elasticity*. Amsterdam: North-Holland (1988).

- CIARLET P. *The Finite Element Method for Elliptic Problems*. Classics in Applied Mathematics. Society for Industrial and Applied Mathematics, 2002.
- CIHAN M., ALDAKHEEL F., HUDOBIVNIK B. & WRIGGERS P. 3d virtual elements for elastodynamic problems. *PAMM*, 20 (2021a) (1).
- CIHAN M., HUDOBIVNIK B., ALDAKHEEL F. & WRIGGERS P. 3d mixed virtual element formulation for dynamic elasto-plastic analysis. *Computational Mechanics*, 68 (2021b) (3): 1432–0924.
- CIHAN M., HUDOBIVNIK B., ALDAKHEEL F. & WRIGGERS P. Virtual element formulation for finite strain elastodynamics. *Computer Modeling in Engineering & Sciences*, 129 (2021c) (3): 1151–1180.
- CIHAN M., HUDOBIVNIK B., KORELC J. & WRIGGERS P. A virtual element method for 3d contact problems with non-conforming meshes. *Computer Methods in Applied Mechanics and Engineering*, 402 (2022): 115–385. A Special Issue in Honor of the Lifetime Achievements of J. Tinsley Oden.
- DZIEWIECKI P., WEISSENFELS C. & WRIGGERS P. Modelling of soil structure interaction by applying a hypoplastic material behaviour within mortar contact formulation. *Lecture Notes in Applied and Computational Mechanics*, 77 (2015): 59–72.
- EL-ABBASI N. & BATHE K.J. Stability and patch test performance of contact discretizations and a new solution algorithm. *Computers & Structures*, 79 (2001) (16): 1473–1486.
- FARAH P., POPP A. & WALL W. Segment-based vs. element-based integration for mortar methods in computational contact mechanics. *Computational Mechanics*, 55 (2015).
- FISCHER K.A. & WRIGGERS P. Frictionless 2d contact formulations for finite deformations based on the mortar method. *Computational Mechanics*, 36 (2005): 226–244.
- FRANCAVILLA A. & ZIENKIEWICZ O.C. A note on numerical computation of elastic contact problems. *International Journal for Numerical Methods in Engineering*, 9 (1975) (4): 913–924.
- GAIN A.L., TALISCHI C. & PAULINO G.H. On the virtual element method for three-dimensional linear elasticity problems on arbitrary polyhedral meshes. *Computer Methods in Applied Mechanics and Engineering*, 282 (2014): 132 – 160.
- GUYAN R.J. Reduction of stiffness and mass matrices. *AIAA Journal*, 3 (1965) (2): 380–380.
- HALLQUIST J. & LABORATORY L.L. *NIKE2D, an Implicit Finite-deformation, Finite-element Code for Analyzing the Static and Dynamic Response of Two-dimensional Solids*. UCRL.: Lawrence Radiation Laboratory. Department of Energy, Lawrence Livermore Laboratory, 1979.

- HARDWICK M., CLAY R., BOGG P., WALSH E. ET AL. Dart system analysis presented to simulation sciences seminar. *Sandia National Laboratories, Albuquerque*, (2005).
- HAUPT P. *Continuum Mechanics and Theory of Materials*. Springer-Verlag Berlin Heidelberg, 2002.
- HERTZ H. Ueber die berührung fester elastischer körper. *Angewandte Mathematik*, 92 (1882): 156–171.
- HOFFMAN J. & FRANKEL S. *Numerical Methods for Engineers and Scientists*. CRC Press, 2018.
- HOLZAPFEL G. *Nonlinear Solid Mechanics - A Continuum Approach for Engineering*, volume 37. 2002.
- HUDOBIVNIK B., ALDAKHEEL F. & WRIGGERS P. Low order 3d virtual element formulation for finite elasto-plastic deformations. *Computational Mechanics*, 63 (2018): 253–269.
- HUDOBIVNIK B. & KORELC J. Closed-form representation of matrix functions in the formulation of nonlinear material models. *Finite Elements in Analysis and Design*, 111 (2016): 19–32.
- HUGHES T. *The Finite Element Method: Linear Static and Dynamic Finite Element Analysis*. Dover Civil and Mechanical Engineering. Dover Publications, 2012.
- HUGHES T., TAYLOR R., SACKMAN J., CURNIER A. ET AL. Finite element method for a class of contact-impact problems. *Computer Methods in Applied Mechanics and Engineering*, 8 (1976) (3): 249–276.
- HUNĚK I. On a penalty formulation for contact-impact problems. *Computers & Structures*, 48 (1993) (2): 193–203.
- HUSSEIN A., ALDAKHEEL F., HUDOBIVNIK B., WRIGGERS P. ET AL. A computational framework for brittle crack-propagation based on efficient virtual element method. *Finite Elements in Analysis and Design*, 159 (2019): 15–32.
- HUSSEIN A., HUDOBIVNIK B. & WRIGGERS P. A combined adaptive phase field and discrete cutting method for the prediction of crack paths. *Computer Methods in Applied Mechanics and Engineering*, 372 (2020).
- JANTOS D.R., HACKL K. & JUNKER P. An accurate and fast regularization approach to thermodynamic topology optimization. *International Journal for Numerical Methods in Engineering*, 117 (2019) (9): 991–1017.
- JUNKER P. & BALZANI D. A new variational approach for the thermodynamic topology optimization of hyperelastic structures. *Computational Mechanics*, 67 (2021) (2): 455–480.
- KAMOULAKOS A. A simple benchmark for impact. *Bench Mark*, (1990): 31–35.

- KIENZLER R. & SCHRÖDER R. *Einführung in die Höhere Festigkeitslehre*. Springer Vieweg Berlin, Heidelberg, 2019.
- KIKUCHI N. & ODEN J.T. *Contact Problems in Elasticity: A Study of Variational Inequalities and Finite Element Methods*. SIAM, Philadelphia, 1988.
- KORELC J. Multi-language and multi-environment generation of nonlinear finite element codes. *Eng. Comput.*, 18 (2002) (4): 312–327.
- KORELC J. AceGen 7.0 - multi-language, multi-environment numerical code generation. <http://symech.fgg.uni-lj.si/>, (2022).
- KORELC J., LENGIEWICZ J. & STUPKIEWICZ S. *A study of symbolic description, numerical efficiency and accuracy of 2D and 3D contact formulations*. Springer-Verlag Berlin, 2006.
- KORELC J., SOLINC U. & WRIGGERS P. An improved eas brick element for finite deformation. *Computational Mechanics*, 46 (2010): 641–659.
- KORELC J. & STUPKIEWICZ S. Closed-form matrix exponential and its application in finite-strain plasticity. *International Journal for Numerical Methods in Engineering*, 98 (2014).
- KORELC J. & WRIGGERS P. *Automation of Finite Element Methods*. Springer, Cham, 2016.
- KRSTULOVIĆ-OPARA L., WRIGGERS P. & KORELC J. A c1-continuous formulation for 3d finite deformation friction contact. *Computational Mechanics*, 29 (2002): 27–42.
- KRYSL P. Mean-strain eight-node hexahedron with optimized energy-sampling stabilization for large-strain deformation. *International Journal for Numerical Methods in Engineering*, 103 (2015a): 650–670.
- KRYSL P. Mean-strain eight-node hexahedron with stabilization by energy sampling. *International Journal for Numerical Methods in Engineering*, 103 (2015b): 437–449.
- KUMAR S., DANAS K. & KOCHMANN D.M. Enhanced local maximum-entropy approximation for stable meshfree simulations. *Computer Methods in Applied Mechanics and Engineering*, 344 (2019): 858–886.
- LAURSEN T. Computational contact and impact mechanics. *Meccanica*, 38 (2003).
- LAURSEN T. & SIMO J. Algorithmic symmetrization of coulomb frictional problems using augmented lagrangians. *Computer Methods in Applied Mechanics and Engineering*, 108 (1993) (1): 133–146.
- LENGIEWICZ J., KORELC J. & STUPKIEWICZ S. Automation of finite element formulations for large deformation contact problems. *International Journal for Numerical Methods in Engineering*, 85 (2011): 1252 – 1279.

- LI B., HABBAL F. & ORTIZ M. Optimal transportation meshfree approximation schemes for fluid and plastic flows. *83* (2010) (12): 1541–1579.
- LIU D., BOOM S., SIMONE A. & ARAGÓN A. An interface-enriched generalized finite element formulation for locking-free coupling of non-conforming discretizations and contact. *Computational Mechanics*, 70 (2022).
- MARFIA S., MONALDO E. & SACCO E. Cohesive fracture evolution within virtual element method. *Engineering Fracture Mechanics*, 269 (2022): 108 464.
- MAZUMDER S. *Numerical Methods for Partial Differential Equations: Finite Difference and Finite Volume Methods*. Elsevier Science, 2015.
- MCDEVITT T.W. & LAURSEN T.A. A mortar-finite element formulation for frictional contact problems. *International Journal for Numerical Methods in Engineering*, 48 (2000) (10): 1525–1547.
- MENGOLINI M., BENEDETTO M.F. & ARAGÓN A.M. An engineering perspective to the virtual element method and its interplay with the standard finite element method. *Computer Methods in Applied Mechanics and Engineering*, 350 (2019): 995–1023.
- MEYER M., BARR A.H., LEE H.H. & DESBRUN M. Generalized barycentric coordinates on irregular polygons. *Journal of Graphics Tools*, 7 (2002): 13 – 22.
- NEWMARK N.M. A method of computation for structural dynamics. *Proceedings of ASCE, Journal of Engineering Mechanics*, 85 (1959): 67–94.
- NGUYEN-THANH V.M., ZHUANG X., NGUYEN-XUAN H., RABCZUK T. ET AL. A virtual element method for 2d linear elastic fracture analysis. *Computer Methods in Applied Mechanics and Engineering*, 340 (2018).
- ODEN J. & REDDY J. *An Introduction to the Mathematical Theory of Finite Elements*. Dover Books on Engineering. Dover Publications, 2012.
- PARK K., CHI H. & PAULINO G. Numerical recipes for elastodynamic virtual element methods with explicit time integration. *International Journal for Numerical Methods in Engineering*, 121 (2019a).
- PARK K., CHI H. & PAULINO G. On nonconvex meshes for elastodynamics using virtual element methods with explicit time integration. *Computer Methods in Applied Mechanics and Engineering*, 356 (2019b): 669–684.
- PERUMAL L. A brief review on polygonal/polyhedral finite element methods. *Mathematical Problems in Engineering*, 2018 (2018): 1–22.
- PETERSEN C. *Stahlbau - Grundlagen der Berechnung und bauliche Ausbildung von Stahlbauten*, volume 4. Springer Vieweg, 2013.

- PIETRZAK G. & CURNIER A. Large deformation frictional contact mechanics: continuum formulation and augmented lagrangian treatment. *Computer Methods in Applied Mechanics and Engineering*, 177 (1999): 351–381.
- POPOV V., HESS M. & WILLERT E. *Handbook of Contact Mechanics: Exact Solutions of Axisymmetric Contact Problems*. Springer-Verlag Berlin, 2019.
- POPP A. & WALL W.A. Dual mortar methods for computational contact mechanics – overview and recent developments. *GAMM-Mitteilungen*, 37 (2014) (1): 66–84.
- PUSO M.A. A 3D mortar method for solid mechanics. *International Journal for Numerical Methods in Engineering*, 59 (2004) (3): 315–336.
- PUSO M.A. & LAURSEN T.A. A mortar segment-to-segment contact method for large deformation solid mechanics. *Computer Methods in Applied Mechanics and Engineering*, 193 (2004) (6): 601–629.
- RUST W. Numerical contact method with adaptive polygonal meshing using the virtual element method. *PhD Thesis*, (2019).
- SABAT L. & KUNDU C.K. History of finite element method: A review. In *Recent Developments in Sustainable Infrastructure*, pages 395–404. Springer Singapore, Singapore, 2021.
- SCHWEIZERHOF K., J.O.HALLQUIST & D.STILLMAN. Efficiency refinements of contact strategies and algorithms in explicit finite element programming. pages 359–384. 1992.
- SIMO J. Algorithms for static and dynamic multiplicative plasticity that preserve the classical return mapping schemes of the infinitesimal theory. *Computer Methods in Applied Mechanics and Engineering*, 99 (1992) (1): 61–112.
- SIMO J. Numerical analysis and simulation of plasticity. 6 (1998): 183–499.
- SIMO J. & HUGHES T. *Computational Inelasticity*, volume 7. 1998.
- SIMO J., TAYLOR R. & PISTER K. Variational and projection methods for the volume constraint in finite deformation elasto-plasticity. *Computer Methods in Applied Mechanics and Engineering*, 51 (1985a) (1): 177–208.
- SIMO J.C., TAYLOR R.L. & PISTER K.S. Variational and projection methods for the volume constraint in finite deformation elasto-plasticity. 51 (1985b): 177–208.
- SIMO J.C., WRIGGERS P. & TAYLOR R. A perturbed lagrangian formulation for the finite element solution of contact problems. *Computer Methods in Applied Mechanics and Engineering*, 50 (1985c): 163–180.
- SINGER M.H. A general approach to moment calculation for polygons and line segments. *Pattern Recognition*, 26 (1993) (7): 1019–1028.

- SUKUMAR N. & TABARRAEI A. Conformal polygonal finite elements. *INTERNATIONAL JOURNAL FOR NUMERICAL METHODS IN ENGINEERING Int. J. Numer. Meth. Engng*, 61 (2004): 2045–2066.
- SUN G., YI Q., SUN Y. & WANG J. The goodman contact element in geotechnical engineering based on the virtual element method. *Archive of Applied Mechanics*, (2023): 1–27.
- TAYLOR G.I. The use of flat-ended projectiles for determining dynamic yield stress i. theoretical considerations. *Proceedings of the Royal Society of London. Series A. Mathematical and Physical Sciences*, 194 (1948) (1038): 289–299.
- TAYLOR R.L. & PAPADOPOULOS P. On a finite element method for dynamic contact/impact problems. *International Journal for Numerical Methods in Engineering*, 36 (1993) (12): 2123–2140.
- TEMIZER I. A mixed formulation of mortar-based frictionless contact. *Computer Methods in Applied Mechanics and Engineering*, 223-224 (2012): 173–185.
- THOMKE S. & FUJIMOTO T. The effect of “front-loading” problem-solving on product development performance. *Journal of Product Innovation Management*, 17 (2000) (2): 128–142.
- TUR M., FUENMAYOR F. & WRIGGERS P. A mortar-based frictional contact formulation for large deformations using lagrange multipliers. *Computer Methods in Applied Mechanics and Engineering*, 198 (2009) (37): 2860–2873.
- VASSILEVSKI P., SENDOV B., ILIEV O., KASCHIEV M. ET AL. *Recent Advances In Numerical Methods And Applications Ii - Proceedings Of The Fourth International Conference*. World Scientific Publishing Company, 1999.
- BEIRÃO DA VEIGA L., BREZZI F., CANGIANI A., MANZINI G. ET AL. Basic principles of virtual element methods. *Mathematical Models and Methods in Applied Sciences*, 23 (2013a) (01): 199–214.
- BEIRÃO DA VEIGA L., BREZZI F. & MARINI L. Virtual elements for linear elasticity problems. *SIAM Journal on Numerical Analysis*, 51 (2013b).
- BEIRÃO DA VEIGA L., BREZZI F., MARINI L. & RUSSO A. The hitchhiker’s guide to the virtual element method. *Mathematical Models and Methods in Applied Sciences*, 24 (2014).
- BEIRÃO DA VEIGA L., GYRYA V., LIPNIKOV K. & MANZINI G. Mimetic finite difference method for the stokes problem on polygonal meshes. *Journal of Computational Physics*, 228 (2009): 7215–7232.
- BEIRÃO DA VEIGA L., LOVADINA C. & MORA D. A virtual element method for elastic and inelastic problems on polytope meshes. *Computer Methods in Applied Mechanics and Engineering*, 295 (2015): 327–346.

- WASHIZU K. *Variational Methods in Elasticity and Plasticity*. Pergamon Press, Oxford, 1975, second edition.
- WIRASAET D., KUBATKO E., MICHOSKI C., TANAKA S. ET AL. Discontinuous galerkin methods with nodal and hybrid modal/nodal triangular, quadrilateral, and polygonal elements for nonlinear shallow water flow. *Computer Methods in Applied Mechanics and Engineering*, 270 (2014): 113–149.
- WOHLMUTH I.B. A mortar finite element method using dual spaces for the lagrange multiplier. *SIAM journal on numerical analysis*, 38 () (3): 989–1012.
- WOOD W.L. *Practical Time-stepping Schemes*. Clarendon Press, Oxford, 1990.
- WOOD W.L., BOSSAK M. & ZIENKIEWICZ O.C. An alpha modification of newmark's method. 15 (1981): 1562–1566.
- WRIGGERS P. Penalty and augmented lagrangian formulations for contact problems. 1985.
- WRIGGERS P. *Computational Contact Mechanics*. Springer-Verlag Berlin, 2006.
- WRIGGERS P. *Nonlinear Finite Element Methods*. Springer-Verlag Berlin Heidelberg, 2008.
- WRIGGERS P. & HUDOBIVNIK B. Virtual element formulation for gradient elasticity. *Acta Mechanica Sinica*, 39 (2023): 722–306.
- WRIGGERS P., REDDY B., RUST W. & HUDOBIVNIK B. Efficient virtual element formulations for compressible and incompressible finite deformations. *Computational Mechanics*, 60 (2017): 253–268.
- WRIGGERS P. & RUST W. A virtual element method for frictional contact including large deformations. *Engineering Computations*, 36 (2019).
- WRIGGERS P., RUST W. & REDDY B. A virtual element method for contact. *Computational Mechanics*, 58 (2016).
- WRIGGERS P., VAN T.V. & STEIN E. Finite element formulation of large deformation impact-contact problems with friction. *Computers & Structures*, 37 (1990) (3): 319–331.
- ZAVARISE G. & DE LORENZIS L. A modified node-to-segment algorithm passing the contact patch test. *International Journal for Numerical Methods in Engineering*, 79 () (4): 379–416.
- ZAVARISE G. & WRIGGERS P. A segment-to-segment contact strategy. *Mathematical and Computer Modelling*, 28 (1998) (4): 497–515. Recent Advances in Contact Mechanics.
- ZHU Y. & CESCOTTO S. Unified and mixed formulation of the 4 node quadrilateral elements by assumed strain method: Application to thermomechanical problems. 38 (1995): 685 – 716.

ZIENKIEWICZ O. & TAYLOR R. The finite element patch test revisited a computer test for convergence, validation and error estimates. *Computer Methods in Applied Mechanics and Engineering*, 149 (1997) (1): 223–254. Containing papers presented at the Symposium on Advances in Computational Mechanics.

ZIENKIEWICZ O. & TAYLOR R. *The Finite Element Method*, volume I. Oxford: Butterworth-Heinemann, 2005.

ZOHDI T. & WRIGGERS P. *An Introduction to Computational Micromechanics*, volume 20. 2005.

List of Figures

1.1	Simulation process steps from HARDWICK ET AL. (2005).	2
1.2	Engineering time for commercial modeling (normalized) from HARDWICK ET AL. (2005).	2
1.3	Virtual element discretization with arbitrary shaped elements, including non-convex animal type elements.	3
2.1	Motion of a body from the initial configuration \mathcal{B}_0 to the current configuration \mathcal{B}_t	5
2.2	Infinitesimal volume element with stresses, which are relevant for the equilibrium of linear momentum in the direction x_1	9
2.3	Infinitesimal volume element with stresses, which are relevant for the equilibrium of angular momentum around the x_3 -axis.	10
3.1	Motion of two body from the initial configuration \mathcal{B}^α to the current configuration $\varphi^\alpha(\mathcal{B}^\alpha)$	19
3.2	Contact kinematics of two bodies $\varphi^\alpha(\mathcal{B}^\alpha)$ in the current configuration.	20
3.3	Schematic illustration of different contact discretizations.	23
4.1	Discretization of the solid.	26
4.2	Comparison of interpolation functions for FEM and VEM.	28
4.3	Isoparametric mapping of the deformation of single finite element Ω_E	29
4.4	Single three dimensional virtual element with faces and edges.	31
4.5	Virtual element with polygonal faces, subdivided in to triangles.	33
4.6	Virtual element with polygonal faces.	35
4.7	Virtual element with polygonal faces, subdivided in to tetrahedrons.	42
4.8	VEM shape functions for displacements \mathbf{u}_π , pressure p_π and dilatation Θ_π	42
4.9	Contourplots showing stresses S_{zz} for patch test with H1 shaped virtual elements and different stabilizations, integration schemes for the virtual parameters and load parameters.	44
4.10	Contourplots showing stresses S_{zz} for patch test with VO shaped virtual elements and different stabilizations, integration schemes for the virtual parameters and load parameters.	45
4.11	Stabilization parameter β^{stat} as a function of the plastic deformation α	49
4.12	Patch test with applied displacement boundary condition at the upper face.	50
4.13	Deformation plot showing the displacements in X -, Y - and Z -direction.	50
4.14	Deformation plot showing the stresses in X -, Y - and Z -direction.	51

4.15	Projection test of a simple block.	51
4.16	Single triangular finite and virtual element.	52
4.17	Single quadrilateral finite and virtual element in (a) and (b) and the internal submesh of the virtual element with linear finite element triangles in (c). . .	53
5.1	Triangle in parametric space (left) and 3D Euclidian space (right).	56
5.2	Node-to-surface discretization.	56
5.3	Node-to-node discretization using node insertion.	58
5.4	Node insertion from B^1 to B^2 and vice versa with a) initial mesh, b) two particular elements from B^1 and B^2 , c) faces of this two elements, which get projected to each other, d) nodes which will be inserted due to intersecting edges and vertices, e) nodes which are inserted and new faces of elements and f) new final mesh with conforming nodes.	58
5.5	Update of history field and mapping between current and initial configuration	61
5.6	Surface-to-surface discretization using node insertion.	62
5.7	Body \mathcal{B}^1 discretized with solid elements and contact interface discretized with contact elements based on a surface-to-surface contact formulation in (a) and contact element with polygon pairs from both bodies \mathcal{B}^1 and \mathcal{B}^2 with node numbering in (b).	63
5.8	Rotation of polygonal face.	64
5.9	Projected displacements \mathbf{u}_π^1 and \mathbf{u}_π^2 from both contact pairs in (a), projected gap function $g_{N\pi}$ in (b) and the function $g_{N\pi}^2$ in (c) which has to be integrated in equation (5.28).	66
6.1	3D Cook's membrane for testing of different integration schemes for the computation of the virtual parameters.	69
6.2	3D Cook's membrane - Convergence study for edge integration (EI) and triangle integration (TI) with stabilization based on an internal energy (s1) and stabilization based on the degrees of freedom (s2).	71
6.3	3D Cook's membrane - Contourplots showing stresses S_{xx} with voronoi shaped virtual elements.	72
6.4	3D Cook's membrane - Contourplots showing stresses S_{xx} with H1 shaped virtual elements.	72
6.5	3D Cook's membrane - Contourplots showing stresses S_{xx} with H2S shaped virtual elements.	73
6.6	Eigenfrequencies ω_n in Hz of a single element (free-free) for different stabilization parameters β^{stat} and β^{dyn}	74
6.7	Eigenfrequencies ω_n and modeshapes for single element with free-free boundary condition and stabilization parameters $\beta^{stat} = \beta^{dyn} = 0.4$	75
6.8	Eigenvalues of stiffness and mass matrix for 2D beam (C-F).	76
6.9	Eigenfrequencies for 2D beam (C-F).	77
6.10	Wave propagation in longitudinal beams - Boundary value problem.	78
6.11	Wave propagation in longitudinal beams - Displacement over time response.	78
6.12	Transversal beam vibration.	79
6.13	Transversal beam vibration - Different meshes.	79

6.14	Transversal beam vibration - Displacement over time response at $X = L$ (1).	80
6.15	Transversal beam vibration - Displacement over time response at $X = L$ (2).	80
6.16	2D Cook's membrane problem.	81
6.17	2D Cook's membrane problem - Von Mises stress distribution at time $t = 0.035$ ms for different elements at same scale.	82
6.18	2D Cook's membrane problem - Displacement over time response at the tip with element division 2^N , where N increases from (a) to (d)	83
6.19	Wave propagation in a bar - Displacement over time response with initial velocity of $v_{0,x} = 20 \frac{\text{m}}{\text{s}}$	84
6.20	Transversal vibration of a thick beam - Boundary value problem.	84
6.21	Transversal vibration of a thick beam.	85
6.22	Transversal vibration of a thick beam - Von Mises stress distribution at time $t = 0.1$ ms with different element types.	85
6.23	Transversal vibration of a thick beam - Displacement over time response with element division 2^N , where N increases from (a) to (d)	86
6.24	Vibration of a thick plate - Boundary value problem.	87
6.25	Vibration of a thick plate - Vertical displacement over time response at the center of the plate.	88
6.26	Vibration of a thick plate - Evolution of the displacement in the Z -direction with different deformation states.	88
6.27	Necking problem - Boundary value problem.	91
6.28	Necking problem - Force-displacement response with two different mesh densities.	91
6.29	Necking problem - Deformation state with different elements, showing the accumulated plastic strain.	92
6.30	3D Beam - Displacement over time response for different element types and mesh discretization in (a) to (c) with $\nu=0.3$ and (d) to (f) with $\nu = 0.499999$	93
6.31	3D Beam - Error of the maximum displacement over time for different element types and various Poisson's ratios in (a) to (c)	93
6.32	Taylor Anvil test.	94
6.33	Taylor Anvil test - Deformation state for different elements, showing the accumulated plastic strain.	95
6.34	Taylor Anvil test - Length change over time for different mesh densities and element formulations.	96
6.35	Taylor Anvil test - Evolution of the mushroom radius r_m for different mesh densities and element formulations.	96
6.36	Punch problem - Boundary value problem.	97
6.37	Punch problem - Deformation state for different elements, showing the accumulated plastic strain.	98
6.38	Punch problem - Time history of maximum displacement at the tip in (a) , error of the maximum displacement over number of elements in (b) and maximum displacement over number of elements in (c)	99
6.39	Contact patch test - Boundary value problem with mesh at contact interface.	100

6.40	Contact patch test - Deformed state showing the stresses σ_{zz} for node-to-node (NTN) and node-to-surface (NTS) contact.	101
6.41	Node-to-node contact with non-matching triangles and tetrahedrons at the contact interface.	102
6.42	Node-to-node contact with matching triangles and tetrahedrons at the contact interface.	102
6.43	Hertzian contact - Boundary value problem.	103
6.44	Hertzian contact - Stress distributions in normal direction defined as $\sigma_{zz} = (\boldsymbol{\sigma}\mathbf{n}) \cdot \mathbf{n}$ with node-to-node in (a, c) and node-to-surface contact in (b, d).	104
6.45	Hertzian contact - Stress distributions in deformed configuration with actual stress in normal direction σ_{zz} in (a, b, c, d) and von Mises stress σ_{vm} in (e, f, g, h).	105
6.46	Rotating blocks - Stress distributions σ_{zz} for different rotation angles from a) to f) showing both bodies and g) to l) showing the lower block with $\theta \in \{0, 18, 36, 54, 72, 90\}$	106
6.47	Rotating blocks - Reaction forces over rotation angle with rotation increment $\Delta\theta = 2^\circ$	106
6.48	Rotating blocks - Reaction forces over rotation angle with rotation increment $\Delta\theta = 5^\circ$. Comparison with Weissenfels et al. DZIEWIECKI ET AL. (2015).	107
6.49	Mesh at the interface of both contact pairs in (a) and contact elements at the interface in (b)	108
6.50	Contourplots for S_{zz} for the contact patch test with regular shaped virtual elements showing different contact formulations.	108
6.51	Contourplots for S_{zz} for the contact patch test with regular shaped virtual elements and surface-to-surface contact formulation.	109
6.52	Contourplots for S_{zz} for the contact patch test with regular shaped virtual elements and node-to-node contact formulation.	110
6.53	Coupled Taylor Anvil impact - Different energies over time responses for.	112
6.54	Coupled Taylor Anvil impact - Deformed state showing the accumulated plastic deformation distributions at different time from a) to e).	112
7.1	Topology optimization of a beam which is under bending. Different optimization steps from top to bottom with Voronoi elements as initial mesh and refinement of the mesh.	115

List of Tables

4.1	Major differences between FEM and VEM.	28
6.1	Material parameters used for the numerical examples	70
6.2	Eigenfrequencies ω_n in Hz for 2D beam (C-F) with 1600 elements for mod- etype: T=Transversal and L=Longitudinal.	77
6.3	Material parameters used for the numerical examples	89
6.4	Material parameters used for the Taylor Anvil test	94
6.5	Taylor Anvil test - Comparison of different results obtained in the literature.	97
6.6	Taylor Anvil test - Comparison of results for different element types.	97
6.7	Numerical parameters used for coupled Taylor Anvil contact example.	111
A.1	One-dimensional Gauss-Integration.	119
A.2	Two-dimensional Gauss-Integration for triangular elements.	119
A.3	Three-dimensional Gauss-Integration for tetrahedral elements.	119

Curriculum vitae

Mertcan Cihan

born December 26, 1992 in Bremen, Germany

Professional Experience

since 04.2019 Research assistant at the Institute of Continuum Mechanics,
Leibniz Universität Hannover

Education

10.2016 - 01.2019 University of Bremen
Production Engineering
Focus: General Engineering
Degree: M. Sc.

10.2012 - 09.2016 University of Bremen
Production Engineering
Focus: General Engineering
Degree: B. Sc.

1999 - 2012 Elementary education at Grundschule an der Melanchthonstraße,
Orientierungsstufe an der Helgolanderstraße,
Secondary education at SZ Findorff and SZ Walle, Bremen

